SURFACE-BASED TEMPERATURE INVERSIONS AND PERMAFROST DYNAMICS IN THE MOUNTAINS OF NORTHCENTRAL YUKON: LINKING OBSERVATIONS AND DOWNSCALED CLIMATE MODELS

NICK NOAD
Master of Science, University of Lethbridge, 2021

A thesis submitted
in partial fulfilment of the requirements for the degree of

DOCTOR OF PHILOSOPHY

in

EARTH, SPACE, AND PHYSICAL SCIENCE

Department of Geography and Environment
University of Lethbridge
LETHBRIDGE, ALBERTA, CANADA

SURFACE-BASED TEMPERATURE INVERSIONS AND PERMAFROST DYNAMICS IN THE MOUNTAINS OF NORTHCENTRAL YUKON: LINKING OBSERVATIONS AND DOWNSCALED CLIMATE MODELS

Nick Noad

Date of Defense: July 16, 2026

Dr. Philip Bonnaventure Thesis Supervisor	Associate Professor	Ph.D.
Dr. Hester Jiskoot Thesis Examination Committee Member	Professor	Ph.D.
Dr. Yu Zhang Thesis Examination Committee Member Natural Resources Canada Ottawa, Ontario	Research Scientist	Ph.D.
Dr. Robert Way Thesis Examination Committee Member Queen's University Kingston, Ontario	Associate Professor	Ph.D.
Dr. Sebastian Westermann External Examiner University of Oslo Oslo, Norway	Professor	Ph.D.
Dr. Craig Coburn Chair, Thesis Examination Committee	Professor	Ph.D.

Dedication

I dedicate this thesis document to each of the friends and family, especially my wife Elizabeth and son Edmund. They are the reason I do any of this.

Abstract

Surface-based temperature inversions (SBIs) exert a dominant control on surface air temperature patterns in high-latitude mountain environments. Long-term climate observations are sparse in these regions, so gridded climate datasets are commonly utilized. However, SBIs are poorly represented in these datasets, introducing systematic bias into permafrost models that rely on gridded or downscaled air temperature fields. In this thesis, I investigate the role of SBIs in shaping surface air temperature variability in subarctic Yukon valleys and evaluate how improved representation of these patterns influence permafrost modelling outcomes. Using a dense network of in-situ air temperature sensors along elevational transects, we quantify the spatial and temporal variability of SBIs in dissimilar valley environments. Results demonstrate that strong SBIs in subarctic valleys with strong gradients of warming with elevation near the valley bottom and much weaker gradients above. These inversion-driven patterns are poorly resolved in coarse-resolution reanalysis datasets, leading to systematic biases in air temperature estimates. To address this limitation, inversion-aware bias reduction approaches for downscaling reanalysis air temperatures are evaluated and developed. A physically informed model (DReaMIT) is introduced to improve transferability. Results show that incorporating SBI processes substantially improves representation of air temperature patterns and reduces model error. Finally, the influence of SBI-aware climate forcing on permafrost and ground thermal regimes is assessed using the Northern Ecosystem Soil (NEST) model. Results demonstrate that SBI-driven temperature adjustments can significantly alter predicted ground temperatures and active layer thickness. While snow redistribution remains the dominant control on local variability, SBI-related air temperature adjustments can exceed its influence at some sites. Overall, this thesis highlights the critical importance of representing SBIs in permafrost

modelling and provides new methods for reducing SBI-related bias in climate forcing data in high-latitude complex terrain, improving confidence in predictions of permafrost change in high-latitude mountain environments.

Use of Generative AI

Generative AI tools (ChatGPT, OpenAI) were used to assist in editing text for clarity, grammar, and readability. These tools were also utilized to support troubleshooting of R and Python scripts used for the analysis presented in this thesis. All analytical decisions, interpretations, and final content were developed and verified by the author. No generative AI tools were used to generate original research content, results, or interpretations.

Preface

This thesis is presented in manuscript format. Chapters 3-6 are presented as standalone manuscripts prepared for submission to a peer-reviewed journal. Co-authorship and individual contributions for each chapter are outlined below.

Chapters One was conceived by Philip Bonnaventure and me. I led the writing of this chapter, with editorial support from Philip Bonnaventure.

Chapter Two was conceived by Philip Bonnaventure and me. I led the writing of this chapter, with editorial support from Philip Bonnaventure.

Chapter Three was conceived by Philip Bonnaventure and me. I led the analysis and writing of this manuscript, with extensive editorial contributions from Philip Bonnaventure. Preparation of this manuscript for submission to *Arctic, Antarctic, and Alpine Research* was led by me, with support from Philip Bonnaventure.

Chapter Four was conceived by Philip Bonnaventure, Stephan Gruber, Victor Pozsgay, and me. I led the analysis and writing of this manuscript. All co-authors reviewed the work and provided feedback to support its preparation for submission to *Arctic Science*.

Chapter Five was conceived by Stephan Gruber, Victor Pozsgay, Philip Bonnaventure, and me. Victor Pozsgay led the analysis and writing of this manuscript. I contributed to the study design, provided consultation throughout the analysis, assisted with portions of the modelling and analysis, and wrote sections of the manuscript, including the introduction, study area, and parts of the methods and discussion. I was also the primary editor of the manuscript in preparation for submission to *Geoscientific Model Development*.

Chapter Six was conceived by Yu Zhang, Philip Bonnaventure, and me. I led the analysis and writing of this manuscript. Yu Zhang and Philip Bonnaventure provided editorial feedback and suggested additional analyses to support preparation for submission to *Permafrost and Periglacial Processes*.

Chapter Seven was conceived and written by me. It was edited by Philip Bonnaventure.

Acknowledgments

I would like to acknowledge the support of the many individuals who contributed to my PhD research. I am especially grateful to my supervisor, Philip Bonnaventure, for his guidance, mentorship, and continued support throughout my graduate studies. His time, insight, and encouragement have been invaluable, and I am deeply appreciative of the role he has played in both my academic and professional development.

I would also like to thank my supervisory committee members. Hester Jiskoot has spent many hours supporting me throughout my academic journey, from my undergraduate degree through to the completion of this PhD. Yu Zhang generously contributed his time and expertise, particularly in helping me develop a deeper understanding of the NEST model. Robert Way provided valuable feedback and support during the final years of my degree. I also thank Derek Peddle, who previously served on my PhD committee, for his guidance during my proposal and comprehensive exam. I thank Laura Chasmer for serving as an external examiner for my comprehensive exam and Craig Coburn who served as chair for both my comprehensive examination and proposal defence. I am grateful to Sebastian Westermann for serving as the external examiner for this thesis. I want to thank Craig Coburn for being willing to serve a chair of this PhD defense and for my comprehensive examination.

This research would not have been possible without the many individuals who assisted with fieldwork. I sincerely thank Philip Bonnaventure, Scott Lamoureux, Madeleine Garibaldi, Ria Nicholson, Scott Vegter, Aidan Musk, Jeremy Benson, Rebecca Thiesen, Mitch Codd, Sophie MacLean, Emma Marnik, Caroline Aubry-Wake, Corbin Friesen, Zeeshan Hamayun, Jenn White, Dave Atkinson, Seamus Daly, Oliver Kienzle, Kyle Bexte, and Rory Gibson for their time, effort, and support in the field.

Finally, I gratefully acknowledge the financial support provided by the University of Lethbridge, NSERC, and NSTP, as well as funding received through the NSERC CGRS-D program, the Alberta Graduate Excellence Scholarship, and the University of Lethbridge Research Award, which financially supported both my research and my family during my graduate studies.

Table of Contents

List of Tables

List of Figures

List of Abbreviations

ALT – Active Layer Thickness
DReaMIT – Dynamical Reanalysis Model for Inversions of Temperature
dTmin – Monthly air temperature adjustment factors for daily minimum temperatures
dTmax – Monthly air temperature adjustment factors for daily maximum temperatures
ECCC – Environment and Climate Change Canada
EFT – East Facing Transect
ERA5 – ECMWF Reanalysis 5
ERA5-Land – Land-surface component of ERA5
ETA – Elevation Transect Analysis
F_{snow} – Snow Redistribution Input Factor
GST – Ground Surface Temperature
GT – Ground Temperature
JRA-3Q – Japanese Three Quarters of a Century Reanalysis (JMA product)
KGE – Kling–Gupta Efficiency
LAI – Leaf Area Index
LSCF – Land Surface Correction Factor
MAE – Mean Absolute Error
MAGT – Mean Annual Ground Temperature
MAGST – Mean Annual Ground Surface Temperature
MAAT – Mean Annual Air Temperature
MBE – Mean Bias Error
MRVBF – Multi-Resolution Valley Bottom Flatness Index
NEST – Northern Ecosystem Soil Temperature model
nf – Freezing n-factor
NSE – Nash–Sutcliffe Efficiency
NFT – North Facing Transect
nt – Thawing n-factor
REDCAPP – REanalysis Downscaling Cold Air Pooling Parameterization
RMSE – Root Mean Square Error
R^2 – Coefficient of Determination
SBI – Surface-Based Temperature Inversion
SFT – South Facing Transect
SLR – Surface Lapse Rate
T_{mod} – Inversion Bias Correction Modelled Temperature
T_{obs} – In-situ Recorded Temperature
T_{pl} – Reanalysis Pressure Level Temperature
T_{sur} – Reanalysis Surface Air Temperature
TTOP – Temperature at the Top Of Permafrost
UTC – Coordinated Universal Time
WFT – West Facing Transect
WS01 / WS02 – Weather Station 1/2

1. Introduction and Thesis Statement

Permafrost is a critical part of the cryosphere and consists of ground material that is perennially frozen for two or more consecutive years (Harris et al., 1988; Lewkowicz et al., 2025). Permafrost is found predominantly in high latitude and high elevation areas where cold climate supports its persistence and/or ecosystem structure remains optimal for its continuation (French & Williams, 2013). Permafrost provides important ecosystem services including carbon storage (Olefeldt et al., 2016; Ping et al., 2015; Schuur et al., 2015), landscape stability (Kokelj & Jorgenson, 2013), regulation of solute movement (Abbott & Jones, 2015; Olson et al., 2018), and hydrological stability (Carpino et al., 2021; Connon et al., 2015; Connon et al., 2014). Furthermore, permafrost is the only component of the cryosphere on which people live year-round and build long-term infrastructure such as settlements, roads, and pipelines (French & Williams, 2013; Hjort et al., 2018).

Permafrost underlies approximately 15% of the exposed land area of the Northern Hemisphere (Obu et al., 2021), with the vast majority occurring in Arctic and subarctic lowlands. In contrast, alpine permafrost is restricted to high-elevation mountain environments worldwide and occupies a much smaller, discontinuous area, although its global extent remains difficult to quantify due to its fragmented distribution and limited observations (Gruber, 2012). Mean annual air temperature (MAAT) is the primary control on broad-scale patterns of permafrost distribution across large geographic regions (Gruber, 2012; Smith & Riseborough, 2002). Unlike lowland regions where MAAT is fairly consistent across large areas (e.g., Garibaldi et al., 2021; Vegter et al., 2024), upland permafrost regions have a MAAT that varies significantly across complex mountainous terrain due to elevational-dependent surface air temperature patterns and other topoclimatic factors (Etzelmüller, 2013; Riseborough et al., 2008).

One phenomenon that produces positive surface lapse rates (SLRs), is a surface-based temperature inversion (SBI) (Ross, 2024; Whiteman, 2000). SBIs occur when surface air temperature increases with elevation, denoted as positive SLR, rather than the common adiabatically driven decrease in temperature with elevation (Bradley et al., 1992; Whiteman, 2000). SBIs have been measured in subarctic valleys to shape mean annual SLRs to be as positive as 12 °C km^{-1} (Noad & Bonnaventure, 2022). However, these local SBI patterns are poorly resolved in commonly used gridded climate datasets, leading to systematic biases in near-surface air temperature (Cao et al., 2017; Noad & Bonnaventure, 2022; Pozsgay & Gruber, 2025) that can propagate directly into permafrost modelling. In remote high-latitude mountain environments, long-term climate forcing is often limited to gridded climate datasets because in-situ meteorological observations are sparse (Way & Bonnaventure, 2015). Therefore, SBIs have been identified as an important variable to consider in permafrost modelling for high-latitude mountainous regions of Northwestern Canada. Until recently, permafrost modelling has underrepresented the magnitude of impact SBIs have on elevational surface air temperature patterns in northwestern Canada (Lewkowicz et al., 2012). This impact of SBIs must be included in permafrost modelling on both local and regional scales to continue to improve the accuracy of estimated permafrost distribution, thermal state, and active layer thickness and how they respond to climate warming. A complicating factor for predicting permafrost distribution is the non-linear relationship between MAATs and mean annual ground surface (MAGST) and mean annual ground depth temperatures (Gubler et al., 2013; Henry & Smith, 2001; Smith & Riseborough, 2002). Variables such as vegetation cover, snow cover, soil substrate properties, and hydrology all interact with MAAT to define ground temperature (Way & Lewkowicz, 2018). Though SBIs impact surface air temperature, how this impact translates to ground depth temperature is still not fully understood. Recent permafrost modelling has begun the process of addressing this gap (Garibaldi et al., 2024a, 2024b), but there remains work to be done to quantify this relationship, particularly in a region where thermal disequilibrium reigns due to arctic amplification (Serreze & Barry, 2011) and elevation-dependent warming (Pepin et al., 2015).

This thesis addresses the challenge of bias induced by SBIs in climate forcing datasets by investigating how SBIs shape air temperature patterns in subarctic valleys, developing methods to incorporate inversion effects into downscaled climate data, and evaluating how these improvements influence model simulations of permafrost thermal dynamics.

The remainder of this thesis is organized as follows. Chapter 2 provides a literature review of (1) the processes governing the thermal state of permafrost, (2) approaches to modelling permafrost and its thermal state; (3) the strengths, limitations, and recent advances in downscaling climate data in complex mountainous terrain; (4) SBIs impact on surface air temperatures both generally and more specifically in high-latitude valleys; and (5) the implications of these processes for ground thermal dynamics in subarctic mountain environments. In this literature review, key knowledge gaps are identified and are used to inform research objectives and hypotheses which are addressed in subsequent chapters. Chapters 3-6 present original research presented in this thesis, progressing from the characterization of surface-based temperature inversions to the development and evaluation of inversion-aware climate downscaling methods, and finally to the application of these methods in transient permafrost modelling. Chapter 7 summarizes the main findings of the thesis, discusses their implications, and outlines directions for future research.

2. Literature Review

2.1 The Geographical Distribution and Thermal State of Permafrost

The presence of permafrost is governed by annual and long-term balance between atmospheric input, surface modification processes, and subsurface heat transfer. When annual and multi-year heat losses balance or offset seasonal heat gains, ground temperature remains at or below 0 °C for at least two consecutive years (French & Williams, 2013). Spatial patterns of permafrost distribution therefore reflect heterogeneity in atmospheric forcing, snow cover, and vegetation controls on surface energy exchange, as well as substrate properties, and Pleistocene permafrost conditions.

At broad scales, mean air temperature (MAAT) serves as a metric of atmospheric energy forcing and therefore explains broad patterns of permafrost distribution (Gruber, 2012; Shur & Jorgenson, 2007; Smith & Riseborough, 2002). These broad patterns of permafrost distribution are commonly classified according to the proportion of the land underlain by permafrost and include continuous (90-100%), extensive discontinuous (50-90%), sporadic discontinuous (10-50%) and isolated patches (0-10%) (Heginbottom et al., 1995) (Figure 2-1). The transition from continuous permafrost to discontinuous permafrost occurs broadly between a MAAT of -6 to -8 °C (French & Williams, 2013; Smith & Riseborough, 2002). In addition, permafrost may also persist in relict settings, including areas of subsea permafrost that were once exposed during lower sea levels in glacial periods but are now submerged (French and Williams, 2013).

Figure 2-1: Permafrost distribution in Canada modified from Heginbottom et al. (1995) (Canadian Permafrost Association, 2024, © Copyright Canadian Permafrost Association).

Spatial variability in permafrost thermal state emerges from interactions between atmospheric forcing, surface energy modifiers (snow and vegetation), and subsurface heat transfer processes (French & Williams, 2013; Smith & Riseborough, 1996; Williams & Smith, 1989). These interactions are commonly conceptualized using three linked temperature components: mean annual air temperature (MAAT), mean annual ground surface temperature (MAGST), and temperature at the top of permafrost (TTOP) (Henry & Smith, 2001; Smith & Riseborough, 1996) (Figure 2-2). Together, these temperature fields describe how atmospheric energy forcing is progressively modified at the surface and within the subsurface.

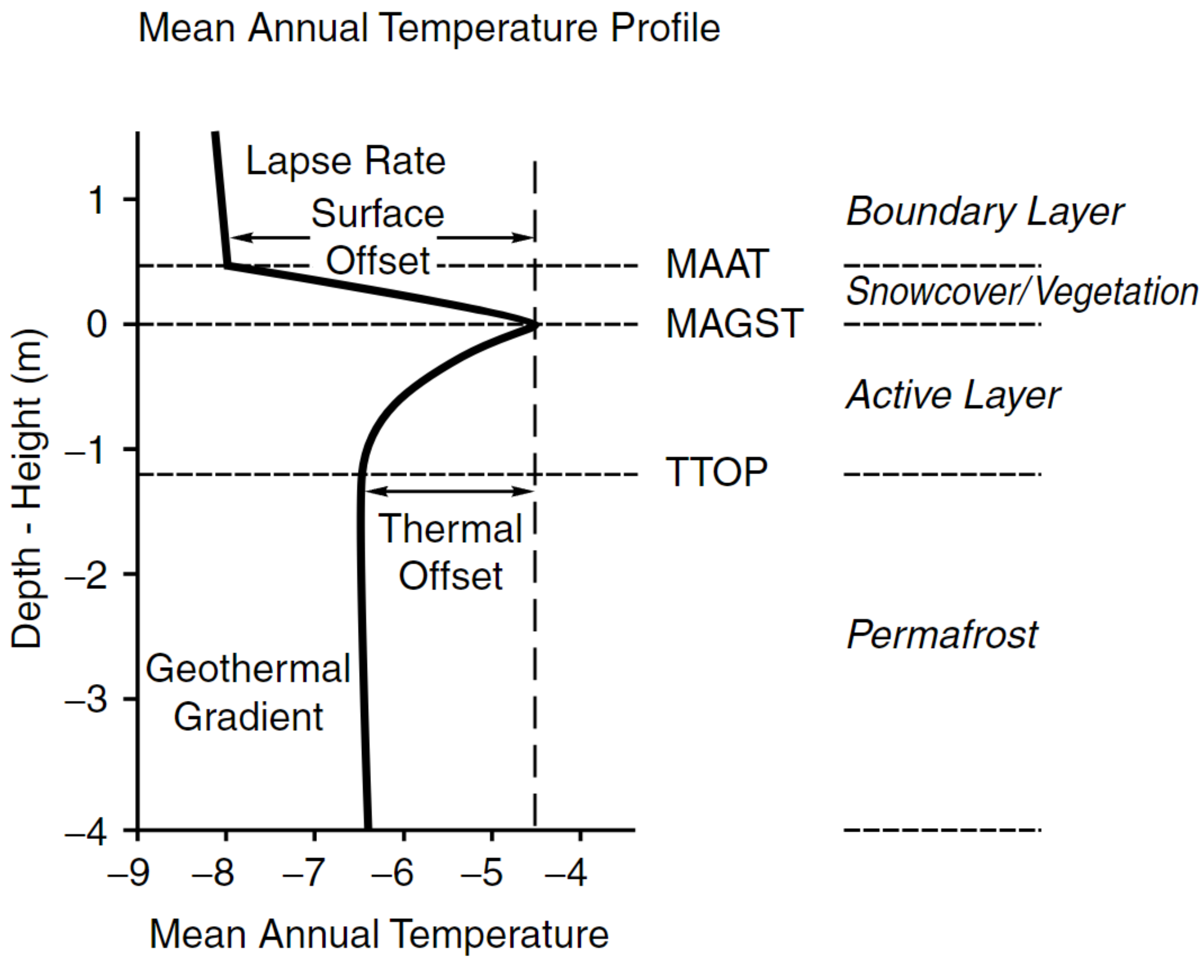

Figure 2-2: Mean annual temperature profiles and associated offsets from the boundary layer of the atmosphere to the permafrost layer (Henry and Smith, 2001, p. 3, Copyright © 2001 John Wiley & Sons, Ltd.). Mean annual air temperature (MAAT) is related to the mean annual ground surface temperature (MAGST) through a term called the surface offset. The MAGST is related to the temperature at the top of permafrost (TTOP) through the thermal offset.

2.1.1 Surface Energy Modification and Surface Offset

The difference between MAAT and MAGST is known as the surface offset and reflects seasonal modification of atmospheric energy when it reaches the ground surface (French & Williams, 2013). This offset is primarily dependent on snow cover and vegetation, which regulates heat flux through insulation, shading, and changes in surface albedo (Henry & Smith, 2001; Smith & Riseborough, 2002). These surface covers are considered the buffer layer, and the temperature offsets of this layer can be quantified by transfer functions called n-factors (Vincent et al., 2017).

2.1.1.1 Freezing season surface offsets and snow cover

Snow exerts a dominant control on winter surface energy exchange due to its low thermal conductivity (0.024 to 0.8 W $m^{-1}K^{-1}$) (Zhang, 2005), which restricts heat loss from the ground into the cold winter atmosphere (Zhang et al., 2018). As snow depth increases and air temperature decreases, the ground becomes more insulated causing the ground surface to remain warmer than the overlying air (Smith & Riseborough, 2002). This decoupling between air and ground temperature is referred to as the nival offset (Karunaratne & Burn, 2004).

The magnitude of this decoupling can be quantified using the freezing n-factor (nf), defined as the ratio of freezing degree days at the ground surface to those in the air (Henry & Smith, 2001; Riseborough et al., 2008) (Lunardini, 1978).

$$n_{\mathrm{f}} = \frac{FDD_{\mathrm{s}}}{FDD_{\mathrm{a}}} \qquad \text{(Eq. 2-1)}$$

nf is on a scale of 0 to 1, with lower values indicating stronger insulation and greater decoupling of the ground surface temperature (GST) from the 2 m surface air temperature, whereas values approaching 1 indicated stronger atmospheric control (Garibaldi et al., 2021; Way & Lewkowicz, 2018). The effects of *nf* are typically greater in warmer MAAT with shallower snow depths, due to the reliance of snow metamorphism and density on temperature (Smith & Riseborough, 2002) (Figure 2-3).

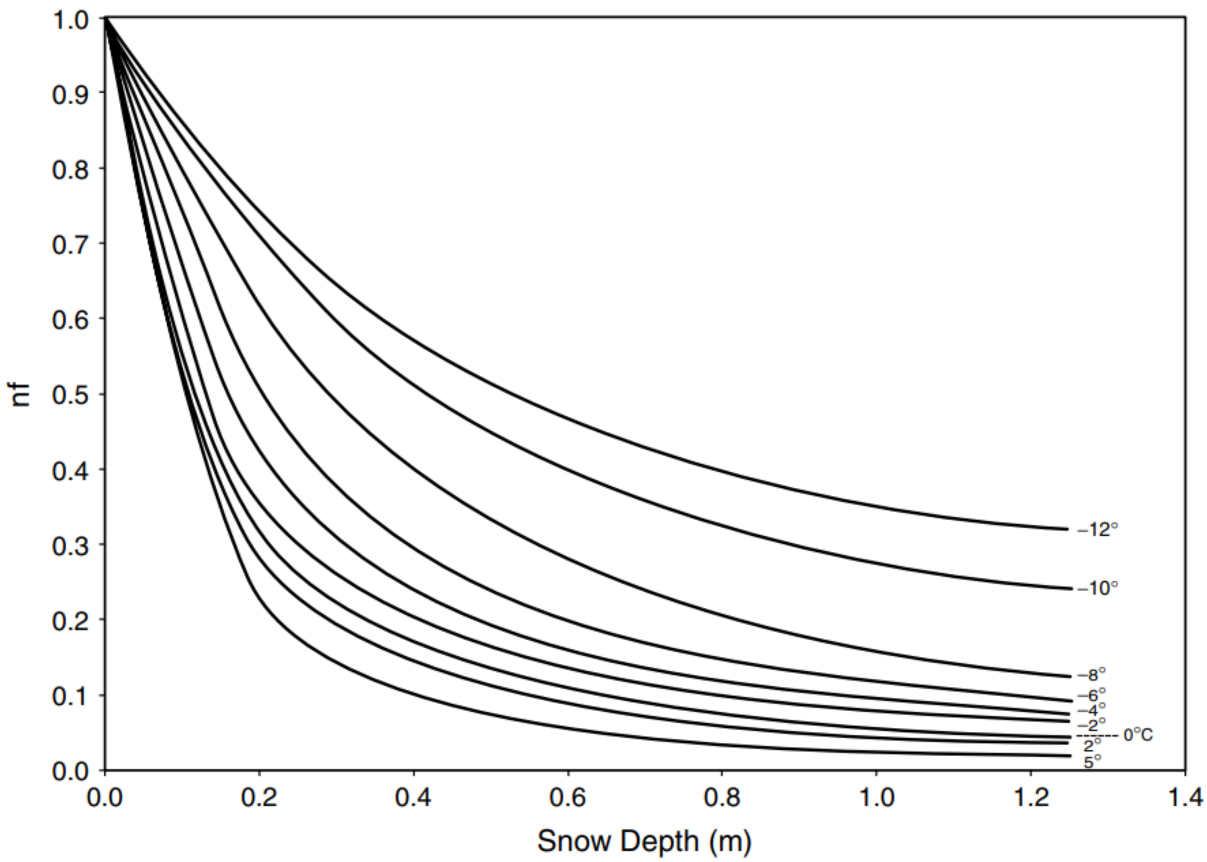

Figure 2-3: nf as a function of snow depth and MAAT (Smith and Riseborough, 2002, p. 7, Copyright © 2002 John Wiley & Sons, Ltd.).

Denser snow contains less pore space and therefore exhibits a higher thermal conductivity, increasing conductive heat loss from the ground (Zhang, 2005). Sensitivity analysis demonstrates that realistic changes in snow depth and density can substantially alter winter surface offsets, reducing thermal conductivity of snow from 0.7 W m^{-1} K^{-1} to 0.1 W m^{-1} K^{-1} and the surface offset increased by up to 5.5 °C (Goodrich, 1982). Projected climate-driven changes in snowfall, compaction, and rain-on-snow events therefore have the potential to significantly modify the winter surface offset (Winstral & Marks, 2014; Zhang, 2005). Since snow properties vary spatially and interannually, freezing n-factors are not easily transferable between regions (Way & Lewkowicz, 2018).

High-latitude cold climate areas are particularly reliant on snow cover and resulting *nf* to determine spatial variability in permafrost thermal conditions (Garibaldi et al., 2026). For example, at Cape Bounty in the High Canadian Arctic, where MAAT varied little across the 19.6 km^2 study area, incised terrain where snow accumulates had *nf* that were as low as 0.33 and the resulting MAGST was as great as -3.9 °C. Whereas on elevated terrain where snow was scoured, MAGST was -13.8 °C (Garibaldi et al., 2021). Thus, in the Arctic and sub-Arctic terrain, snow redistribution by wind and topography can generate multi-degree differences in MAGST within tens of metres, even when MAAT is nearly uniform (e.g., Jorgenson et al., 2010; Romanovsky et al., 2010).

Snow strongly controls winter energy flux but is spatially heterogenous and difficult to measure directly at a meaningful scale (Clark et al., 2011; Egli et al., 2011; Jost et al., 2007). Wind redistribution, topographic exposure, and vegetation structure generate substantial sub-grid variability, often producing up to 6 °C variability in ground temperatures within area represented by a single model grid cell (Gisnås et al., 2017; Gisnås et al., 2014; Gisnås et al., 2016; Gubler et al., 2011). Consequently, coarse-resolution permafrost models frequently underrepresent snow-driven thermal heterogeneity, particularly in mountainous regions.

High-resolution snow depth and density can be measured using in situ observations (Deems et al., 2013; Tutton & Way, 2021) or airborne LiDAR (Barnes et al., 2020; Cartwright et al., 2020), however such approaches are costly and logistically challenging in high-latitude environmnets. As a result, High-resolution long-term monitoring of snow redistribution and density variability remains sparse, particularily in mountainous Arctic and sub-Arctic regions (Przybylak, 2016).

Given the difficulty of directly resolving snow heterogeneity, many permafrost modelling approaches rely on proxies that capture dominant snow redistribution processes. Topography controls snow redistribution through wind exposure and incised terrain (Young et al., 1997), while vegetation modifies snow trapping and compaction (Rasmus et al., 2011; Roy-Léveillée et al., 2014). These controls can be parameterized using terrain indices, land cover classifications, or empirically derived factors (Garibaldi et al., 2024b; Quéno et al., 2024; Winstral et al., 2002).

Vegetation structure can serve as an effective proxy for snow redistribution patterns. Coniferous forest canopies promote interception of snow leading to reduced winter insulation (Duchesne et al., 2015; Rasmus et al., 2011), while shrubs promote trapping of snow leading to stronger winter insolation (Frost et al., 2018; Marsh et al., 2010; Ménard et al., 2014; Myers-Smith et al., 2011), and tundra and sparsely vegetated terrain are more susceptible to wind scour leading to effective transfer of heat from the ground to air in the winter (Garibaldi et al., 2021; Way & Lewkowicz, 2018).

2.1.1.2 Thaw season surface offsets and vegetation

Vegetation modifies the thaw-season surface energy balance primarily by reducing shortwave radiation reaching the ground and decoupling of the air and ground surface temperature (Smith & Riseborough, 2002). Canopy shading lowers soil energy input, limiting seasonal heat penetration and producing a thaw-season surface offset that is commonly parameterized using the thawing n-factor (n_t) (Riseborough, 2003):

$$n_t = \frac{TDD_s}{TDD_a} \qquad \text{(Eq. 2-2)}$$

where TDD_s and TDD_a are the thawing degree days for the ground surface and air respectively. The n_t, ideally ranges from 0 to 1 with lower values indicating stronger decoupling of the air and ground temperature (French & Williams, 2013). n_t is often lowest in forest areas with a thick canopy, while it is highest (often greater than 1) in unvegetated areas (Jorgenson et al., 2010; Juliussen & Humlum, 2007; Morse et al., 2016). In areas where vegetation is sparse or absent, n_t can be greater than 1 as these exposed surfaces warm quicker under direct incoming solar radiation than the air above (Garibaldi et al., 2021; Lewkowicz et al., 2012; Lin et al., 2015).

Since vegetation structure strongly influences shading conditions, landcover classification derived from remote sensing and in-situ stratified random sampling are commonly used to spatially parametrize n_t in permafrost models (Bevington & Lewkowicz, 2015; Vegter et al., 2024; Way & Lewkowicz, 2018).

Thus vegetation functions as both a radiative modifier during the thaw season and a snow redistribution control during the freezing season, linking summer and winter offsets within an annual energy balance framework.

2.1.2 Substrate properties and thermal offset

The thermal offset is the difference between GST and TTOP. This offset is largely driven by the phase-dependent differences in thermal conductivity of the substrate (Biskaborn et al., 2019; French & Williams, 2013; Smith & Riseborough, 1996, 2002; Way & Lewkowicz, 2016).

When soils freeze, the presence of ice substantially increases thermal conductivity relative to thawed conditions, particularly in fine-grained organic-rich substrates with higher moisture content (Smith & Riseborough, 2002). As a result, conductive heat loss in the winter is often more efficient than heat gain in the summer. This seasonal asymmetry in heat transfer leads to colder ground temperatures at depth than at the surface (Way & Lewkowicz, 2016, 2018).

Soil texture, moisture content, and soil organic layer thickness regulate the magnitude of the thermal offset (Burn & Smith, 1988). Dry, coarse substrates exhibit smaller contrasts between frozen and thawed conductivity and consequently smaller offsets, whereas moist fine-grained or organic soils tend to produce larger offsets (Hasler et al., 2015).

The magnitude of the thermal offset is commonly parametrized using an index value called the r_k value, which expresses the ratio of thawed to frozen thermal conductivity (Riseborough et al., 2008). Lower r_k values correspond to stronger winter-dominated heat transfer and larger thermal offsets (Smith & Riseborough, 2002). In some dry or well-drained substrates, r_k values can be greater than 1, indicating more efficient summer heat transfer and reduced or reversed offsets (Garibaldi et al., 2024b; Li et al., 2019; Luo et al., 2018; Zou et al., 2017).

The influence of substrate properties on permafrost thermal state is closely linked to ecological conditions. Therefore, thermal offsets are often estimated spatially from in-situ stratified random sampling and remote sensing derived landcover type (Bonnaventure et al., 2017; Obu et al., 2019; Vegter et al., 2024). In colder, sparsely vegetated environments, thermal offset exerts relatively limited control because atmospheric forcing (e.g. freezing degree days) dominates (Garibaldi et al., 2026). In contrast, in warmer and more southerly discontinuous permafrost regions, variations in substrate moisture and organic layer development can protect permafrost from climate conditions no longer suitable for permafrost persistence (Shur & Jorgenson, 2007) (Figure 2-4). For example, perturbations in the TTOP model for the r_k and n_t had minimal (near 0 °C) impact on predicted TTOP in the High Arctic while in Central northwest Yukon there was variation of upwards to 3.2 °C when these variables were altered by 50% (Garibaldi et al., 2026).

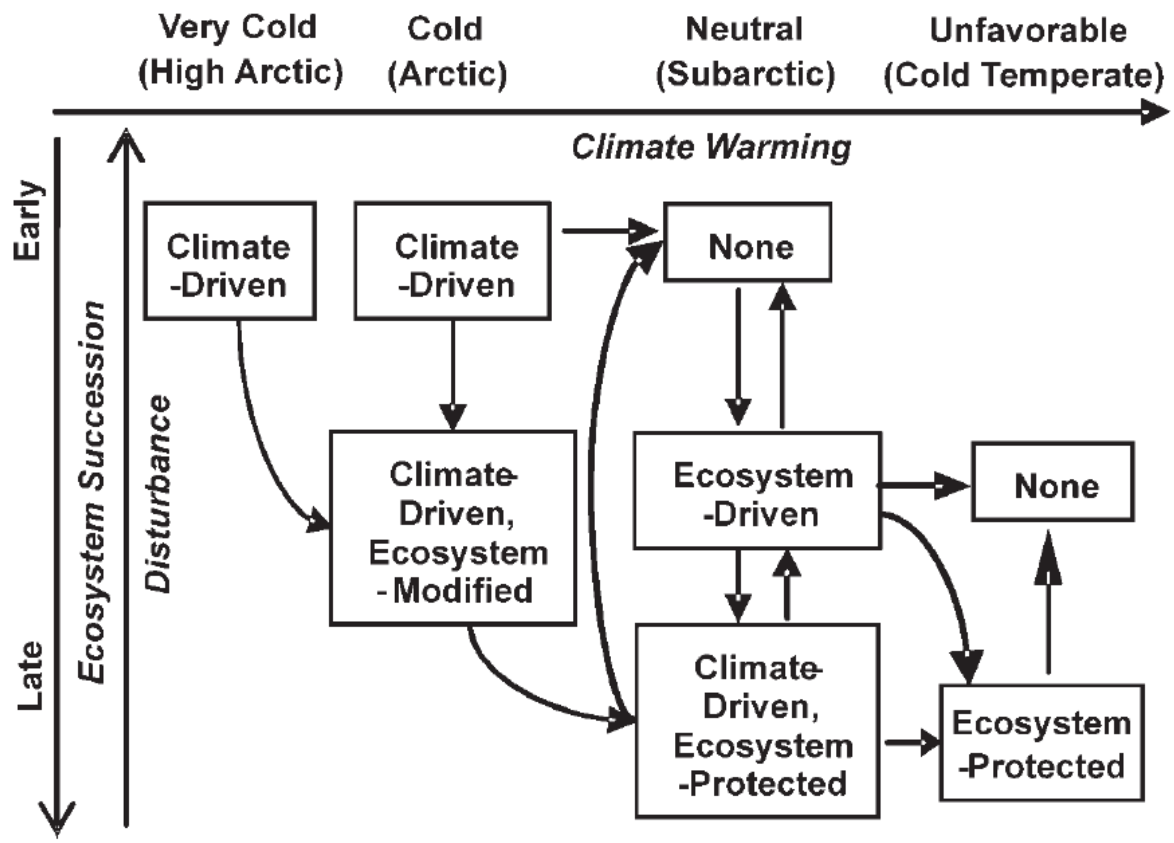

Figure 2-4: The conceptual relationship between permafrost conditions and ecosystem succession (Shur & Jorgenson, 2007, p.11, Copyright © 2007 John Wiley & Sons, Ltd.).

These controls on permafrost thermal state highlight the importance of accurately representing interactions between atmospheric forcing and ground processes. Across the landscape, some environments exhibit strong coupling between air and ground temperatures, while others are buffered by snow, vegetation, and substrate properties. This variability has important implications for how atmospheric forcing is represented in permafrost models, particularly in complex terrain where near-surface temperature patterns may deviate from large-scale climate gradients.

2.2 Representation of Permafrost Thermal Regimes in Models

Having established that permafrost thermal state emerges from interaction among atmospheric forcing, surface offsets, and substrate-dependent thermal processes, it is necessary to consider how these components are represented in modelling frameworks. Permafrost models translate atmospheric energy input into subsurface temperature conditions through varying degrees of physical complexity, ranging from empirical relationships based on mean annual air temperature to fully transient heat transfer models.

Since direct measures of ground thermal conditions are spatially sparse and logistically challenging across much of the circumpolar north, modelling provides the primary means of estimating permafrost distribution, active layer thickness, and long-term thermal change. However, regardless of model complexity, the air temperature field constitutes a fundamental boundary condition. Errors in air temperature magnitude, lapse rate vertical structure, or seasonal degree-day representation propagate through surface and thermal offsets and influence predicted TTOP and ground thermal regimes.

This section examines how atmospheric forcing and energy transfer processes are represented in different permafrost modelling approaches. Emphasis is placed on limitations in complex terrain, where local temperature patterns deviate from large-scale climate gradients and can introduce bias into model forcing.

2.2.1 Empirical-Statistical Process Based model

Empirical-Statistical permafrost models estimate the probability of permafrost occurrence using relationships between observed permafrost presence and topoclimatic variables such as elevation, aspect, slope, potential incoming solar radiation, MAAT, topographic index, and soil moisture (Bonnaventure & Lewkowicz, 2012; Daly et al., 2022; Riseborough et al., 2008). These topoclimatic variables are derived from digital elevation models utilizing geomatics (Bonnaventure & Lewkowicz, 2011; Lewkowicz & Ednie, 2004). This model is most often applied in mountainous environments because of the challenges of large heterogeneity across the landscape and limited availability of input data that is collected in-situ (Etzelmüller et al., 2006; Gubler et al., 2013).

Unlike physically based models, statistical approaches do not explicitly simulate surface or subsurface energy fluxes. Instead, they assume that spatial patterns in MAAT and terrain derived predictors adequately capture the controls on permafrost distribution (Etzelmüller, 2013; Riseborough et al., 2008). In complex topography, air temperature is often estimated using elevation-based SLRs (Minder et al., 2010; Noad & Bonnaventure, 2022) applied to local observations (Bonnaventure et al., 2012). Consequently, these models can implicitly assume linear decrease in temperature with elevation which may not resolve local deviations from free-air conditions (Lewkowicz & Bonnaventure, 2011; Lewkowicz et al., 2012).

In valleys prone to surface-based temperature inversions (SBIs) and associated cold air pooling, expected lapse rates may be weakened or reversed, and the assumption of negative lapse rates could introduce systematic bias in predicted permafrost probability (Noad & Bonnaventure, 2022). To address this limitation, empirical-statistical permafrost modelling in Yukon utilizes positive lapse rates associated with SBIs below treeline and a negative lapse rate above treeline (Lewkowicz & Bonnaventure, 2011). While this improved permafrost probability predictions, recent findings indicate that the assumption of lapse rate reversal at treeline is too simplistic for some of the most continental subarctic mountain valley environments in northwestern Canada (Garibaldi et al., 2024b; Noad & Bonnaventure, 2022). These results further highlighted the sensitivity of empirical-statistical permafrost models to how near-surface atmospheric temperature fields are represented.

Validation of these probability-based outputs present additional challenges, as point measurements of permafrost absence and presence may not directly correspond to modelled grid-cell probabilities (Gruber, 2012). Additionally, since these models do not explicitly represent energy balance processes, the mechanistic drivers of predicted permafrost probability remain absent (Gruber, 2012; Riseborough et al., 2008). Nevertheless, these models remain widely used due to the relative simplicity and limited data requirements as well as their ability to produce continuous spatial distribution maps of permafrost probability or thermal state.

2.2.2 TTOP model

The temperature at the top of permafrost (TTOP) model is a process-based analytical equilibrium model that predicts the temperatures at the base of the active layer (Bonnaventure & Lamoureux, 2013; Bonnaventure et al., 2017; Riseborough et al., 2008). The model combines the concept of thermal offset (Romanovsky & Osterkamp, 1995) (Section 2.1.2) with empirically derived freezing and thawing n-factors (Juliussen & Humlum, 2007; Wright et al., 2003) (Section 2.1.1):

$$TTOP = \frac{(n_{\mathrm{t}} * \lambda_{\mathrm{T}} * TDD_{\mathrm{a}}) - (n_{\mathrm{f}} * \lambda_{\mathrm{F}} * FDD_{\mathrm{a}})}{\lambda_{\mathrm{F}} * P} \qquad \text{(Eq. 2-3)}$$

where n_f and n_t are the freezing and thawing n-factors, λ_f and λ_T are the freezing and thawing thermal conductivities of the soil, FDD_a and TDD_a are the freezing and thawing degree days of the air temperature, and P is the annual period of 365 days.

Since TTOP is expressed directly as a function of freezing and thawing degree days. The model is strongly dependent on accurate representation of air temperature. Sensitivity analysis conducted across northwestern Canada demonstrated that TTOP predictions are highly responsive to freezing parameters (n_f and FFD_a), particularly in northern regions where freezing degree days are large (Garibaldi et al., 2026). Therefore, errors in air temperature estimates can propagate into TTOP estimates, particularly in mountainous terrain where near-surface air temperatures may deviate substantially from free-air conditions (Garibaldi et al., 2024a).

The TTOP model assumes that permafrost is in thermal equilibrium with the climate. However, permafrost is frequently out of equilibrium due to disturbance, latent heat effects and ongoing climate change (French & Williams, 2013). For example, community scale TTOP-based predictions have underestimated permafrost persistence in recently burned boreal landscapes where ground temperatures have not yet equilibrated to post-disturbance air temperature regimes (Bonnaventure et al., 2026; Vegter et al., 2024). At circumpolar scales, the largest TTOP model errors occur where ground ice approaches 0 °C and latent heat effects dampen warming ground conditions (Obu et al., 2019). These limitations highlight that while the TTOP model is computationally efficient and widely applied, this model is sensitive to both disequilibrium conditions and to how atmospheric forcing is represented.

Thus, with accelerated climate warming observed in both high-latitude (Johannessen et al., 2016; Serreze & Barry, 2011) and high elevation (Palazzi et al., 2019; Pepin et al., 2015) regions, extra care must be taken to ensure that error introduced by disequilibrium between T_a and the ground thermal regime (Zhang et al., 2008a, 2008b) is accounted for when utilising the TTOP model, or other equilibrium models.

2.2.3 Physically Based Numerical Models

Physically based numerical permafrost models simulate ground thermal regimes by using heat transfer equations through discretized soil profiles using prescribed upper and lower boundary conditions (Kurylyk & Hayashi, 2016; Perreault et al., 2021; Yin et al., 2018; Zhang et al., 2003). These models explicitly represent conductive and advective heat transport, phase change processes, and transient responses of the active layer and permafrost to climatic forcing (Riseborough et al., 2008). Numerical models must undergo six processes during development which include 1) definition of temporal and spatial restraints along with upper and lower boundaries; 2) divide continuous time and space into finite pieces; 3) specification of the governing heat transfer equation; 4) assignment of the thermal properties of the substrate (e.g., thermal conductivity, heat capacity); 5) initialize the model with a starting temperature for each part of the profile; and 6) iteration of the governing equation (typically the 1-D heat conduction equation) to update temperatures at each time step based on the defined properties and boundary conditions (Riseborough et al., 2008).

The primary strength of process-based numerical models is their ability to simulate non-equilibrium behaviour. Applications have quantified processes such as thaw from evolution, disturbance-driven permafrost degradation, groundwater heat advection, and influence of slope, aspect and snow conditions of ground temperatures (Devoie & Craig, 2020; Devoie et al., 2021; Jorgenson et al., 2010; Zhang et al., 2015). As a result, numerical models provide the most physically realistic representation of permafrost thermal dynamics.

However, this process realism comes at a significant cost as to run these numerical models, extensive site-specific parameters of soil properties, snow conditions, and atmospheric forcing, as well as significant computational resources are required (Etzelmüller, 2013; Oelke et al., 2003). Consequently, applications have historically focused on point locations or coarse spatial domains where required datasets are available (e.g., Anisimov & Reneva, 2006; Kurylyk et al., 2014; Marchenko et al., 2008; Sazonova & Romanovsky, 2003).

To address the limitations of modelling permafrost distribution spatially in complex terrain, higher-resolution transient permafrost models have been developed (Jafarov et al., 2012; Luo et al., 2019; Zhang et al., 2013). That said, challenges exist in remote high-latitude valleys where data collection has been traditionally limited, and the terrain is highly heterogenies.

Importantly, since numerical models explicitly simulate surface energy exchange, their performance is sensitive to the accuracy of the atmospheric boundary conditions. Many spatial implementations rely on coarse reanalysis products or elevation-based lapse rate interpolation that assumes free-air temperature gradients (e.g., Yin et al., 2018; Zhang et al., 2013). In complex mountain terrain, however, surface-based temperature inversions and cold-air pooling produce significant deviations from those expectations (Noad and Bonnaventure, 2022). Consequently, even physically sophisticated numerical models may inherit systematic bias when atmospheric forcing fails to resolve local valley climate processes.

2.2.4 The NEST model

The Northern Ecosystem Soil Temperature (NEST) model is a one-dimensional process based numerical model designed to simulate transient permafrost thermal regimes by explicitly representing coupled energy exchange between the atmosphere, vegetation, snow cover, and subsurface soils (Chen et al., 2003; Zhang et al., 2003). In NEST, these components are treated as an integrated system of heat transfer, where ground temperatures emerge from interactions among radiative fluxes, turbulent heat exchange, snow insulations, vegetation shading, and conductive heat transfer through a layered soil profile (Zhang, 2025) (Figure 2-5).

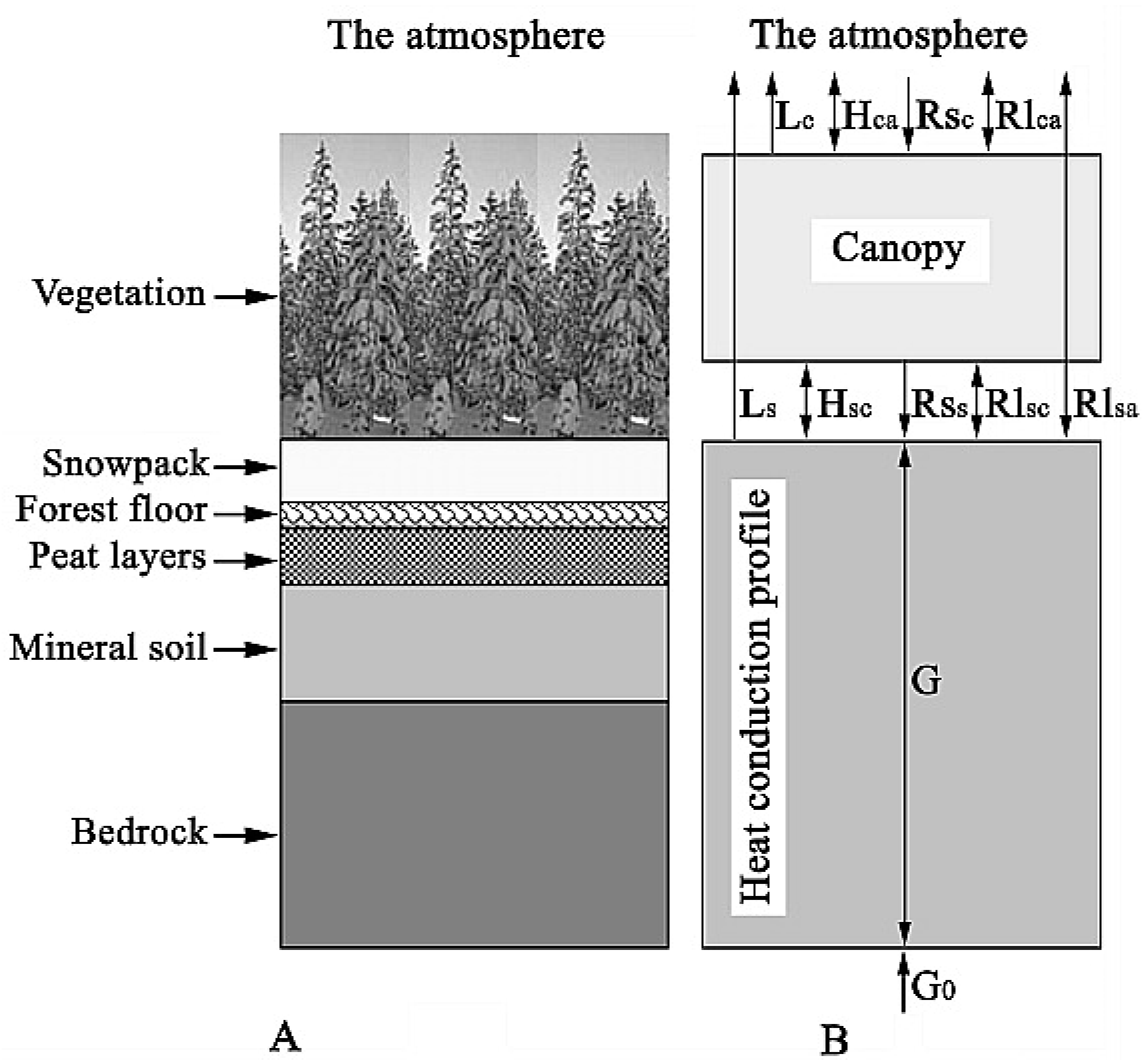

Figure 2-5: A) Components of the NEST system and B) variables for the energy balance equation which include the sensible heat flux (H), the latent heat flux (L), solar radiation (Rs), long-wave radiation (Rl), and the convective heat flux (G) exchange between the ground surface (s), the vegetation canopy (c), and the atmosphere (a). G_0 is the geothermal heat flux (Zhang et al. 2003, p.5-3, Copyright 2003 by the American Geophysical Union).

The upper boundary condition is defined by the surface energy balance at either the ground surface or snow surface, while the lower boundary is constrained by geothermal heat flux (Zhang, 2025). By solving one-dimensional heat conduction equations through time, NEST simulates non-equilibrium evolution of soil temperature and active layer dynamics. This integrated framework allows the model to explicitly represent many of the processes in Section

2.1, including surface temperature offsets driven by snow and vegetation and thermal offsets controlled by substrate properties.

Sensitivity analysis demonstrate that simulated ground temperatures are strongly controlled by atmospheric forcing variables, particularly air temperature, solar radiation, snow conditions, and vegetation effects on surface energy exchange (Zhang et al., 2003). Since these variables define the surface energy balance, inaccuracies in the near-surface atmospheric temperature propagate directly into simulating ground thermal regimes. Meanwhile, the soil temperature at 50 cm and active layer thickness is not influenced greatly by variation in the geothermal flux, lower boundary depth, and soil depth but these factors are important to accurately represent the depth of the permafrost layer (Zhang et al., 2003, 2006, 2008a).

NEST has since expanded to include additional processes such as topographic effects, snow redistribution, lateral water flow, ground-ice, and disturbance-related changes in vegetation and the top organic layer (Zhang et al., 2013, 2015; Zhang, 2025).

Despite its strong process representation, application of NEST in complex high-latitude environment remains challenging because atmospheric forcing data are commonly derived from coarse climate reanalysis products or elevation-based interpolation schemes that do not resolve SBIs. Consequently, errors in valley air temperature fields may propagate through the sophisticated process models, motivating the need for improved representation of inversion-controlled climate forcing prior to numerical permafrost modelling.

2.2.5 Data Requirements and Atmospheric Forcing Limitations

Process-based numerical models such as NEST require representation of the environmental factors that control ground-atmosphere energy exchange, including terrain geometry, vegetation structure, snow conditions, soil properties, and long-term climate forcing (Riseborough et al., 2008; Tutton et al., 2021). These inputs allow models to represent the physical processes governing surface and subsurface heat transfer but also substantially increase data requirements compared to statistical or equilibrium modelling approaches.

Many local environmental parameters (e.g. topographic shading, slope, and aspect) can be derived from digital elevation models, ecosystem classifications, soil and geological surveys, and remotely sensed observations (Zhang et al., 2013). Accurate representations of the long-term atmosphere remain a primary challenge. Numerical models require continuous climate recording extending decades into the past to initialize simulations and resolve transient response of permafrost to climatic change. In high-latitude and mountainous regions, observational meteorological networks are sparse (Przybylak, 2016; Serreze & Barry, 2014; Urban et al., 2013), forcing reliance on interpolated climate surfaces or reanalysis products. Therefore, the characteristics and limitations of gridded climate datasets are considered in the following sections.

2.2.6 Gridded Climate Datasets and Their Limitations

High-resolution Gridded climate datasets have been developed to provide spatially continuous atmospheric forcing for environmental modelling in regions where observational data are sparse (Cao et al., 2019; Zhang et al., 2020). These datasets include climate reanalysis products, interpolated datasets, and empirical-statistical downscaled products. While they improve spatial coverage, they often rely on large scale atmospheric relationships and therefore inherit uncertainties associated with coarse model resolution and simplified representation of near-surface processes (Ehret et al., 2012). These limitations can be pronounced in complex terrain where near surface temperature is strongly influenced by local processes such as cold air pooling and surface-based temperature inversions (SBIs) that strongly influence near-surface temperatures

(Cao et al., 2017; Noad & Bonnaventure, 2022; Pozsgay & Gruber, 2025).

Climate reanalysis datasets combine historical observational data (e.g., satellite, radiosonde, and surface measurements) with coupled atmosphere-land-ocean models to reconstruct past meteorological conditions (Compo et al., 2011). Widely used products such as ERA5, MERRA-2, and JRA-3Q provide temporally continuous datasets (Gelaro et al., 2017; Hersbach et al., 2020; Kosaka et al., 2024) that are well suited for long term modelling, including permafrost studies (e.g., Obu et al., 2019). However, coarse spatial resolution (typically 10's of km) limits their ability to resolve fine-scale variability in temperature associated with elevation and topographic driven processes (Riseborough et al., 2008). As a result, sub-grid variability is not represented, which can introduce systematic bias when the datasets are applied to heterogenous mountain environments (Etzelmüller, 2013).

Interpolated climate datasets derived from station observations are an alternative approach. One example of this method is called ANUSPLIN, which uses spatial interpolation techniques to generate continuous climate surfaces from unevenly distributed station networks (MacDonald et al., 2020). While these datasets can achieve higher spatial resolution than reanalysis products, their accuracy is limited by the density and distribution of observations (Peterson & Vose, 1997; Werner et al., 2019). Collection of meteorological data are spatially unevenly distributed across regions, continents, and the world. For example, ocean covers 71% of the planet's surface, while most weather stations have historically been on the landmasses most densely deployed in developed countries (World Meteorological Organization, 2012). The spatial coverage of meteorological stations has recently expanded into areas that historically have been sparsely populated and difficult to access, such as high-latitude areas (Way & Bonnaventure, 2015). Furthermore, accuracy of observational data is limited by the need for homogenization to account for changes in instrumentation and station location. For example, a station deployed in Amos Quebec 1927 was positioned at the bottom of a hill, but in 1963 this station was relocated only a few meters away from the hill and the result was a step change in temperatures by 2.4 °C as the station was no longer positioned in an area of local cold pooling at night (Zhang et al., 2019). Therefore, statistical methods of homogenization for climate datasets are often needed to avoid false trends and accurately represent climate from observational data in an area (Vincent et al., 2018; Vincent et al., 2012; Vincent et al., 2002; Wang et al., 2010; Wang et al., 2007).

Hybrid empirical-statistical datasets, such as ClimateNA, attempt to address these limitations by combining interpolated baseline climate grids with elevation-based adjustments (Wang et al., 2016). These approaches incorporate terrain attributes and apply locally derived lapse rates to improve estimates in complex terrain (Daly et al., 2008). While these methods can improve predictions in complex terrain, they still rely on assumptions of linear relationships between temperature and elevation. In environments where SBIs and cold air pooling dominate, these assumptions break down, leading to bias that persists for surface air temperatures (Noad & Bonnaventure, 2022; Pozsgay & Gruber, 2025).

Across these different approaches, a common limitation becomes apparent, gridded climate datasets generally do not resolve terrain driven atmospheric processes that occur at fine scales. In many mountain valley environments, strong and frequent SBIs decouple near surface temperature from free-air conditions (Daly et al., 2010), which violates the lapse rate assumptions that underpin both reanalysis and interpolation-based methods. Consequently, systematic errors occur and are often most prevalent in the minimum daily temperature predictions (Roberts et al., 2019), which are critical for modelling ground thermal regimes and permafrost dynamics (Chen et al., 2003; Zhang et al., 2003).

These limitations highlight the need for approaches that better represent fine-scale atmospheric variability in complex terrain. As a result, downscaling methods have been developed to improve the representation of surface climate conditions from coarse-resolution datasets. These approaches are discussed in the following section.

2.2.7 Downscaling of Climate Reanalysis Data in Complex Terrain

Downscaling methods are used to translate coarse-resolution atmospheric datasets into climate fields that better represent local conditions required for environmental modelling (Benestad et al., 2008). Broadly, there are two main types of downscaling that include empirical-statistical methods, which relate large scale climate variables to local predictors (Daly et al., 2008) and dynamical methods, which use nested atmospheric models to explicitly simulate finer-scale processes (Bieniek et al., 2016; Wang et al., 2021). In practice, empirical and hybrid approaches are most commonly applied in permafrost modelling due to their lower computational demands and flexibility in data sparse regions (Etzelmüller, 2013; Riseborough et al., 2008).

A commonly used approach for downscaling reanalysis data is implemented in the GlobSim framework, which extracts and interpolates variables from coarse-resolution products such as ERA5, MERRA-2, and JRA-3Q to user defined locations (Cao et al., 2019). First the software downloads the existing climate reanalysis data for each model, then these reanalysis data are interpolated using a 3-dimensional bilinear interpolation method created for an Earth System Modelling Framework based on pressure levels in the reanalysis datasets (O'Kuinghttons et al., 2016). Finally, the resulting dataset is scaled to represent the desired temporal increments of the output so that it can be used to drive land surface and permafrost models (Cao et al., 2019).

To address these limitations, additional downscaling and bias-correction approaches have been developed to better represent terrain driven temperature variability. Many methods apply elevation-based adjustments using lapse rates derived from reanalysis pressure levels, allowing for temperature to be scaled according to local topography (Fiddes et al., 2022; Fiddes & Gruber, 2012, 2014; Gao et al., 2012; Sen Gupta & Tarboton, 2016). While these approaches improve representation of large-scale vertical temperature gradients, they rely on the assumption that free air lapse rates are representative of near surface conditions.

In complex terrain this assumption is frequently violated. SBIs and cold air pooling are controlled by local topographic and surface energy balance processes that operate at spatial scales much finer than the resolution of reanalysis products (Cao et al., 2017). As a result, inversion strength and structure are often underestimated in reanalysis derived temperature fields, even when vertical gradients are resolved for the free atmosphere (Noad & Bonnaventure, 2022).

2.2.8 Inversion-Aware Bias Correction Reanalysis Methods

REanalysis Downscaling Cold Air Pooling Parameterization (REDCAPP) was developed to improve downscaling of reanalysis air temperatures in mountain terrain prone to persistent cold air pooling (Cao et al., 2017). Its central idea is that surface air temperature structure can be treated as the sum between two components including (1) free atmosphere temperature structure from the reanalysis pressure levels and (2) a land-surface influence term that becomes strongest in valley bottoms. REDCAPP therefore first interpolates pressure level temperatures to elevation at fine scales, then applies a terrain dependent land surface correction factor to account for frequent cold air pooling. In this approach, geomorphometric variables such as hypsometric positions and valleyness (Gallant & Dowling, 2003) are used to scale how strongly the land surface influences the surface air temperature.

This REDCAPP method moves beyond traditional lapse rate based downscaling (Fiddes & Gruber, 2012, 2014; Sen Gupta & Tarboton, 2016) by explicitly downscaling accounting for terrain-controlled boundary processes that decouple valley bottom temperature from the free air conditions (Daly et al., 2010). REDCAPP has been shown to substantially reduce warm biases in the valley bottoms and cold biases at higher elevation, achieving RMSE values of 0.26 °C and 0.29 °C in the Swiss Alps and Qilian Mountains respectively (Cao et al., 2017).

However, REDCAPP still requires regional calibration and was developed as a generalized terrain-based parametrization of cold air pooling rather than a model of long-term temporal evolution of inversion strength. In subarctic mountain environments the highly stable wintertime planetary boundary layer often supports multiple inversion layers that are deep (Mayfield & Fochesatto, 2013) and surface air temperature variability with elevation remain difficult to represent using terrain-based scaling alone (Pozsgay & Gruber, 2025).

To address these limitations, Pozsgay and Gruber (2025) developed a model to explicitly represent the temporal dynamics of subarctic valley SBIs using reanalysis data calibrated with observational data from five weather stations near Dawson, Yukon. Rather than relying only on local-lapse rate adjustment, their method uses a single downscaled atmospheric column from reanalysis and estimates inversion strength as temporally varying.

In this framework, inversion strength is defined as the difference between the reanalysis surface temperature and temperature at the top of the inversion layer. DT corresponds with the surface-based temperature inversion magnitude (SBI_{mag}) from Noad et al. (2023) and is the difference between the reanalysis grid elevation surfaced temperature or the temperature at a stations elevation and the temperature that would occur at those same elevations should the free air lapse rate extend to the surface. This is evaluated using the following:

$$DT = T_{sur} - T_{lapse\ grid} \qquad \text{(Eq. 2-4)}$$

$$DT_{station} = T_{obs} - T_{lapse\ station} \qquad \text{(Eq. 2-5)}$$

the relationship between grid scale and local SBI strength is then expressed as:

$$DT_{station} = \alpha(z) \cdot DT + \beta(\mathrm{t}) \qquad \text{(Eq. 2-6)}$$

where α(z) represents the fraction of inversion strength experienced at elevation z, and β(t) represents the temporally varying regional bias. The parameter α(z) is conceptualized geometrically (Figure 2-6) and varies linearly with elevation within the inversion layer, approaching 1 at the valley bottoms and 0 near the top of the inversion. The parameter β(t) accounts for systematic seasonal deviations not explained by the inversion structure, this term is entirely independent of elevation and assumes bias oscillates seasonally. This leads to the full expression written as:

$$T_{obs} = T_{lapse\ station} + \alpha(z) \cdot (T_{sur} - T_{lapse\ grid}) + \beta(\mathrm{t}) \qquad \text{(Eq. 2-8)}$$

Both α and β need to be calibrated using in-situ observations spanning a wide range of elevations and temporal conditions.

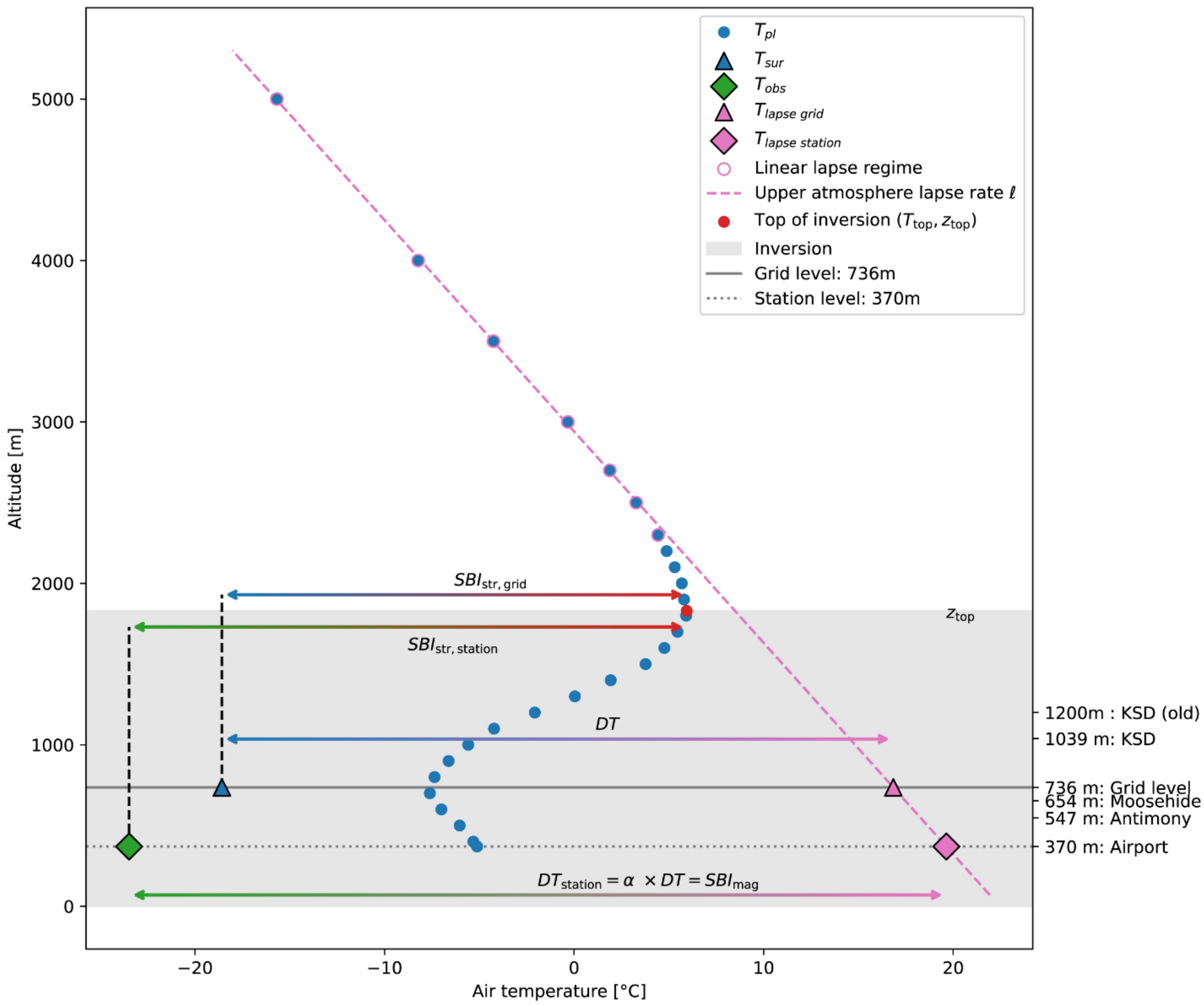

Figure 2-6: Illustrates the Dawson inversion-correction framework, showing how downscaled reanalysis temperatures are combined with a model of inversion strength calibrated against observations from stations spanning the local elevation gradient (Pozsgay and Gruber, 2025, p. 4).

A major strength of this method is that it is designed to not only reproduce the spatial structure of SBIs, but also their multi decadal temporal evolution. The model parameters account for observed increases and decreases in SBI frequency, strength, and depth since 1948 around Dawson. Once calibrated, the method relies only on global reanalysis data and should therefore be applicable to nearby terrain where observations are unavailable. This is especially valuable to permafrost modelling, which demands continuous long term meteorological forcing datasets in areas where observational networks are sparse.

However, a critical limitation remains in the transferability of calibrated parameters. In particular, the dependence of $\alpha(z)$ on absolute elevation may limit application across regions with differing valley geometry or topographic context. Evaluating and improving the transferability of this framework is therefore an important area of future research.

While SBI-aware downscaling approaches improve the representation of near-surface air temperature, the extent which these corrections influence ground temperatures depends on surface and subsurface buffering processes (Section 2.1). Snow cover, vegetation, and substrate properties regulate how decoupled the ground temperature is from air temperature. Consequently, improvements in atmospheric forcing are expected to produce spatially variable responses to modelled ground temperatures and active layer thickness. Understanding how these corrections propagate through the ground thermal regime is therefore critical to evaluating their impact within process-based numerical permafrost models such as NEST.

Overall, process-based approaches to permafrost modelling require long-term, continuous climate forcing datasets. In subarctic mountainous terrain, however, coarse-resolution climate data are often affected by SBI induced biases, reducing the realism of model inputs. While methods have been developed to correct these biases, their performance and transferability remain insufficiently evaluated, particularly in complex terrain where high-resolution in situ observations are limited. To provide the necessary context, the following section examines the processes governing valley-based SBIs and their implications for permafrost distribution and thermal state.

2.3 SBIs and Permafrost

2.3.1 Surface-Based Temperature Inversions

Air temperature inversions occur when air temperature increases with elevation or altitude, contrary to typical decrease in temperature with height in the troposphere (Bradley et al., 1992; Whiteman, 2000). When the temperature inversion begins near the earth's surface then it is called a surface-based temperature inversion (SBI) (Bourne et al., 2010; Gilson et al., 2018; Noad & Bonnaventure, 2022). SBIs create a stable atmospheric layer that limits vertical mixing and decouples near surface air temperature from the free atmosphere above (Rendón et al., 2020; Sheridan, 2019).

This decoupling has important consequences including, trapping of pollutants (Feng et al., 2022; Green et al., 2015; Largeron & Staquet, 2016; Sun & Holmes, 2019; Ye & Wang, 2020), development of extreme cold conditions (Harris, 1982; Whiteman et al., 2004a), freezing precipitation events (McCray et al., 2019), dense fog (Gilson et al., 2018; Tjernström et al., 2019), and inversions in precipitation phase (Pigeon and Jiskoot, 2008). Most importantly for this research, SBIs strongly control surface air temperatures in mountain valleys, causing deviations from free air conditions and the decoupling of surface air temperatures in mountain valleys from those of the free atmosphere due to frequent occurrence of SBIs (Daly et al., 2010; MacDonald et al., 2025; Pepin et al., 2011).

In mountain environments SBIs are most commonly associated with radiative cooling of the surface and subsequent cold drainage and pooling (Dawn Reeves & Stensrud, 2009; Lundquist & Cayan, 2007; Rupp et al., 2020). Cold dense air accumulates in the valley bottoms, while warmer air remains aloft, producing a strong vertical gradient of temperature (Clements et al., 2003; Noad & Bonnaventure, 2023; Schroeder & Buck, 1970; S. A. Smith et al., 2010) (Figure 2-7).

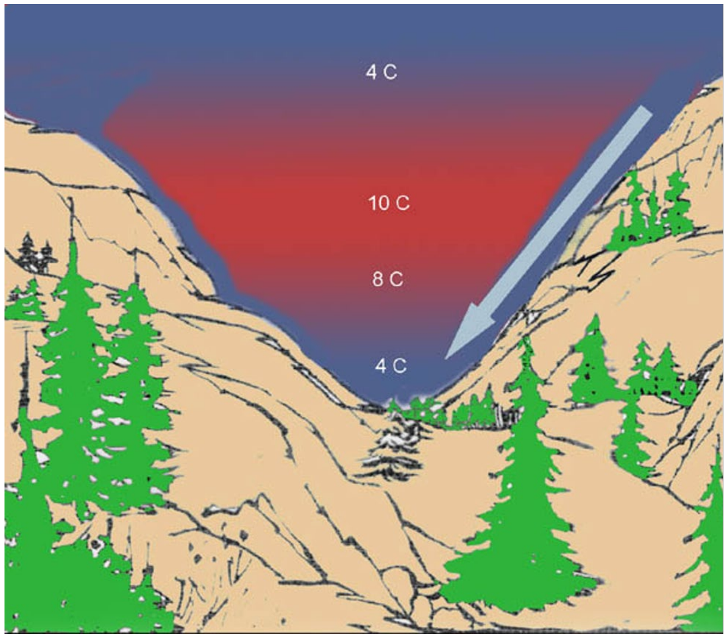

Figure 2-7: The process of SBI development from radiative cooling, cold air drainage, and cold air pooling in topographic low spots (Schroeder & Buck, 1970, p. 26).

Development of mountain valley SBIs and cold air pools can be driven and reinforced by several factors (Figure 2-8a). First, gentle katabatic flows from cold air drainage promote weak turbulent mixing of the atmosphere near the valley bottom which allows for further cooling of the select part of the atmosphere due to air in contact with the cold surface being continuously replaced with air higher up in the contained SBI layer (Sheridan, 2019). On the other hand, intense katabatic flow will enhance the shear-induced mixing of the cold pool and will preclude the cold air pool from being established and stratified into an SBI (Figure 2-8b). Next, synoptic conditions influence the development of valley SBI in several ways. Decoupling of the valley atmosphere from the synoptic flow aloft promotes more intense cold air drainage and pooling (Figure 2-8a). If the atmosphere aloft remains coupled to the valley atmosphere, air from aloft can mix out the cold pool through shear-induced mixing, and advective overspill (Sheridan, 2019) (Figure 2-8b).

Breakup of mountain valley SBIs and associated cold air pools is most often driven by two diurnal processes. First, as solar radiation warms the surface the lower atmosphere warms through conduction, and a convective boundary layer grows promoting vertical mixing (Whiteman & McKee, 1982). As the convective boundary layer grows, the SBI is mixed out from bottom to top (Neff & King, 1989; Whiteman et al., 2008). The second process is the lowering of the top of the SBI layer as upslope flow is initiated in the valley bottom and up the sidewalls near the surface, while downslope flow is maintained in the stable core of the SBI which slowly deflates the stable layer (Largeron & Staquet, 2016; Whiteman, 1982). These two processes are illustrated in Figure 2-8c as valley scale convection and advective venting.

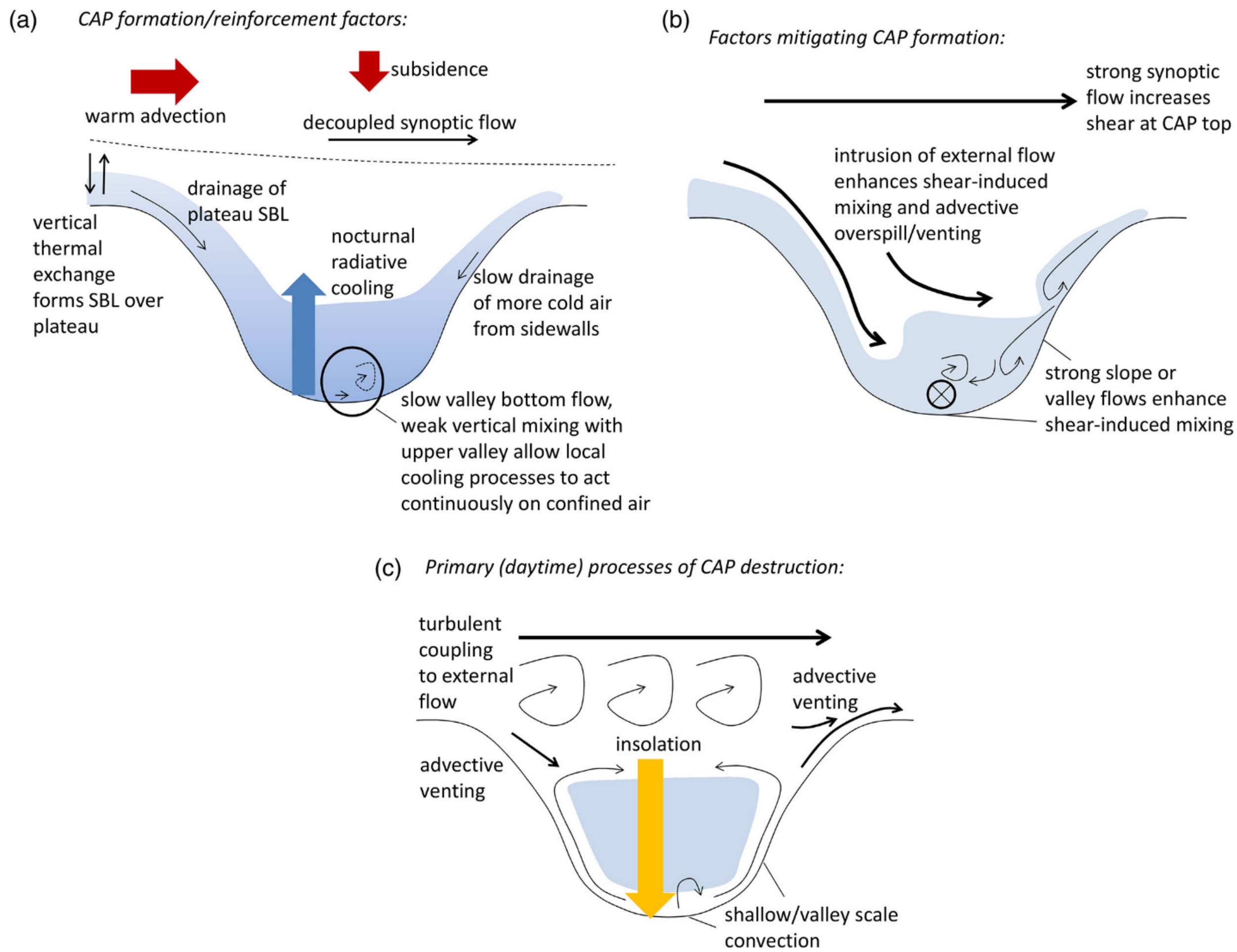

Figure 2-8: The processes associated with cold air pooling and valley SBI formation, persistence, and breakup (Sheridan, 2019, p. 1637, © 2019 Crown copyright. Quarterly Journal of the Royal Meteorological Society). CAP stands for cold air pooling and SBL stands for stable boundary layer.

SBI events can persist beyond a diurnal cycle and can overcome the SBI breakup mechanisms described above. Persistent SBIs are defined as events that last for greater than or equal to 18 hours (Noad & Bonnaventure, 2022; Noad et al., 2023; Whiteman et al., 2001). These events are infrequent and almost exclusively occur during the winter season in the mid-latitude regions (Whiteman et al., 2001), and are much more common and most frequently occur during the winter season in high-latitude regions due to the short winter daylight periods and synoptic conditions that regularly reinforce stability (Fochesatto et al., 2015; Mayfield & Fochesatto, 2013; Mayfield & Fochesatto, 2018; Noad & Bonnaventure, 2022).

2.3.2 SBIs in High-Latitude Regions

In high-latitude regions, SBIs are more frequent, stronger, and more persistent than in mid-latitude mountain environments due to prolonged periods of negative surface energy balance (Bourne et al., 2010). Long polar nights, low sun angles, and extensive snow cover promote sustained radiative cooling and stabilizes atmospheric stratification, often resulting in semi-permanent SBI conditions during the winter (Bourne et al., 2010; Serreze & Barry, 2014). This leads to serious implications of SBIs on the climate of high-latitude regions (Zhang et al., 2011).

In addition to SBIs, high-latitude environments commonly exhibit multiple elevated inversion layers formed through warm air advection and subsidence aloft, producing deep and complex vertical temperature structure (Mayfield & Fochesatto, 2013) that promote weak synoptic winds and therefore minimal vertical mixing (Sheridan, 2019) (Figure 2-9). As a result, SBIs in these regions not only are more persistent but are typically stronger and deeper than those observed in mid-latitudes (Seidel et al., 2010; Zhang et al., 2011).

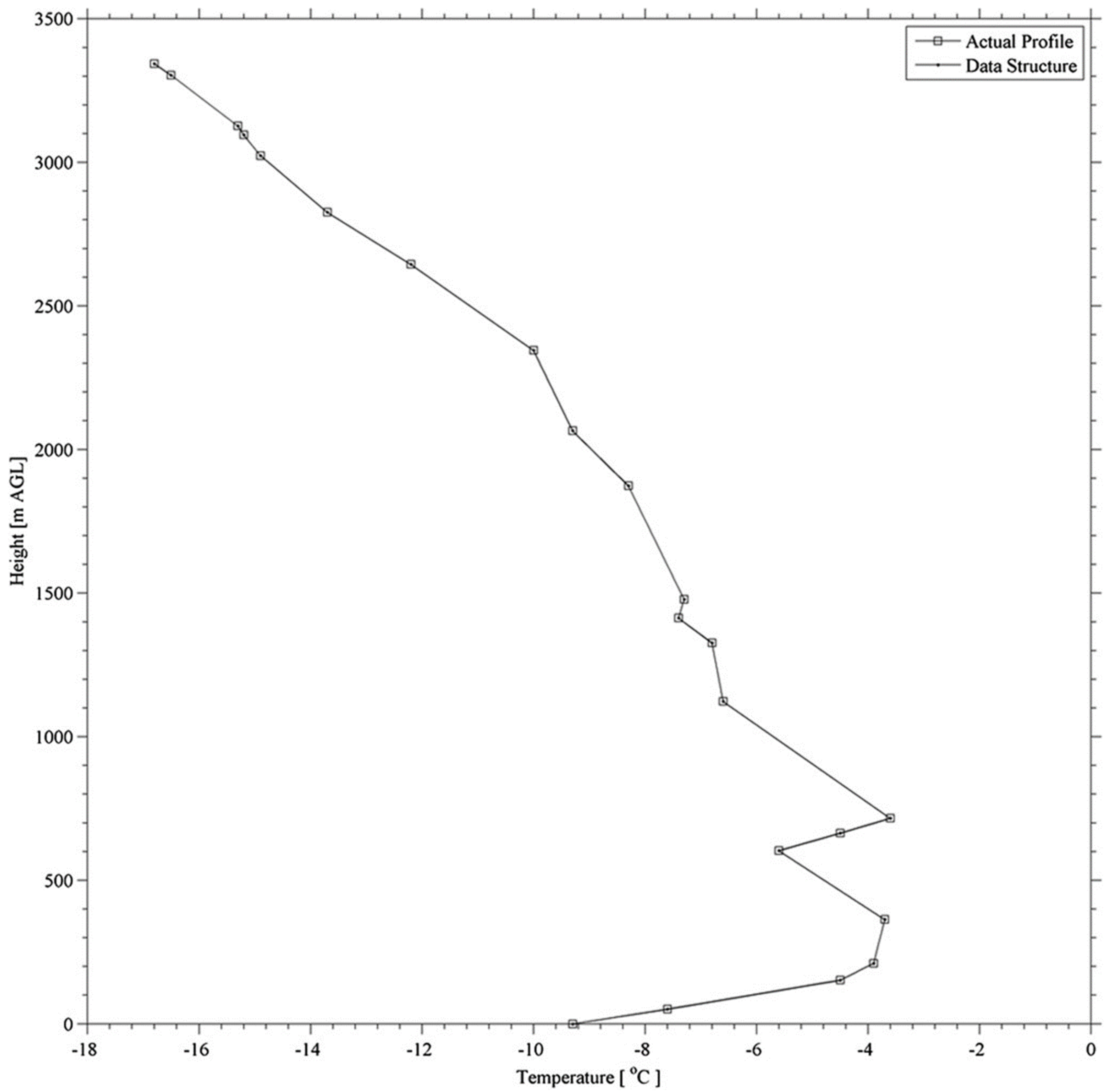

Figure 2-9: Vertical Temperature profile in Fairbanks Alaska at 1200 UTC on the 18th of November 2001. There is an intense surface-based temperature inversion (SBI) with multiple elevated inversion layers overlying it (Mayfield and Fochesatto, 2013, p. 956).

The frequency, depth, and strength, of SBIs increases with latitude (Kahl et al., 1992; Noad et al., 2023; Seidel et al., 2010; Zhang et al., 2011). In high-latitude regions of northern Canada and Alaska, SBIs can occur up to 70-80% of the time (Bourne et al., 2010), strength (increase in temperature from bottom to top of the SBI) typically ranges from 3 to 10 °C (Noad et al., 2023; Zhang et al., 2011), and they are up to 1100 m deep (Kahl et al., 1992).

To quantify the influence of SBIs on surface air temperature, Noad et al. (2023) introduced the concept of SBI impact, which integrates inversion depth, strength, and frequency into a single metric which is expressed as:

$$T_{pa} = (SBI_z \times ELR) \quad \text{(Eq. 2-9)}$$

where T_{pa} is the projected air temperature, SBI_z is the depth of the SBI, and ELR is the environmental lapse rate of -6.5 °C km^{-1}. The T_{pa} is then utilized to calculate a magnitude of the SBI using:

$$SBI_{mag} = T_{pa} + SBI_{str} \quad \text{(Eq. 2-10)}$$

where SBI_{mag} is the magnitude of the SBI and SBI_{str} is the SBI strength. The SBI_{mag} is then used to calculate the SBI impact:

$$SBI_{imp} = \frac{SBI_{mag\,(000\,UTC)} \times SBI_{freq\,(000\,UTC)} + SBI_{mag\,(1200\,UTC)} \times SBI_{Freq\,(1200\,UTC)}}{2} \quad \text{(Eq. 2-11)}$$

where SBI_{imp} is the SBI impact and SBI_{freq} is the frequency of the readings with an SBI present. The different UTC time stamps for SBI_{mag} and SBI_{freq} represent the bi-daily radiosonde readings these calculations are based on (Noad et al., 2023). SBI impact in Northwestern Canada ranged from 1.6 °C yr^{-1} in Whitehorse to 5.2 °C yr^{-1} in Inuvik. Therefore, if SBIs are absent in these landscapes, MAAT may be upwards to 5.2 °C warmer. This signifies just how significant SBIs are to the climatology of high-latitude regions. The concept of SBI impact and magnitude was used to inform the creation of the inversion-aware bias correction model outlined in section 2.2.8 (Pozsgay & Gruber, 2025) (Figure 2-6).

Additionally, an important consideration is that the spatial and temporal structure of SBIs vary over short distances due to differences in valley geometry, vegetation, and topographic position (Noad & Bonnaventure, 2022; 2023). This variability highlights the strong control of local terrain on surface air temperature and underscores the limitations of coarse-resolution climate datasets, which often fail to resolve these processes (Sections 2.2.6, 2.2.7, and 2.2.8).

Since SBIs fundamentally alter near-surface temperature gradients, they directly influence the atmospheric forcing used in permafrost models. In mountain valleys, this leads to systematic deviations between modelled and actual ground temperatures, particularly where lapse rate assumptions fail. As a result, understanding and representing SBIs is critical for accurately simulating permafrost distribution and thermal dynamics.

2.3.3 How do SBIs Impact Permafrost?

SBIs fundamentally alter the relationship between elevation and air temperature in mountain environments, with important consequences for permafrost distribution. Under typical conditions in maritime or lower latitude mountains, air temperature typically decreases with elevation, resulting in negative SLRs. In these environments, permafrost distribution generally follows a predictable elevational pattern, with permafrost absent at lower elevations and increasingly likely at higher elevations (Boeckli et al., 2012; Bonnaventure & Lewkowicz, 2012) (Figure 2-10a). As climate warms, permafrost retreats upslope (Rangecroft et al., 2016) in response to increasing air temperature and elevation dependent warming (Palazzi et al., 2019; Pepin et al., 2015; Pepin et al., 2022) (Figure 2-10b).

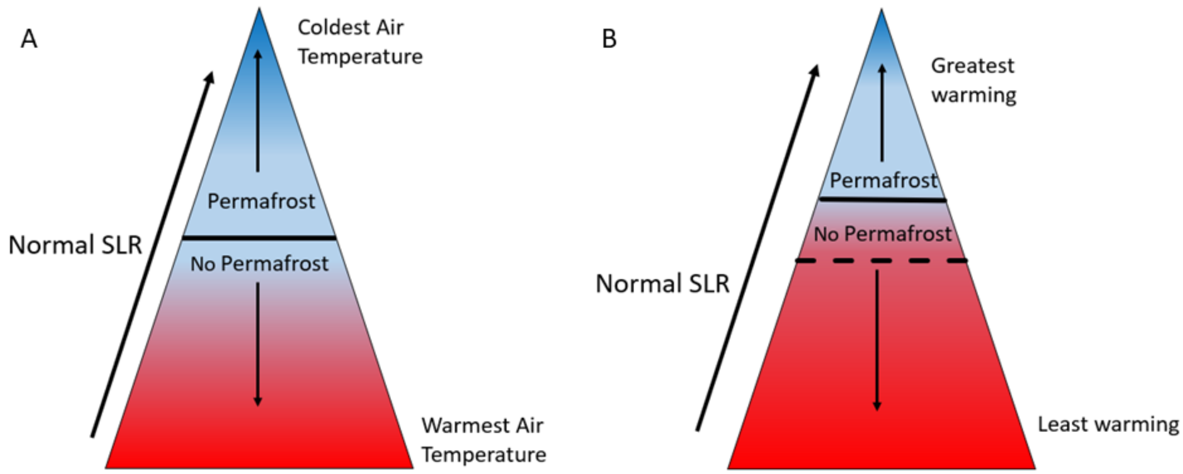

Figure 2-10: The elevational temperature profile and conceptualized patterns of permafrost distribution in a maritime or lower-latitude mountain valley (Garibaldi, 2023, p. 12, © University of Lethbridge).

Conversely, in mountain valleys where SBIs are frequent and persistent, this relationship is reversed. Positive SLRs can develop below the top of the typical inversion layer (Bonnaventure & Lewkowicz, 2013; Lewkowicz & Bonnaventure, 2011), producing a thermal belt where the mean annual air temperature is the warmest at mid elevations, while colder conditions occur both in the valley bottom and at high elevations (Bonnaventure & Lewkowicz, 2013; De Wekker et al., 2018; Lewkowicz & Bonnaventure, 2011) (Figure 2-11). As a result, permafrost probability is highest in valley bottoms and at high elevations, and lowest near the elevation of the SBI top (Bonnaventure et al., 2012).

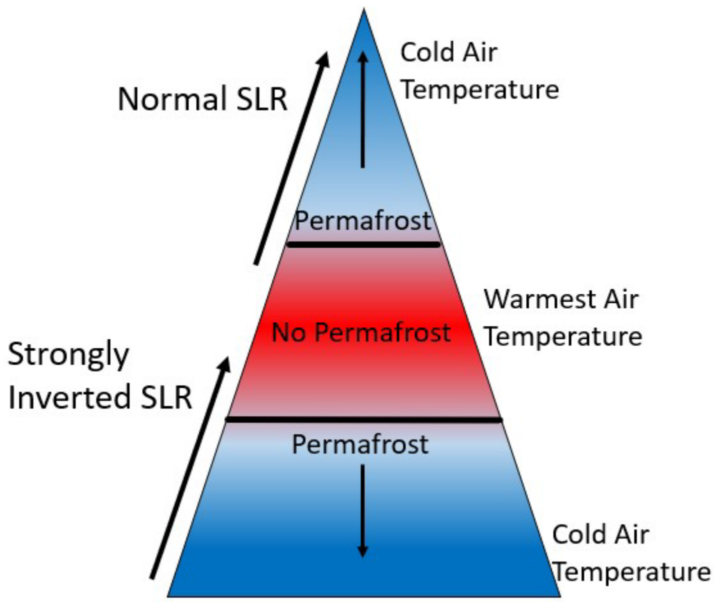

Figure 2-11: The elevational temperature profile and conceptualized patterns of permafrost distribution in a mountain valley prone to frequent and strong SBIs (Garibaldi, 2023, p. 13, © University of Lethbridge).

These inversion-driven temperature patterns can substantially modify ground thermal regimes. For example, freezing degree days have been shown to be significantly greater in the valley bottoms compared to adjacent slopes due to the combined effects of cold air pooling and topographic shading (Garibaldi et al., 2024b; Jorgenson et al., 2010). Field observation in subarctic Yukon valleys similarly demonstrate permafrost presence in the valley bottom but absent at adjacent mid-slopes (Noad & Bonnaventure, 2022).

Importantly, this inversion-controlled temperature structure implies that permafrost response to climate warming may be different from the typical upslope retreat observed in environments with less frequent SBIs. Instead, permafrost thaw may occur both upwards and downwards from the thermal belt at the typical top of the SBI, depending on how SBI strength and frequency evolve under changing climate conditions (Bonnaventure & Lewkowicz, 2013).

Changes in SBI characteristics therefore have the potential to significantly influence the spatial patterns of permafrost degradation and loss in high-latitude mountain environments.

2.3.4 Recent Advances in Modelling SBIs and Permafrost in Northwest Canada

Recent studies in northwestern Canada have demonstrated the strong impact of SBIs on surface air temperature (Noad et al., 2023) and the ground thermal regime (Garibaldi et al., 2024b). Observations from a network of air and ground temperature sensors in subarctic valleys show that mean annual surface lapse rates from valley bottom to mid-slope can become strongly positive, exceeding + 10 °C km^{-1} in some cases, reflecting persistent cold air pooling and SBIs in these valleys (Noad & Bonnaventure, 2022). Recent work has expanded the sensor network beyond mid-elevations to the highest ridgetop elevations in these valleys (Garibaldi et al., 2024a, 2024b) but have not explicitly quantified the spatial-temporal structure of SBIs including how the SLRs, SBI strength, depth and frequency vary spatially in subarctic valleys. This limits the ability to parameterize and evaluate SBI-aware bias correction approaches.

These SBI-driven temperature patterns have significant implications for permafrost modelling. Application of the TTOP model in these valleys demonstrates that accounting for SBI-driven SLRs reversals produces substantially different estimates of ground thermal conditions when compared to models that assume standard environmental lapse rates (Garibaldi et al., 2024b). When SBIs were ignored, there were cold biases upwards to 6.8 °C near the ridgetops, where the temperature was systematically underestimated (Garibaldi et al., 2024b) (Figure 2-12). As a result, permafrost distribution and thermal state can be significantly misrepresented if SBIs are not considered.

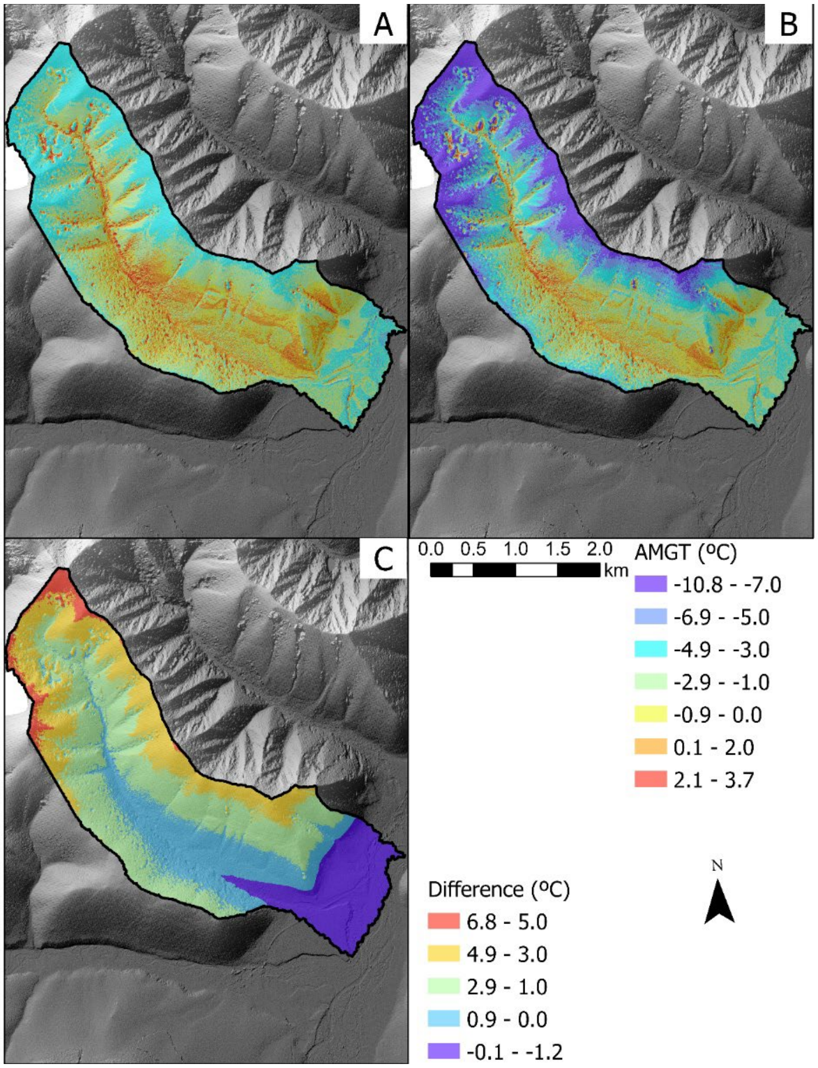

Figure 2-12: The annual mean ground temperature (AMGT) in WS01 for (a) calculated using the TTOP model with consideration of inverted annual average SLRS, (b) calculated using the TTOP model assuming that the SLRs were -6.5 °C km^{-1}, and (c) the difference between the two surfaces (a-b) (Garibaldi et al., 2024b, p. 620).

These studies also illustrate that permafrost response to climate change in SBI-prone environments differs from conventional expectations of accelerated warming at high elevations (Palazzi et al., 2019; Pepin et al., 2015; Pepin et al., 2022). Rather than simple upslope retreat, permafrost degradation can occur bidirectionally from mid-elevation thermal belts, with valley bottoms and upper slopes experiencing distinct thermal responses depending on changes to SBI strength and frequency (Garibaldi et al., 2024a). Alterations in the SLR magnitude and sign (positive or negative) associated with evolving SBI conditions therefore play a critical role in determining how warming is distributed across the landscape. Locations predicted by the TTOP model to being most prone to changes in SLRs were higher elevation locations that lacked vegetation cover and organic layers (Figure 2-13) (Garibaldi et al., 2024a).

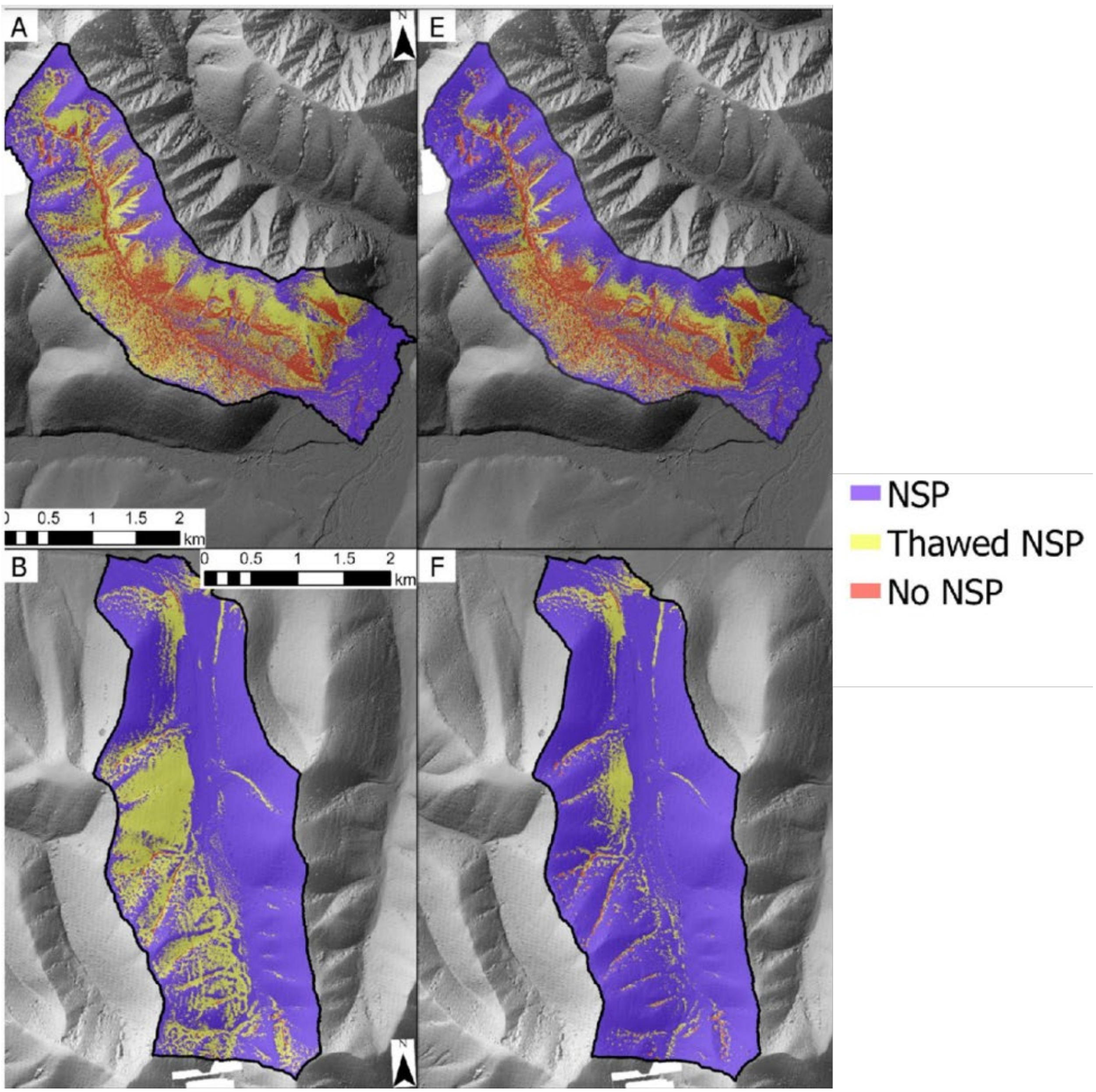

Figure 2-13: Maps illustrating near surface permafrost, no near surface permafrost currently, and near surface permafrost thaw (a) WS01 and (b) WS02 and under the baseline warming with a 5 °C km $^{-1}$ weakening of the inverted SLR scenario for (e) WS01 and (f) WS02 (Garibaldi et al., 2024a, pp. 10).

Despite these advances, most existing modelling approaches rely on equilibrium modelling methods such as the TTOP model, which do not account for the transient response of the ground thermal regime to climate change and disturbance (Riseborough et al., 2008). This limitation introduces uncertainty in predictions of permafrost change, particularly in environments where the ground is not in thermal equilibrium with current climate conditions (e.g., Vegter et al., 2024; Zhang et al., 2008a). Unlike equilibrium approaches, transient models simulate the temporal evolution of ground temperature profiles and can therefore represent non-equilibrium responses to climate forcing (Riseborough, 2007). These models enable estimation of active layer thickness, freeze–thaw dynamics, and the response of permafrost to changing climate conditions (Burn & Zhang, 2010; Riseborough et al., 2008).

Overall, SBIs are a common feature of high-latitude mountain valleys and can persist throughout much of the winter season, exerting a strong influence on surface air temperature patterns and elevational temperature structure. Despite their importance, the spatial and temporal variability of SBIs remains insufficiently characterized in subarctic environments, particularly using high-resolution in situ observations. This limits the ability to evaluate inversion-driven biases in climate forcing data and to assess how these biases propagate into process-based permafrost models. These limitations motivate the need to better quantify SBIs, improve bias correction approaches, and evaluate their implications for modelling transient permafrost thermal dynamics.

2.4 Knowledge gaps

The following are three main knowledge gaps identified in this literature review that are used to inform the objectives of this thesis.

1) **Limited understanding of spatial and temporal structure of SBIs in high-latitude mountain valleys**. While SBIs are known to be deeper, stronger, and more persistent in high-latitude regions (Mayfield & Fochesatto, 2013; Noad & Bonnaventure, 2022; Noad et al., 2023; Seidel et al., 2010; Shahi et al., 2020; Zhang et al., 2011), most detailed observations of SBI structure and cold air pooling have been conducted in mid-latitude environments (e.g., Müller & Whiteman, 1988; Rupp et al., 2020; Sakiyama, 1990; Whiteman et al., 1999; Whiteman et al., 2004b). In-situ measurements of SBIs across elevational transects in high-latitude mountain valleys remains limited (e.g., Noad & Bonnaventure, 2022; Pike et al., 2013; Williams & Thorp, 2015). As a result, understanding of the spatial and temporal variability of SBI strength, depth, and frequency and their impact on surface air temperatures remains constrained.
2) **Lack of SBI-aware atmospheric forcing in climate datasets used for permafrost modelling**. SBIs and their effects on SLRs are poorly represented or absent in most climate reanalysis and downscaled datasets. As a result, valley-scale temperature structure and its temporal variability are not accurately captured (Noad & Bonnaventure, 2022; Pozsgay & Gruber, 2025), leading to systematic biases in permafrost modelling (Garibaldi et al., 2024b; Lewkowicz & Bonnaventure, 2011). Recently developed methods to account for SBI induced biases in downscaled climate datasets (Cao et al., 2017; Pozsgay & Gruber, 2025) require testing of transferability and performance using a high-resolution network of air temperature loggers. With the results of this model evaluation can be used to inform adjustments to the model to improve its generalizability and performance in predicting air temperature patterns broadly across high-latitude valleys without local calibration.

3) **Uncertainty in representing SBI impact in transient permafrost modelling frameworks.** Most permafrost modelling in these regions has relied on equilibrium approaches such as the TTOP model, which does not account for transient responses of the ground thermal regime to changing climate or disturbance (Riseborough, 2007; Riseborough et al., 2008). While these models have demonstrated the importance of SBIs to permafrost distribution and thermal state (Garibaldi et al., 2024a, 2024b), their ability to represent time-dependent processes such as active layer dynamics and evolving ground temperatures remains limited. Thus, there is a need to evaluate how SBI-aware atmospheric forcing influences transient permafrost simulations, and whether these models can better capture the evolution of air and ground temperature relationship in SBI prone environments.

Overall, the literature review in this chapter highlights the central challenge in permafrost modelling in high-latitude complex terrain: surface air temperature is strongly impacted by SBIs, yet those processes are poorly resolved in commonly used climate datasets, leading to systematic biases in atmospheric forcing for permafrost models. Addressing this challenge requires first improving understanding of the spatial and temporal patterns of SBIs in subarctic valleys, then developing methods to correct SBI-related biases in downscaled climate data and improving transferability of these corrections across regions. Finally, these advances must be evaluated within process-based transient modelling frameworks to determine the thermal dynamics of permafrost in response to SBI-aware climate forcing. This thesis is structured to address each of these parts in sequence.

2.5 Objectives

The following four objectives will be addressed in the manuscript chapters 3 to 6 in this thesis:

1) To quantify the spatial and temporal structure of SBIs in two dissimilar high-latitude mountain valleys, and to assess the extent to which these patterns and their controlling mechanisms are transferable between neighbouring valleys (Chapter 3).
2) To evaluate the performance and transferability of a recently developed SBI-aware bias correction approach (Pozsgay & Gruber, 2025) using high-resolution in-situ observational networks in subarctic valleys (Chapter 4).
3) To improve the inversion bias correction modelling framework by addressing limitations affecting its transferability and general applicability across high-latitude mountain regions (Chapter 5).
4) To simulate the spatial and temporal dynamics of the ground thermal regime in high-latitude mountain valleys using a process-based transient model (NEST), and to assess the sensitivity of ground temperatures and active layer thickness to SBI-aware atmospheric forcing and snow redistribution under historical climate conditions (1950-2025) (Chapter 6).

Together, these objectives address the central challenge of representing SBI-driven biases in atmospheric forcing and their implications for permafrost modelling.

2.6 Hypotheses

The following hypotheses are broken up into four sections that correspond to the objectives section.

1) Surface-based temperature inversions (SBIs) exhibit consistent spatial structure across high-latitude mountain valleys, characterized by stronger inversion magnitude and more

frequent positive lapse rates at lower elevations compared to upper slopes, despite differences in overall inversion intensity between valleys.

2) An inversion-aware bias correction model calibrated using absolute elevation will exhibit reduced performance when applied outside its calibration region, while locally calibrated model scenarios will demonstrate improved predictive accuracy of elevational temperature patterns than other downscaling methods in SBI prone terrain.
3) A modified inversion bias correction framework incorporating relative elevation and a *valleyness* term will improve model performance and transferability across high-latitude mountain environments without site-specific recalibration.
4) The inclusion of SBI-aware atmospheric forcing will significantly influence modelled ground temperatures and active layer thickness, with the greatest sensitivity occurring at exposed mid- to upper-slope locations where surface and subsurface buffering is limited. In contrast, sites with greater snow accumulation and organic insulation will exhibit reduced sensitivity. Additionally, spatial variations in snow cover will exert a stronger control on the ground thermal regime than SBI-aware atmospheric forcing at most sites.

3. Spatiotemporal variability of surface-based temperature inversions in high-latitude northcentral Yukon valleys utilizing a dense network of elevation transects

Noad, N. C., & Bonnaventure, P. P. (2026). Spatiotemporal variability of surface-based temperature inversions in high-latitude northcentral Yukon valleys utilizing a dense network of elevation transects. *Arctic, Antarctic, and Alpine Research*, *58*(1), 2614790. https://doi.org/10.1080/15230430.2026.2614790

Department of Geography and Environment, University of Lethbridge, Lethbridge, AB, T1K 3M4, Canada

Keywords: Surface lapse rates, Surface-based temperature inversions, High-latitude mountain valleys, Dempster Highway, Elevational transect analysis.

3.0 Abstract

SBIs strongly influence air temperature variability in high-latitude mountains, yet their spatial structure remains poorly resolved. To address this gap, a dense network of air temperature sensors was deployed and elevational transect analysis (ETA) was applied to quantify SLRs and SBI characteristics at fine temporal and spatial scales. SBI frequency and SLR magnitude increased significantly in anomalously warm summers, linking large-scale climate variability and valley-scale elevational temperature patterns. Contrary to the common assumption of linear lapse rates, annual and monthly mean SLRs were most strongly positive within the lowest 60 meters of the valleys and weakened rapidly upslope. This highlights the importance of sampling valley bottoms and lower slopes to capture SBI intensity. Using ETA, SBI depth was quantified for the first time and found on average to be shallow (<250 m), rarely extending above the ridgetops (500 m). SBI development and breakup were not solely driven by cold-air pooling and daytime convective mixing, but also by processes such as warming or cooling aloft. These findings provide new insights into the SBI structure in subarctic valleys. They strengthen the physical basis for representing temperature variability, essential to modelling surface phenomena such as permafrost distribution.

3.1 Introduction

A key question in mountainous high-latitude regions is how climate warming is distributed across the landscape. An important variable in this distribution of warming is of elevational patterns of warming (Byrne et al., 2024; Pepin et al., 2022). A key control on elevational patterns of temperature in high-latitude regions is SBIs (Noad and Bonnaventure, 2022; O'Neill et al., 2015; Smith and Bonnaventure, 2017). SBIs occur when temperature increases with altitude or elevation from the earth's surface to the inversion top in the lower troposphere (Ross, 2024). SBIs are common in mountain valleys due to cold air pooling in valley bottoms primarily at night or in winter (Clements et al., 2003; Daly et al., 2010; Vitasse et al., 2017; Whiteman & McKee, 1982; Whiteman et al., 2001) and are a dominant feature in high-latitude mountain valleys (Mayfield & Fochesatto, 2018; Przybylak, 2016; Serreze & Barry, 2014). If SBIs become less prevalent, shallower, or weaken, warming at lower elevations may be amplified (Noad et al., 2023). This would result in patterns of warming contrary to elevation dependent warming (Pepin et al., 2015) in this region, an idea postulated by Garibaldi et al. (2024a).

Frequent SBIs drive prevailing patterns of increasing air temperature with elevation, which can be described as a positive SLR (Lewkowicz & Bonnaventure, 2011; Lewkowicz & Ednie, 2004; Noad & Bonnaventure, 2022; Pike et al., 2013). SLRs in mountain valleys of northcentral Yukon were measured to be as steep as 1.2 °C 100 m^{-1} on annual average and 2.5 °C 100 m^{-1} in winter (December through February) (Noad and Bonnaventure, 2022). These positive SLR patterns have been conceptualized (Bonnaventure & Lewkowicz, 2013) and shown by modelling to significantly alter the distribution of permafrost in high-latitude mountain valleys (Garibaldi et al., 2024b).

Radiosondes are commonly used to measure SBIs (Bourne et al., 2010; Bradley et al., 1992, 1993; Fochesatto et al., 2015; Gilson et al., 2018; Maillard et al., 2022; Mayfield & Fochesatto, 2013; Noad et al., 2023; Zhang et al., 2021). These datasets are limited by instrument changes over time and sparse spatial coverage in high-latitude regions (Zhang and Seidel, 2011). Climate reanalysis products provide another way to quantify SBIs (Akperov et al., 2019; Ruman et al., 2022; Shahi et al., 2020) but remain too coarse to resolve the local processes of cold air pooling in narrow mountain valleys (Cao et al., 2017). Efforts to downscale climate reanalysis data to account for local processes (e.g. Benestad & Chen, 2008; Bieniek et al., 2016) include GlobSim (Cao et al., 2019). Due to the coarse horizontal and vertical resolution of the original reanalysis products, both downscaling approaches failed to capture local cold-air pooling and positive SLRs in narrow Yukon valleys (Noad & Bonnaventure, 2022; Pozsgay and Gruber, 2025). Despite their importance, the spatio-temporal structure of SBIs in high-latitude valleys remain poorly quantified because existing approaches lack the resolution to capture valley-scale processes.

SLRs in narrow valleys can be measured using Elevation Transect Analysis (ETA) (Noad and Bonnaventure, 2022). This involves deploying shielded air temperature sensors roughly 2 meters above the surface at set elevation intervals. Similar methods have been applied in high-latitude mountains (Bonnaventure et al., 2011; Lewkowicz et al., 2012; Pike et al., 2013; Smith & Bonnaventure, 2017; Williams & Thorp, 2015), and in mid-latitude mountain valleys in areas such as Western North America (Lundquist & Cayan, 2007; Minder et al., 2010, Rupp et al., 2020), the European Alps (Vitasse et al., 2017) and the Spanish Pyrenees (Pagès et al., 2017).

Research on cold-air pools and SBIs in high-latitude alpine regions is limited because these areas are difficult to access. ETA with three sensors measured SLRs from the valley bottom to roughly 150 vertical meters above the valley floor in northcentral Yukon valleys (Noad and Bonnaventure, 2022). The air temperature sensor network was extended from valley bottom to near the ridge to model permafrost (Garibaldi et al., 2024a, 2024b) allowing for a high-resolution quantification of SLRs, SBI frequency, SBI strength, and SBI depth (definitions in section 3.3.4).

In this study, spatio-temporal SLR patterns and SBI characteristics are quantified for two dissimilar Yukon valleys. A 7-year record of temperature is used to test the hypothesis that warmer than normal years or winters correspond to weaker or less frequent SBIs and less positive SLRs. Synoptic conditions and local-scale thermal forcing are characterized to explain interannual variations in SBI frequency and strength. High-resolution elevational transects resolve the spatial structure of SBIs, with focus on annual and monthly averages of SBI structure, as these time scales are particularly relevant for permafrost modelling (e.g. Smith & Riseborough, 2002; Zhang et al., 2008b). We hypothesize that the lowest elevation sites will exhibit the coldest monthly and annual temperatures due to persistent cold-air pooling, leading to the valley-outlet sites being colder than valley bottom sites further up-valley. Measurements from neighboring valleys are used to evaluate the transferability of SLR and SBI patterns between valleys. Finally, mechanisms of SBI development and breakup are investigated. SBIs are expected to develop primarily through cold-air pooling at low elevations and to break up as solar heating warms the valley bottoms (Whiteman, 1982). This research aims to improve understanding of the spatio-temporal structure of SBIs and the processes driving their development and breakup, providing a stronger basis for process-based modelling of air temperature and permafrost in high-latitude alpine regions.

3.2 Study Region and Area

This study was conducted in the Ogilvie Mountains along the Dempster Highway in northcentral Yukon (Figure 3-1). The region is characterized by moderate relief narrow valleys with steep slopes (30-40 °) (Yukon Ecoregions Working Group, 2004). Elevation ranges from approximately 550 m a.s.l. in mountain valleys of the northernmost part of the region to approximately 2300 m a.s.l. on the mountain peaks of the southernmost part of the region. The nearest climate station, Dawson City (75 km southwest), recorded 1981-2010 mean annual air temperature of -4.1 °C and 324.4 mm of annual precipitation, 38 % of that snow (Environment and Climate Change Canada, 2025). Intense cold air pooling leads to strong SBIs with MAAT as low as -9.2 °C in valley bottoms (Burn et al., 2015), while surrounding slopes are roughly -4 °C (Garibaldi et al., 2024b). The vegetation consists of boreal forest cover at lower elevations and alpine tundra above treeline (Scudder, 1997). This region lies within the transition from discontinuous (50-90 %) to continuous (90-100 %) permafrost (Heginbottom et al., 1995).

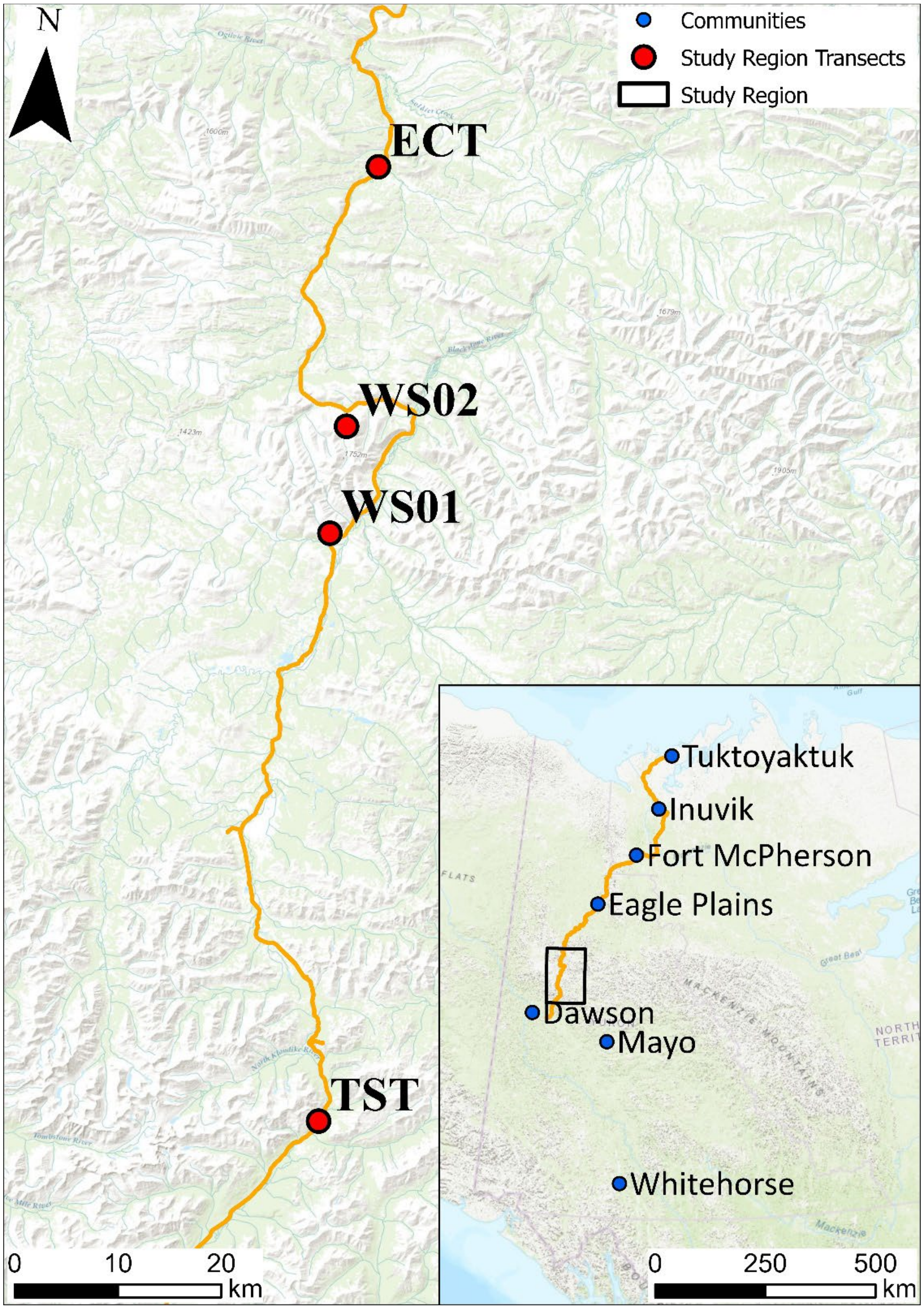

Figure 3-1: The Ogilvie Mountains study region in northcentral Yukon along the Dempster Highway, showing the study site locations: Tombstone Transect (TST), Weather Station Valley 1 (WS01), Weather Station Valley 2 (WS02), and Engineer Creek Transect (ECT). The Esri Topographic Basemap illustrates the topography of the region.

There are 4 study areas examined (all unofficial names) (Figure 3-1). The two primary locations are Weather Station 1 (WS01) study area and Weather Station 2 (WS02) study area. The other study areas include the Tombstone Transect (TST) and Engineer Creek Transect (ECT). The TST study area (southernmost transect) ranges in elevation from roughly 950 m to 1900 m, transitioning from boreal forest cover to alpine tundra cover. The ECT study area (northernmost transect) ranges from 650 m to 1000 m and is entirely contained in the boreal forest.

The WS01 study area has a primary valley that is V-shaped, ranging in elevation from roughly 950 m to 1720 m, with open boreal forest at lower elevations (below 1150 m on the south aspect slope) and blockfields with patches of moss at higher elevations (Figure 3-2a). The ridge to the southwest of the valley is 200 to 300 m high while the ridge to the northeast is 400 to 500 m high. Fetch length of the valley is roughly 5.5 km. The valley just north of the WS01 primary valley is called the Daly valley and it has a similar range in elevation (900 m to 1500 m) with forest only in the valley bottom and shrubs and moss on the surrounding slopes. The fetch length is slightly less than the primary WS01 valley at roughly 4.5 km. Both valleys are orientated east-west with the valley curving to the north in the up-valley direction.

The WS02 study area is roughly 8 km north of WS01 and features a primary valley that is U-shaped, spanning a range of elevation from roughly 1050 m to 1790 m, with alpine tundra in the valley bottom and moss and grass patches near seeps on the blockfield slopes (Figure 3-2b). The ridge to the west of the valley is roughly 400 to 600 m above the valley floor. The ridge to the east of the valley begins at around 200 m above the valley floor, reaches a peak of 500 m above the valley floor then tapers to around 250 m above from valley outlet to top. The fetch length of the WS02 primary valley is roughly 6.5 km. The valley that is just to the east of this primary valley is called Bexte valley and ranges in elevation from roughly 1050 m to 1600 m. The fetch length is roughly 2 km from the outlet to the top of the valley. WS02 study area valleys have a north-south orientation.

The WS01 and WS02 study areas were selected to test the hypothesis that positive annual average SLRs occur below treeline and negative SLRs above (Bonnaventure & Lewkowicz, 2013; Wahl, 1987). These valleys were chosen because they are within 10 km of each other; WS01 has forest cover while WS02 is predominately treeless, and both are accessible via the Dempster Highway.

3.3 Methods

3.3.1 Sensor Types and Specifications

Air temperature was measured using HOBO U23 and MX2300 Bluetooth loggers (accuracy ±0.25 °C; resolution 0.04 °C and 0.02 °C, respectively) housed in passively ventilated RS01 radiation shields (Onset, USA). All shields were mounted 1.5–2 m above the ground to record surface air temperature.

3.3.2 Sensor Network Design and Rationale

A total of 54 surface air temperature stations were used to populate this study. This includes 24 and 25 air in WS01 and WS02 study areas respectively. The 5 remaining air stations used were deployed along the Dempster Highway from near the Tombstone Interpretive Center in the south to near the Engineer Creek Yukon Territory campground in the north (Figure 3-1; Table 3-1). The network was first installed in August 2017 and was expanded extensively between 2021 and 2023.

Table 3-1: Coordinates, elevation of the lowest and highest station, the number of stations, and the initial year of installation for each study area in the study region. The WS01 study area includes the Daly valley which is adjacent to the primary WS01 valley. The WS02 study area includes the Bexte valley which is adjacent to the primary WS02 valley.

Study Area	Latitude	Longitude	Bottom Elevation (m a.s.l)	Top Elevation	# of Stations	First Sites Installed	Latest Expansion Year
Tombstone Transect (TST)	64.4579°	-138.2151°	982	1088	3	2017	2023
Weather Station 1 (WS01)	64.9585°	-138.2803°	935	1427	25	2017	2023
Weather Station 2 (WS02)	65.0498°	-138.2634°	1045	1595	26	2017	2023
Engineer Creek Transect (ECT)	65.2732°	-138.2382°	671	874	2	2017	2017

Initial transects in 2017 placed a weather station in the valley bottom and sensors 100–150 m above the valley floor (Figure 3-2). Using ETA methodology, prior work showed consistently positive SLRs on all transects, regardless of tree cover (Noad & Bonnaventure, 2022). The expanded network addresses remaining questions about the vertical extent of SBIs and SLRs toward the highest ridgetops.

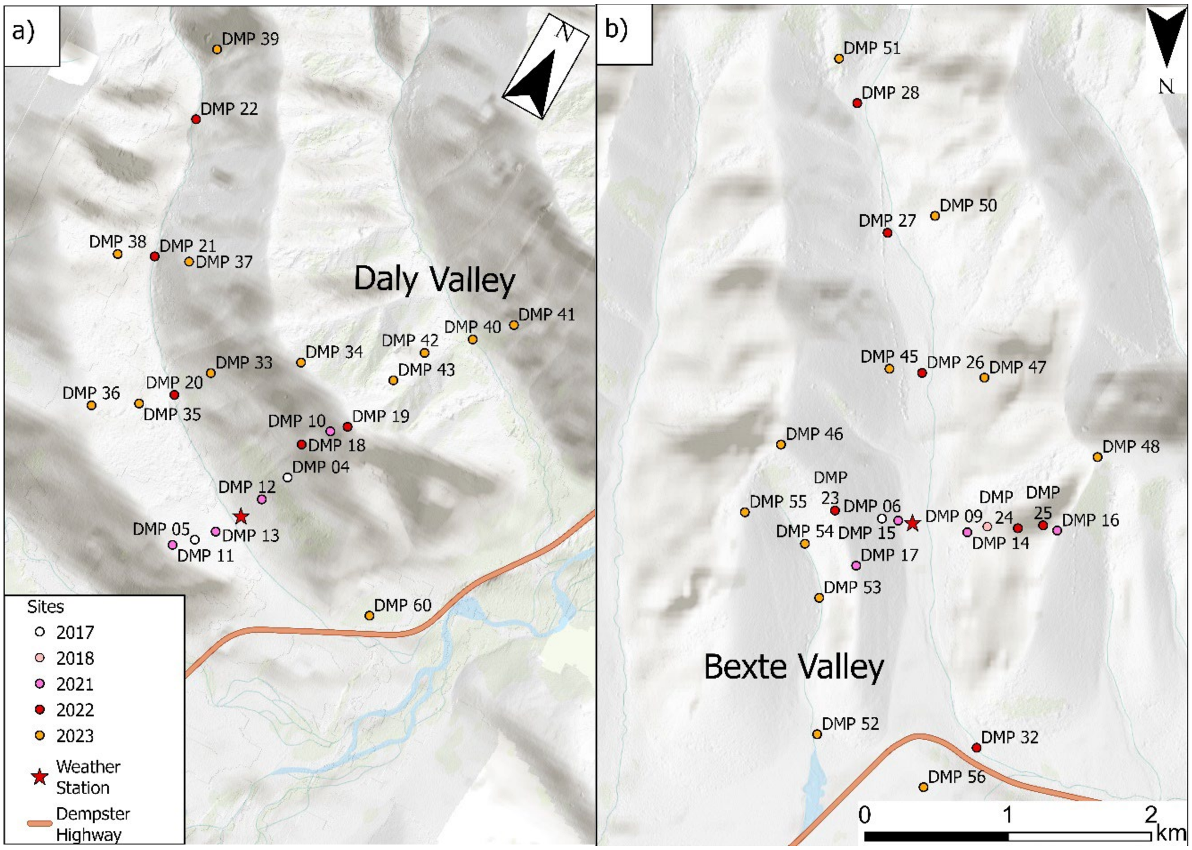

Figure 3-2: The sensor network set up in (a) WS01 and (b) WS02 study areas. This includes the Daly valley which is adjacent to the WS01 primary valley and the Bexte valley which is adjacent to the WS02 primary valley. The colours of the site points denote the year they were deployed. The Esri Satellite Imagery basemap underlays the map.

3.3.3 Climate Typicality and Interannual SLR Patterns

The nearest long-term climate station, Dawson YT (370 m a.s.l.), is 75 to 150 km to the southwest of the study area and is not representative of higher elevation terrain studied here (671 to 1595 m a.s.l.). To obtain site-specific climate information, monthly temperature data were extracted from ClimateNA, a tool that downscales gridded climatology data to point locations using elevation-dependent adjustments (Wang et al., 2016). ClimateNA was used to generate 1) 1991-2020 climate normals for each month and 2) mean monthly temperatures for the study period (2017-2024) at the WS01 weather station location.

Climate anomalies were calculated by subtracting the 1991-2020 monthly normal from the monthly ClimateNA values for 2017-2024. Positive (negative) climate anomalies indicate warmer (colder) than average months.

In-situ air temperatures at WS01, DMP04, and DMP05 were aggregated into monthly and annual averages. Anomalies were computed relative to the study-period baseline, defined as the mean temperature for each month over 2017-2024. These observed anomalies were compared with ClimateNA-derived anomalies to assess consistency between local measurements and regional climate variability.

SLRs, SBI strength, and SBI frequency (definitions in section 3.3.4) were average at monthly, seasonal, and annual scales across the 6 original transects including TST, WS01 South Facing Transect (SFT main), WS01 North Facing Transect main (NFT main), WS02 East Facing Transect main (EFT main), WS02 West Facing Transect main (WFT main), and ECT (Tables 3-2 and 3-3). Prior to 2021, the WS01 and WS02 study area main transects consisted only of a valley bottom station and one site approximately 100 to 150 meters up the adjacent slopes; therefore, only these sites were used in the temporal analysis. For each metric, anomalies were calculated by subtracting the study period baseline for that transect and then combined across transects to produce a regional anomaly series. Data from the TST were excluded because snow periodically covered the air temperature logger at DMP08 site.

Pearson correlation coefficients were used to quantify the strength and statistical significance of linear relationships between SLR/SBI anomalies and ClimateNA temperature anomalies. Pearson correlations were selected because the variables are continuous, approximately normally distributed at aggregated time scales, and the goal was to assess linear covariation.

3.3.4 Calculating Surface Lapse Rates and SBI Characteristics

Surface lapse rates (SLRs) were calculated by taking the difference between the temperature of the lower elevation site and adjacent higher elevation site. This temperature difference was divided by the vertical separation between the two sites and standardized °C per 100 m. Mean temperatures and mean SLRs were utilized to quantify typical valley-scale thermal patterns and SBI structure. This approach aligns with common practice for permafrost and climate modelling, which generally rely on mean temperature inputs.

SBI strength was the magnitude of all positive SLRs on a transect segment, averaged to monthly and annual time scales.

SBI frequency was the proportion of SLR readings on a segment of transect that were positive over a period (monthly, annual, or study period).

The depth of SBIs was estimated along the main transects as the elevation where the SLRs transitioned from positive to negative. For example, if the SLR remained positive to site DMP18 (239 vertical meters above the valley floor) but became negative at DMP10 (367 m), then the inversions depth assigned was 239 – 367 m.

These next characteristics were calculated using the segments of transect along only the four main transects (WS01 SFT and NFT, WS02 EFT and WFT).

An SBI event was defined as a positive SLR that occurred within the first 100-150 vertical meters of the transect, consistent with standard approaches in high-latitude regions (e.g. Gilson et al., 2018; Noad et al., 2023). The event continued until SLRs became negative on both first two segments of the transect, at which point an SBI breakup event was recorded.

Event duration was defined by the number of consecutive 2-hour interval readings and SBI event occurred. For example, an SBI event that lasted for 3 readings was classified as a 6-hour SBI event.

3.3.5 The Elevation Transects

SLRs were derived from 51 air-temperature station pairs, each consisting of one low-elevation and one high-elevation site, across the WS01 and WS02 valleys. The main transects (WS01 SFT, WS01 NFT, WS02 EFT, and WS02 WFT) provide the finest vertical resolution, with sensors roughly 50 vertical meters above the valley floor, then roughly 100 vertical meter intervals to the ridgetops (Table 3-2, Figure 3-2). It is important to note that prior to 2021, these main transects only had two sites, one valley bottom site and one site positioned 100 to 150 m up each adjacent slope. Thus, only these transect segments were used for the temporal analysis described in section 3.3.3. The WS01, WS02, TST, and ECT study areas have additional transects that include other low-high elevation station pairs (Table 3-3). The full network and all segments of transect were only available in August 2023 to August 2024 year.

Table 3-2: The site ID, elevations, elevation range, and number of stations on each main transect in the WS01 and WS02 study area.

Transect ID	Site ID	Elevation (m a.s.l.)	Elevation Range	# of Sensors
WS01 NFT Main	WS01	997	243	4
	DMP13	1059		
	DMP05	1147		
	DMP11	1225		
WS01 SFT Main	WS01	997	445	6
	DMP12	1035		
	DMP04	1142		
	DMP18	1236		
	DMP10	1364		
	DMP19	1427		
WS02 EFT Main	WS02	1109	484	7
	DMP14	1150		
	DMP09	1202		
	DMP24	1321		
	DMP25	1417		
	DMP16	1475		
	DMP48	1593		
WS02 WFT Main	WS02	1109	486	6
	DMP15	1128		
	DMP06	1203		
	DMP17	1308		
	DMP23	1406		
	DMP46	1595		

Table 3-3: The low and high elevation site ID, elevations, and vertical distance of each transect other than the four main transects.

Study Area	Low-High Site ID	Elevation (m a.s.l.)	Vertical Distance (m)
WS01 Study Area	DMP60-WS01	935-997	62
	WS01-DMP20	997-1036	39
	DMP20-DMP21	1036-1085	49
	DMP21-DMP22	1085-1180	95
	DMP20 - DMP35	1036-1137	99
	DMP35 - DMP36	1137-1316	179
	DMP20-DMP33	1036-1136	100
	DMP33-DMP34	1136-1425	289
	DMP21-DMP38	1085-1190	105
	DMP21-DMP37	1085-1211	126
	DMP22-DMP39	1180-1307	127
	DMP40-DMP41	999-1107	108
	DMP40-DMP42	999-1103	105
	DMP42-DMP43	1103-1221	118
WS02 Study Area	DMP32-WS02	1045-1109	64
	WS02-DMP26	1109-1150	41
	DMP26-DMP27	1150-1209	59
	DMP27-DMP28	1209-1259	50
	DMP28-DMP51	1259-1373	114
	DMP26-DMP47	1150-1259	109
	DMP47-DMP48	1259-1593	334
	DMP26-DMP45	1150-1224	74
	DMP45-DMP46	1224-1595	371
	DMP27-DMP50	1209-1309	100
	DMP27-DMP49	1209-1283	74
	DMP28-DMP51	1259-1373	114
	DMP52-DMP53	1071-1184	113
	DMP53-DMP54	1184-1254	70
	DMP54-DMP55	1254-1472	218
	DMP55-DMP46	1472-1595	123
TST	DMP08-DMP07	982-1088	106
ECT	DMP02-DMP03	671-874	203

3.3.6 Statistical Relationship between temperature and Elevation on the Valley Scale

Simple linear regressions were performed for mean annual and monthly temperatures in both weather station valleys (August 2023-August 2024). Piecewise linear regressions were conducted in R using the dseg library (Machne and Stadler, 2020) with a penalty parameter optimized iteratively to constrain the number of break points to less than or equal to 3. The final penalty parameter value was 1500 for WS01 and 600 for WS02.

3.3.7 Determining Mechanisms of SBI Development and Breakup

SBI development and breakup were assessed by computing the temperature differences between low and high sites on each segment of transect immediately prior to and after each event. This approach identifies whether SBIs developed due to cooling at low sites, warming at high sites, or a combination of both and if it breaks up due to warming at low sites, cooling at high sites, or a combination of both.

3.3.8 Synoptic and Thermal Drivers of SLRs and SBI Characteristics

Two additional metrics were reviewed to investigate the drivers of the significant increase in SBI frequency and SLRs during warm summers. This analysis included the valley-bottom weather stations and the paired air-temperature stations located approximately 100-200 m up-slope on the 6 primary transects that spanned the full study period (WS01 SFT main, WS01 NFT main, WS02 EFT main, WS02 WFT main, TST, and ECT).

For synoptic-scale influences, 700 hPa relative vorticity derived from ERA5 reanalysis product was downloaded (Copernicus Climate Change Service, 2017; Hersbach et al., 2020) and extracted to the coordinates of each transect at two-hour intervals matching in-situ temperature records (August 2017- August 2024). Vorticity values were grouped into summer-specific quartiles to classify them as cyclonic, anticyclonic, or neutral conditions. Nights with any positive SLRs were classified as SBI present nights. For each vorticity category between the 6 transect segment used in the temporal analysis (Section 3.3.3) in the two study areas, the frequency of SBI nights, mean SBI strength (Section 3.3.4), and mean SLRs (Section 3.3.4) were computed.

For local-scale thermal forcing, diurnal temperature amplitude was calculated as the difference between daily maximum and minimum surface air temperature at the valley bottom station. Diurnal temperature amplitude was aggregated between inversion and non-inversion nights to evaluate whether inversions are associated with increased amplitude of air temperature. In addition, linear regressions were performed between diurnal temperature amplitude and both SLRs and SBI strength.

3.3.9 Time-Step Progression of SBI Events

The temporal progression of SBI was analyzed along the four main transects to characterize changes in the vertical temperature profile over time. Each SBI event was assigned a unique identifier and a duration, which were then used to extract and group all events. For each duration class, SBI vertical temperature structure was at 2-hour intervals to illustrate progression. To complement these individual trajectories, aggregated median profiles were calculated for each duration class, providing a representative evolution of SBI structure and allowing comparison with the variability among individual events.

3.4 Results

3.4.1 Climate Anomalies and Interannual Variation of SLRs and SBI Characteristics

The ClimateNA derived 1991 to 2020 climate normal at the WS01 site, which had a mean annual air temperature of -6.2 °C, with mean January and July temperature of -23.3 °C and 11.4 °C respectively. During the study period (2017-2024), the valley was roughly 0.5 °C warmer than this baseline, with January and July averages of –22.5 °C (+0.8 °C) and 12.4 °C (+1.0 °C). Annual climate anomalies ranged from -0.4 °C (2019-2020) to +1.5 °C (2023-2024).

Observed anomalies at WS01, DMP04, and DMP05 tracked ClimateNA anomalies closely ($R^2 > 0.95$, $p < 0.01$). ClimateNA anomalies also correlated strongly with in-situ data at TST and ECT ($R^2 \geq 0.87$, $p < 0.01$), confirming that the downscaled product captured regional-scale variability.

Interannual variability of SLRs was low across the network, with the coefficient of variation ranging from 7% (WS01 SFT main) to 22% (WS02 EFT main). The exception to this was the TST (28%) which showed anomalous variability likely due to an artifact in the dataset (Section 3.5.1). As a result, the TST dataset was excluded from the remainder of the temporal analysis. SBI strength varied by 3–10% between sites (0.19–0.39 °C 100 m^{-1}), while SBI frequency showed the lowest variability (5–6%).

Annual average SLRs on each transect were below the study-period mean during the two coldest years (2019-2020 and 2021-2022) and above the mean during the two warmest years (2018-2019 and 2023-2024). Similarly, the SBI frequency between all the transects showed the same pattern, with higher-than-average frequency in warmer years and lower frequency in colder years. SBI strength, however, did not display a consistent relationship with interannual climate anomalies.

Significant relationships between climate anomalies, SLRs, and SBI frequency occurred primarily in the summertime. SLRs increased with warmer summers ($R^2 = 0.67$, $p = 0.05$), and SBI frequency also increased with warm summers ($R^2 = 0.75$, $p = 0.03$). Winter anomalies showed the opposite tendency (e.g., stronger SBIs in colder winters), but these relationships were weak ($R^2 < 0.15$) and not statistically significant ($p > 0.05$).

3.4.2 Synoptic and Thermal Drivers of SBI Variability

Given the significant summer-only relationships, synoptic drivers and local thermal forcing were tested to attempt to explain this seasonal pattern. To represent synoptic drivers, 700 hPa vorticity from ERA5 reanalysis product was compared with the frequency of nights with an SBI present. Across the six transects, the proportion of inversion nights was 59% under anticyclonic conditions, 60% under cyclonic conditions, and 67% under neutral conditions. Although these groups were all statistically distinct (χ^2 p-value = 0.0001), the difference was small. Furthermore, linear relationships between vorticity and both valley-scale SBI strength and the valley-scale SLR were exceptionally weak ($R^2 < 0.05$).

Local thermal forcing was represented by diurnal temperature amplitude at the valley bottom site of each transect. In summer, inversion nights had more than double the diurnal amplitude of non-inversion nights (12.1 °C vs. 5.9 °C; t-test $p < 0.001$) (Figure 3-3). Meanwhile, in the winter the same pattern was observed but was weaker (9.0 °C vs. 5.0 °C; t-test $p < 0.001$). SLRs and SBI strength both showed significant (p-value < 0.001) linear relationships with diurnal temperature amplitude in the summer ($R^2 > 0.3$), but only a weak association in the winter ($R^2 < 0.08$) (discussion in Section 3.5.1).

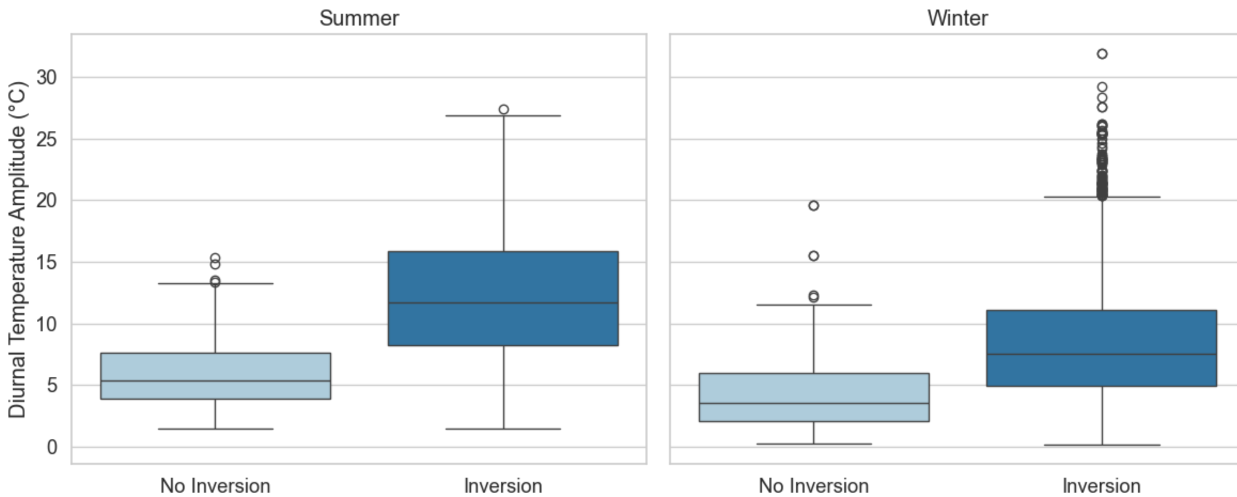

Figure 3-3: Boxplot illustrating the mean (black line), interquartile range (blue box), range of the data (black whiskers), and outlier data points (black circles) for daily temperature amplitude during inversion nights and non-inversion nights in the summer (Jun-Aug) and winter (Dec-Feb) seasons.

3.4.3 Spatial SLRs and SBI Characteristics

Annual average SLRs through the valleys ranged from a strongly positive (2.46 °C 100 m^{-1}; 19 vertical meters) between WS02 and DMP14 (near the valley bottom) to negative (-0.64 °C 100 m^{-1}; 58 vertical meters) between DMP25 and DMP16 (near the ridgetop) (Figure 3-4). Across both WS01 and WS02, the steepest positive SLRs occurred within the first 150 vertical meters (mean = 0.76 °C 100 m^{-1}), especially between the weather stations and the first microclimate sites (mean = 1.88 °C 100 m^{-1}). Above this, SLRs became less positive or negative (mean = -0.19 °C 100 m^{-1}). Neighboring Daly valley showed comparable low-elevation SLRs to WS01, while the Bexte valley exhibited more gently positive SLRs, more like mid-slope SLRs in WS02.

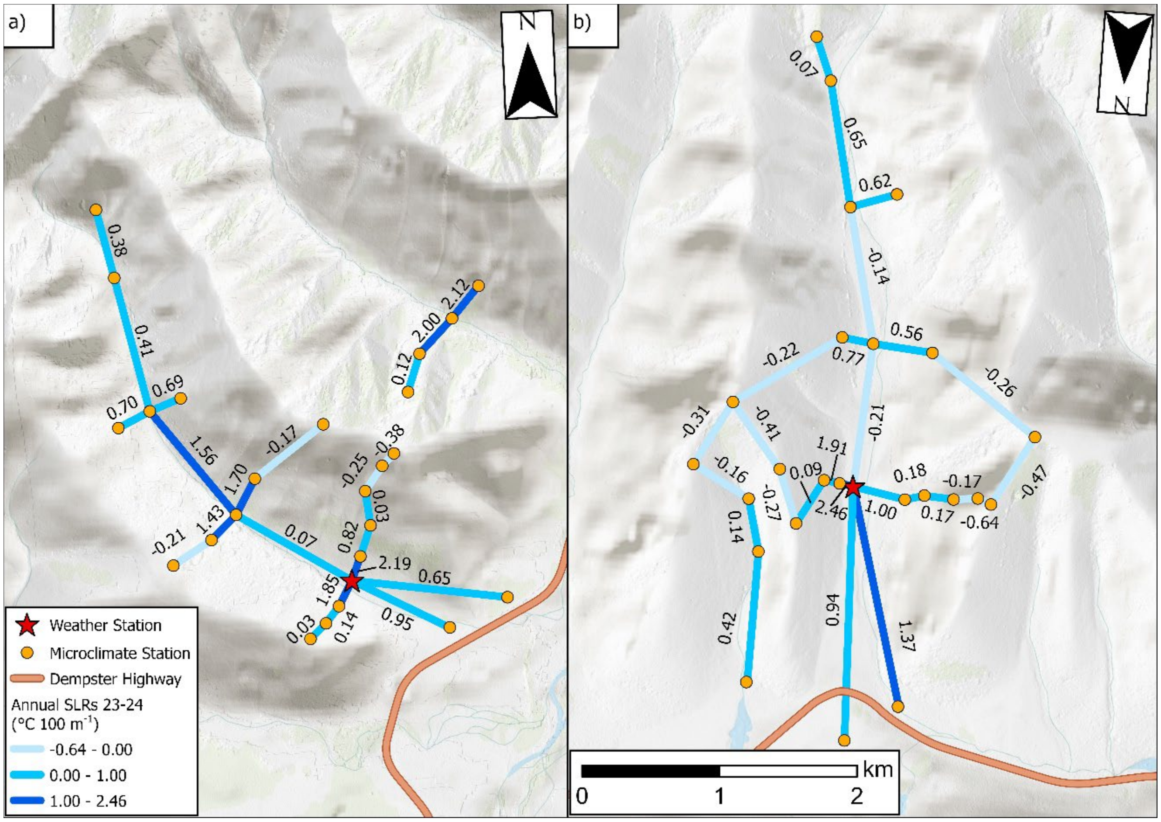

Figure 3-4: Annual average SLRs (August 2023-August 2024) along the transects in the (a) WS01 and (b) WS02 study areas. The Esri Topographic Basemap underlays the map.

SBI strength followed the same spatial structure as SLRs with the strongest mean inversion between the lowest elevation sites and the weakest mean SBI strength between high elevation sites (Figure 3-5). The strongest mean inversions (up to 4.68 °C 100 m^{-1}) occurred within the lowest 19-60 vertical meters of WS01 and WS02, with the Daly valley having nearly equally as strong inversions within the first 100 vertical meters. In contrast, mean SBI strength was much weaker (roughly 1.2 °C 100 m^{-1}) in the Bexte valley, indicating reduced inversion intensity relative to the neighboring primary WS02 valley.

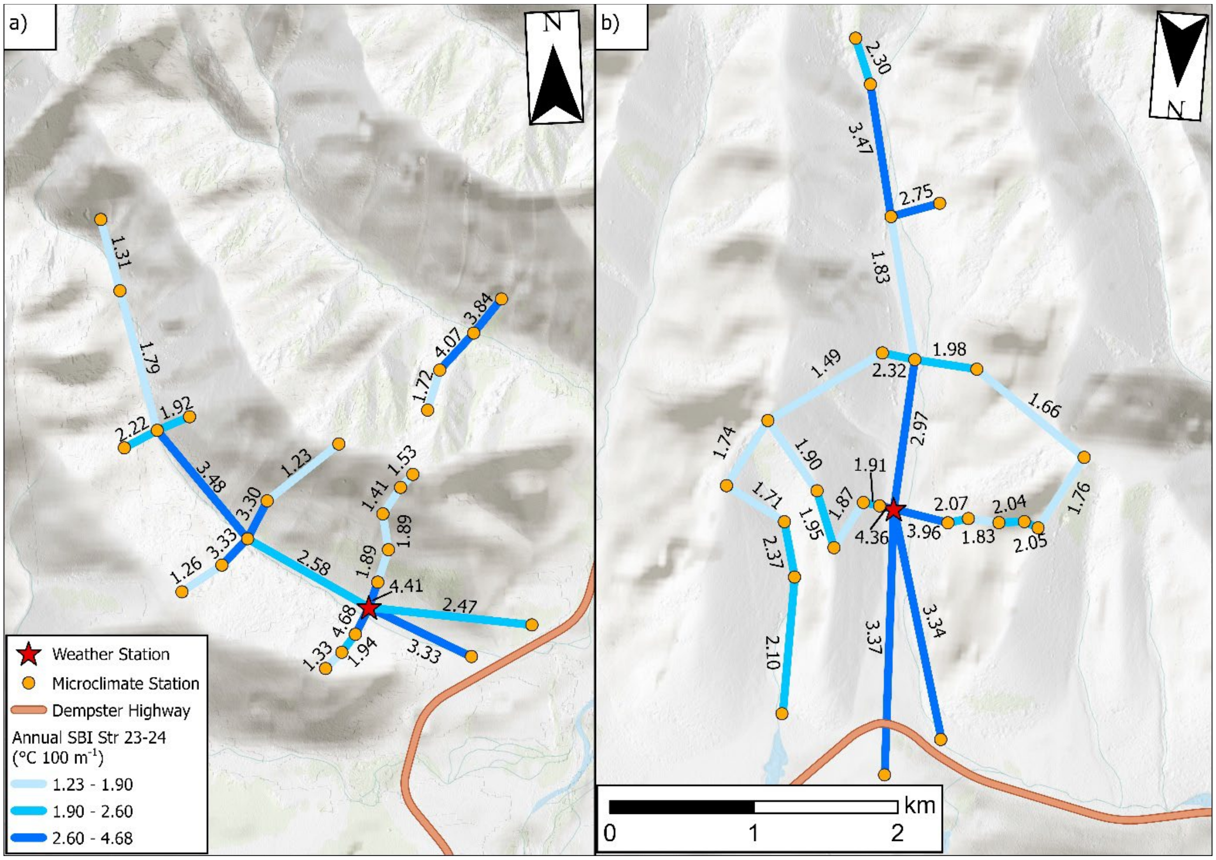

Figure 3-5: Annual average (August 2023-August 2024) SBI strength along the transects in the (a) WS01 and (b) WS02 study areas. The Esri Topographic Basemap underlays the map.

SBI frequency was also highest within the first 100 vertical meters of the WS01 and Daly valleys (47 – 61 % of the time) (Figure 3-6). SBI frequency was greatest only between sites at the outlet of the WS02 valley and within the first 50 vertical meters of the weather station (47%-71%). The lowest frequency of SBIs (13-33 %) was recorded between sites 150 vertical meters above the valley floor as well as three transects in the valley bottom along the valley length of WS02. Again, SBI frequency in the Bexte valley resembled these weaker higher elevation SBI frequencies (18-41 %).

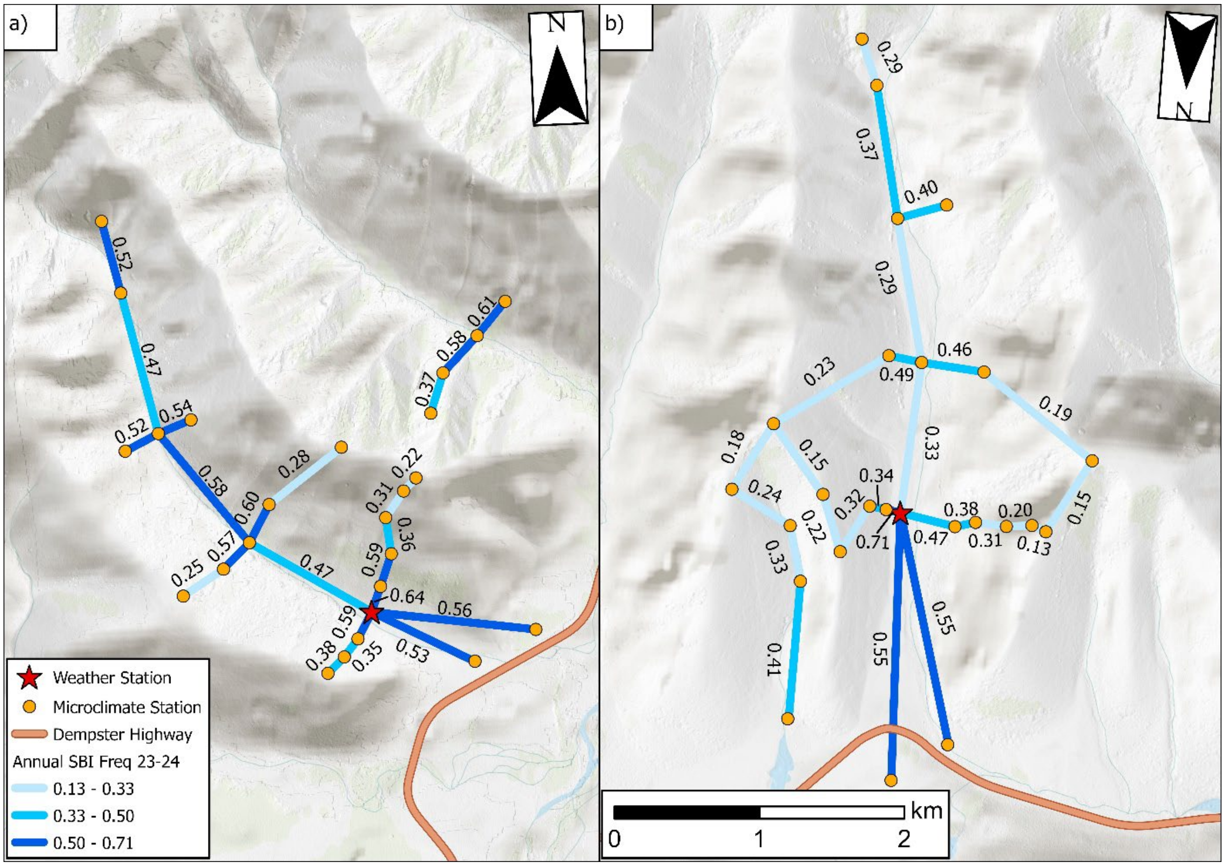

Figure 3-6: Annual average (August 2023-August 2024, the only year the full sensor network was deployed) SBI Frequency along the transects in the (a) WS01 and (b) WS02 study areas. The Esri Topographic Basemap underlays the map.

The strongest, most frequent SBIs occurred in the winter. In January, nearly all transect segments exhibited mean SLRs that were hyper-inverted (>1 °C 100 m^{-1}), the only exceptions were between a few near ridgetop segments of transects in both valleys. In contrast, mean monthly SLRs were negative on most segments of the transects in both valleys in September. In this month, positive mean monthly SLRs were confined to only the segments of transect within the first roughly 100 vertical meters of each valley.

Similarly, SBI strength and frequency followed the same seasonal cycle. Aggregated across both valleys, SBI strength peaked in January (3.57 °C 100 m^{-1} vs. annual mean 2.38 °C

100 m^{-1}) and reached a minimum in September (1.04 °C 100 m^{-1}). Similarly, SBI frequency averaged 69% in January compared to just 18% in September (annual mean 40%).

3.4.4 Temperature vs Elevation

From August 2023 to August 2024 (the only year the full sensor network was deployed), valley-scale temperature-elevation relationships had strong seasonal contrasts. In January, March, and December, both valleys exhibited significant positive relationships (inverted SLRs), with the strongest in January (WS01 = 2.11 °C 100 m^{-1}, WS02 = 1.58 °C 100 m^{-1}; $R^2 > 0.9$) (Table 3-4). In February, the strength of the linear relationship between temperature and elevation was reduced to 1.01 °C 100 m^{-1} ($R^2 = 0.62$) in WS01 and the relationship was not significant in WS02.

In contrast, late spring, summer, and early autumn months (May through September) exhibited significant negative temperature-elevation relationships, with the steepest negative lapse rates in September (WS01 = –0.48 °C 100 m^{-1}, WS02 = –0.66 °C 100 m^{-1}; $R^2 > 0.85$). Transitional spring and autumn months (April, October, and November) had weak or insignificant relationships ($R^2 \leq 0.42$).

At an annual scale, WS01 showed a weak but significant positive SLR (0.35 °C 100 m^{-1}; $R^2 = 0.35$), while WS02 had no significant relationship (SLR = 0.05 °C 100 m^{-1}; $R^2 = 0.03$).

Table 3-4: The linear fitted SLR (slope) each month from August 2023-August 2024 (the year the full sensor network was deployed) for the surface air temperature measurements in both the WS01 and WS02 Valleys. **Bolded** values indicated significant p-values and red values indicate negative lapse rates.

	WS01			WS02		
Month	SLR (°C 100 m^{-1})	R^2	p-value	SLR (°C 100 m^{-1})	R^2	p-value
Jan	**2.11**	**0.94**	**<0.01**	**1.58**	**0.91**	**<0.01**
Feb	**1.01**	**0.62**	**<0.01**	0.22	0.14	0.06
Mar	**1.09**	**0.83**	**<0.01**	**1.11**	**0.90**	**<0.01**
Apr	0.19	0.13	0.08	**-0.21**	**0.37**	**<0.01**
May	**-0.42**	**0.62**	**<0.01**	**-0.41**	**0.72**	**<0.01**
Jun	**-0.26**	**0.42**	**<0.01**	**-0.55**	**0.79**	**<0.01**
Jul	**-0.39**	**0.77**	**<0.01**	**-0.65**	**0.94**	**<0.01**
Aug	**-0.41**	**0.44**	**<0.01**	**-0.62**	**0.74**	**<0.01**
Sep	**-0.48**	**0.85**	**<0.01**	**-0.66**	**0.98**	**<0.01**
Oct	-0.03	0.01	0.62	**-0.21**	**0.34**	**0.02**
Nov	**0.43**	**0.42**	**<0.01**	-0.03	0.01	0.64
Dec	**1.01**	**0.70**	**<0.01**	**0.46**	**0.56**	**<0.01**
Annual	**0.35**	**0.44**	**<0.01**	0.05	0.03	0.42

In WS01, a piecewise linear relationship between mean annual air temperature and elevation was optimized for three segments of data (Figure 3-7). For the 19 lower sites (≤1225 m a.s.l), the linear fit showed a significant positive slope (SLR = 0.74 °C 100 m^{-1}; $p < 0.001$; $R^2 = 0.71$). The largest positive residuals from this slope occurred at DMP 13 (0.55 °C), DMP 33 (0.54 °C), DMP 04 (0.54 °C), and DMP 41 (0.53 °C), while the largest negative residuals were observed at DMP 40 (-0.97 °C), DMP 20 (-0.50 °C), and DMP 11 (-0.48 °C). Above these lower sites, all linear slopes relating mean annual temperature and elevation were negative and statistically insignificant.

In WS02, two linear segments were identified (Figure 3-7). For the 15 lower sites (≤1259 m a.s.l), the linear relationship between mean annual air temperature and elevation showed a significant positive slope (SLR = 0.51 °C 100 m^{-1}; p-value = 0.02; $R^2 = 0.55$). The largest negative residuals from this linear slope were at DMP 32 (-0.46 °C), DMP 27 (-0.44 °C), DMP 56 (-0.38 °C) and DMP 28 (-0.38 °C), while the largest positive residuals occurred at DMP 15

(0.60 °C) and DMP 14 (0.36 °C). For the 11 higher sites (≥1283 m a.s.l.), the fitted linear slope was significant and negative (SLR -0.31 °C 100 m^{-1}; p-value < 0.001; $R^2 = 0.87$).

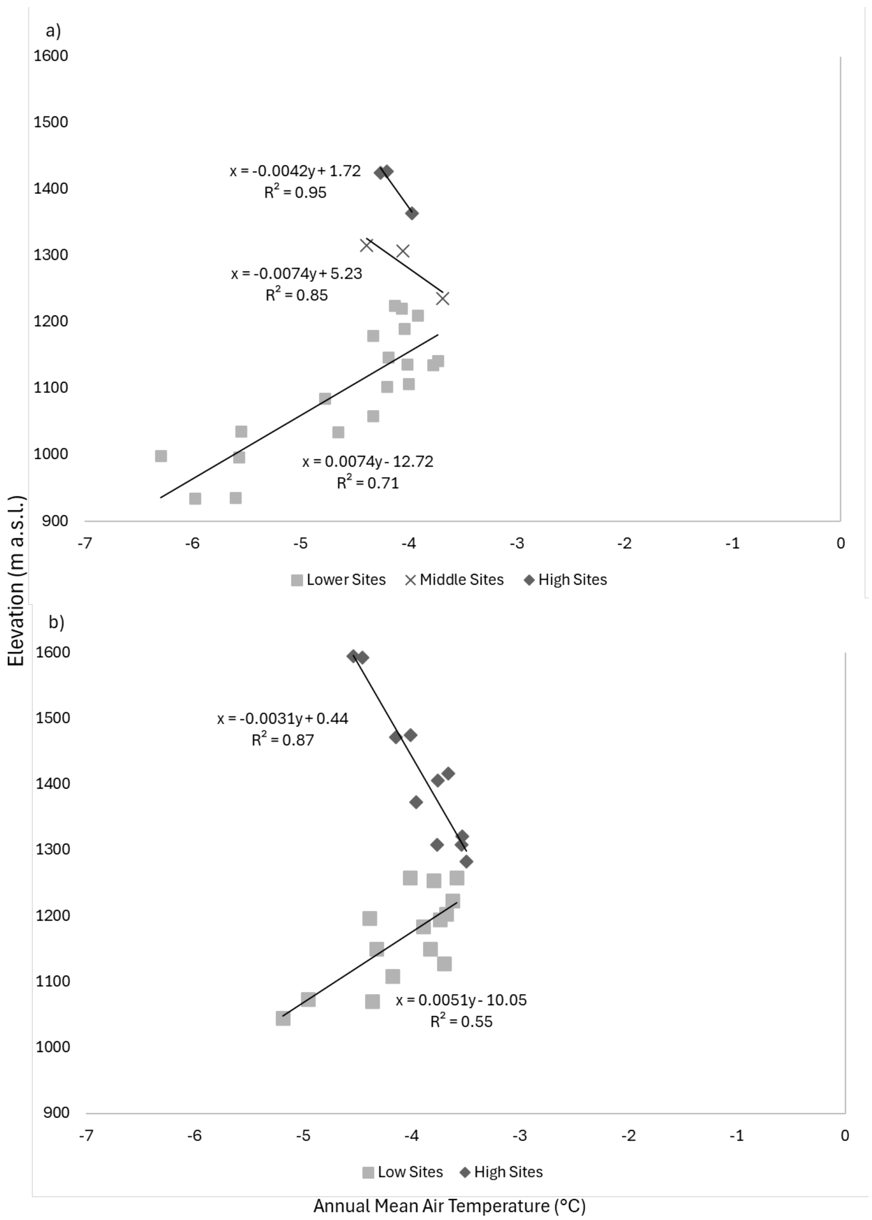

Figure 3-7: Result of the piecewise linear regression in both (a) the WS01 Valley and (b) the WS02 Valley. The elevation is on the y-axis and August 2023-August 2024 annual mean air temperature is on the x-axis.

3.4.5 SBI Depth

The mean annual SBI depth was 194 m, 136 m, 114 m, and 129 m on the SFT, NFT, WFT, and EFT mains, respectively. In WS01, most SBI events remained shallow: 61% of SBI readings (61% of events) on the SFT main were 38 – 239 m deep, while 45% (30%) on the NFT main were confined to the lowest 62 m (Figure 3-8). In WS02 SBIs similarly remained less than 212 m deep. On the WFT main 70 % (72 %) of all SBI readings (events) were 19-199 vertical meters deep, and on the EFT main, 68 % (69%) of all SBI readings (events) were 41-212 vertical meters deep.

Across both study areas, SBIs rarely reached the ridgetop as generally less than 9% of readings and less than 15% of events reached the ridgetop. This excludes the NFT main as the ridgetop along this transect is only 239 vertical meters above the valley floor and the other ridgetops are greater than 400 vertical meters above the valley floor. Most SBIs extended no further than the second or third station along each transect, highlighting that inversions are typically shallow and confined to lower slopes rather than valley ridges.

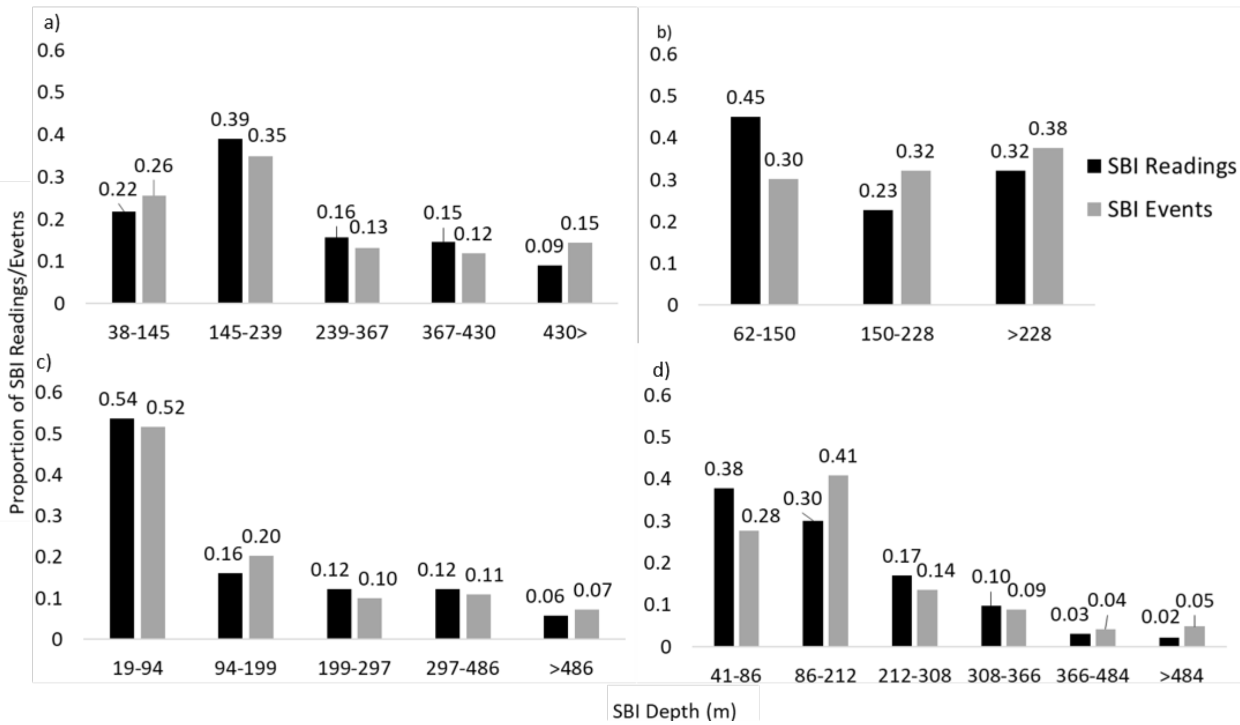

Figure 3-8: The proportion of SBIs readings within each SBI Depth bin on a) the SFT main, b) the NFT main, c) the WFT main, and d) the EFT main.

3.4.6 SLRs during SBI Events

SBI events ranging from 6 to 18 hours were analyzed across all main transects. The 16-hour SBI events were presented in the main text (Figure 3-9) as they were broadly representative of other event lengths (Figures 3-11–3-14). The median temperature profile shows the characteristic shape of each SBI event, while the interquartile range indicates that individual events often deviate from this median, particularly between the low elevation sites and during the middle of the SBI event. Across all SBI event durations, the SLRs at the lowest two to three sites along each transect exhibited the most pronounced changes during the first half of the SBI event, followed by a gradual decrease during the latter half. Above these sites, temperature profiles were generally more uniform, often near-isothermal, and showed smaller temporal changes. This rapid change in SLRs at lower elevations was the primary driver of relative temperature shifts at upper sites compared to the valley bottom weather station.

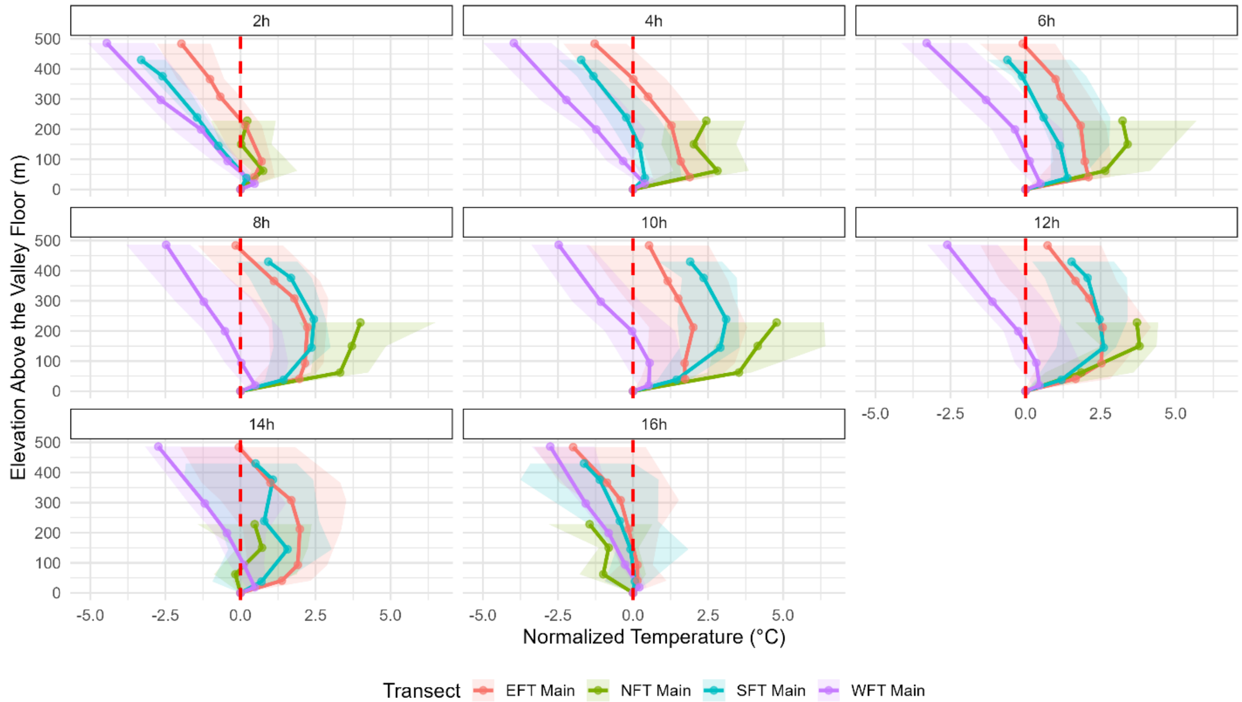

Figure 3-9: The median temperature relative to the weather stations and the interquartile range (IQR) along SFT main, NFT main, WFT main, and EFT main during all 16-hour long SBIs recorded on each transect (August 2023-August 2024).

3.4.7 SBI Development and Breakup Types

The dominant mechanism for SBI development along the four main transects was decrease of temperature at the lower site, especially within the first roughly 150 vertical meters of the transect where this mechanism accounted for greater than or equal to 50% of events (Figure 3-10a). At these lower elevations, development by upper-site warming or combined mechanisms also occurred frequently (40-50%). In contrast, at higher-elevation segments (sites 5-6 and 6-7), development was primarily driven by upper-site warming or combined mechanisms (70-80%).

Breakup of SBIs most often occurred through warming of the lowest sites, especially between the first three sites on each transect (≥50%) (Figure 3-10b). At higher-elevation segments, breakup mechanisms were more evenly distributed among the three mechanisms (warming of the lower site, cooling of the upper site, or a combination of both), though warming at the lower site generally remained the most common (30-40%).

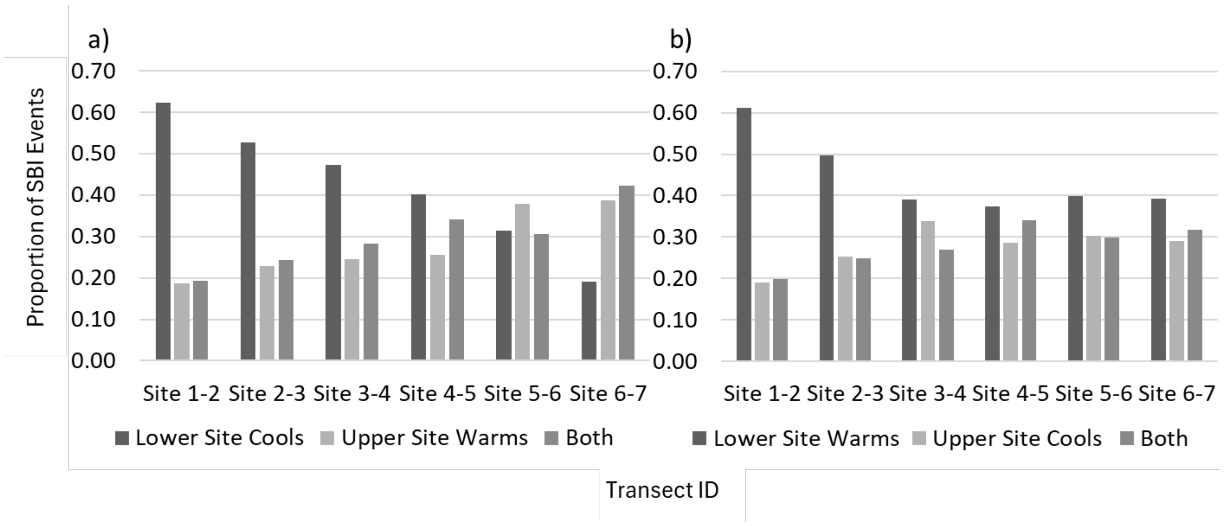

Figure 3-10: The proportion of SBI events (between the four main transects) that a) develop through cooling of the lower site on the transect, cooling of the higher site on the transect, or both mechanisms and b) breakup up through warming of the lower site on the transect, cooling of the higher site on the transect, or both mechanisms for the year August 2023 to August 2024.

3.5 Discussion

3.5.1 Short Term Temporal Patterns of SBIs

This study, spanning August 2017 to August 2024, characterizes short-term variability in SLRs and SBI frequency. While not addressing long-term change, it highlights interannual variability. The greatest interannual variability occurred at TST, partly driven by periodic snow burial of the DMP08 sensor.

Despite limited interannual variability, summer (June through August) temperature anomalies showed significant relationships with SLRs and SBI frequency. Warmer than average summers were associated with more positive SLRs and more frequent SBIs. Synoptic conditions likely play a role in reinforcing SBI occurrence (Sheridan, 2019), as anticyclonic conditions can promote clear skies (Ross, 2024) that can enhance radiative cooling, drive katabatic flows, and facilitate cold-air pooling in valley bottoms (Neff & King, 1989; S.A. Smith et al., 2010; Vosper

& Brown, 2008; Whiteman et al., 2004a, 2004b). Long, dry, sunny days typical of high-pressure systems could promote warmer than normal summers (Ross, 2024). Conversely, low-pressure systems are been linked to unstable conditions that promote negative lapse rates (Blandford et al., 2008; Dawn Reeves & Stensrud, 2009), with increased cloudiness and precipitation likely driving cooler summers (Ross, 2024).

SBIs in mid-latitude Cascade Mountains, were consistently influenced by synoptic-scale conditions (Rupp et al., 2020). Previous work suggests that 700 hPa vorticity could be used to represent a synoptic driver of cold air pooling (Daly et al., 2010), but no notable relationships with SLRs or SBI frequency were observed in this study, indicating that vorticity alone is insufficient to explain interannual SBI variability. Similarly, Daly et al., (2010) found that in fact during cold air pooling and SBIs in mid-latitude mountains the locations within a cold air pool can be decoupled from the synoptic flow and local processes can dominate. The results of our study support this finding. High diurnal temperature (range between daily minimum and maximum temperature) emerged as a useful local thermal driver in the summer, with larger amplitudes associated with increased nighttime SBI frequency and SLRs. Studies of diurnal temperature range and inversion depth in sinkholes (Whiteman et al., 2004a), along with boundary-layer analyses, suggest that large diurnal temperature swings are linked to stable nocturnal conditions under clear and calm skies (Holtslag et al., 2013; Mahrt, 2014). Similarly, Noad et al. (2023) found that SBI impacts on surface air temperature in northwestern Canada were strongest at sites with the largest temperature amplitude between the warmest and coldest month.

Diurnal temperature amplitude had much weaker relationships with inversion night frequency and SLRs in the winter months (December through February). This seasonal contrast aligns with findings from interior Alaska, where winter inversions are primarily governed by synoptic forcing rather than diurnal cycles (Malingowski et al., 2014; Mayfield & Fochesatto, 2013). This coincides with an absence of significant wintertime association between interannual variability of SLRs and SBI characteristics and mean wintertime temperature anomalies.

The short photoperiod and persistent snow cover in winter limit diurnal temperature amplitude, suggesting that synoptic-scale metrics may remain more relevant for predicting SBI occurrence. However, the lack of a clear signal with vorticity signifies the need to test other indicators of synoptic influences such as cloud cover, frontal passages, or precipitation. Future work should test and link metrics more directly to the occurrence of SBIs, particularly in the winter when diurnal thermal drivers are weaker.

Preliminary analysis of winter 2024 highlights a significant month-to-month variability in SBI characteristics and the temperature-elevation relationship in the valleys. January 2024 in both weather station study areas was remarkably colder than the study period average and exhibited greater SBI strength and frequency than February 2024, which showed much weaker temperature-elevation relationships (Section 3.4.4). Although only one January was sampled across the full network, this suggests that SLRs and SBIs may be sensitive to short-term meteorological variability. Future work should explore how wind, precipitation, and synoptic-scale pressure anomalies interact with projected rapid winter warming in northwestern Canada (Zhang et al., 2019) and how these combined factors influence SLRs and SBI characteristics.

3.5.2 The Structure of SBIs in the valleys

SBIs in the study valleys are typically shallow (< 150 vertical meters) but intense near the valley floor (<60 vertical meters). During the median SBI event (Figure 3-9), temperature increases steeply between the two or three lowest sites, then becomes nearly isothermal or negative above.

This non-linear structure contrasts with previous studies that assumed a consistent inflection point of linear lapse rates from positive to negative near treeline (Bonnaventure & Lewkowicz, 2013; Lewkowicz & Bonnaventure, 2011; Wahl, 1987). Nonetheless, the general pattern of transition from positive to negative SLRs with elevation is supported by our observations, even if the position of the transition is not closely linked to treeline.

Similar shallow but intense near-surface SBIs have been observed in High Arctic regions, such as near Alert, Canada, (Smith & Bonnaventure, 2017), and can have profound impact on surface air temperatures measured across the low relief terrain (Noad et al., 2023). Measurements near Eureka, Canada, in February and March of 2017 to 2020 found lapse rates of 10 – 30 °C 100 m^{-1} over just 10 m above the surface followed by a gentle or near isothermal profile roughly 30 vertical meters above the surface (Tikhomirov et al., 2021). In this study, the strongest positive SLR between WS02 and DMP14 (19 vertical meters) was 43.1 °C 100 m^{-1} (8.1 °C warmer at DMP14 than WS02). This is consistent with the largest mean SBI strength being recorded between closely spaced near valley bottom sites, while strength is greatly reduced at higher elevations along with the mean SLRs (Section 3.4.2). These patterns show that SBI strength peaks near the valley bottom and decays rapidly with elevation.

The temperature profile for the median SBI event (Figures 3-9; 3-11 to 3-15) shows that the intensity of the SBI is largely controlled by the lapse rate between the lowest two or three sites (< 150 m above the valley floor). These SLRs determine the initial steepness of the temperature increase with height and, consequently, how much warmer the mid- and upper-slope sites become relative to the valley bottom. The vertical temperature structure between sites above roughly 150 m, simply reflects the strength of this bottom-layer SLR.

These findings demonstrate that measurements in the valley bottom and the first tens of meters up the adjacent slopes are critical for quantifying the SBI strength. The non-linear temperature-elevation relationship also has implications for permafrost modelling as low-lying areas experience more intense cold air pooling than the adjacent slopes. Meanwhile, higher elevations SLRs are often near isothermal or gently negative (e.g. Bonnaventure et al., 2012; Garibaldi et al., 2024b). Additionally, the assumption of the environmental lapse rate (-0.65 °C 100 m) on higher slopes is not appropriate in these subarctic valleys, even for SLRs between high elevation sites.

3.5.3 Increased Resolution of Elevation Transects

Originally SLRs were measured between three sites in each valley, comprising a total of four elevational transects (Noad & Bonnaventure, 2022). On these original transects, SLRs were sampled between the valley bottom and 100-150 vertical meters up each adjacent slope. In this study, we present observations of a much higher vertical resolution along each of the original transects (SFT main, NFT main, EFT main, and WFT main), including sensors positioned between each of the original sensors. This allowed for sampling of SLRs between the valley bottom and 19-62 vertical meters above it, providing insight into the limitations of lower-resolution SLR measurements in ETA.

For example, the original SLR measurement on the SFT was 1.2 °C 100 m^{-1} across the 145 vertical meters between the WS01 and DMP04 sites from August 2017 to August 2021 (Noad & Bonnaventure, 2022). DMP12 was added between these sites in August 2021. In the 38 vertical meters between WS01 and DMP12, the average SLR was 2.19 °C 100 m^{-1} from August 2023-August 2024, while in the 107 vertical meters between DMP12 and DMP04 the average SLR was 0.82 °C 100 m^{-1} from August 2023 to August 2024. In the same year, measuring SLRs only between WS01 and DMP04 would have yielded an SLR of 1.21 °C 100 m^{-1}. This demonstrates that coarser sampling near the valley bottom would have overestimated the SLR farther up the slope.

The vertical spacing of sensors in this study (19-62 m near the valley bottom) provides higher vertical resolution than, for example, the vertical spacing of transects used in the mid-latitude Cascade Mountains (roughly 50-100 m increments) (Rupp et al., 2020). This enabled detection of sharp near-surface SLR gradients that coarser transects may miss. This highlights the importance of focusing sampling near the valley bottom in high-latitude mountain valleys, particularly given the non-linear SLR patterns observed in this study.

3.5.4 SLRs and SBI Characteristics in the Primary Valleys Compared to the Adjacent Valleys

The Daly and Bexte valleys are adjacent to the WS01 and WS02 primary valleys, providing an opportunity to assess the replicability of SLRs and SBI characteristic measurements between neighboring valleys with similar but not identical topography or vegetation cover. The Bexte valley is much shorter, the valley floor is steeper, and the valley is narrower than the neighboring WS02 primary valley. The Daly valley is a similar length but contains less of a curve, has a slope on the north facing slope that is greater than 200 vertical meters taller, and has tree cover only in the valley bottom rather than extending 150 vertical meters above the valley floor like in the WS01 primary valley. Overall, SLRs and SBI characteristics were comparable between the main weather station valleys and these adjacent valleys (Section 3.4.2), indicating that measurements in the primary valleys are generally representative.

In the WS01-Daly pair, SLRs and SBI frequency measured over small vertical distances in WS01 (< 61 vertical meters) were similar to those measured over roughly 100 vertical meters in the Daly valley. Furthermore, DMP 40 (the valley bottom site in the Daly valley) was an outlier for how cold it is in relation to its elevation (Section 3.4.3). These finding suggest that SBIs are particularly intense in the Daly valley, possibly even more so than the neighboring WS01 primary valley. This could be attributed to the taller ridge to the south of Daly valley solidifying the topographic shading for a larger part of the year in the valley bottom of this valley.

For the WS02-Bexte pair, SLRs were less positive and SBIs weaker and less frequent in the Bexte valley. This likely reflects the steeper valley floor, which elevates valley-bottom sites in Bexte compared to WS02. Combined with the larger vertical spacing between transect segments, this often-placed sensors above the most intense portion of the SBI. These observations support the idea that SBI strength and frequency are greatest near valley bottoms and that vertical resolution of measurements is important for capturing the full intensity of inversions.

3.5.5 Local conditions at sites driving elevational temperature patterns

The relationship between elevation and temperature was generally significant across months, but during transitional periods (April, October, and November) it weakened, reflecting spatial variability in snow cover, surface moisture, and topographic shading (Table 3-4). Several sites emerged as outliers, suggesting how local conditions can at times override the broader elevational patterns.

At night, forests can suppress turbulent mixing (Karlsson, 2000), while daytime shading and evapotranspiration will reduce temperatures (Li et al., 2015; Oke, 2002). Yet in WS01, lower elevation, not canopy, appeared to dominate temperature patterns. The valley bottom site, DMP60 (935 m a.s.l.), was in a large clearing of trees but was still colder than a higher-elevation valley-bottom forested site (997 m a.s.l.). The forest cover in WS01 consists of an open, 3-10 m tall canopy, which is far less dense and shaded than the tall, closed forests examined in the studies referenced above. This likely reduced the magnitude of canopy-driven cooling mechanisms, making elevation the primary control on mean air temperature in the WS01 study area.

On treeless slopes (NFT main in WS01; both main transects in WS02), warm outliers were concentrated within the first 60 m above the valley floor. These sites reflect the steep nonlinear increase in temperature with elevation near the valley bottoms, where the linear model systematically underestimates temperatures. The largest negative residuals (e.g., DMP 40 in Daly, DMP 32 and DMP 56 in WS02) likewise occurred at the lowest sites, confirming that these sites were within this intense non-linear inversion layer that encapsulated the lowest elevation sites.

Around 100 to 150 vertical meters above the valley floor, positive residuals occurred on the south-facing slopes (DMP 04 and DMP 33). These sites are drier, more exposed, and receive greater solar radiation due to aspect and sparse canopy, which explains their warmer conditions relative to elevation. Solar radiation and topographic shading have been postulated to influence inversion patterns particularly during the summer days (Pike et al., 2013; Rupp et al., 2020).

Strong negative residuals at DMP 20 (WS01) and DMP 27 (WS02) align with valley narrowing and curvature, which can enhance cold air pooling through reduced ventilation of cold air (Kiefer & Zhong, 2015; Kossmann & Sturman, 2003). DMP 20 also sits in dense roughly 1-meter-tall shrub cover, where redistributed snow likely accumulates (Frost et al., 2018). Prolonged spring snow cover and ground moisture could maintain high albedo and increased latent heat fluxes, suppressing sensible warming and lower air temperature locally at this site (Oke, 2002).

3.5.6 Measurement of SBI Depth and the Uncertainties

SBI events were most commonly shallow, typically extending <150 m up the adjacent slopes (Section 3.4.4). The SBIs were somewhat deeper on the SFT main transect, with an average depth of 194 m above the weather station. As with SBI frequency and strength the average SBI depth on the SFT was greater than those measured on other transects. This is likely related to both aspect (topographic shading) and tree cover from the valley bottom to roughly 150 vertical meters (Noad & Bonnaventure, 2023).

As discussed in Noad et al. (2023), the impact of SBIs in mountain valleys is limited because a large proportion of the land surface sits above the average SBI layer. This appears to be particularly true for this study region where SBIs are relatively shallow and are strongest near the valley floor. As a result, much of the slopes and ridgetops lie outside of the zone of maximum SBI impact. In contrast, flat and low-lying regions, such as those near Inuvik, NT can experience the full impact of the SBI across much of the landscape (Noad et al., 2023).

Two major limitations of using ETA to measure SBI depth emerged in this study. First, SBI occurrence was defined as a positive SLR between any of the first three sites along the main transects (within the first 100 to 150 vertical meters) (Section 3.3.6). This follows the convention of defining SBI as beginning within the first 100 vertical meters of the atmosphere (e.g. Gilson et al., 2018). However, this convention was originally developed for free-air lapse rates, not for SLRs measured along slopes. Technically, any SLR could be considered a SBI as it occurs along the surface of a mountain. Thus, any positive SLRs that occur independently of an inversion layer within the first 150 vertical meters of the valley bottom could still be considered an SBI event. This type of situation typically accounted for < 25 % of all inversion readings measured between the upper sites of the main transects. While this is a relatively low number, it is still significant. Therefore, future consideration must be given to the occurrence of inversion events only measured on the upper slopes and how to define what an SBI is when measuring SLRs rather than free air lapse rates.

Second, ETA can only resolve SBI depth in discrete vertical intervals above the valley bottom. It indicates to which site an SBI extends, but not how far the SBI may extend beyond that site to the next measurement level. Therefore, SBI depth is a continuous variable, but ETA can only be captured in finite elevation bands. Furthermore, if an SBI layer extends above the highest sensor, depth can only be reported as “greater than” the elevation of that site. These constraints limit the details with which SBI depth can be characterized in these valleys.

3.5.7 Mechanism of SBI development and breakup

The development of positive SLRs along the transect segments was governed primarily by decrease in temperature at the lower site (Section 3.4.7). This aligns with the classic process of nocturnal surface radiative cooling and cold-air pooling in valley bottoms, which has been widely documented in mountain environments (Jemmett-Smith et al., 2018; S.A. Smith et al., 2010; Vosper et al., 2014; Whiteman, 1982). Downslope drainage flows will further reinforce cold air pooling, concentrating the coldest air near the valley floor (Zhong et al., 2001).

A significant proportion of positive SLRs developed due to warming of the high-elevation site, or a combination of cooling of the lower site and warming of the higher site. This mechanism became more common on the upper-slope segments, where warm air advection or subsidence under high-pressure systems can promote elevated inversion layers (Mayfield & Fochesatto, 2013; Bourne et al., 2010). These processes reinforce near-surface decoupling and persistent cold air pools (Sheridan, 2019). Local controls such as aspect and shading could enhance warming at high elevation exposed sites (Noad & Bonnaventure, 2023; Pike et al., 2013; Rupp et al., 2020).

Breakup of SBIs occurred through several mechanisms, most commonly through warming of the lower site on the transect segment. The SBI erodes from below as convective turbulence forms through solar heating of the surface (Whiteman, 1982). In other cases, particularly between higher elevation sites, positive SLR became negative because of cooling aloft. This pattern indicates top-down erosion of cold pool and is often triggered by cold-air advection, shear-driven turbulence, or frontal systems passage that destabilizes the stratified atmosphere (Cullen & Marshall, 2011; Fochesatto et al., 2015; Lareau & Horel, 2015a, 2015b; Whiteman et al., 2001; Zhong et al., 2001).

Taken together, these results suggest that SBI dynamics in this study region reflect both local controls (radiative cooling, drainage flows, shading, snow cover) and synoptic influences (subsidence warming, frontal passages, advection). This is consistent with other high-latitude work (Bourne et al., 2010) and mid-latitude mountain settings (Rupp et al., 2020), where SBI development and breakup depend on the interplay of surface processes and larger-scale atmosphere forcing. Future modeling efforts could help disentangle the relative contribution of bottom-up versus top-down mechanisms across different seasons and synoptic conditions.

3.6 Conclusions

This study used a high-resolution network of air temperature measurements to quantify spatial and temporal patterns of SLRs and SBI characteristics in high-latitude mountain valleys. Interannual variability in SBI frequency and strength was linked to the summer climate anomalies, with warmer summers associated with increasing SLRs and SBI frequency. Elevation was a strong primary control on temperature, except during the transitional months between snow covered and snow free months.

The average SBI was shallow and the strongest between the valley bottom and sites near the base of the adjacent slope. This produced non-linear SLRs that decreased rapidly from the valley floor and stabilized mid-slope. No consistent inflection point existed where SLRs became negative. These findings highlight the importance of measuring air temperatures between valley bottoms and the lower slopes in particular to accurately represent thermal variability in these landscapes.

Mechanisms of SBI development and breakup were complex, influenced by local topography, shading, and synoptic-scale processes. Understanding these mechanisms is essential for predicting SBI behavior under changing climate conditions. This will be needed to understand the distribution of warming across these complex landscapes.

Overall, this research demonstrates that SBIs are a dominant control on thermal structure in subarctic valleys. By clarifying where and when SBIs form, how deep they are, and how they break up, this study provides critical knowledge for reducing biases in high-latitude climatological datasets (e.g. downscaled climate reanalysis data) and for improving modelling of surface processes, such as permafrost. These insights highlight that shifts in SBI behavior under climate warming could alter patterns of surface air temperatures and therefore ecosystem and permafrost responses across high-latitude mountain regions.

Data Availability Statement

Data used in this study can be requested upon request by contacting the corresponding author at nick.noad@uleth.ca.

Funding Statement

This research was funded by the NSERC Discovery Grant and by funding provided to do field work by the Northern Scientific Training Program.

Conflict of Interests Statement

The authors of this manuscript have no conflicts of interest to declare in association with research presented in this article.

Acknowledgements

We acknowledge and thank the Tr'ondëk Hwëch'in and the Na-Cho Nyäk Dun First Nations for supporting our research on their traditional territory. We thank the Government of Yukon for providing us with Yukon Scientists and Explorers research licenses each year to continue this work in their Territory. We thank all of the hard work provided by various field teams of researchers and students since 2017. Without this important and difficult work this research would not be possible. We acknowledge Hester Jiskoot, Robert Way, and Yu Zhang who provided valuable feedback regarding the manuscript as members of Nick Noad's PhD committee. We thank the reviewers, assistant editors, and editor who provided in-depth and constructive reviews of this paper that significantly improved its clarity and scientific rigor. We acknowledge the support that the University of Lethbridge has provided to assist us in this research. The funding provided by both NSERC and the Northern Scientific Training program since 2017 has been essential for the success of this research.

3.7 Appendix

The following figures (3-11 – 3-15) illustrate the progression of the median SBI events in 2-hour time steps. This is to illustrate that the 16-hour SBI event figure (Figure 3-9, Section 3.4.6) is representative of other event durations.

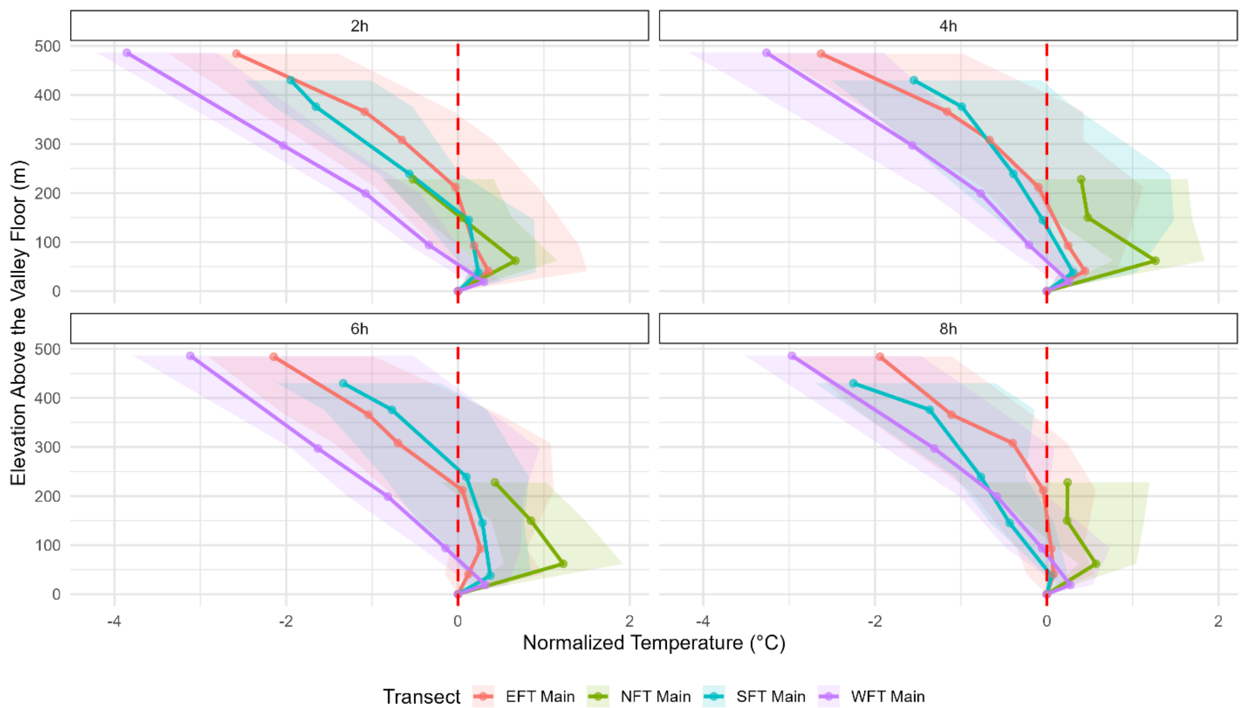

Figure 3-11: The median temperature relative to the weather stations and the interquartile range (IQR) along SFT main, NFT main, WFT main, and EFT main during all 8-hour long SBIs recorded on each transect (August 2023-August 2024).

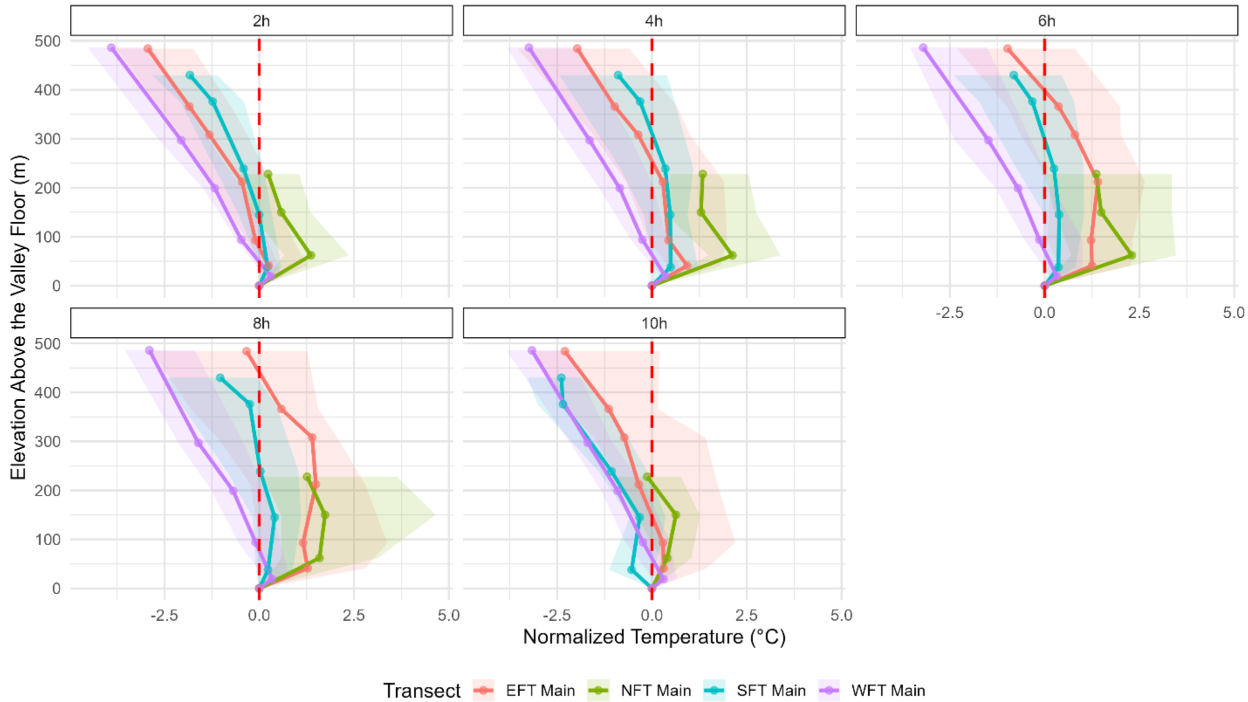

Figure 3-12: The median temperature relative to the weather stations and the interquartile range (IQR) along SFT main, NFT main, WFT main, and EFT main during all 10-hour long SBIs recorded on each transect (August 2023-August 2024).

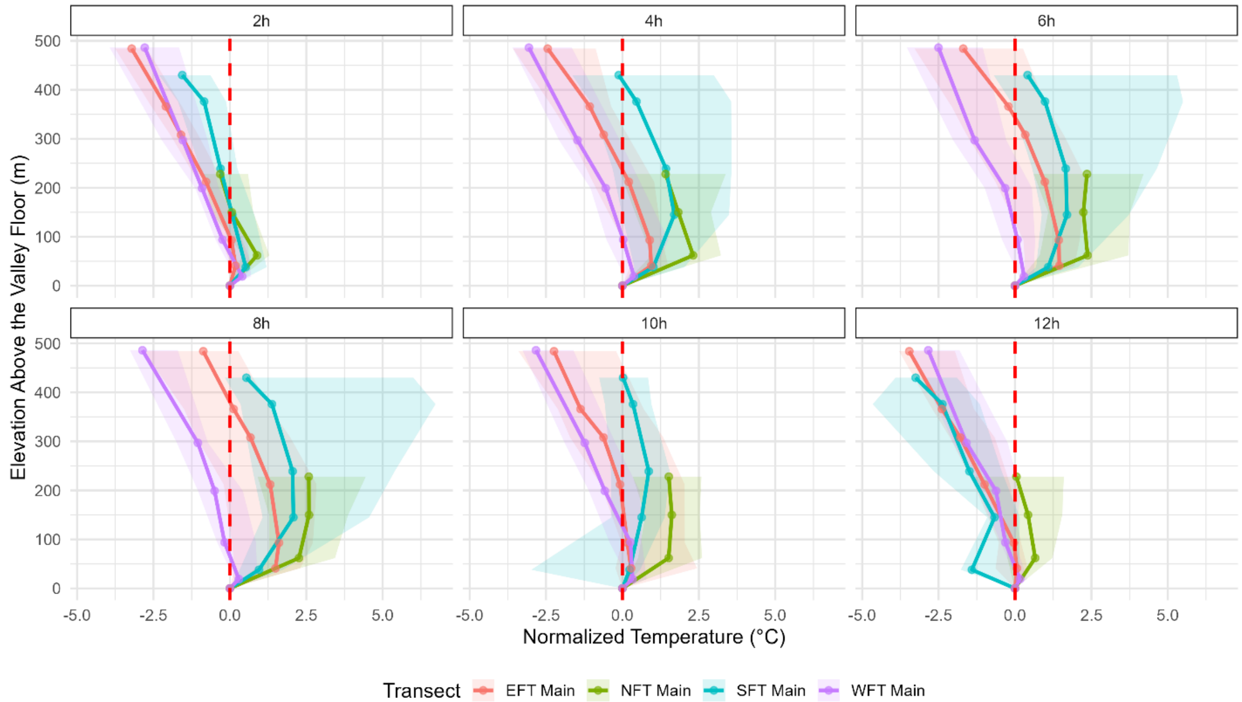

Figure 3-13: The median temperature relative to the weather stations and the interquartile range (IQR) along SFT main, NFT main, WFT main, and EFT main during all 12-hour long SBIs recorded on each transect (August 2023-August 2024).

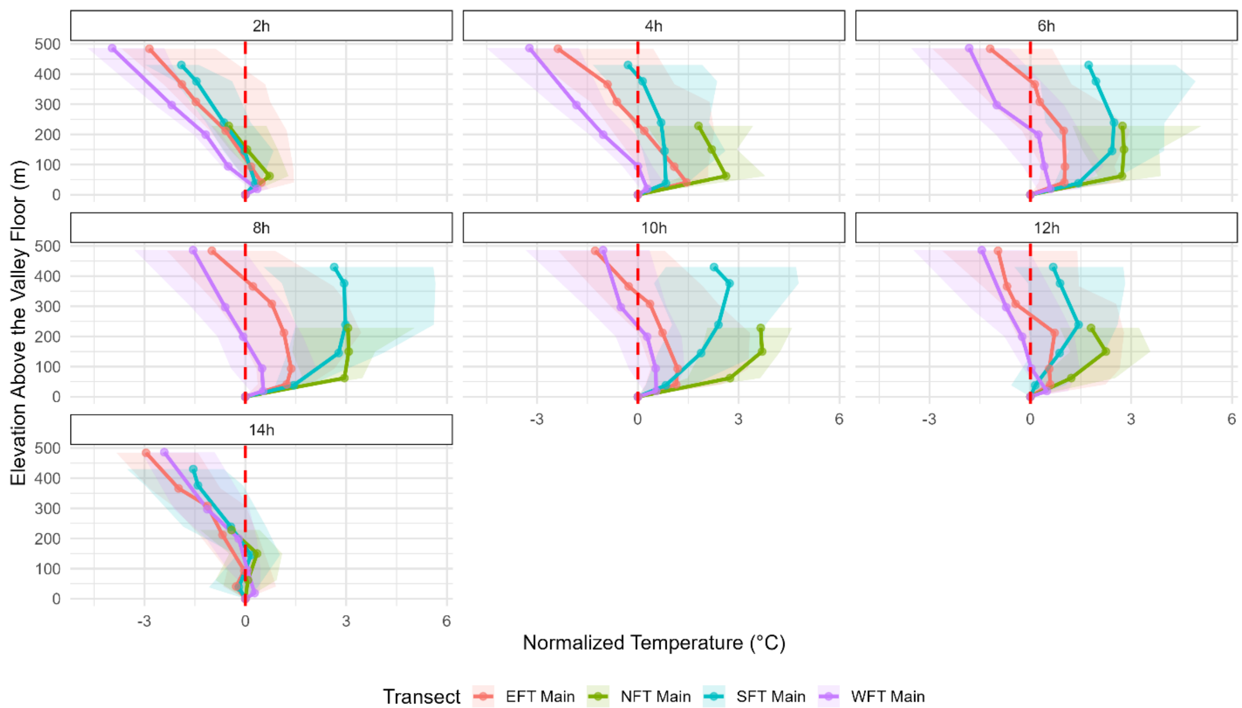

Figure 3-14: The median temperature relative to the weather stations and the interquartile range (IQR) along SFT main, NFT main, WFT main, and EFT main during all 14-hour long SBIs recorded on each transect (August 2023-August 2024).

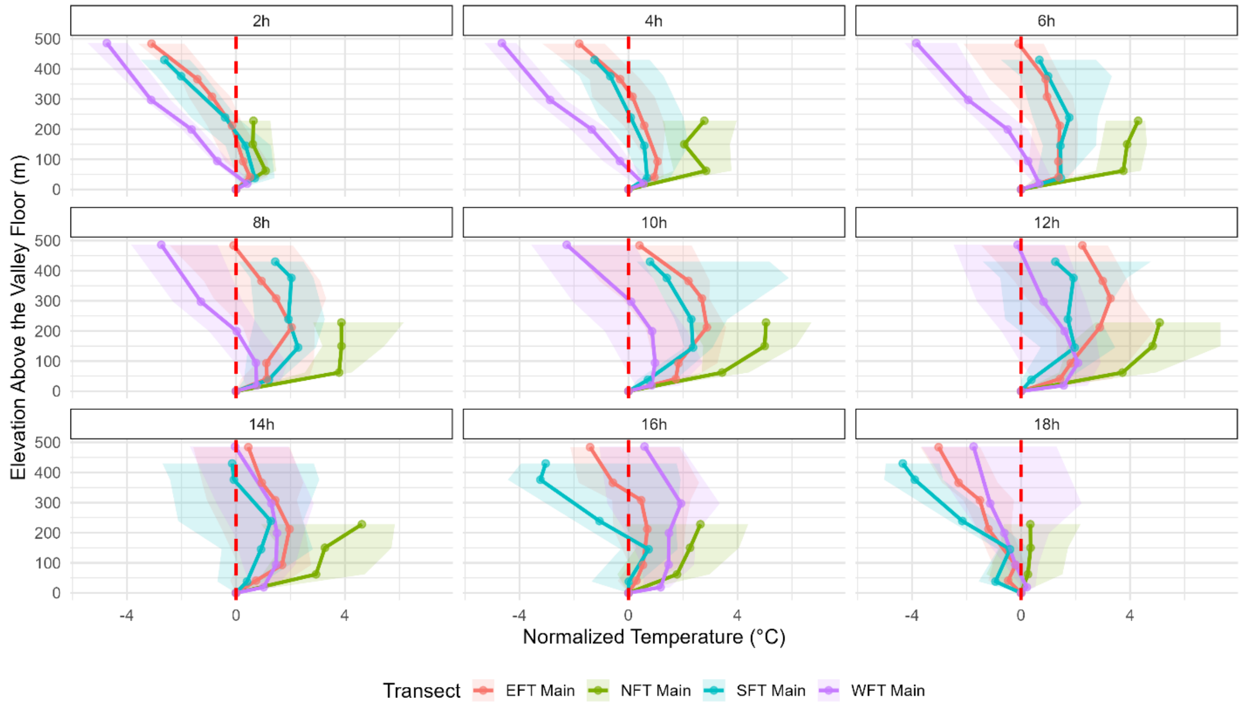

Figure 3-15: The median temperature relative to the weather stations and the interquartile range (IQR) along SFT main, NFT main, WFT main, and EFT main during all 18-hour long SBIs recorded on each transect (August 2023-August 2024).

4. Testing a Temperature Inversion Correction Model for Downscaled Reanalysis Temperatures in Subarctic Yukon Valleys

Submitted to *Arctic Science* February 23, 2026

Authors: Nick C. Noad[1], Victor Pozsgay[2], Philip P. Bonnaventure[1], & Stephan Gruber[2]

[1]Department of Geography and Environment, University of Lethbridge, Lethbridge, AB, T1K3M4, Canada

[2]Department of Geography and Environmental Studies, Carleton University, 1125 Colonel By Drive, Ottawa, K1S5B6, Ontario, Canada

Keywords: Surface-based temperature inversions, Downscaled climate reanalysis, Reanalysis bias correction, High-latitude mountain valleys, Inversion correction model validation

4.0 Abstract

SBIs strongly influence near-surface temperatures in subarctic mountain valleys, yet they are poorly represented in coarse-resolution reanalysis datasets. This study evaluated the performance and physical robustness of the Pozsgay and Gruber (2025) inversion bias correction model in two subarctic valleys along the Dempster Highway, Yukon. The model dynamically adjusts reanalysis air temperature at each timestep using a correction factor derived from the free lower-tropospheric lapse rate and estimated SBI strength allowing for temperature-elevation relationships to vary in response to changing SBI conditions. When calibrated locally, the model reduced mean absolute temperature errors up to 0.8 °C and bias to within ±0.2 °C at the valley scale. Performance was strongest under moderate SBI strength but declined for shallow or very strong SBIs due to limited reanalysis vertical resolution and the assumption of linear lapse rates. Locally calibrated models outperformed transferred ones, reflecting differences in absolute elevation range between the valleys and other study areas. Despite these limitations, explicitly accounting for SBI dynamics substantially improves temperature estimates in high-latitude complex terrain. The resulting corrected datasets provides a valuable input for transient permafrost modelling and assessing how changing SBI characteristics may influence ground thermal regimes in subarctic alpine environments.

4.1 Introduction

Air temperature is a fundamental variable across numerous scientific fields including permafrost science (e.g., Gruber, 2012), ecology (e.g., Hassink et al., 2025; MacDonald et al., 2025), forest fire risk assessment (e.g., Fazel-Rastgar & Sivakumar, 2022), agriculture (e.g., Steiner et al., 2018), and hydrology (e.g., Rawlins & Karmalkar, 2024). However, long-term in-situ air temperature records remain sparse in high-latitude (Cowtan & Way, 2013; Way & Bonnaventure, 2015) and mountainous regions (Gultepe, 2015), limiting our understanding of regional climate variability and elevation-dependent warming (Byrne et al., 2024; Pepin et al., 2015). The deficiency of in-situ observations of temperature is compounded in high-latitude mountainous regions (Williamson et al., 2020). In these data-scarce environments, researchers increasingly rely on climate reanalysis models that assimilate global observations with atmospheric physics to generate spatially- and temporally-continuous meteorological datasets (Compo et al., 2011; Graham et al., 2019).

While reanalysis products such as ERA5 or JRA-3Q provide broad spatiotemporal coverage, their coarse spatial resolution (≈0.25°) (Hersbach et al., 2020; Kosaka et al., 2024) limits the representation of fine-scale topo-climatic processes in complex terrain (Etzelmüller, 2013; Riseborough et al., 2008). Key sub-grid processes that are often inadequately represented include orographic precipitation enhancement and rain shadowing (e.g., Chen et al., 2021), convective precipitation events typical of mountain terrain (e.g., Lavers et al., 2022), and cold air pooling in valleys (e.g., Cao et al., 2017). To reduce these biases, a range of statistical and dynamical downscaling approaches have been developed to better represent local topo-climatic variability in reanalysis products (Benestad & Chen, 2008; Bieniek et al., 2016).

Downscaling methods such as GlobSim (Cao et al., 2019) improve representation of local meteorological conditions by interpolating reanalysis data to point locations based on longitude, latitude, and topography. Although GlobSim improves on coarse reanalysis predictions, it remains limited in representing cold-air pooling and SBIs that frequently occur in subarctic mountain valleys (Noad & Bonnaventure, 2022; Pozsgay & Gruber, 2025). These SBIs are particularly frequent and intense in mountain valleys in northwestern Canada and the Alaska interior (Fochesatto et al., 2015; Noad & Bonnaventure, 2023; 2026). SBIs exert strong control on near-surface air temperature variability, producing mean annual temperature differences exceeding 1.5 °C between valley bottoms and adjacent slopes only 150 m higher (Noad & Bonnaventure, 2026), with implications for permafrost distribution and thermal conditions (Bonnaventure & Lewkowicz, 2013; Garibaldi et al., 2024b).

To address these biases, Pozsgay and Gruber (2025) developed an inversion correction model that dynamically calculates the upper-troposphere lapse rate to estimate the hourly SBI strength and adjust the near-surface air temperature accordingly. Model parameters are calibrated using in-situ observations to reflect the frequency, strength, and seasonal variability of SBIs (Pozsgay & Gruber, 2025). Calibration against local observations near Dawson City, Yukon, demonstrated that the model substantially improves temperature estimates where inversions are common. However, its transferability and physical robustness outside the calibration area remain untested.

Here we provide a point-scale test of the Pozsgay and Gruber (2025) inversion correction model using a large network of elevational transects located approximately 100 km northeast of Dawson City (Noad & Bonnaventure, 2026). This network provides spatially-extensive in-situ temperature records spanning large elevation gradients, enabling a detailed evaluation of the model performance relative to the original GlobSim downscaled reanalysis. The three following objectives will be addressed:

1) Examine the limits of transferability of the inversion correction model parameters calibrated in one region to other nearby valleys.
2) Identify the spatial and temporal strengths and limitations of the inversion correction model.
3) Quantify model sensitivity to variations in SBI strength and frequency.

Improved representation of near-surface air temperature would enhance the reliability of reanalysis-based inputs for permafrost and other surface process models, while providing clearer insight into the physical processes that constrain model performance.

4.2 Study Areas

This study takes place in the Ogilvie Mountains of northcentral Yukon, Canada (Figure 4-1). Sites were selected for their accessibility from the Dempster Highway and their suitability for measuring elevational temperature patterns associated with SBIs. Two primary study areas were established in a subrange of mountains: the Weather Station 1 (WS01) area on the southeast side of the subrange and Weather Station 2 (WS02) (unofficial names) area approximately 8 km to the north. They differ in valley geometry and vegetation cover (Table 4-1). The highest local peak, Distincta Peak (official name) (1790 m), rises between the two areas. Each study area consists of two valleys, a primary valley and a secondary adjacent valley, referred to as the Daly valley in WS01 and the Bexte valley (unofficial names) in WS02.

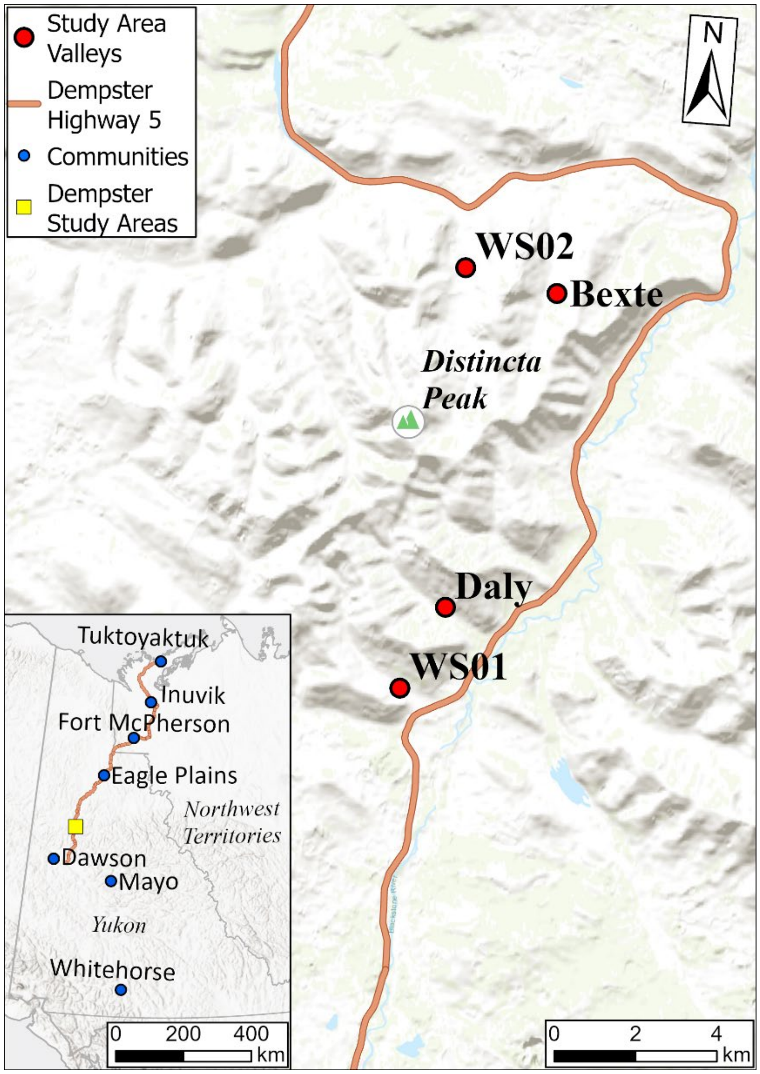

Figure 4-1: The inset map illustrates where the study area is in northcentral Yukon along the Dempster Highway (drawn in orange). This map is underlain by the Esri Light Grey Canvas Basemap. The Esri Topographic Basemap underlays the main map to illustrate the topography of the area.

Table 4-1: WS01 and WS02 study area attributes.

Attribute	WS01 (Daly Valley Area)	WS02 (Bexte Valley Area)
Coordinates	64.9585 °N 138.2803 °W	65.0498 °N 138.2634 °W
Valley type / morphology	Two steep (30–40°) V-shaped valleys curving west-northwest to north	Two U-shaped valleys oriented north-south
Valley length (primary / secondary)	5.5 km / 4.5 km	6.5 km / 2.5 km
Elevation range (m a.s.l.)	935–1720	1040–1790
Relief (vertical range)	~785 m	~750 m
Dominant vegetation (valley floor → slope)	Open black spruce forest to 150 m above valley floor → tundra and blockfield	Sparse forest at outlets → mosses, hummocks, and exposed blockfields
Notable topographic features	Curving valley axes; enclosed basins favoring cold-air pooling	Open valley geometry; less topographic confinement

Both study areas experience intense, frequent, and long duration SBIs, particularly in the winter (Noad & Bonnaventure, 2022; 2026). Within the lowest 150 vertical meters of the valley floors mean annual SLRs are positive (indicating increase in temperature with elevation), driven by persistent cold-air pooling. WS01 exhibits more frequent SBIs with mean annual SLRs of +8-+12 °C km^{-1}, whereas WS02 has less frequent SBIs with average SLRs approximately +4-+5 °C km^{-1} (Noad & Bonnaventure, 2022). Above 150 vertical meters, mean lapse rates approach isothermal conditions (0 °C km^{-1}) or negative, reaching approximately -4.7 °C km^{-1} at the highest elevations (Noad & Bonnaventure, 2026).

4.3 Methods

4.3.1 In-Situ Data Collection

4.3.1.1 Air Temperature Logger Specifications

Air temperature was measured using Onset U23 and MX2300 relative humidity and temperature loggers (accuracy ±0.25 °C, resolution 0.04 °C and 0.02 °C respectively). All sensors were housed in a passively ventilated RS01 radiation shield (Onset USA) and mounted roughly 2 m above the ground to reduce radiative and surface effects.

4.3.1.2 Sensor Network

A total of 27 air temperature stations were used for each of the WS01 and WS02 study areas (Figure 4-2). Measurements were recorded at 2-hour intervals from each station's installation date through August 2024, providing records from 1 to 7 years in duration.

The network was designed to sample air temperature at a variety of elevations over relatively small horizontal distances. The air temperature loggers were deployed at the lowest elevations near the valley outlets (935 m a.s.l. in WS01 study area and 1042 m a.s.l. in the WS02 study area) to the adjacent ridgetops (1425 m a.s.l. in WS01 and 1595 m a.s.l. in WS02). These data were used to measure SLRs and characterize the frequency, strength, depth, and duration of SBIs (Noad and Bonnaventure, 2026).

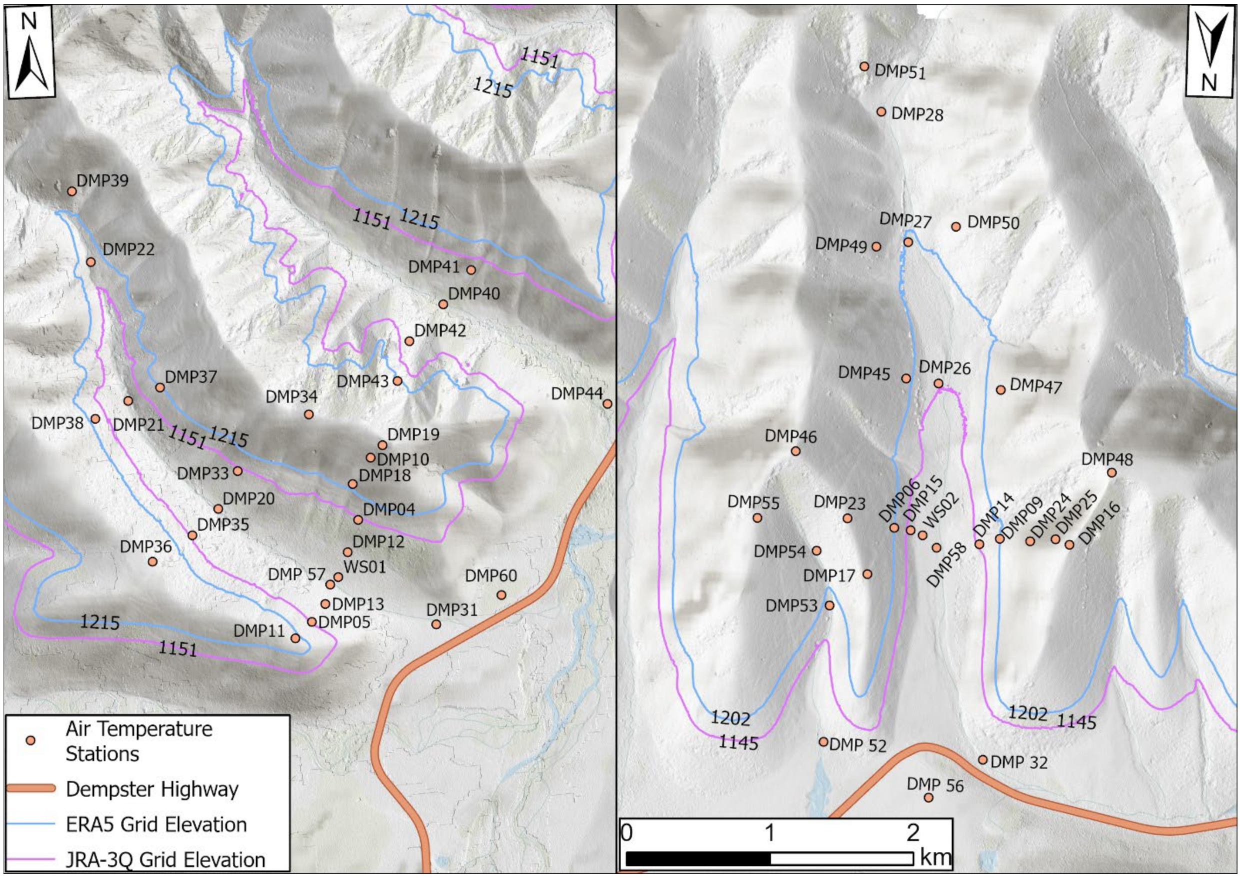

Figure 4-2: The sensor set up and reanalysis product grid cell elevation contours for (a) WS01 and (b) WS02 study areas. The map panes are underlain by a hillshade to illustrate the position of the study sites in the topography. The elevation ranges in WS01 from 935 m to 1720 m and in WS02 from 1040 m to 1790 m. The Esri Topographic Basemap underlays the maps.

4.3.2 Reanalysis Data

Two global reanalysis products: ERA5 from the European Centre for Medium-Range Weather Forecasts (ECMWF; Hersbach et al., 2023a, b) and JRA-3Q from the Japan Meteorological Agency (JMA) (Kosaka et al., 2024) were used. The former is available at an hourly temporal resolution on a regular 0.25° × 0.25° grid (roughly 46 N-S x 20 km E-W at this study area latitude) in latitude and longitude from 1940 onward. The latter also produces data hourly (since 1947) but uses a TL479 Gaussian grid instead with a spatial resolution of 0.375° × 0.375° (roughly 59 N-S x 30 km E-W).

Data were downloaded for the period of July 31, 2017-September 1, 2024, and included constant fields (geopotential, land-sea mask), single level 2 m temperature, and pressure level air temperature.

Both products were downscaled to the individual station locations and elevations while accounting for local topography using the GlobSim model (Cao et al., 2019). For each site, pressure-level air temperatures (T_{pl}) were extracted from the free-atmosphere profile extending from the elevation of the highest station to 4800 m a.s.l. Specifically, pressure-level data were interpolated bilinearly to the location of interest, and vertically every 100 m in the range 1500–2300 m, every 200 m in the range 2300–2700 m, and every 300 m in the range 2700–4800 m. Downscaled single-level 2 m surface temperature T_{sur} were derived from the GlobSim model based on the reanalysis grid elevation in each valley (Figure 4-2).

4.3.3 Temperature Inversion Model

4.3.3.1 Model Overview

This study compares air temperature from reanalysis data with in-situ observations in subarctic valleys characterized by strong, frequent, and persistent temperature inversions. Previous work by Pozsgay and Gruber (2025) demonstrated that downscaled reanalysis data (whether single-level surface temperature T_{sur} or pressure-level temperature T_{pl}) fail to capture the full vertical profile of SBIs.

To address this, Pozsgay and Gruber (2025) developed a dynamic temperature inversion correction model designed to bridge the gap between the near-surface and free tropospheric temperature domains. The model, originally calibrated near Dawson City, Yukon, dynamically computes the free-tropospheric lapse rate each hour from vertical profiles of air temperature above each valley. The model demonstrates improved performance over both GlobSim downscaled T_{pl} and T_{sur} for nearly all combinations of elevation, time, and reanalysis product.

4.3.3.2 Model Formulation

At each time step, the model estimates the hypothetical temperature at the reanalysis product grid level if the lapse rate of the free atmosphere continued without SBI effects and compares it with the GlobSim surface (grid-level) temperature:

$$DT = T_{\mathrm{sur}} - T_{\mathrm{lapse\ grid}}, \qquad \text{(Eq. 4-1)}$$

where T_{sur} is the reanalysis surface temperature and $T_{\mathrm{lapse\ grid}}$ is the free atmosphere lapse-rate-derived temperature at the grid level. The difference between the surface (grid-level) temperature given by reanalysis and the would-be temperature without any inversions (DT) corresponds to the SBI_{mag} metric from Noad et al. (2023). The equivalent definition at the station's elevation reads,

$$DT_{\mathrm{station}} = T_{\mathrm{obs}} - T_{\mathrm{lapse\ station}}, \qquad \text{(Eq. 4-2)}$$

where T_{obs} is the observed temperature. The model assumes that inversion strength varies linearly with elevation and that a periodically-varying error is present over the annual cycle:

$$DT_{\mathrm{station}} = \alpha(z) \cdot DT + \beta(t), \qquad \text{(Eq. 4-3)}$$

Note that the temporality of the inversion strength is fully characterized by the temporality of DT. Finally, the modelled temperature reads,

$$T_{\mathrm{mod}}(z, t) = T_{\mathrm{lapse\ station}} + \alpha(z) \cdot (T_{\mathrm{sur}} - T_{\mathrm{lapse\ grid}}) + \beta(t) \qquad \text{(Eq. 4-4)}$$

with

$$\alpha(z) = \alpha_{\text{slope}} \cdot z + \alpha_{\text{intercept}}, \tag{Eq. 4-5}$$

$$\beta(t) = \beta_{\text{amplitude}} \cdot \cos(2\pi(t - t_*)) + \beta_{\text{bias}}, \tag{Eq. 4-6}$$

where z stands for elevation, and t for the yearly time fraction. Here, $\alpha(z)$ defines how inversion strength changes with height, while $\beta(t)$ captures seasonal modulation of error in reanalysis predictions.

4.3.3.3 Calibration

The inversion correction model (Eq. 4-4) requires calibration before it can generate predictions. As an initial step, modelled temperature (T_{mod}) was computed using the parameter values calibrated for Dawson City area (α_{slope}, $\alpha_{\text{intercept}}$, $\beta_{\text{amplitude}}$, β_{bias}, t_*) as reported in Pozsgay and Gruber (2025). This configuration, referred to as $T_{\text{mod Dawson}}$, served as an initial validation test to assess the transferability of the model to valleys in the same general region (approximately 100 km away).

Since the structure and strength of temperature inversions can be highly variable in space (Noad & Bonnaventure, 2022; 2026), it was anticipated that the Dawson calibrated parameters would exhibit limited predictive skill when applied to the Dempster Highway study areas. Consequently, the model was recalibrated using a subset of local in-situ observations from each study area valley.

Independent calibrations were performed for each combination of study area (WS01 or WS02) and reanalysis product (ERA5 or JRA-3Q) (Table 4-2). The calibration dataset spanned the broadest available temporal and elevational ranges, including all stations with complete records at 2-hour intervals. Although a two-week gap occurs in mid-August, this period coincides with minimal SBI activity and therefore had negligible effects on calibration results.

All parameters found in Equation (4-4) were optimized using a least-square regression applied to the calibration subset (Table 4-3). The model output based on parameters calibrated within each study area is denoted by $T_{\text{mod DMP}}$, representing model performance when trained and validated using local observations.

Table 4-2: Subset of the observation dataset used for model calibration. The removed stations either were incomplete (DMP 31) or had erroneous readings of data in the August 2023 to August 2024 period (DMP 44, DMP 60, and DMP 49).

	WS01	WS02
Start (UTC)	2023-08-23 19:00	2023-08-24 19:00
End (UTC)	2024-08-09 15:00	2024-08-04 1:00
Frequency	2-hour	2-hour
Stations Removed	DMP31, DMP44, and DMP60	DMP49
Data used for calibration (%)	36%	36%

Table 4-3: Model calibration results for both Dempster Highway study areas and reanalysis products.

		ERA5		JRA-3Q	
Parameter	Unit	WS01	WS02	WS01	WS02
α_{slope}	km^{-1}	-1.168	-0.901	-1.227	-0.961
$\alpha_{\text{intercept}}$		2.209	1.868	2.355	2.054
$\beta_{\text{amplitude}}$	°C	0.730	1.474	0.604	1.482
β_{bias}	°C	0.996	1.742	-0.047	0.937
t_*		0.902	0.012	0.858	0.014

To evaluate spatial transferability, the calibrated parameter sets were swapped between the valleys: parameters derived from each valley were utilized to predict temperatures in the other study area valley ($T_{\text{mod swap}}$).

4.3.4 Comparison Between Observed and Modelled Data

Model performance was assessed by comparing temperatures predicted by GlobSim and inversion correction (T_{pl}, T_{sur}, $T_{\text{mod Dawson}}$, $T_{\text{mod DMP}}$, and $T_{\text{mod swap}}$) against in-situ observations. Mean Bias Error (MBE) and Mean Absolute Error (MAE) between the observed and modelled temperatures were calculated at 2-hour intervals. Site-specific MBE and MAE were averaged at monthly and study period temporal scales (August 2017-August 2024) and spatially at a study area scale to evaluate seasonal, elevational, and overall model skill.

4.3.5 Assessing Temperature Prediction Improvement from Model Components

To evaluate the contribution of each component of the inversion correction model, temporal bias correction (Eq. 4-6, $\beta(t)$) and the elevation-based correction (Eq. 4-5, $\alpha(z)$), we compared raw GlobSim downscaled reanalysis data to adjusted temperature predictions. Three scenarios were tested: 1) applying only the temporal bias correction $\beta(t)$ to the raw GlobSim data, 2) removing the bias correction $\beta(t)$ inversion correction model, and 3) applying the full inversion correction model (Eqs. 4-1 to 4-6, T_{mod}). MAE and MBE were computed for each scenario, separately for both reanalysis products (ERA5 and JRA-3Q) and each GlobSim metric (T_{pl} and T_{sur}). The relative improvement in different model runs was assessed as (1) decrease in MAE and (2) an MBE closer to 0 °C.

4.3.5 SLR, SBI Metrics, and Model Performance

4.3.5.1 Surface Lapse Rates

SLRs were calculated for T_{obs} and T_{mod} DMP to *c*haracterize elevational air temperature gradients on monthly and annual scales. Linear regression of temperature with elevation was performed across all stations in each study area. Predicted free air lapse rates were derived similarly from the T_{pl} for metrics for both the reanalysis products (ERA5 and JRA-3Q).

4.3.5.2 SBI Frequency in Observations and Reanalysis Products

SBI frequency in the downscaled reanalysis datasets was determined by identifying instances where a temperature inversion occurred in the lower troposphere and extended at least two interpolated pressure levels below approximately 5000 m. In most cases, inversion layers extended down to the reanalysis grid elevation, although some shallower inversions may have been identified that did not extend to the surface.

Observed SBI frequency was computed in two complementary ways:

1) Shallow SBI frequency method: A linear regression of temperature with elevation was performed among the three original sites in each valley (valley bottom and two adjacent slopes, ~100-150 m above the floor), identifying time steps when a SBI (positive SLR) occurred in the valley bottom.

2) Valley-scale SBI frequency method: A regression across all sites within each valley identified valley-scale inversion events. Since the full network was only operational after August 2023, this analysis covers August 2023-August 2024.

A confusion matrix was constructed by tallying cases of hits (observed and reanalysis both flag SBI), misses (observed SBI but not in reanalysis), false alarm (reanalysis SBI but not observed), and true negative (non SBI in either). This matrix quantified how effectively each reanalysis product detects observed SBIs, a diagnostic for assessing the inversion correction model's foundation.

4.3.5.3 SBI Strength

SBI strength was defined as the difference between mean observed temperatures at the valley-bottom sites (i.e., sites located at or below the elevation of each study areas weather station) and mean observed temperatures from sites greater than 150 vertical meters above the weather station. This depth threshold was chosen as prior work (Noad and Bonnaventure, 2026) shows that most inversion-related warming occurs in the layer below 150 vertical meters, where the lowest temperatures occur at the valley bottom sites. Sensitivity to other thresholds is presented in Section 4.7.5.

4.4 Results

4.4.1 Overall model performance in each valley

4.4.1.1 The overall performance of each inversion correction model calibration

For the GlobSim and inversion correction model (Eq. 4-4) the ERA5 and JRA-3Q reanalysis products perform comparably in predicting near-surface air temperature, with a mean absolute error of roughly 2-4 °C and systematic bias ranging between -2.7- -0.5 °C (Table 4-4). ERA5

GlobSim-derived T_{pl} tends to be slightly warmer, while JRA-3Q T_{pl} has a small cold bias, particularly in the WS02 valley. For both reanalysis products, GlobSim-derived T_{sur} exhibits a cold bias with slightly larger MAE than the T_{pl} metric.

Among the inversion correction model predicted temperatures, $T_{mod\ DMP}$ shows minimal positive bias (< 0.2 °C) for both valleys, and the MAE is roughly 2.2-2.7 °C, with a slightly smaller MAE in the WS01 valley than the WS02 valley. When the calibrated models are swapped between the valleys, the $T_{mod\ swap}$ shows a mean bias of roughly 1 °C in WS01 valley and -0.8 °C in WS02 valley, indicating that the swapped calibration predicts the WS01 valley to be colder and the WS02 valley warmer than observed.

The inversion correction model, when calibrated to the original Dawson City Yukon dataset (approximately 100 km southwest of our study area) (Pozsgay & Gruber, 2025), shows consistently positive bias (0.5-2.1 °C) and larger absolute error (3.3-3.7 °C) than locally-calibrated models and most GlobSim-derived metrics.

Overall, the $T_{mod\ DMP}$ achieves the lowest absolute errors and near-zero mean bias, indicating that it provides the most reliable estimates. In WS01, locally calibrated $T_{mod\ DMP}$ reduced winter MAE by approximately 1 °C relative to GlobSim metrics, but in WS02 error reduction was smaller or non-existent relative to the GlobSim T_{pl} metric.

Table 4-4: A heat map illustrating the Mean bias Error (MBE) and the Mean Absolute Error (MAE) for all the sites in each valley aggregated over the study period (August 2017-August 2024). For the MBE the blue cells denote the strongest cold bias, the red cells the strongest warm bias, and white cells the bias nearest to 0 °C. For the MAE the grey cells denote the largest absolute errors while the white cells indicate the smallest absolute error. **Bolded** values indicate the lowest bias or error for each reanalysis product. For context, the mean inter-valley difference in observed mean annual temperature at similar elevations (~1050 m) was 0.1 °C, indicating that model biases often substantially exceed natural cross-valley variability.

Error Metric	Valley	ERA5					JRA-3Q				
		T_{pl}	T_{sur}	T_{mod_Dawson}	$\boldsymbol{T_{mod\_DMP}}$	T_{mod_swap}	T_{pl}	T_{sur}	T_{mod_Dawson}	$\boldsymbol{T_{mod\_DMP}}$	T_{mod_swap}
MBE	WS01	1.5	-2.0	1.5	0.2	1.2	-0.2	-0.5	2.1	0.1	1.0
	WS02	0.2	-2.7	0.5	0.1	-0.7	-0.8	-1.1	1.1	0.0	-0.8
MAE	WS01	2.8	3.0	3.5	2.2	2.5	2.6	2.6	3.7	2.4	2.5
	WS02	1.8	4.0	3.3	2.7	2.8	2.4	3.3	3.3	2.6	2.8

4.4.1.2 Performance of each component of the inversion correction model

To test whether the addition of the temporal bias term (Eq. 4-6 , $\beta(t)$) was the reason for reduced bias, the raw GlobSim reanalysis metrics (T_{pl} and T_{sur}) were compared to (1) the $\beta(t)$-corrected raw GlobSim reanalysis data, (2) the inversion correction model predictions without $\beta(t)$ correction applied, and 3) the full inversion correction model with both the elevation-based correction using inversion strength $\alpha(z)$ (Eq. 4-5) and the $\beta(t)$ applied (Eq. 4-4).

When $\beta(t)$ was applied to the downscaled GlobSim data, the MAE typically decreased for the T_{sur} metric for ERA5 and JRA-3Q (Table 4-5). However, the temporal bias correction performed poorly on its own for the T_{pl} metric, particularly ERA5, where MAE increased by as much as 0.72 °C relative to the original GlobSim data.

The inversion correction model without the $\beta(t)$ bias correction term applied reduced MAE relative to the original GlobSim prediction in all cases in WS01. Applying $\beta(t)$ term to the inversion correction model predictions (the full inversion correction model, $T_{\mathrm{mod\ DMP}}$, Eq. 4-4) further reduced MAE by roughly 0.03-0.38 °C, indicating that the full inversion correction model generally performs best in reducing absolute error. In WS02 this improvement was only observed relative to the T_{sur}, as the T_{pl} metrics had a larger MAE than when only the $\beta(t)$ was applied.

The full inversion models use of both $\beta(t)$ and the $\alpha(z)$ led to large reductions in absolute MBE (how much closer the MBE is to 0 °C), up to 2.7 °C relative to the raw GlobSim T_{sur} data. In contrast, for ERA5 T_{pl} in WS02, MBE relative to zero was increased significantly (approximately 1.5 °C) when the temporal bias term was applied to the raw GlobSim data and when the inversion correction term was applied without temporal bias correction, but when combined together in the full inversion correction model the biases nearly cancelled out to provide a marginal reduction of bias (0.08 °C). This suggests that in some cases, the full inversion correction model may be overfitting the data to reduce bias, sometimes at the cost of increasing MAE.

Overall, these results indicate that the full inversion correction model ($T_{\text{mod DMP}}$) generally produces smaller absolute error and MBE closer to zero than the original GlobSim data with and without the seasonal bias term applied and the inversion correction model without the seasonal bias correction term. The remaining analysis therefore will focus on comparing the full inversion correction model against the raw GlobSim reanalysis for a combination of both ERA5 and JRA-3Q products.

Table 4-5: Differences in MAE and the absolute value of MBE between the raw GlobSim reanalysis (ERA5 and JRA-3Q) for T_{pl} and T_{sur} and three scenarios: (1) the temporal bias correction (β) applied to the raw GlobSim reanalysis metrics, (2) the inversion correction model using only the elevation-based adjustment (α), and (3) the full inversion correction model ($T_{\mathrm{mod\ DMP}}$). Positive values indicate a reduction in absolute error or bias relative to the raw GlobSim products, while negative values indicate an increase. All values are in °C and are aggregated across the full study period (August 2017-2024).

Valley	Product	Metric	dMAE_β	dMAE_α	dMAE_full	d|MBE_β|	d|MBE_α|	d|MBE_full|
WS01	ERA5	T_{sur}	0.39	0.61	0.7	1.01	1.24	1.71
		T_{pl}	-0.49	0.67	0.77	-1.01	0.95	1.42
	JRA-3Q	T_{sur}	0.03	0.18	0.21	-0.04	0.33	0.37
		T_{pl}	-0.07	0.16	0.19	-0.04	0.03	0.07
WS02	ERA5	T_{sur}	0.69	0.87	1.25	1.77	1.18	2.69
		T_{pl}	-0.72	-1.34	-0.96	-1.77	-1.43	0.08
	JRA-3Q	T_{sur}	0.42	0.39	0.67	0.96	0.21	1.17
		T_{pl}	0.03	-0.44	-0.16	0.69	-0.16	0.8

4.4.2 Relationship between observed and predicted lapse rates

In this section we present the lapse rate patterns derived from the in-situ observations, GlobSim T_{pl}, and inversion correction $T_{\mathrm{mod\ DMP}}$ for ERA5 and JRA-3Q reanalysis products, aggregated from August 2023-August 2024. These plots highlight the limitations of the downscaled GlobSim T_{pl} product at lower elevations below the reanalysis grid elevation (Figure 4-3). At these lower sites, T_{pl} predicts temperatures that decrease with elevation, whereas observed temperature increases with elevation, especially in WS01. This divergence produces a pronounced warm bias and larger absolute errors in the lower valley. Since T_{sur} represents a single temperature value at the reanalysis grid elevation, it cannot represent these sub-grid elevation differences.

$T_{\mathrm{mod\ DMP}}$ applies a linear elevation-based correction that is variable in time to reanalysis temperatures, based on observed inversion strength and the lapse rates of the atmosphere above the SBI layer. Consequently, when aggregated over a full year, $T_{\mathrm{mod\ DMP}}$ produces a linear, nearly isothermal temperature-elevation relationship (-0.9–1.6 °C km^{-1}). This adjustment substantially reduces the warm bias at low elevations and decreases overall error relative to T_{pl}. However, $T_{\mathrm{mod\ DMP}}$ still underestimates the coldest annual mean temperatures at the lowest elevation sites, where cold air pooling and SBIs lead to a non-linear lapse rate.

The linear model predicts positive corrections alpha(z) up to an elevation z_0 (1900 and 2100 m a.s.l. in WS01 and WS02 respectively) given by $z_0 = -\alpha_{\mathrm{intercept}} / \alpha_{\mathrm{slope}}$. Since z_0 lies far above the highest sites, the model applies linear corrections across all elevations, including at higher elevation sites where SBIs do not typically extend. The relationship between observed temperatures and elevation is not linear when aggregated over time due to the presence of SBIs in some readings and negative lapse rates in others. This leads to an overfitting of predicted temperatures by $T_{\text{mod DMP}}$ that is most pronounced at the lowest and highest elevation sites.

Observed annual mean temperature increases with elevation in the lower valley and then transitions to normal decrease with elevation above the SBI layer, forming a parabolic temperature-elevation relationship.

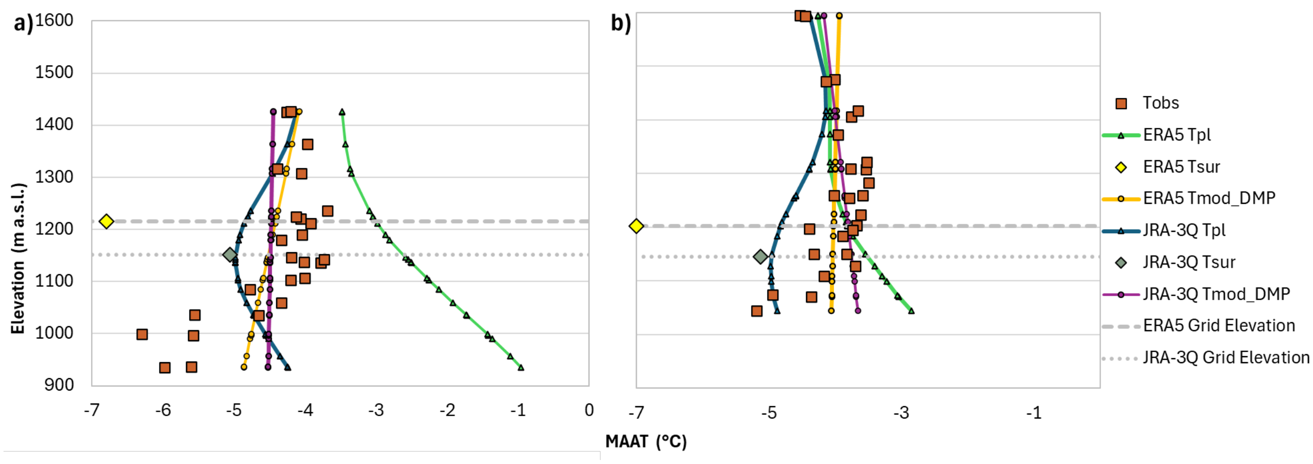

Figure 4-3: The elevational temperature profile for the observed and predicted mean annual air temperature (MAAT) at each site in (a) WS01 study area and (b) WS02 study area. The observed and predicted temperatures are based on a subset of data that spans from August 2023-August 2024.

4.4.3 Elevational patterns of error and bias

There was a strong elevational dependence for GlobSim metrics MBE and MAE across the two valleys (Figure 4-4). When aggregated between both reanalysis products, T_{pl} exhibited a warm bias (up to 3.4 °C in WS01 and 1.1 °C in WS02) at the lowest elevations (<1050 m a.s.l.). The bias rapidly decreased to near 0 °C between 1050 and 1100 m a.s.l. and remained small (±1 °C) above that in both valleys. The absolute error for T_{pl} was *e*xceptionally large at the lowest elevation sites of WS01 (up to 4.9 °C) but decreased consistently with elevation to roughly 1.5 °C at the highest sites.

T_{sur} displayed an almost universally negative bias, being only slightly positive at the lowest WS01 sites. The cold bias intensified with elevation, reaching roughly -2 °C at mid-elevation sites (≈1100-1425 m a.s.l.), before decreasing slightly at the highest sites in WS02. The absolute error for T_{sur} generally increased with elevation, from 3.3 °C at valley bottom sites to 4.7 °C at the highest elevation in the WS02 valley. These patterns likely follow lapse rate patterns in the valley, as T_{sur} represents the GlobSim surface temperature, which does not inherently account for subgrid elevational effects.

For $T_{\mathrm{mod\ DMP}}$, the bias at the lowest elevations was negative but smaller in magnitude than that of T_{pl} (1-2 °C in WS01). Above these lowest elevations, the bias stabilizes near zero, similar to the T_{pl} at mid- and high-elevation sites. The MAE for $T_{\mathrm{mod\ DMP}}$ was lowest (2.5-3.0 °C) at elevations below 1150 m a.s.l. in WS01, indicating the locations where the inversion correction model performed best. At the higher elevations in both valleys, MAE for $T_{\mathrm{mod\ DMP}}$ was modestly (up to 1 °C) greater than the T_{pl}.

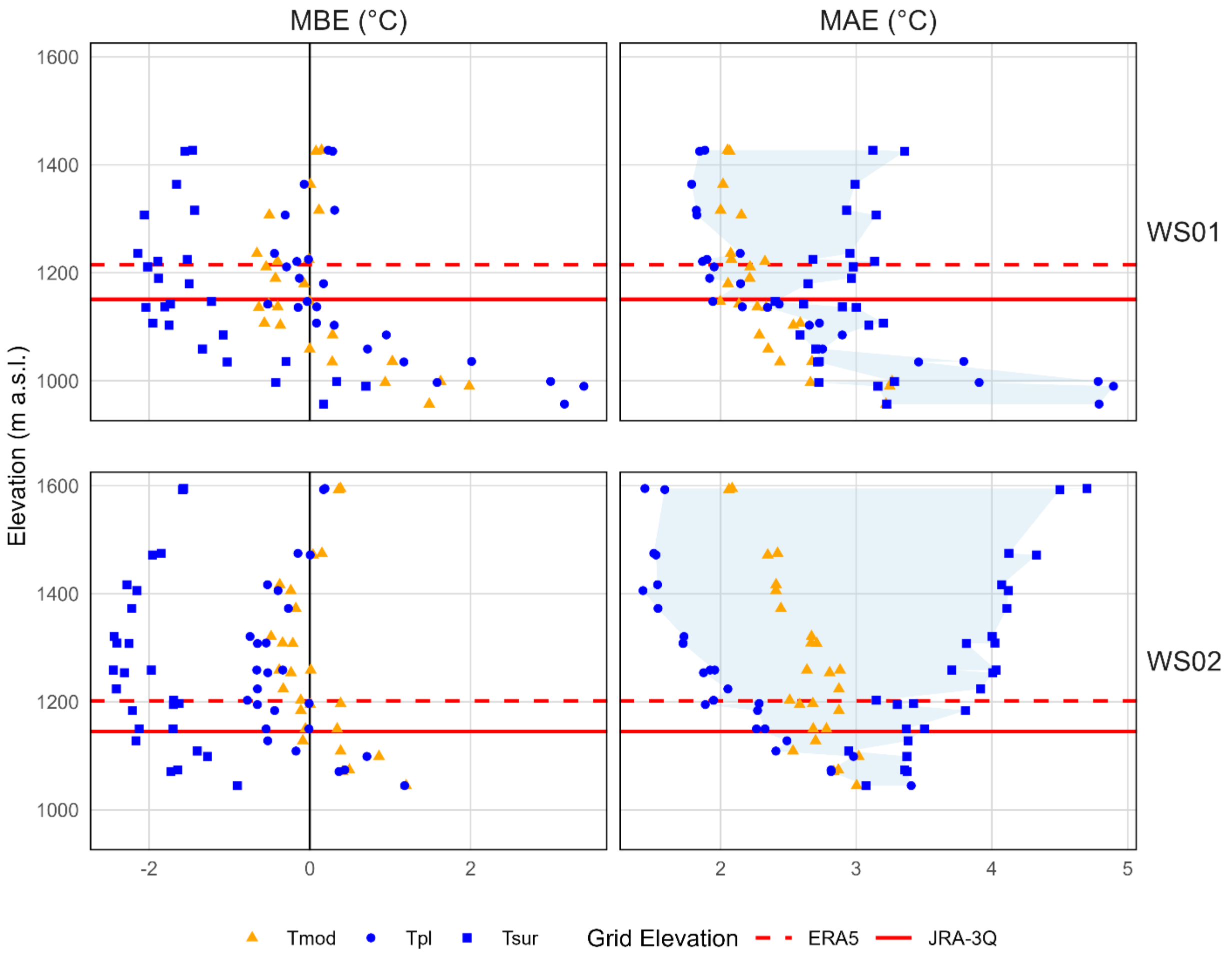

Figure 4-4: Error metrics including Mean Bias Error (MBE) and Mean Absolute Error (MAE) for each site in relation to elevation in the WS01 and WS02 valleys. The dashed lines indicate the elevation of the reanalysis grid as interpolated for each of the weather stations in the Dempster valleys.

4.4.4 Seasonal patterns of bias and error

Monthly MBE and MAE values, aggregated across both GlobSim (T_{pl} and T_{sur}) downscaled reanalysis products (ERA5 and JRA-3Q), exhibited a clear seasonal cycle across both valleys (Figure 4-5).

For both valleys, $T_{\mathrm{mod\ DMP}}$ MBE was generally consistent throughout the year, typically less than ±1 °C, with slightly larger deviations (±1.0–1.5 °C) observed in winter months

(January–March). In contrast, T_{pl} and T_{sur} exhibited stronger seasonal fluctuations ranging from approximately -6–+4 °C in the winter and stabilized near ±1 °C from April to September. The T_{pl} product showed a pronounced warm bias in the winter that shifted to a weaker cold bias in the summer, whereas T_{sur} displayed strong cold bias in the winter transitioning to a weak warm bias in the summer.

For all products, MAE peaked in the winter months (December–February), reaching values upwards to 6.0 °C, and declined to less than 2.0 °C during the late spring, summer, and early autumn months (May–September). Winter MAE for $T_{\mathrm{mod\ DMP}}$ was between approximately 3–4 °C, compared to 4.5–6 °C for the T_{pl} and T_{sur}.

Overall, $T_{\mathrm{mod\ DMP}}$ consistently outperformed both GlobSim components, exhibiting lower MAE and MBE closer to 0 °C across most of the year. Model performance was especially improved during the winter months in WS01. For WS02, the $T_{\mathrm{mod\ DMP}}$ still showed the most stable bias pattern when considering both MBE and MAE, though T_{pl} had a smaller MAE throughout the year.

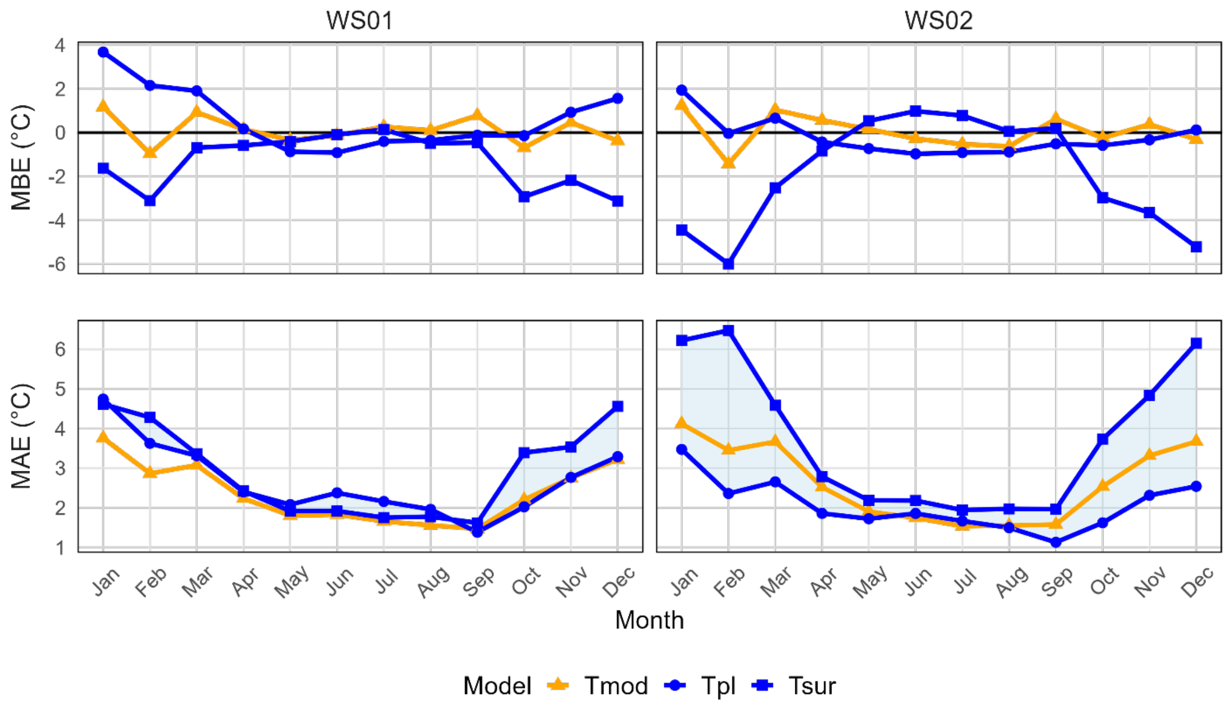

Figure 4-5: The monthly pattern of Mean Absolute Error (MAE) between the GlobSim downscaled reanalysis metrics (T_{pl} and T_{sur}) averaged for each time-step between the ERA5 and JRA-3Q products and the locally-calibrated inversion-correction model ($T_{\mathrm{mod\ DMP}}$) in the WS01 study area and WS02 study area.

4.4.5 Representation of SBIs in Reanalysis Data

The reanalysis products (ERA5 and JRA-3Q) showed comparable skill in identifying valley-scale inversion and non-inversion conditions; therefore, results were aggregated for clarity (Figure 4-6). The ability of the reanalysis datasets to flag valley-scale SBI conditions closely followed the observed seasonal cycle. During winter, when SBIs were most frequent, missed detections of observed SBIs were rare, only 6% (2%) of the time in WS01 (WS02). In contrast, during summer when SBIs were least frequent, the proportion of missed SBIs increase to as much as 20% (14%) in WS01 (WS02).

False alarms of SBI occurrence in the reanalysis products were most frequent from October through April, reaching 35% (53%) in WS01 (WS02). False alarms were minimal in summer (<10%). Accuracy (sum of hits and correct negative) was highest in months with either very frequent (e.g., January) or very infrequent (e.g., September) SBIs, typically exceeding 80%. Accuracy declined to as low as 42% in transitional months (late autumn, some winter periods such as February, and early spring), when the reanalysis products tended to overpredict SBI occurrence relative to valley-scale observations.

These patterns indicate that shallow, short-lived SBIs associated with nocturnal cold-air pooling are often underrepresented in the reanalysis products during the summer, while deeper, persistent wintertime inversions are more effectively captured.

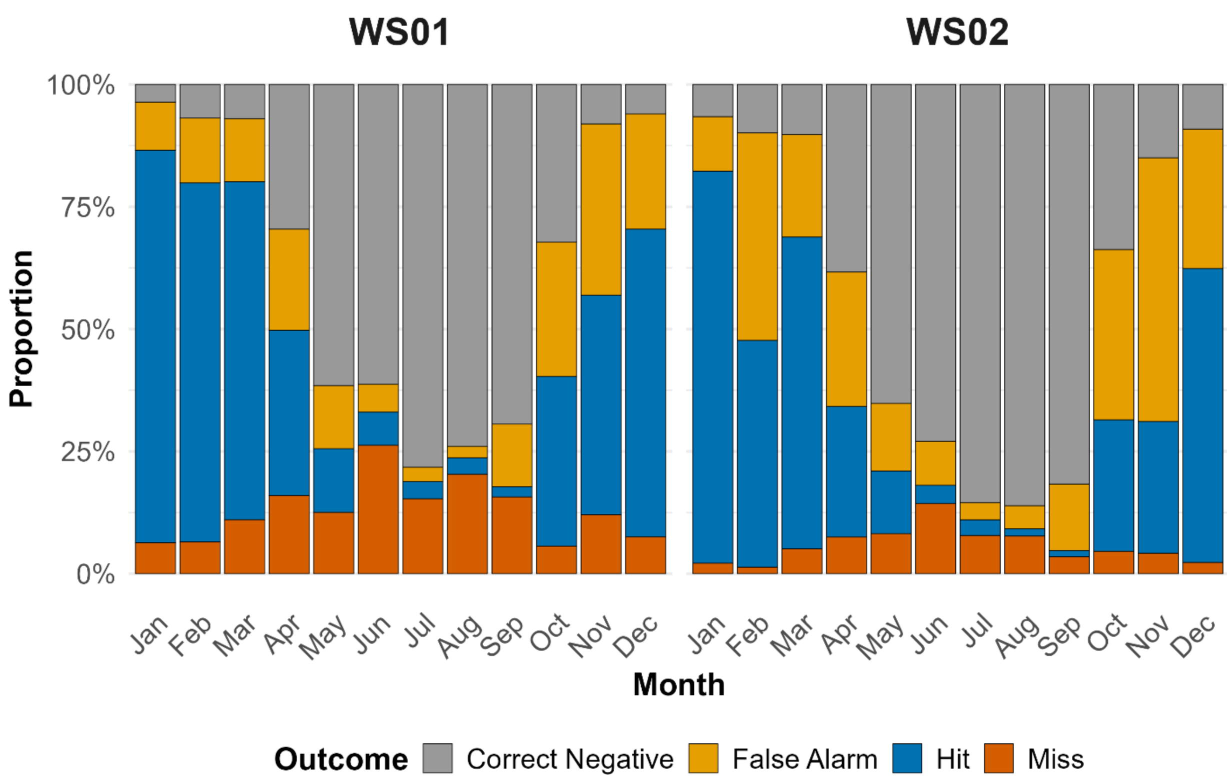

Figure 4-6: The count of all readings summed up between both reanalysis products (ERA5 and JRA-3Q) in WS01 and WS02 where an observed valley-scale SBI was flagged by the reanalysis product (Hit, blue), an observed SBI was missed by the reanalysis products (Miss, orange), no inversion was observed but was flagged by the reanalysis (False Alarm, yellow), and where there was no observed SBI or one flagged in the reanalysis (Correct Negative, grey) for August 2023-

August 2024. Observed valley-scale SBI frequency is quantified for each month by adding up the total misses and hits.

4.4.6 Error Metrics During and Outside of SBIs

Patterns in model bias differed distinctly between SBI and non-SBI periods (Figure 4-7). In WS01, T_{pl} had an MBE of approximately +2.5 °C during observed valley-scale SBIs and -1.2 °C during observed non-SBI conditions, while in WS02 the corresponding values were +1.5 °C and -1.1 °C. The $T_{\mathrm{mod\ DMP}}$ bias was much smaller, roughly 0.1 °C during SBI conditions and -0.1 °C outside of them, reflecting its calibration using in-situ observations from August 2023-August 2024, when the complete valley-scale inversion record was available.

MAE was consistently higher during valley-scale SBIs than during non-SBI conditions in both valleys. In WS01, MAE values under non-SBI conditions were similar among all model types, with $T_{\mathrm{mod\ DMP}}$ showing only minor improvement (<0.3 °C). However, during SBIs, $T_{\mathrm{mod\ DMP}}$ reduced MAE by 0.5-1.0 °C relative to the other two datasets, indicating that the inversion correction model primarily improves performance when valleys scale SBIs were observed.

In WS02, T_{pl} has the smallest MAE under both conditions, 2.8 °C during SBIs and 1.7 °C otherwise. The $T_{\mathrm{mod\ DMP}}$ MAE was somewhat larger, at roughly 3.9 °C during SBI conditions and 2.0 °C during non-SBI conditions. Thus, while the inversion correction model reduces bias (MBE) in WS02, it did not reduce overall error magnitude (MAE), particularly during times when a valley-scale SBI was observed.

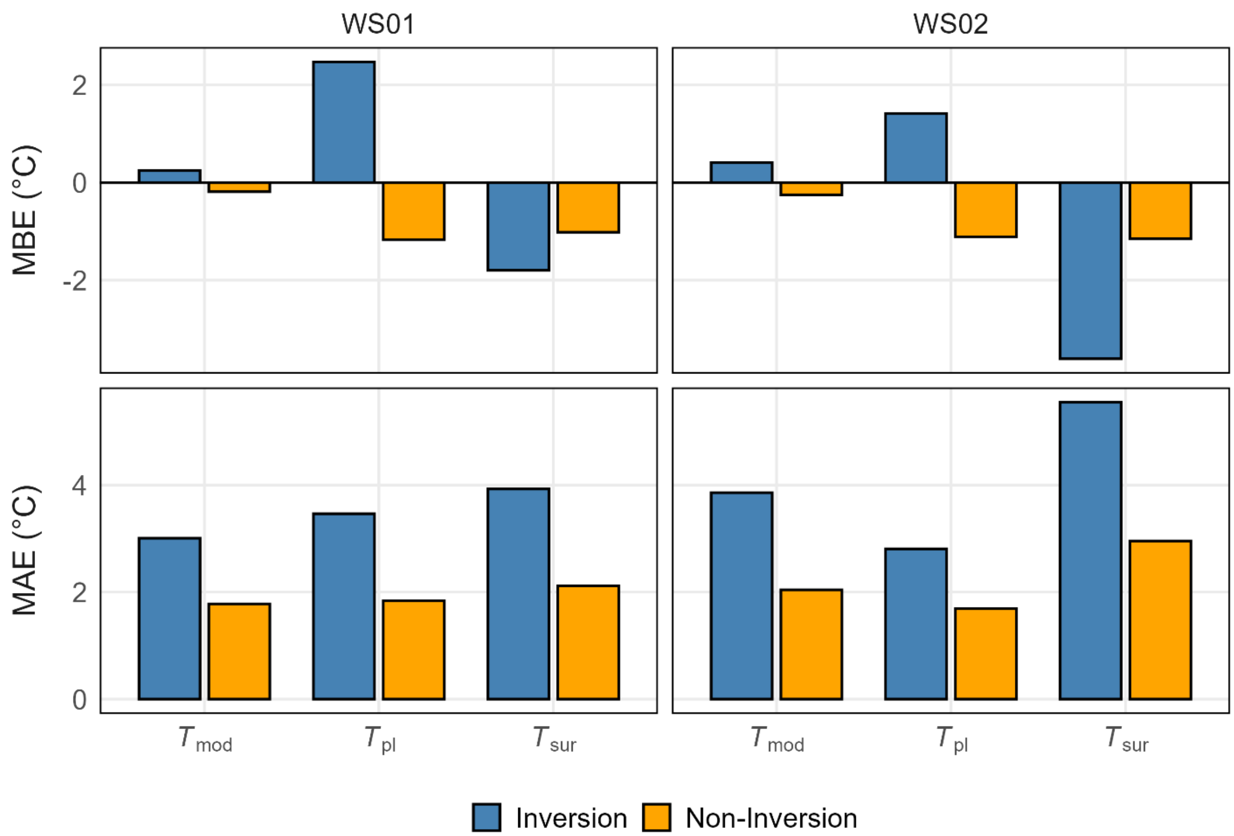

Figure 4-7: Mean bias error (MBE) and mean absolute error (MAE) represented with bars for $T_{mod\ DMP}$, T_{pl}, and T_{sur} modelled temperatures aggregated between the ERA5 and JRA-3Q reanalysis products. Errors were aggregated across all sites in WS01 and WS02 from August 2023-August 2024 during and outside of observed valley-scale SBIs.

When SBI conditions occur, both MBE and MAE exhibited strong elevational dependance that was substantially reduced by the inversion correction model ($T_{mod\ DMP}$) (Figure 4-8). For example, T_{pl} showed a warm bias of close to +8 °C during SBIs at the lowest elevation sites, while the $T_{mod\ DMP}$ reduced this bias to approximately +4 °C, only slightly larger than the T_{sur} positive bias of about +3.5 °C. At high elevations, T_{sur} exhibited a pronounced cold bias of roughly -5 to -6 °C, whereas $T_{mod\ DMP}$ reduced this to near -1 °C, and T_{pl} showed only a small positive +1 °C bias.

Similarly, MAE patterns with elevation are muted by the $T_{\text{mod DMP}}$ metric. At the lowest elevations, $T_{\text{mod DMP}}$ has an MAE of roughly 5 °C, compared to roughly 8 °C for T_{pl} and 4 °C for T_{sur}. At higher elevations the MAE for $T_{\text{mod DMP}}$ is between 2–3 °C, like T_{pl}, which is slightly lower at around 2 °C, while T_{sur} exhibits much larger errors of approximately 7 °C. Outside of observed SBI conditions, $T_{\text{mod DMP}}$ shows little to no elevation dependance, with MAE remaining consistent near 2 °C at all sites, closely resembling the T_{pl} metric.

These patterns demonstrate that during observed valley-scale SBIs the inversion correction model effectively integrates the low-elevation strengths of T_{sur} with high-elevation strengths of T_{pl}, yielding a more balanced temperature prediction across valley transects.

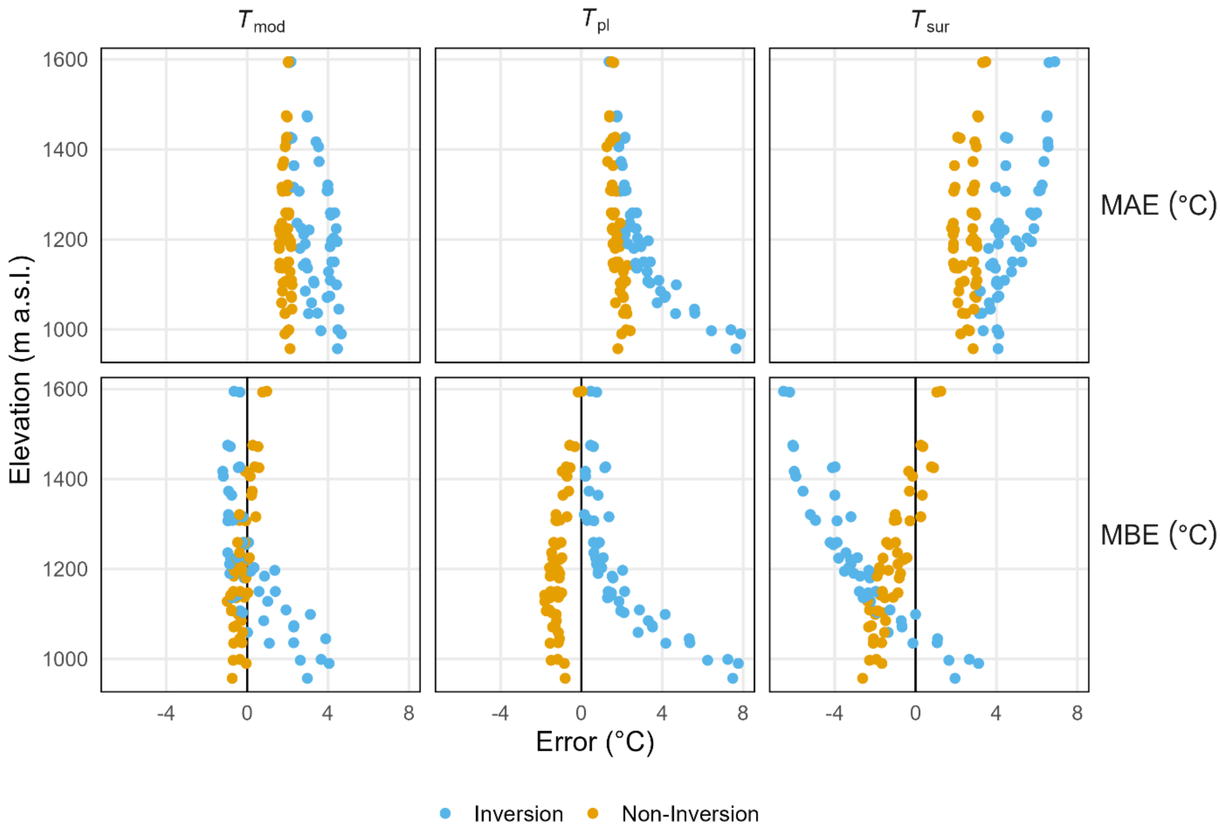

Figure 4-8: Mean bias error (MBE) and mean absolute error (MAE) at each site in both WS01 and WS02 for T_{pl}, T_{sur}, and $T_{mod\ DMP}$ under SBI (blue) and non-SBI (orange) conditions. The ERA5 and JRA-3Q products are aggregated together.

4.4.7 Inversion Correction Model Improvement and SBI Strength

Model improvement relative to the base GlobSim T_{pl} and T_{sur} metrics varied systematically with inversion strength seasonally in the two valleys (Figure 4-9). Maximum improvements (approximately an average of 1.6 °C in WS01 and 1.4 °C in WS02) occur in the winter during SBIs with a strength of roughly 5–15 °C in WS01 and 5–10 °C in WS02. In the winter, SBI stronger than 20°C in WS02 had negative $T_{mod\ DMP}$ improvements suggesting that the inversion correction model had a larger MAE than the T_{pl} and T_{sur} metrics during these readings. SBI strength was weakest and model improvement in MAE was reduced during the summer months (June through August). This supports the findings of seasonality to the inversion correction model performance indicating that the typically deeper and stronger wintertime inversions were better represented by the correction model than the shallower and weaker summertime inversions.

During the spring, summer, and autumn in the WS01 study area, improvement in MAE by the $T_{\mathrm{mod\ DMP}}$ steadily increased with SBI strength. In contrast, improvement in MAE was small or negative for inversions of all strengths in the WS02 study area.

When SBI strength approached zero in both valleys during all seasons the absolute error for the $T_{\mathrm{mod\ DMP}}$ was roughly equal to that of the average between the T_{pl} and T_{sur} metrics. The overall decrease in improvement of temperature prediction for SBIs of all strengths in WS02 suggests that the model skill depends on the valley geometry and SBI structure in that valley.

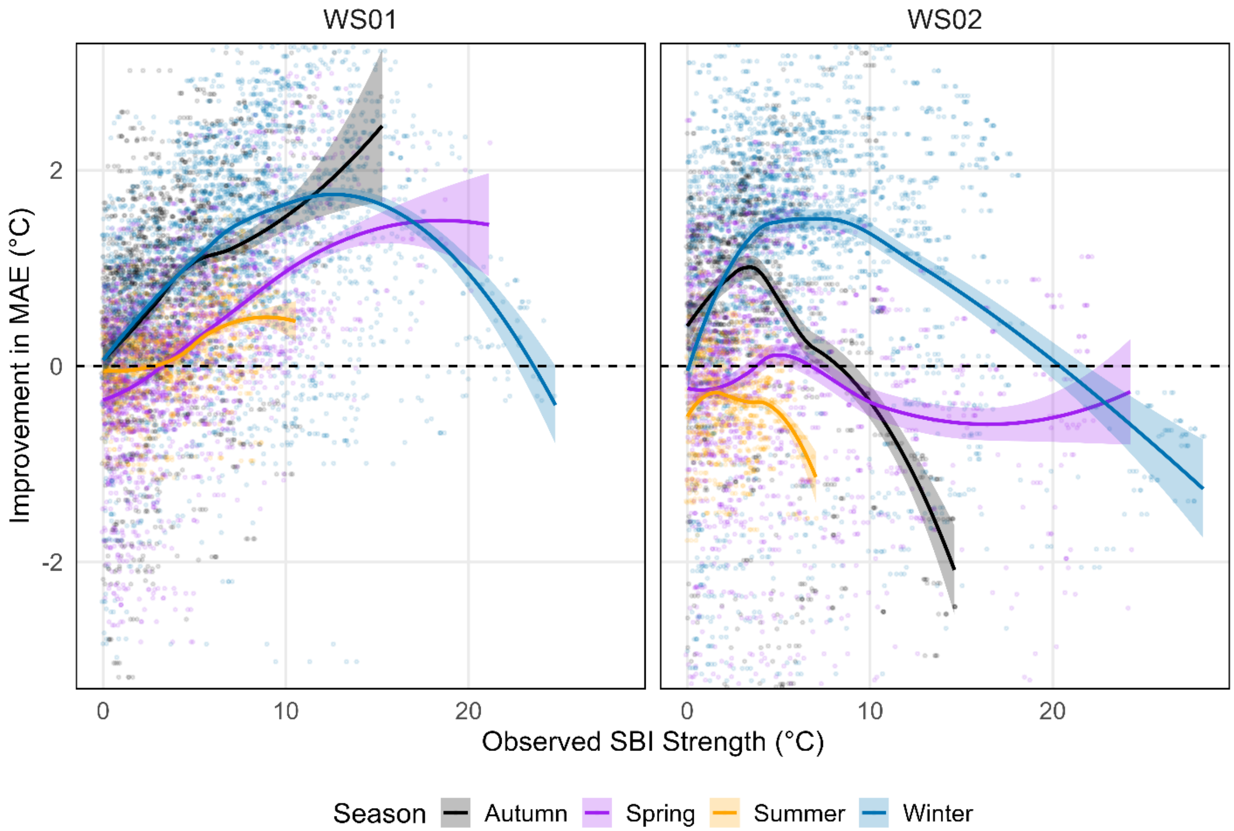

Figure 4-9: Scatterplot of improvement in MAE between the average GlobSim metrics (T_{pl} and T_{sur}) for both reanalysis products aggregated together and the inversion-correction model calibrated to the study valleys ($T_{\mathrm{mod\ DMP}}$) as a function of observed SBI strength. SBI strength was calculated as the difference between mean temperatures of valley bottom sites at or below the weather station and the mean temperature of sites greater than 150 m above the weather station. The lines represent the locally smoothed (LOESS) mean relationship, and the shaded bands indicate the 95 % confidence interval of these fitted trends. The black dashed line marks where the improvement equals 0 °C (the MAE of $T_{\mathrm{mod\ DMP}}$ equals the average MAE of T_{pl} and T_{sur}). MAE improvement is zoomed to ±3 °C to emphasize the seasonal variations in model performance.

4.5 Discussion

4.5.1 Strengths of the Inversion Correction Model

The inversion correction model effectively integrates the two downscaled GlobSim temperature metrics, T_{pl} which performs best at higher elevations, and T_{sur} which better represents near-surface temperature at lower elevations. By combining these metrics through a simple linear regression with elevation-based inversion correction term (Eq. 4-5) and season specific bias term (Eq. 4-6), the model consistently improves temperature prediction across both study valleys relative to the raw GlobSim data, the temporal bias corrected GlobSim data, and the inversion correction model without the temporal bias correction applied (Sections 4.4.1.1 and 4.4.1.2). This confirms its value as a simple yet powerful approach for correcting reanalysis temperatures in regions where SBIs strongly influence near-surface air temperature patterns.

Inclusion of the DT term (Eq. 4-1; analogous to the SBI_{mag} term in Noad et al., 2023) provides physically-based means of adjusting sub-daily reanalysis temperatures to capture short-term SBI dynamics without adding substantial model complexity. The model achieved its best performance at low-elevation sites below the reanalysis grid elevation in WS01, where the reanalysis bias and error were the greatest (Section 4.4.3). When aggregated across all sites during the full study period in WS01, MAE improvements of roughly 0.2-0.8 °C and mean bias (MBE) reductions to within ±0.2 °C demonstrated robust correction of reanalysis warm and cold biases.

Even when parameters were transferred between valleys, model bias generally remained within roughly ±1 °C, indicating moderate spatial transferability. These findings align with Pozsgay and Gruber (2025) and reinforce that a locally calibrated, linear correction model can effectively capture SBI influence on near-surface temperatures in subarctic valleys while remaining computationally efficient.

4.5.2 Limitations and Sources of Uncertainty in the Inversion Correction Model

Air temperatures were measured using passively ventilated radiation shields, which can introduce a positive measurement bias under conditions of strong solar radiation and low wind speeds due to radiative heating of the sensor (Erell et al., 2005; Hubbard et al., 2001; Nakamura

& Mahrt, 2005). Such biases are generally expected to be small during the winter inversion conditions that are the primary focus of this study because solar radiation is limited, although sunny, low-wind periods may still introduce minor warm biases. Consequently, a small portion of the residual error attributed to the inversion correction model may instead reflect uncertainty in the reference air temperature measurements used for model evaluation. While this source of uncertainty should be acknowledged, it is unlikely to alter the overall conclusions regarding model performance.

Beyond uncertainties associated with the reference observations, the inversion correction model itself has several limitations that should be considered. Although the inversion correction model showed moderate spatial transferability between the two adjacent study areas, its improvements diminished when applied outside its calibration area. When parameters from WS01 were applied to WS02 (and vice versa), the model introduced systematic biases: a warm bias (+1.0-1.2 °C) in WS01 and cold bias (-0.7--0.8 °C) in WS02 (Table 4-4). These patterns likely reflect local differences in inversion frequency and strength, with WS01 experiencing more frequent and deeper SBIs (Noad and Bonnaventure, 2022; 2026). Transferability dropped further when applying the $T_{\text{mod Dawson}}$ parameters originally calibrated for near Dawson City, Yukon (Pozsgay and Gruber, 2025), where MAE increased by up to 1.5 °C and MBE exceeded +2 °C. These results indicate that while the model structure is robust, local calibration remains essential for reliable application in subarctic valleys.

A key reason for this limited transferability is the model's reliance on absolute elevation to represent SBI strength. While this parameter performs well locally, it does not generalize between regions with different elevation ranges. For instance, the Dawson City study area spans 370 to 1200 m a.s.l (Pozsgay and Gruber, 2025), whereas the Dempster areas valley bottom sites correspond with the ridgetops in the Dawson region. To address this, future versions of the model could incorporate relative elevation metrics, such as height above the valley bottom or hypsometric position (see Cao et al., 2017, REDCAPP). Efforts to do this have been made in the recent update of the inversion correction model, now called Dynamical Reanalysis Model for Inversions of Temperature (DReaMIT), where the hypsometric positions relative to a 50 km radius is used in place of absolute elevation (Pozsgay et al., 2026). This new approach preserves the model's physical grounding while improving spatial transferability without requiring local recalibration, an important step given the scarcity of observations in high-latitude mountain regions (Urban et al., 2013).

At mid and high elevation sites, particularly in WS02, the model occasionally overcorrects temperatures above the SBI layer (Figure 4-3), where free-air lapse rates dominate. In these cases, the GlobSim T_{pl} metric performs better, suggesting that the inversion correction could need to be restricted to elevations within or below the typical SBI depth, while T_{pl} temperature prediction could be used on the upper slopes. Since $\alpha(z)$ becomes negative only at elevations far above the instrumented sites (approximately 1900–2100 m a.s.l.), the model partially overfits an unrealistic warming to the highest elevation sites. If $\alpha(z)$ were constrained to non-negative values (e.g., $\alpha'(z) = \max(\alpha(z), 0)$) prior to fitting, the resulting $\alpha_{intercept}$ and α_{slope} would likely shift, lowering the zero-crossing elevation and reducing this high-elevation artefact. Additionally, a more flexible approach, such as an exponential suppression of inversion correction, as implemented in the DReaMIT model (Pozsgay et al., 2026), may limit the influence of the correction above the SBI layer while preserving the performance near the valley floor.

Finally, the model assumes linear lapse rates during SBI events. Observed vertical temperature profiles are markedly nonlinear, warming rapidly in the lowest approximately 60 m, then transitioning to near isothermal above 150 m (Noad and Bonnaventure, 2026), consistent with other basin and mountain observations (Shen et al., 2016). This structure cannot be fully captured with a simple linear model, producing residual warm bias at the coldest valley bottom sites, sometimes larger than those in the original T_{sur} metric. Incorporating a simple nonlinear or piecewise lapse rate formulation (Cullen & Marshall, 2011) could address this limitation, but risks overfitting and potentially undermines the model's computational simplicity (Höge et al., 2018).

Overall, the inversion correction model effectively reproduces the main thermal structure of SBIs when locally calibrated, but its simplicity imposes physical and spatial limits. Future refinements should focus on (1) incorporating relative elevation to improve regional scalability, and (2) testing nonlinear lapse-rate formulations that maintain stability and interpretability.

4.5.3 SBI Frequency Observed vs Reanalysis

During observed SBI readings, the inversion correction model substantially reduced both bias and absolute error, especially at lower elevations where the largest deviations occurred in the GlobSim T_{pl} *and* T_{sur} products (Figure 4-8). This confirms that the model effectively integrates the complementary strengths of the downscaled reanalysis pressure level and surface temperature metrics under SBI conditions.

Reanalysis products showed strong skill, accuracies above 80%, when SBIs were very frequent (e.g. winter months) or rare (e.g. late summer and early autumn) but fell to roughly 40% during transition seasons when SBIs were intermittent (Section 4.4.5). Most errors arose from overprediction of SBIs from October to April (Figure 4-6) and missed detection of shallow, short-lived SBIs, mainly in the summer (Figure 4-12). The former may reflect the existence of frequent multiple layered elevated temperature inversions that occur in the subarctic atmospheric boundary layer in the winter season (Mayfield and Fochesatto, 2013). An inversion in the reanalysis datasets is defined as at least two consecutive pressure level temperatures that increase with height above the surface. This can lead to false positives where no SBI is observed in the valley. Future iterations of the model could focus solely on identifying inversion layers that extend all the way to the surface.

Missing shallow SBI layers is expected, as warm-season SBIs tend to be weak, transient, and confined to the lowest tens of meters above the valley floor (Noad and Bonnaventure, 2026). This reflects physical limits of the coarse vertical resolution parent ERA5 and JRA-3Q reanalysis datasets. Pressure level temperatures are positioned tens to hundreds of meters apart near the surface, and the 6-hour sampling of JRA-3Q (Kosaka et al., 2024), interpolated by GlobSim to one-hour frequency, can miss transient nocturnal SBI events (Noad and Bonnaventure, 2022; 2023). Consequently, reanalysis captures deep, persistent winter SBIs better than shallow summer ones. A similar issue was observed by Noad and Bonnaventure (2026) when the resolution of the in-situ elevational transects was increased. In this case, the SBIs were found to be stronger and more frequent than previously measured as the vertical structure was sampled at a higher resolution.

Missed shallow SBIs directly limit the model's ability to apply meaningful corrections. Although the model always applies an $\alpha \cdot DT$ (Eq. 4-4) correction at every hourly time step, the magnitude of this correction depends on reanalysis detection of an overlying inversion layer (Noad et al., 2023; Pozsgay & Gruber, 2025). When the reanalysis fails to detect an inversion, DT tends to be near zero (mean 0.3-0.9 °C compared to mean of -10--8 °C when an inversion is detected by the reanalysis), so the resulting $\alpha \cdot DT$ adjustment is minimal. In these situations, the model may underrepresent the true influence that shallow SBIs exert on temperatures at lower elevation sites. This issue is particularly pronounced during summer nights, when SBIs are shallow and commonly missed by coarse vertical and temporal reanalysis resolutions. Consequently, improving inversion detection, especially for short duration or weak nighttime SBIs, likely offers an opportunity for enhancing model accuracy.

Future versions of the model could integrate empirical predictors of SBI occurrence, such as surface and 10 m wind speed, net radiation, daily temperature amplitude, or atmospheric stability indices (e.g. Richardson number), to probabilistically flag likely SBI readings even when reanalysis vertical resolution is insufficient. Observations show that summertime SBI strength and frequency in these valleys closely follow daily temperature amplitude (Noad and Bonnaventure, 2026), suggesting that combining such variables with reanalysis data could improve detection of shallow SBIs and further enhance model performance.

4.5.4 SBI Strength in Relation to Model Performance

Model performance peaked under moderate SBI strength, while both weak and strong SBIs were represented less accurately (Figure 4-9). Weak SBIs are often shallow and transient, making them difficult for the reanalysis products to detect and for the correction model to adjust temperature effectively. Since the correction term scales with DT (Eq. 4-3), minimal SBI strength produces little modification relative to the base GlobSim metrics as DT is typically close to 0 °C during weak observed inversions, yielding small or negligible improvements during these readings.

Conversely, strong, persistent winter SBIs often exhibit non-linear vertical temperature structure (Noad and Bonnaventure, 2026), which the model’s single linear lapse-rate correction cannot fully reproduce. This leads to underestimation of steep near-surface temperature gradients and residual bias at the coldest valley sites. Introducing adaptive lapse-rate segments or empirically derived non-linear adjustments when strong SBIs are detected could improve performance, provided computational simplicity is maintained.

The 150 vertical meter threshold used to calculate SBI strength (Section 4.3.5.3) reflects typical maximum SBI depth (Noad and Bonnaventure, 2026) but may underestimate deep wintertime SBIs or dilute shallow summer events. These effects introduce potential bias in the estimated mean SBI strength and should be considered when interpreting the relationships between SBI strength and model error (Section 4.7.5).

4.5.5 Implications and Future Work

Correcting downscaled climate reanalysis data for SBIs can substantially improve near-surface air temperature estimates in subarctic valleys. These improvements have practical implications for climate and permafrost modelling in high-latitude mountainous terrain.

Permafrost models that use reanalysis predicted temperatures can struggle in complex topography (Obu et al., 2019). Bonnaventure and Lewkowicz (2013) provided a conceptual framework describing how SBIs influence permafrost distribution through their control on cold valley bottom temperatures. In the Dempster Highway valleys, most existing work has applied equilibrium modeling approaches (e.g., Garibaldi et al., 2024 a, b), which capture present-day but not transient change. The next logical step is to incorporate SBI-corrected reanalysis temperatures into transient permafrost simulation workflows.

Beyond model enhancement, inversion-corrected reanalysis datasets also provide a means to examine long-term changes in SBI dynamics. Pozsgay and Gruber (2025) demonstrated that trends in SBI frequency and strength derived from corrected reanalysis data can reveal shifts in the boundary-layer stability under a warming climate. Applying this approach to the Dempster Highway region could clarify how evolving lapse rates influence patterns of permafrost thaw and degradation. Notably, permafrost here may degrade bidirectionally from mid-slope towards both the valley bottoms and ridges (Bonnaventure & Lewkowicz, 2013), making it especially sensitive to changes in climate.

A projected decline in SBI strength and frequency would likely accelerate valley-bottom warming, potentially exceeding that at higher elevations (Garibaldi et al., 2024a). This contrasts with the globally observed pattern of elevation-dependent warming (Pepin et al., 2015) and underscores the need for localized, SBI-aware models to accurately capture subarctic climate feedback and permafrost changes.

4.6 Conclusion

Reducing SBI induced bias in reanalysis datasets utilizing an inversion correction model provides a practical foundation for future transient permafrost modelling. By improving the representation of near-surface air temperature in subarctic valleys, the inversion-corrected datasets developed here will directly enhance the accuracy of permafrost models.

This study assessed the performance and physical robustness of the Pozsgay and Gruber (2025) inversion correction model in two subarctic valleys along the Dempster Highway. When calibrated locally, the model reduced MAE by up to 0.8 °C and MBE to within ±0.2 °C relative to the downscaled GlobSim products, confirming its ability to integrate surface and pressure-level reanalysis data to account for SBI-driven vertical thermal structure.

Model performance was strongest under moderate SBI strength, while errors increased under weak or the strongest SBIs due to limited vertical resolution of the parent reanalysis dataset and the model's linear lapse rate assumption. In particular, the reanalysis datasets failed at times to identify shallow, short-lived SBIs, especially during the summer, which constrained the model's ability to apply corrections for those periods. Transferability tests showed that locally calibrated models performed best, whereas inter-valley or inter-regional transfers introduced systematic biases linked to differences in absolute elevation ranges.

Future model development should therefore focus on improving generalization by replacing absolute elevation with a relative topographic measure (e.g., height above valley floor) and incorporating non-linear or segmented lapse-rate terms that retain computational simplicity while better capturing strong SBI thermal structure. These steps have been addressed in recent adjustments to the inversion correction model now called DReaMIT (Pozsgay et al., 2026). Integrating additional reanalysis predictors such as surface radiation balance, wind speed, or stability indices may also improve SBI detection and correction where reanalysis resolution is insufficient.

Overall, this research demonstrates that explicitly accounting for SBI dynamics enhances the accuracy of reanalysis-based air temperature fields and provides a robust input for future permafrost modelling in high-latitude mountainous terrain.

Author contribution

Conceptualization: PB, NN, VP, SG. Data curation: NN, VP. Formal analysis: NN. Funding acquisition: PB, SG. Software: VP. Supervision: PB, SG. Visualization: NN. Writing (original draft preparation): NN. Writing (review and editing): PB, VP, SG.

Acknowledgements

This research was completed on the traditional territory of the Tr'ondëk Hwëch'in and the Na-Cho Nyäk Dun First Nations and we thank them for supporting our research. We appreciate the Government of Yukon for providing us with Yukon Scientists and Explorers research licenses to do this work in their Territory. We cannot thank enough each member of the field teams since 2017 for all their time and effort in setting up this network of stations and downloading data each summer. We would like to thank Nick Brown for his technical support with GlobSim. We acknowledge the support that the University of Lethbridge and Carleton University have provided to assist us in this research. The funding provided by NSERC via PermafrostNet (NETGP 523228-18), CREATE LEAP (575207), Discovery Grant RGPIN-2020-04783, and Discovery Development Grant 110_2024_2025_Q1_4012, the Northern Scientific Training program (NSTP) from Polar Knowledge Canada, the governments of Yukon and British Columbia, and the Digital Research Alliance of Canada (772) each were essential to the success of this research. We would also like to acknowledge ECMWF and JMA for the ERA5 and JRA-3Q reanalysis data.

Data Availability Statement

Data used in this study can be requested upon request by contacting the corresponding author at nick.noad@uleth.ca.

Funding Statement

This research was funded by the NSERC via PermafrostNet (NETGP 523228-18), CREATE LEAP (575207), Discovery Grant RGPIN-2020-04783, and Discovery Development Grant

110_2024_2025_Q1_4012, the Northern Scientific Training program (NSTP) from Polar Knowledge Canada, the governments of Yukon and British Columbia, and the Digital Research Alliance of Canada (772).

Conflict of Interests Statement

The authors of this manuscript have no conflicts of interest to declare in association with research presented in this article.

4.7 Appendix

4.7.1 Seasonal Observed and Predicted Lapse Rate Patterns

Seasonal lapse rate patterns mirror the annual results (Section 4.4.2) but are more pronounced in the winter and weaker in the later summer and early autumn. In January, observed temperatures are much colder than the GlobSim T_{pl} metric at all elevations, particularly below the reanalysis grid elevation where lapse rates remain the standard lapse rate (Figure 4-10). $T_{\mathrm{mod\ DMP}}$ successfully reproduces the observed SBI structure, reducing the warm bias and producing an aggregated lapse rate between 15.8 and 9.6 °C km^{-1}, more consistent with the observed temperatures than the T_{pl} metrics are.

In September, when inversions are least frequent (Section 4.4.5), both the observed and modelled temperatures follow a near linear decrease in temperature with elevation (Figure 4-11). The T_{pl} lapse rate was -7.7 to -6.7 °C km^{-1}, while the $T_{\mathrm{mod\ DMP}}$ ranged -5.6 to -4.6 °C km^{-1}. Observations showed a similar near linear surface lapse rate (-6.6 °C km^{-1}, R^2 = 0.98) in WS02 but were slightly less linear in WS01 (-5.1 °C km^{-1}, R^2 = 0.86), where low elevation sites remained colder than expected. Interestingly, the September bias reverses: T_{pl} shows a weak cold bias, $T_{\mathrm{mod\ DMP}}$ a weak warm bias, and the observed monthly average temperatures fall between them at mid and upper elevations. At the lowest elevations the T_{obs} most closely are represented by GlobSim T_{pl}.

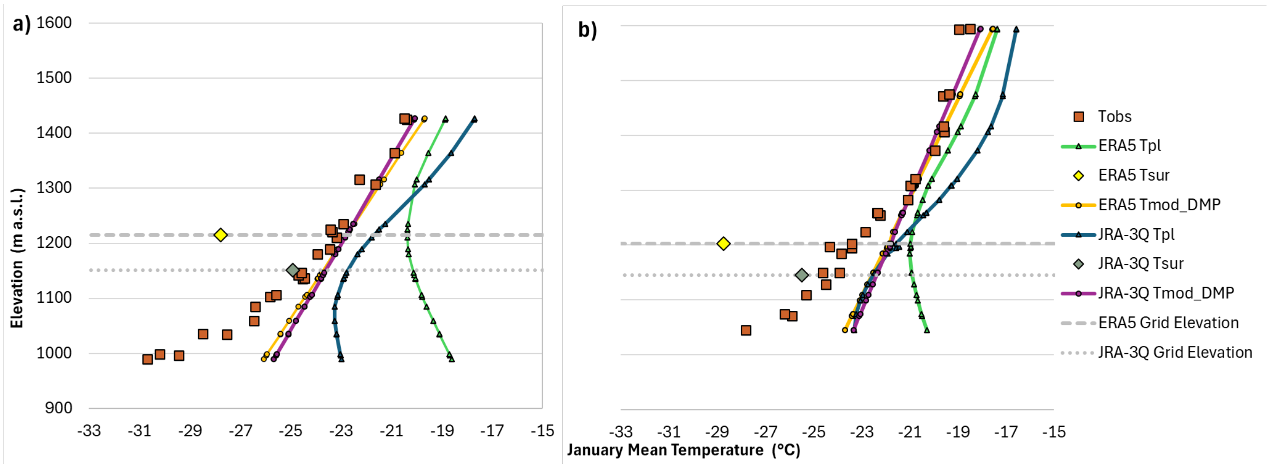

Figure 4-10: The elevational temperature profile for the observed and predicted mean January air temperature at each site in (a) WS01 study area and (b) WS02 study area. The observed and predicted temperatures are based on a subset of the study period data that spans January 2024.

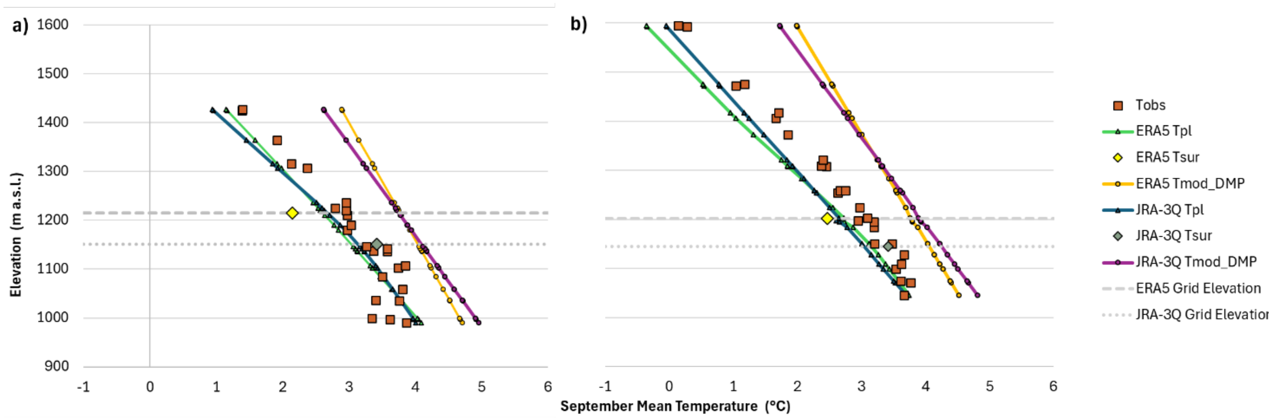

Figure 4-11: The elevational temperature profile for the observed and predicted mean September air temperature at each site in (a) WS01 study area and (b) WS02 study area. The observed and predicted temperatures are based on a subset of the study period data that spans September 2023.

4.7.2 Reanalysis prediction of observed shallow SBIs

When examining shallow SBIs, those confined within 150 m above the valley floor, miss rates increased substantially reaching approximately 35% in summer (Figure 4-12). This reduced summertime accuracy by roughly 20-30%. As with the valley-scale SBIs, shallow SBIs were better represented in winter, with accuracy constantly above 80% and false alarms generally below 25%.

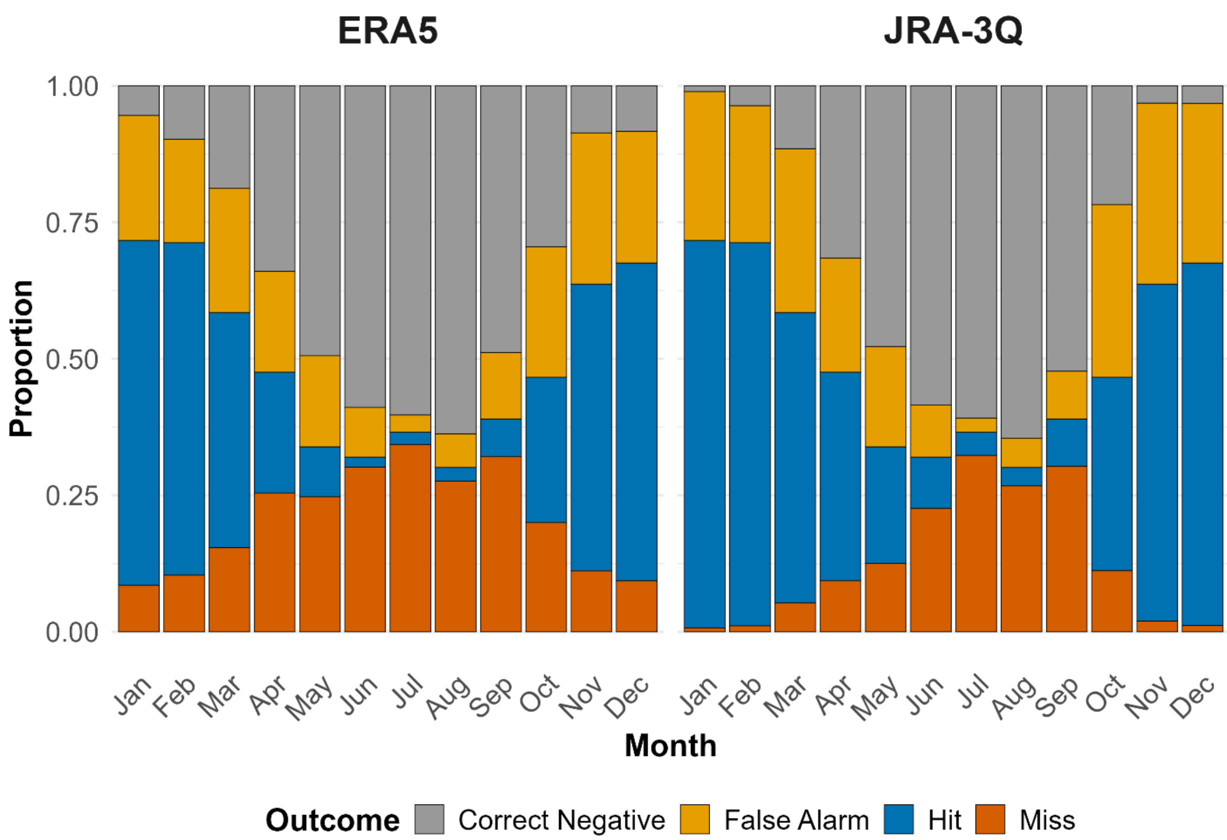

Figure 4-12: The count of all readings summed up between both study areas (WS01 and WS02) for the ERA5 and JRA-3Q reanalysis products where an observed SBI was flagged by the reanalysis product (Hit, blue), an observed SBI was missed by the reanalysis products (Miss, orange), no inversion was observed but was flagged by the reanalysis (False Alarm, yellow), and where there was no observed shallow SBI (<150 m deep) or one flagged in the reanalysis (Correct Negative, grey) for August 2017-August 2024.

4.7.3 Windows of Time and Accuracy of SBI Representation by Reanalysis Products

To test the sensitivity to temporal misalignment between observed and reanalysis SBIs, inversion detection skill was recomputed using aggregated windows ranging from 2 to 24 hours. Some modest improvements in the hit rate and accuracy occur at longer windows, but overall they remain relatively stable indicating that phase errors did not dominate reanalysis performance in predicting SBIs (Figure 4-13).

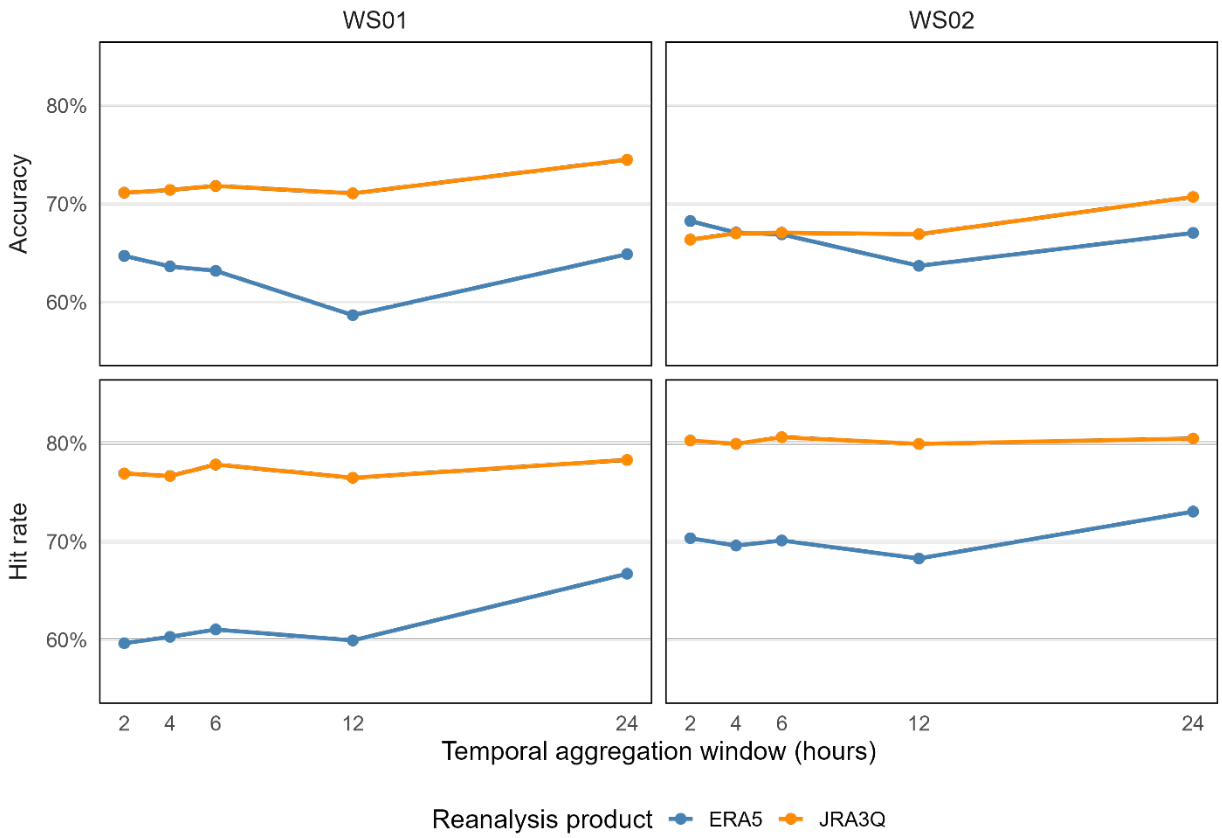

Figure 4-13: Sensitivity of reanalysis skill in predicting SBIs to temporal aggregation window length. Overall accuracy and hit rate for ERA5 and JRA-3Q are shown as a function of aggregation window (2–24 hours) for each valley, based on dynamically diagnosed observed inversions.

4.7.4 The Influence of Temporal Bias Correction on Inversion Correction Model Performance

The full inversion correction model substantially reduces absolute bias, by to 0.56-1.26 °C beyond the GlobSim T_{sur} and T_{pl} products even after the temporal bias correction $\beta(t)$ (Eq. 6) is applied (Table 4-6). This shows that the model still adds predictive value beyond simply correcting the reanalysis data for temporal bias. In most cases, this supports the interpretation that the elevation-dependent term $\alpha(z)$ (Eq. 5) provides additional explanatory power by adjusting for terrain-controlled inversion structure.

The only exception occurs for the T_{pl} metric in WS02, where the full inversion correction model increases absolute error relative to the $\beta(t)$ corrected GlobSim outputs. However, despite the increase in MAE, the model still reduces absolute MBE, moving the mean error closer to 0 °C. This indicates that while the full model better captures the average temperature over time, the day-to-day spread of errors widens.

Table 4-6: The difference in absolute error (dMAE) and absolute reduction in bias (d|MBE|) for the full inversion correction model relative to the GlobSim T_{sur} and T_{pl} metrics with the temporal bias ($\beta(t)$) applied. Positive numbers indicate a decrease in absolute error or a bias that is closer to 0 °C.

Valley	Product	dMAE_T_{sur}	d|MBE_T_{sur}|	dMAE_T_{pl}	d|MBE_T_{pl}|
WS01	ERA5	0.32	0.7	1.26	2.43
	JRA3Q	0.18	0.41	0.26	0.11
WS02	ERA5	0.56	0.93	-0.23	1.84
	JRA3Q	0.26	0.21	-0.19	0.11

Seasonal pattern in the residuals (Figure 4-14) further highlights how the temporal bias correction interacts with the full inversion model. In WS01, both $T_{\mathrm{sur\ beta}}$ and $T_{\mathrm{mod\ DMP}}$ show weak seasonal bias, with mean residuals that are nearly flat across the year. $T_{\mathrm{sur\ beta}}$ is the most stable indicating that the seasonal correction term $\beta(t)$ is especially effective for this study area. In contrast, $T_{\mathrm{pl\ beta}}$ shows stronger seasonality of residuals, with strong winter cold biases (at time > 5 °C) and weak summer cold biases (typically less than 2 °C). This suggests that temporal bias correction is less effective for $T_{\mathrm{pl\ beta}}$, likely because it is lapse rate driven and carries structural errors that $\beta(t)$ alone cannot explain.

In WS02, the $T_{\mathrm{sur\ beta}}$ retains a clearer seasonal structure than in WS01 indicating a reduction of the effectiveness of $\beta(t)$ in this study area. Meanwhile, $T_{\mathrm{mod\ DMP}}$ constantly exhibits the smallest seasonal cycles suggesting that the full inversion correction model successfully removes systematic seasonal bias, reflecting the reduction in absolute MBE towards 0 °C.

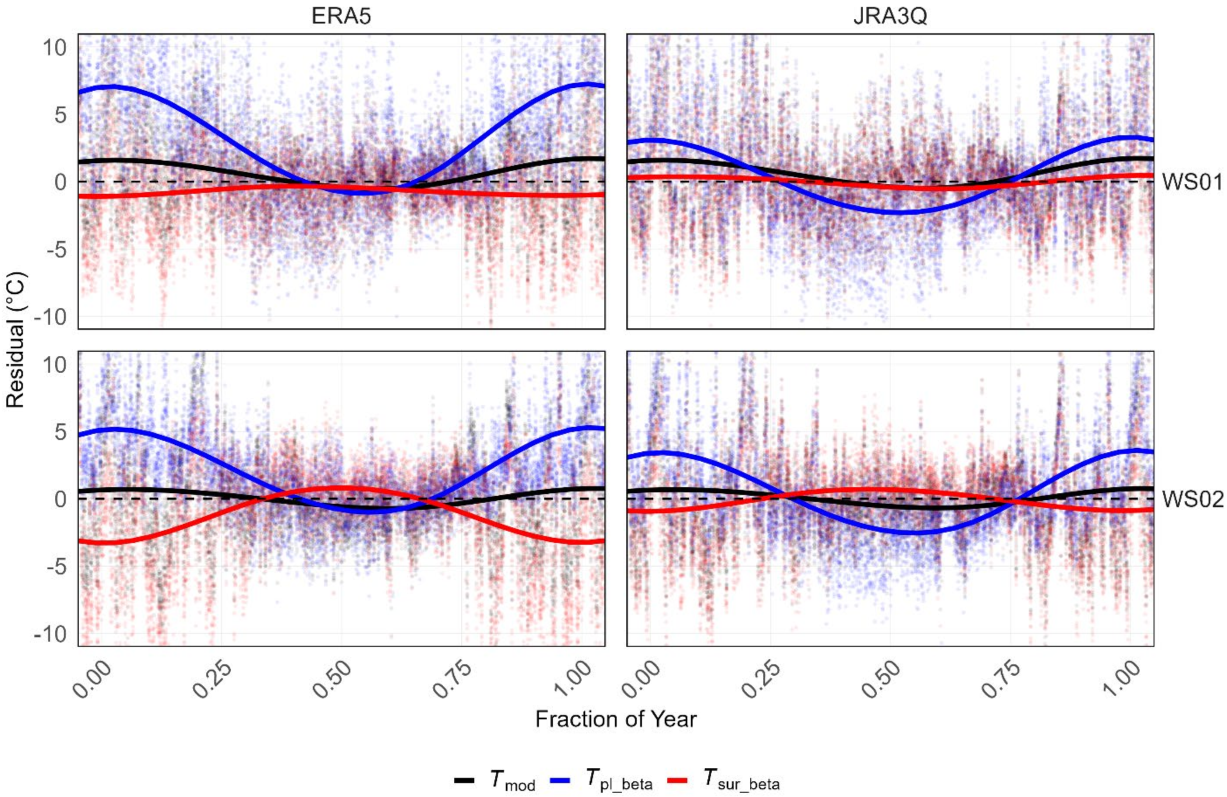

Figure 4-14: Seasonal residuals of valley temperatures comparing the full model ($T_{\text{mod DMP}}$) and bias-corrected GlobSim estimates $T_{\text{pl beta}}$, $T_{\text{sur beta}}$) relative to observed temperatures (T_{obs}). Residuals are plotted as a fraction of the year. GAM smoothers (with a periodic boundary condition imposed) highlight the seasonal bias patterns. Residuals are zoomed to ±10 °C to emphasize the main seasonal variations.

4.7.5 Inversion strength threshold for calculation

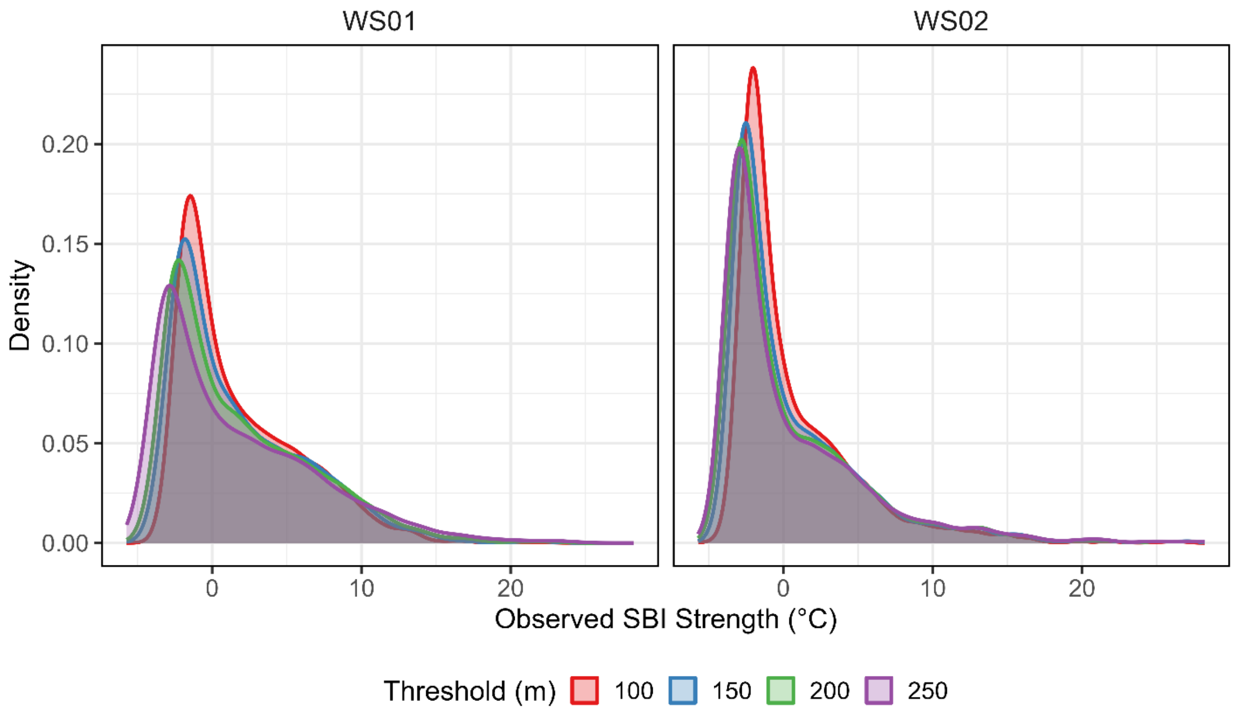

Figure 4-15: Density plots of SBI strength calculated using high-elevation site thresholds of 100, 150, 200, and 250 m above the valley floor. Results show only marginal sensitivity to the choice of elevation threshold, indicating that SBI strength is robust to reasonable variations in the height used to define "high-elevation" sites.

5. DReaMIT: A Dynamical Reanalysis Framework for Modelling Surface-Based Temperature Inversions in Cold Environments

Pozsgay, V., Noad, N. C., Bonnaventure, P., & Gruber, S. (2026). DReaMIT: A dynamical reanalysis framework for modelling surface-based temperature inversions in cold environments. *Geoscientific Model Development, 19*, 7197–7215. https://doi.org/10.5194/gmd-19-7197-2026

Authors: Victor Pozsgay[2], Nick C. Noad[1], Philip P. Bonnaventure[1], & Stephan Gruber[2]

[1]Department of Geography and Environment, University of Lethbridge, Lethbridge, AB, T1K3M4, Canada

[2]Department of Geography and Environmental Studies, Carleton University, 1125 Colonel By Drive, Ottawa, K1S5B6, Ontario, Canada

Key words: Downscaled climate reanalysis data, systematic bias, surface-based temperature inversions, subarctic valleys, GlobSim

5.0 Abstract

Surface-based temperature inversions (SBIs) are critical to high-latitude mountain climatology, shaping permafrost stability and near-surface thermal regimes. This study develops and evaluates a new surface-based inversion model, DReaMIT (Dynamical Reanalysis Model for Inversions of Temperature), that extends the framework of (Pozsgay and Gruber, 2025) by spatializing the inversion strength parameter (α) using hypsometric position rather than absolute elevation. The reformulated approach enables a unified calibration across two contrasting Yukon valleys (WS01 and WS02), improving model transferability and reducing site-specific bias. Exponentiation of the elevation variable captures the observed nonlinear decay of lapse rates within SBIs, consistent with in-valley observations where temperature increases of up to 8 °C over 19 m were recorded. Model performance was assessed across the Yukon and Northwest Territories, where it successfully reproduced inversion structure even in areas with weaker or transient SBIs, such as Whitehorse and Haines Junction. Limitations were observed in flat regions with minimal hypsometric relief (e.g., Tulita, Old Crow), highlighting cases where microtopographic indices may better represent cold-air pooling potential. The new hypsometric formulation enhances the physical realism and spatial applicability of SBI modelling, providing an empirically constrained, transferable tool for predicting near-surface temperature regimes and assessing permafrost sensitivity under northern climate change.

5.1 Introduction

Observational climate data are sparse and discontinuous in high-latitude (Urban et al., 2013; Way and Bonnaventure, 2015) and alpine regions (Oyler et al., 2015; Pepin et al., 2022). In contrast, climate reanalysis products provide spatially and temporally consistent datasets that extend back more than 75 years, since 1940 for ERA5 (Hersbach et al., 2020) and 1948 for JRA-3Q (Kosaka et al., 2024). These datasets are improving through updates to their modelling and forecasting systems, resulting in comprehensive coverage of surface and atmospheric conditions at multiple pressure levels. Consequently, reanalysis products are a valuable resource in areas that have sparse observational data and are used to inform modelling, such as predictions of permafrost (e.g., Liu et al., 2025; Obu et al., 2019; Tao et al., 2019; Fiddes et al., 2015) and hydrological (e.g., Nkiaka et al., 2017; Tarek et al., 2020).

However, the coarse spatial resolution of reanalysis products (tens of kilometers) limits their applicability in mountainous terrain, where complex topography can produce climate variations comparable to those observed across thousands of kilometers in latitude (Riseborough et al., 2008). This sub-grid heterogeneity, and the local processes it drives, are not captured by coarse-resolution (Etzelmüller, 2013).

To address this limitation, a variety of downscaling methods have been developed to scale coarse-resolution climate reanalysis data to finer resolutions or scale-free point locations (e.g., Draeger et al., 2024; Ntagkounakis et al., 2023; Wang et al., 2016; Zhang et al., 2020). Among these, TopoSCALE (Fiddes and Gruber, 2014) and TopoCLIM (Fiddes et al., 2022) use topography-based parameterizations to reproduce small-scale variability, while GlobSim (Cao et al., 2019) extends these methods by integrating multiple reanalysis datasets to generate meteorological time series for specific sites. These models have been shown to effectively predict weather conditions with limited bias; however, residual errors remain in regions where complex local processes are not resolved in the reanalysis model (Daly et al., 2008; Roberts et al., 2019). Furthermore, reanalysis data can have regional or temporal trends in bias, especially given that they are less reliable for earlier periods (Urraca and Gobron, 2023).

To reduce these biases, Pozsgay and Gruber (2025) developed a model that explicitly accounts for the influence of surface-based temperature inversions (SBIs) on near-surface air temperature and that includes a temporal bias correction parameter. This model dynamically corrects downscaled reanalysis data at hourly time steps. This is done by incorporating a conceptual framework introduced by Noad et al. (2023), which defines SBI magnitude as the strength of an SBI (temperature increase from the bottom to the top of the SBI) added to the expected surface air temperature if the lapse rate above the SBI layer were to continue to the surface.

This approach addresses a key limitation in downscaling methods, an assumption that the lapse rates are normal below reanalysis grid elevation, disregarding intense SBIs at these low elevations. In subarctic valleys, prolonged periods of nocturnal radiative cooling during the winter promote deep, intense, and long-lasting SBI events (Fochesatto et al., 2015; Mayfield and Fochesatto, 2013; Noad and Bonnaventure, 2022, 2023). These SBIs generate strongly positive mean annual lapse rates (upwards to 25 °C km^{-1}) within the first 100 to 150 m above the valley floor (Noad and Bonnaventure, 2025), leading to substantial biases when unresolved below the grid level of the reanalysis product. Initial testing of the Pozsgay and Gruber (2025) model using a dense network of air temperature sensors across two subarctic valleys demonstrated that the model performs well when calibrated locally (Noad et al., *Submitted*), but suffers from a lack of transferability. In this study, we aim to enhance the generalizability of the Pozsgay and Gruber

(2025) inversion correction model by testing new parameters beyond the original use of absolute elevation. Specifically, we evaluate additional topographic variables (e.g., relative elevation and hypsometry) to better represent the influence of local terrain on cold-air pooling and SBI dynamics. By calibrating these parameters across multiple valleys and testing them at other locations in northwestern Canada, we will identify the optimal parameters and functional form of the model to increase prediction performance regionally, without requiring additional local calibration. This work contributes to the improved use of reanalysis in their ability to represent sub-grid processes in complex terrain. The resulting model parameterization will increase their reliability for important applications such as permafrost or hydrological modelling.

5.2 Study Area

5.2.1 Dempster

The study area of this paper consists of two northcentral Yukon valleys, approximately 100 km to the north-east of Dawson City, around Distincta Peak (1790 m a.s.l.), the dominant point in the subrange of mountains. These valleys will be referred to as WS01 and WS02 (for weather station 1 and 2), and correspond to valleys labelled as SVWS and NVWS, respectively, in Noad and Bonnaventure (2022). Those sites are easily accessible by road, being located in the immediate vicinity of the Dempster Highway. They were shown to be prone to intense, frequent, and long-lasting inversion events (Noad and Bonnaventure, 2022, 2026).

The two valley floors are separated by approximately 8 km, with WS01 to the south of Distincta Peak, and WS02 to the north. The former is an approximately 5.5 km-long V-shaped valley, with elevations ranging from 950 m at the outlet and 1700 m on the closest highest ridge. The latter is an approximately 6.5 km-long U-shaped valley, with elevations comprised between

1040 and 1790 m. The valleys' outlet is oriented towards the southeast for WS01, and to the north for WS02.

The network of air temperature loggers consists of 24 locations in valley WS01, and 26 in WS02. The locations are chosen to sample the widest range of elevation, slope, aspect angle, and degree of valleyness (Cao et al., 2017).

5.2.2 Dawson

The model calibration of this paper will be tested on the dataset presented in Pozsgay and Gruber (2025), where five weather stations are distributed within a 25 km radius from the Dawson airport, and with elevations ranging from 370 to 1200 m.

5.2.3 ECCC/NAVCAN Weather Stations

Finally, the temperature inversion model will also be applied to various sites across northern Canada, in the Yukon and North-west Territories. We selected 13 ECCC/NAVCAN weather stations (Figure 5-1, see Table 5-3 for coordinates) because they span a wide spatial area and a variety of topographic conditions, from river delta to mountainous terrain.

Then, we report the distribution of elevations in a radius of 50 km around each station in Figure 5-2, together with all sites from the Dempster and Dawson areas.

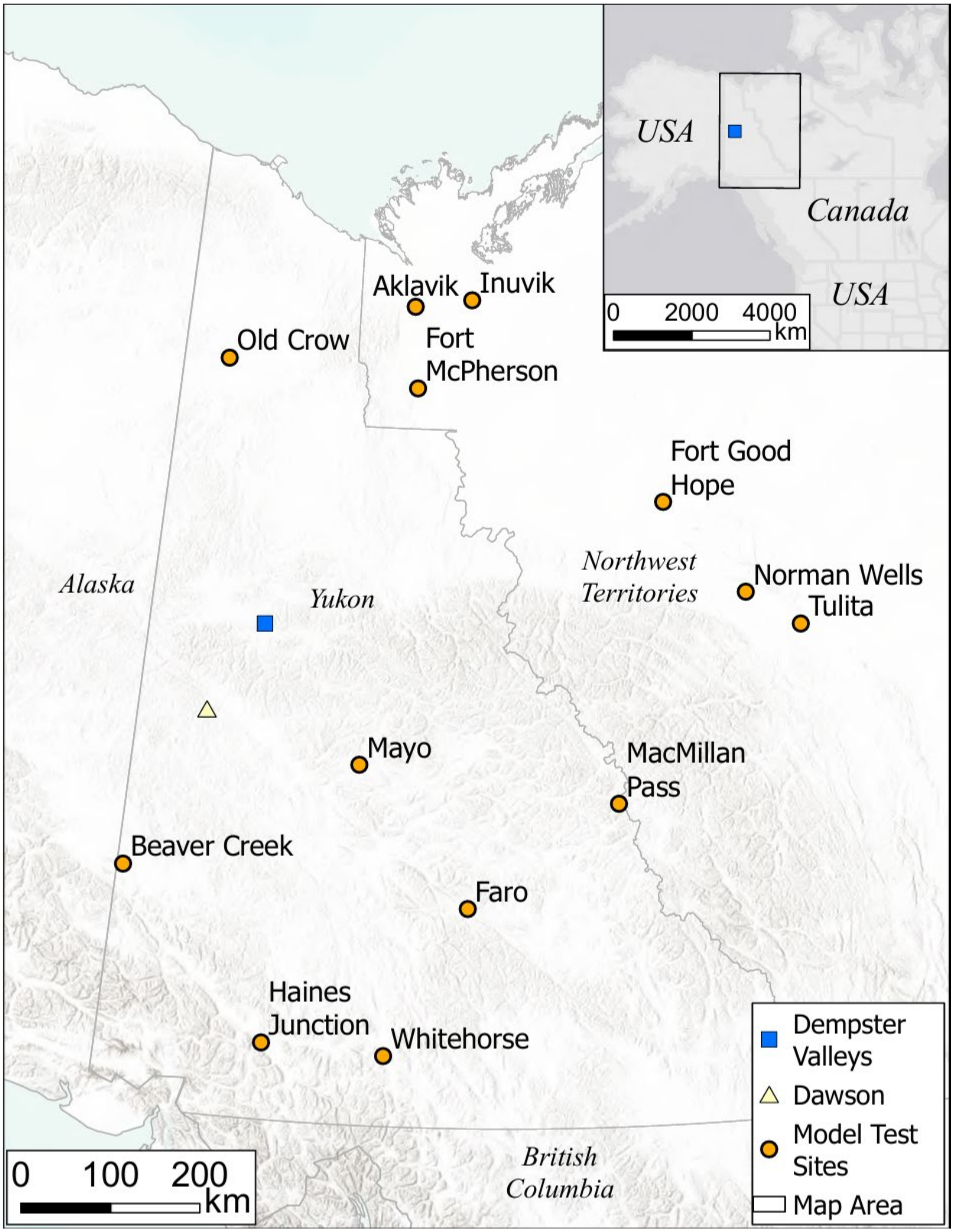

Figure 5-1. The Dempster study valleys (blue point), Dawson City (yellow point), and 13 Environment Climate Change Canada (ECCC) and Navigation Canada (NAVCAN) weather station locations (orange points) situated across Yukon and Northwest Territories.

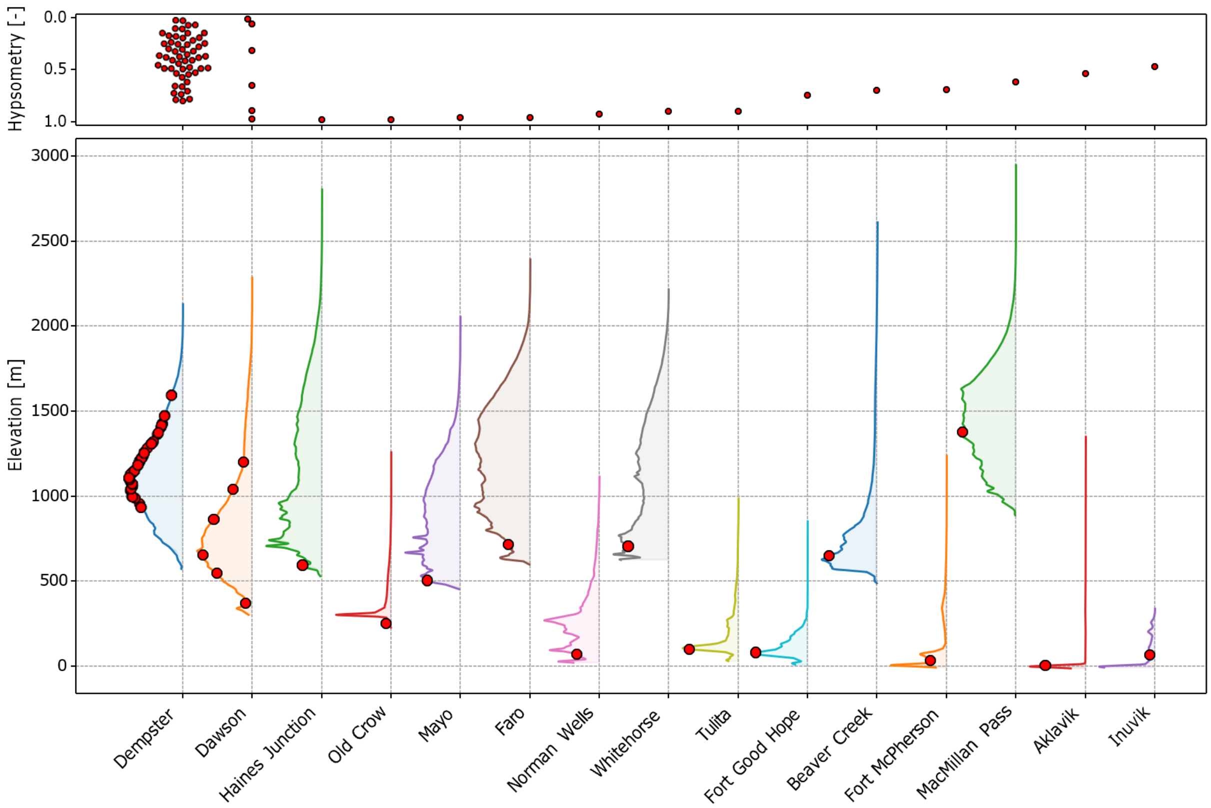

Figure 5-2. Local elevation distribution around each station from the study area (Dempster), the first testing area (Dawson), and the second testing area, made of 13 ECCC/NAVCAN weather stations (ranging from Haines Junction to Inuvik, sorted by decreasing hypsometry). The elevation and hypsometry of each station are indicated by a red dot.

5.3 Methods

5.3.1 In-situ Observations

The 50 locations scattered across the two valleys of the study area are instrumented with passively-ventilated air temperature loggers. Air temperature data was retrieved at the end of the 2024 summer during fieldwork.

Observational data for the Dawson area is taken from Pozsgay and Gruber (2025) and was originally provided by the Yukon Geological Survey. Finally, the air temperature data for the Dawson airport and for the 10 locations described in Table 5-3 is managed by Environment and

Climate Change Canada (ECCC) and is downloaded with the R-package weathercan (LaZerte and Albers, 2018).

5.3.2 Reanalysis Data

Reanalysis data are extend back globally for several decades. They are consistent and gapless in both time and space, allowing researchers to study uninstrumented areas or to provide additional data where observations might be available. In this study, we use hourly ERA5 data from the European Centre for Medium-Range Weather Forecasts (ECMWF) (Hersbach et al., 2023a, b) since 1940 and 6-hourly JRA-3Q data from the Japan Meteorological Agency (JMA) (Kosaka et al., 2024) (downscaled hourly) since 1947. The former is available on a regular 0.25 ° by 0.25 ° grid in latitude and longitude, while the latter uses a TL479 Gaussian grid instead with a spatial resolution of 0.375 ° by 0.375 °. We downloaded data divided into three categories: constant (geopotential, land-sea mask), single level (2 m temperature), and pressure levels (air temperature).

Note that at the latitude of the study area, the reanalysis grid cell approximately corresponds to a 46 km by 20 km cell for ERA5, and 59 km by 30 km for JRA-3Q. We downscale all reanalysis products to the stations' locations and elevations while accounting for local topography using GlobSim. Furthermore, we acquire pressure-level air temperature T_{pl} for a full column above each valley from the highest station upwards, at each available pressure level. For both products, we also interpolate single-level 2 m surface temperature T_{sur}. This is now automated with the addition of the new DReaMIT module into GlobSim.

5.3.3 Temperature Inversion Model

5.3.3.1 Basic Structure

Pozsgay and Gruber (2025) demonstrated that downscaled reanalysis data, both single-level surface temperature T_{sur} and pressure-level temperature T_{pl}, fail to capture the full vertical profile of surface-based inversions. T_{pl} generally performs better at approximating the observed temperature than T_{sur} at higher elevation, while the use of T_{sur} is preferable at lower elevation, in agreement with the previous comment about the lack of reliability of pressure level reanalysis data below grid level.

To bridge the gap between the two reanalysis variables and their non-intersecting domains of reliability, a dynamic model of temperature inversions was proposed in Pozsgay and Gruber (2025). This model was calibrated for sites in the vicinity of Dawson City, Yukon, Canada, an area subject to strong temperature inversions. The model was shown to predict air temperature better than either T_{pl} or T_{sur}, for virtually any combination of elevation, time, and reanalysis product.

Thanks to the full hourly-downscaled vertical profile of air temperatures above each valley, the upper-troposphere lapse rate is computed and updated hourly. The linear relation can be extrapolated to the grid level and the station's elevation, where we define $T_{lapse\ grid}$ and $T_{lapse\ station}$, respectively. The difference between the surface temperature given by reanalysis and the would-be temperature without any inversions at the grid level is given by $DT = T_{sur} - T_{lapse\ grid}$. The equivalent definition at the station's elevation reads $DT_{station} = T_{obs} - T_{lapse\ station}$, which corresponds to the SBI_{mag} metric from Noad et al. (2023). The former model simply states that the inversion's strength α is a linear function of the elevation z,

$$DT_{Station} = \alpha(z) \cdot DT + \beta(t) \quad \text{(Eq. 5-1)}$$

where the function β is a pure temporal regional reanalysis bias, and only depends on the reanalysis product, the study area, and the seasonality, not on the elevation. Note that the temporality of the inversion strength is fully characterized by the temporality of *DT*, a derivative of reanalysis variables.

5.3.3.2 Hypsometry

This manuscript aims to find a parameterization for the inversion model that is more general than the one proposed in Pozsgay and Gruber (2025). There, temperature inversions are successfully modelled, but the number of weather stations are limited, and local calibration cannot be spatialized. Indeed, the calibration used for Dawson City is not suitable for this study area (Noad et al., *Submitted*). The main reason is that cold-air pooling is not driven by absolute elevation (even though highly correlated), but rather relative elevation compared to the surrounding topography.

A simple first step would be to explore the same model but to replace absolute with relative elevation. However, a number of questions remain. First, of all, the notion of lowest point itself is ambiguous, as it depends on the radius around the station. Then, both a valley bottom and a point in the middle of a flat tundra will receive the same null relative elevation, even though the temperature inversion dynamics differ vastly between these two cases. Furthermore, such a definition does not provide any information on higher elevations. Two points can share a similar relative elevation but be close to the bottom of a steep, narrow, and deep valley on the one hand, or be on a gentle ridge on the other hand. Once again, one does not expect these two configurations to lead to similar inversion dynamics.

Thus, a suitable and generic model of temperature inversions should rely on a variable transformation of the elevation that accounts for neighbouring topographic conditions. For the rest of this paper, we will explore the use of the hypsometric position *h* of a point within a given surrounding area, in the same fashion as Cao et al. (2017). This new variable will be bounded between 0 and 1 for the highest and lowest points in the area, respectively.

The calculation of *h* requires a digital elevation model (DEM). We download the Arctic DEM data (mosaics) for a radius of at least 50 km around every point in the study area (Porter et al., 2023). This dataset is available at a 2 m resolution, but we choose to work with one of 10 m as we are not interested in microtopography, but relative cell elevation compared to other cells in a large radius. We study the influence of selecting smaller areas in Section 5.7.1, where we motivate the choice of an ideal radius based on empirical optimization. Next, for each point with coordinates $\boldsymbol{x}_0$, the hypsometry is computed by looking at all cells c (coordinates $\boldsymbol{c}$) within a radius d (we will take $d = 50$ km), and corresponds to the fraction of points with higher elevation within that area,

$$h(x_0) = \frac{\sum \theta(d-|c-x_0|)\theta(z_c-Z_0)}{\sum \theta(d-|c-x_0|)} \qquad \text{(Eq. 5-2)}$$

where θ is the Heaviside step function. In particular, $\theta(d-|c-x_0|)$ selects DEM cells within the predefined area, and $\theta(z_c-z_0)$ further selects the ones with elevation z_c higher than the center point elevation z_0. We study the influence of applying a 2*d* Gaussian weight with varying standard deviation (between 1 and 30 km) in section 5.7.1. With the definition of the hypsometric position given by Eq. (2), we have $h \in [0, 1]$, and

$$h = \begin{cases} 0 & \text{on top of the highest summit} \\ 1 & \text{at the bottom of the lowest valley} \end{cases} \qquad \text{(Eq. 5-3)}$$

The model proposed in this study substitutes the elevation z for the dimensionless and bounded hypsometric position h used in Cao et al. (2017). There, it was used in combination with the multiresolution valley bottom flatness (MRVBF) index υ (Gallant and Dowling, 2003), but we discard it here as we will find it to be superfluous in our analysis. The hypsometric model then takes the form

$$T_{hyps}(h,t) = T_{lapse\,station} + \alpha_{exp}(h) \cdot DT + \beta(t) \qquad \text{(Eq. 5-4)}$$

with

$$\alpha_{exp}(h) = \alpha_{intercept} + (\exp(\alpha_{slope} \cdot h) - 1) \qquad \text{(Eq. 5-5)}$$

$$\beta(t) = \beta_{amplitude} \cdot \cos(2\pi(t - t_*)) + \beta_{bias} \qquad \text{(Eq. 5-6)}$$

where t stands for the yearly time fraction. The wide regional reanalysis air temperature bias is independent of topography and seasonally variable, hence it is described by the sinusoidal function $\beta(t)$. Note that we modify the linear α into an exponential function (which remains bounded since h itself is bounded within [0, 1]). For small values of hypsometric position ($h <<$ 1), we recover the same linear α as the one of Pozsgay and Gruber (2025) to first order, since $\alpha_{\mathrm{exp}}(h) = \alpha_{\mathrm{slope}} \cdot h + \alpha_{\mathrm{intercept}} + O(h^2)$. The exponential correction only affects hypsometric values closer to 1, corresponding to points located in lower terrain, where inversions are most intense (Noad and Bonnaventure, 2026). The flowchart of the model is presented in Figure 5-3. In practical application, DReaMIT requires only two inputs: (1) a digital elevation model to compute hypsometric position, and (2) reanalysis air temperatures for the neighbouring grid cells. Once calibrated, the model produces spatially-continuous hourly temperature fields across complex terrain, enabling inversion-driven corrections even at sites lacking station data, provided surrounding terrain shows meaningful valley-ridge relief.

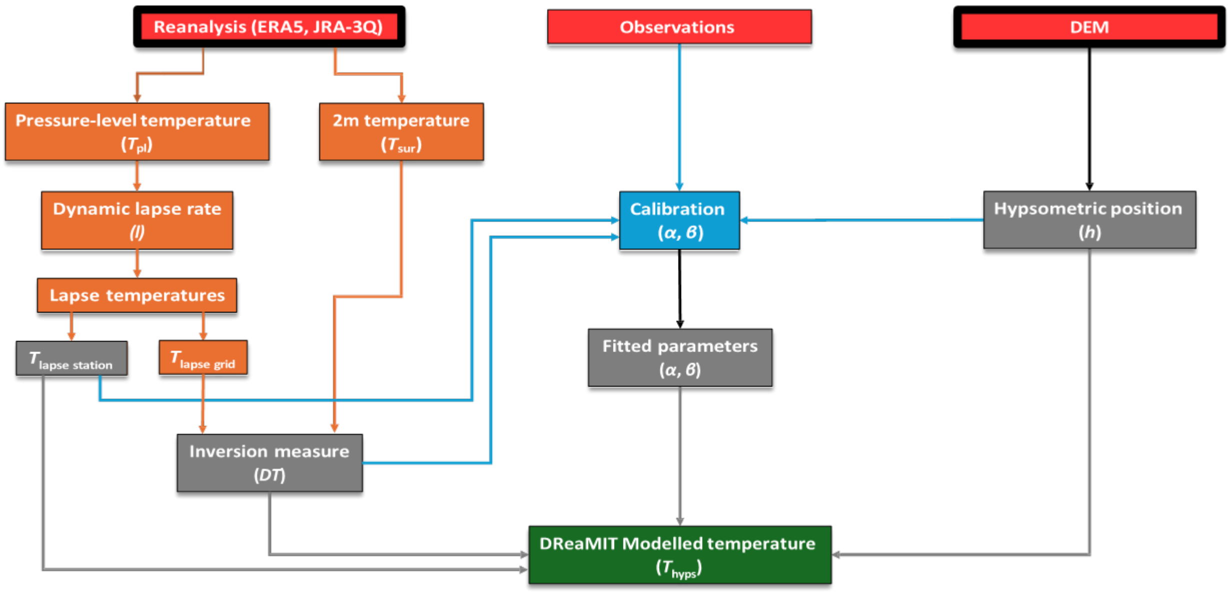

Figure 5-3. Flowchart of the DReaMIT hypsometric model. The input data for this study appear on the first row in red, the intermediate reanalysis steps in orange, the direct model input in grey, and the model output in green. The calibration performed in this study is shown in blue. For future cases when calibration is no longer needed, the user will only need to provide the data corresponding to cells with a thick black outline.

5.3.3.3 Calibration

The main advantage of a model based on hypsometric position, such as the one given in Equation 5-4, is its range of applicability. Here, we no longer need to calibrate the model for each area, or even each valley; instead, we will calibrate it for both valleys of the study area at once (but independently for each reanalysis).

The data used to calibrate the model is selected to cover the widest temporal and elevational range. For each selected time all stations with a valid record contribute to the calibration dataset. We select the maximum period for which all stations are operational, corresponding to a full year (minus 2 weeks in August, which does not bias the calibration since virtually no inversions are recorded then), and keep data at a 2 h frequency. Details can be found in Table 5-1. However, we will nevertheless assign a more important weight to the existing

August datapoints so that each month is equally represented. Moreover, we also account for the non-uniform distribution of the hypsometric positions h in the interval [0, 1] by assigning a weight to each station from Gaussian kernel density estimation (KDE). We will then perform a least-square optimization procedure to find the best model parameters for the calibration dataset. Finally, we will apply the model to the full dataset and evaluate its performance.

Table 5-1. Subset of the observation dataset used for model calibration. The full dataset extends over multiple years for some stations, but we choose to keep a one-year window where all stations were recording for the calibration, roughly corresponding to a third of the dataset.

	WS01	WS02
Start (UTC)	2023-08-23 19:00	2023-08-24 19:00
End (UTC)	2024-08-09 15:00	2024-08-04 01:00
Frequency	2 h	2 h
Data used for calibration	36 %	37 %

A least-square optimization is performed for all parameters of the model found in Equation 5-4, on the calibration subset defined in Table 5-1. The calibration results can be found in Table 5-2.

Table 5-2. Best fit parameters (and their relative uncertainties in parentheses) for the calibration of the model given by Eq. (5-4). The model is also fitted in the absence of the reanalysis bias correction term $\beta(t)$.

		With $\beta(t)$				Without $\beta(t)$			
Parameter	Unit	ERA5		JRA-3Q		ERA5		JRA-3Q	
α_{slope}		0.732	(0.2 %)	0.753	(0.3 %)	0.728	(0.2 %)	0.752	(0.3 %)
$\alpha_{intercept}$		0.449	(0.4 %)	0.525	(0.4 %)	0.352	(0.3 %)	0.478	(0.3 %)
$\beta_{amplitude}$	°C	0.918	(1.7 %)	0.796	(2.1 %)	–		–	
t_*		0.958	(0.2 %)	0.945	(0.3 %)	–		–	
β_{bias}	°C	1.181	(1.0 %)	0.229	(4.9 %)	–		–	

5.3.3.4 Mean Alpha

To demonstrate the advantage of using hypsometric position h over (relative) elevation, we will focus on the main quantity of the model, α, i.e. the factor quantifying the strength of inversion. This factor is purely time-independent, as opposed to all other quantities in the inversion model. In order to visualize the observed α as a function of (relative) elevation, and then of hypsometry, let us start by noting that Equation 5-4 can be rewritten in the following form,

$$\alpha = \frac{DT_{station} - \beta}{DT} \quad \text{(Eq. 5-7)}$$

for every datapoint used for the model calibration. It is more meaningful to average this formula over time to obtain a mean observed factor. The calibration dataset is distributed uniformly over a 1-year span (aside from a small gap that was accounted for in the calculations but omitted here for the sake of the argument), and hence the temporal average corresponds to a yearly mean. Let us denote the yearly mean of a quantity Q with $\bar{Q}$,

$$\alpha_{\text{observed}} = \frac{\overline{DT_{\text{station}}} - \bar{\beta}}{\bar{DT}} \qquad \text{(Eq. 5-8)}$$

and note that, because of the oscillatory nature of the reanalysis bias $\beta(t)$, we have $\bar{\beta} = \beta_{\text{bias}}$, whose value is updated and fitted separately for each case.

5.4 Results

5.4.1 Fitted Parameters

The relationship between hypsometric position and elevation depends on the area from which the hypsometric position is calculated, and the chosen weighting scheme. We find that the best fit is obtained when no weighting is performed (Section 5.7.1), which simplifies the approach.

We calibrate the model from Eq. 5-4 and Eq. 5-5 with a subset of the full dataset (see Table 5-1), where a least-squared fitting method is applied. The input data needed to calibrate the model are the hypsometric position on one side, which is calculated from a DEM, and reanalysis data on the other side (we use both ERA5 and JRA-3Q). The best fit parameters and their uncertainty are reported in Table 5-2. Note that we also fit the model in the absence of the reanalysis bias correction term $\beta(t)$. This reduces the model performances but increases its versatility and applicability in certain cases presented in the Discussion (Section 5.5.5).

The temperature inversion model REDCAPP (Cao et al., 2017) makes explicit use of both hypsometric position h and MRVBF index v. We find that the Akaike and Bayesian information criteria (AIC and BIC, respectively) do not improve when explicitly accounting for v in the model, which motivates the functional form adopted in Eq. (5-4), where the temperature inversions only depend on the hypsometric position h.

5.4.2 Comparing Different Models

We present a comparative analysis on the full northcentral Yukon valleys WS01 and WS02 dataset, which aims to put the performance of the new hypsometric model in context by comparing it to various other models in Figure 5-4. The first model ('Dawson') is the inversion model proposed in Pozsgay and Gruber (2025), with their calibrated parameters. The second row, labelled 'Absolute elevation', uses the same model but with parameters specifically calibrated for the combined WS01 and WS02 valleys. The third row uses relative elevation with respect to valley bottom instead of absolute elevation, and the final row is the hypsometric model of this study. The 'Dawson' model and parameters perform very poorly in this study area with a coefficient of correlation of 0.17 for ERA5 but even as low as −0.60 for JRA-3Q, confirming what was already known, i.e., it is a model that needs to be calibrated locally (Noad et al., *Submitted*), which is done in the second row with much better agreement (R^2 = 0.76 and 0.73 respectively). However, there is a clear distinction between the valleys, with values from WS01 above those of WS02. This is even more visible when looking at relative elevation, where the decoupling between the two valleys becomes so large that the model is clearly inappropriate. However, when turning to the more intricate variable transformation of elevation that hypsometry is (fourth column), we see that both valleys align, and a single model can now be applied confidently in different geographical locations. The correlation coefficient of the mean observed α over the full dataset with respect to the modelled α is equal to R^2 = 0.93 in the case of ERA5, and 0.87 for JRA-3Q.

Finally, we also perform single-valley calibration and demonstrate the stability of the results when applied to the other valley in Section 5.7.2. This constitutes a first step towards demonstrating the spatialization power of the model.

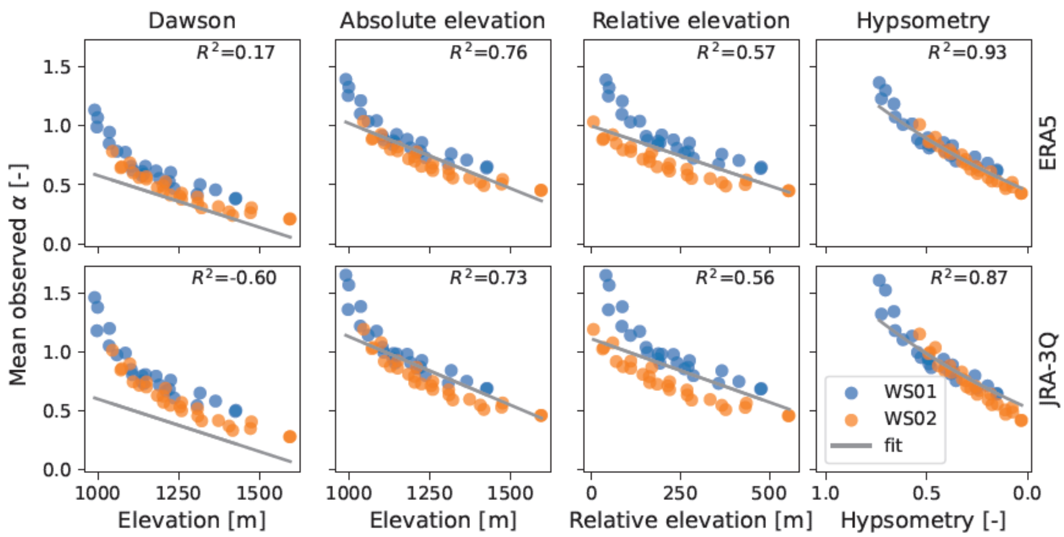

Figure 5-4: Mean observed and modelled values of the factor α (h) for various temperature inversion models and reanalyses.

5.4.3 Application to Other Sites

5.4.3.1 Dawson Area

To evaluate the performance of the hypsometric model Equation 5-4 outside the study area we make use of the weather data from the stations around Dawson City, Yukon, located more than 100 km away from the two Dempster Highway valleys where the hypsometric model is calibrated. For each of the five stations, we download reanalysis data, scale it to the point locations, compute the lapse rate of their respective air columns, and download the ArcticDEM locally to transform elevation information into hypsometric position *h*.

The results are shown in Figure 5-5 below (left panel), and in Section 5.7.3. For each station, we present the statistical metrics MAE and R^2 as a function of hypsometry, for the new hypsometric model, compared to the worst of the surface and pressure-level temperatures given from reanalysis data (downscaled using GlobSim (Cao et al., 2019)). We compare to the worst of T_{pl} and T_{sur} since we cannot know a priori which will be best (Pozsgay and Gruber, 2025). A more complete comparison is presented in Section 5.7.3. Note that we average results for

ERA5 and JRA-3Q and present a relative change rather than absolute metrics. Positive values indicate better predictions from the model compared to reanalysis. However, it is interesting to note that the hypsometric model (whose parameters are given in Table 5-2 and set once and for all) predicts air temperature more consistently than either surface or pressure-level reanalysis data. We recall the fact that the pressure-level reanalysis data performs best at higher elevation (low h, milder inversions) while the strong inversions at the valley bottom (low elevation, high h) are better represented by the surface temperature of the reanalysis data.

In the situation where the user wishes to apply the model to an area where the reanalysis bias could be different than the one from Table 5-2 (column with β) and where no weather stations are available to calibrate β, a good alternative is to use the model calibrated without the β term (column without β of Table 5-2). In this case, the results are slightly worse than with the β term (except for the low h stations), but continue to outperform the reanalysis products. Once again, when no reanalysis correction is applied for the model and T_{pl} and T_{sur}, results are negatively affected but maintain the same order of magnitude. The same conclusions apply.

5.4.3.2 Network of northern ECCC Stations

In this Section, we perform a similar analysis, but extend the testing further away, comparing the model results to the observations at 13 ECCC/NAVCAN weather stations across the Yukon and the Northwest Territories (NT). Results are reported on the right panel of Figure 5-5. The horizontal axis represents the hypsometry, modulated by the potential to drive temperature inversions. If we write dz the difference in elevation between the 90th and 10th percentiles in the area around each point location, then the hypsometric range is given by the product $h \cdot dz$.

For stations with lower hypsometric range, i.e., milder topography, the hypsometric model (with and without reanalysis bias correction) offers better predictions than the original reanalysis data. However, it has poorer performances for intermediate values of the hypsometric range, especially for Tulita, Old Crow, and Norman Wells. When the hypsometric range increases further, the best increase in reliability is observed, reaching a maximum at Beaver Creek with a 30 % and 57 % lowering of the MAE and $(1 - R^2)$, respectively. Particularly good performances are also observed at MacMillan Pass, Faro, and Haines Junction.

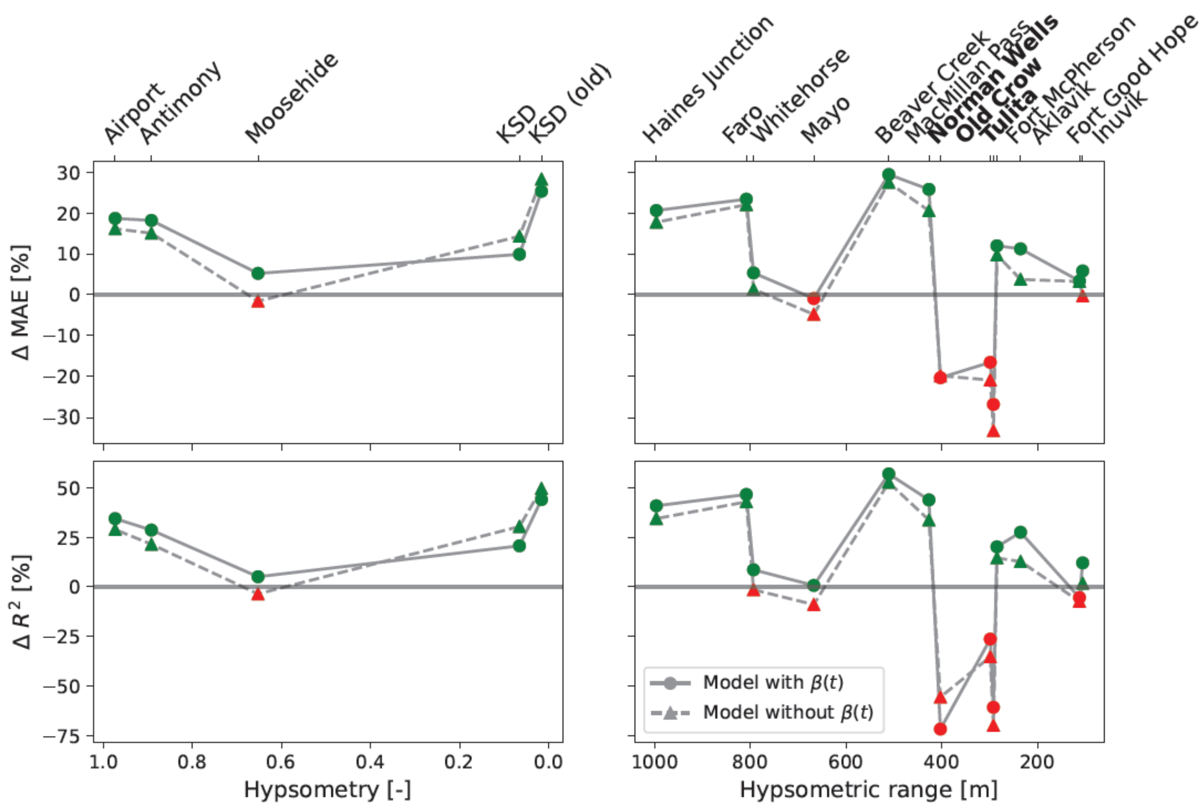

Figure 5-5: Statistical metrics for model versus observations. The hypsometric model calibrated with and without the reanalysis bias term $\beta(t)$ is compared to the worst of T_{pl} and T_{sur} (respectively corrected or not with $\beta(t)$) for MAE and R^2. Green markers indicate better predictions from the model than reanalysis, while red is worse. Stations where the hypsometric model performs worst overall appear in bold. (left) The 5 locations around Dawson City. (right) Same metrics for the 13 ECCC/NAVCAN weather stations in the Yukon and Northwest Territories. The hypsometric range is the product of (a) the hypsometric position and (b) the

elevation range excluding outliers (the elevation difference between the 90^{th} and 10^{th} percentiles in the area around the point location).

5.5 Discussion

5.5.1 Use of Hypsometry Instead of (Absolute) Elevation

The new surface-based inversion model proposed in this study spatializes the model of Pozsgay and Gruber (2025) while making the calculation of the REDCAPP lapse rate (Cao et al., 2017) dynamic. The factor that controls the strength of the temperature inversion events, α, is modified by considering hypsometric position instead of elevation. With this choice, we successfully unify the functional form of α as a function of a variable transformation of elevation for dissimilar valleys (Figure 5-4). A single calibration can now be performed simultaneously for the two valleys (WS01 and WS02) of the study area, and the resulting model is reliable in both valleys. To show that the model is indeed robust against spatialization, we perform cross-valley calibrations and find it to be reliable there too (Figure 5-7).

5.5.2 Physical Interpretation

Another improvement compared to the 'Dawson' model is the exponentiation of the elevation variable, instead of the linear form of α. The functional form of the proposed α_{exp} in Eq. (5-5) reduces to the linear form of Pozsgay and Gruber (2025) for locations with $h << 1$, while allowing for the representation of stronger inversions when $h \lesssim 1$, a frequently observed phenomenon.

SBIs in high-latitude valleys often exhibit non-linear lapse-rate profiles (Tikhomirov et al., 2021), where strong temperature stratification near the surface transitions to weakly stratified or isothermal layers above (Mayfield and Fochesatto, 2013). This pattern was observed in the subarctic valleys used to calibrate this model (Noad and Bonnaventure, 2026). During an SBI, lapse rates typically decayed exponentially within the first roughly 150 m where they often exceeded 25 ° C km^{-1} within the lowest 60 m and then approached isothermal above 150 m. In extreme cases, there was as much as 8 °C temperature increase over 19 m between the valley bottom and adjacent slope site (Noad and Bonnaventure, 2026).

The exponential function therefore better captures the observed behaviour of mean inversion strength (last column of Figure 5-4), while being safe from unwanted divergence given the boundedness of the hypsometric position ($h \in [0, 1]$). Nonetheless, the correction is still slightly underestimating the inversion strength for the points with higher hypsometry (last column of Figure 5-4). For the readers who might be surprised not to find a better fit of the mean observed α, we would like to reiterate that the fit presented there is the full model calibrated with hourly data in both valleys, and not a direct fit of mean yearly observed α.

5.5.3 Spatial Transferability and Scope of Applicability

The model described by Equation 4-5 was tested across a wide geographical range in Yukon and Northwest Territories, encompassing topographic diversity (Figure 5-2). The hypsometric model is more versatile than any of the reanalysis temperatures, even far from the calibration study area, which proves the success of this new formulation. Model performance in Whitehorse, Haines Junction, and MacMillan Pass, which are locations that experience weaker and more transient inversions than the subarctic valleys along the Dempster Highway (Lewkowicz and Bonnaventure, 2011; Noad et al., 2023; Garibaldi et al., 2024b), remained surprisingly strong. This suggests that while the model was calibrated for more continental Dempster valleys, it captures the underlying structure of SBIs well, and that its transferability extends to regions with comparable hypsometric ranges. In these settings, the model appears to represent topographic constraints on cold-air pooling processes that develop within landscapes characterized by large hypsometric range. Although the frequency and intensity of SBIs are less at Whitehorse, MacMillan Pass, and Haines Junction, their structure likely resembles those of the Dempster sites.

However, the model's transferability has limits. First of all, the inclusion of a reanalysis bias correction term β creates issues. Indeed, reanalysis bias is not uniform in time (see Figure 7 of Fiddes and Gruber (2014)), but more importantly, it varies in space while the model explicitly assumes a spatially independent $\beta(t)$. Such a term increases model performances in a region of applicability but is not appropriate for applications elsewhere. Instead, for such locations, we recommend either recalibrating β locally if nearby weather stations exist, or using the model calibrated without the β term (right column of Table 5-2), which increases the model's versatility. We showed that model performances are only minimally affected in the absence of reanalysis bias correction, demonstrating that the spatial scale at which the model can be applied is not limited by the scale over which the reanalysis bias varies. Second, the model performed poorly for certain ECCC stations, including Tulita, Old Crow, and Norman Wells. As shown in Figure 5-2, these locations correspond to those with higher hypsometry, while not in a mountain area. The topography for these areas is mainly flat (the elevation distribution peaks around the elevation of the lowland), and hence, any slight elevation variation has a disproportionate effect on the hypsometry. This is a limiting case of the model. Note that for Old Crow and Tulita, the calculated value of h is close to 1, but the stations are nowhere close to being at the bottom of a deep valley. This constitutes an extreme topographic situation where the model might not be suitable. These exceptions highlight the limits of the domain: in extremely flat, river-dominated terrain, hypsometry becomes unstable and river-generated warm anomalies overwhelm the topographic signal the model relies on. In this context, the inclusion of the MRVBF in a more intricate model might mitigate this undesirable effect by better distinguishing flat from incised terrain.

A related limitation arises in generally flat areas with a low range in hypsometry. Attempts to incorporate a modified variable, a bounded version of the hypsometric range $h \cdot dz$, which accounts for the topographic potential to sustain inversions did not substantially improve performance. Similar challenges have been reported in other lapse rate-based downscaling studies, where the absence of pronounced topographic relief often reduces the prediction of elevation-derived parameters (Fiddes et al., 2022). In such environments, microtopographic indices such as MRVBF used in REDCAPP (Cao et al., 2017) may provide complementary information on the structure of SBIs and resulting elevational patterns of air temperature. This metric, or something similar, could be used as a mechanism, to limit hypsometry closer to 0 in these flat areas.

Our results indicate a clear domain limit: stations situated on low-relief floodplains on the leeward side of mountain ranges (e.g., Norman Wells, Tulita, Old Crow) exhibit degraded performance relative to incised valleys. In such settings, the gravitational pooling that sustains SBIs is weak because slopes and basin geometry are minimal; small uncertainties in hypsometry are therefore amplified, especially when the seasonal temperature contrast DT is large. Leeward positioning further reduces inversion persistence via mechanically driven mixing and episodic flushing (Hrebtov and Hanjalic´, 2017; Dice et al., 2024), while riverine processes (late freeze-up, open water, advective heat) can imprint non-orographic thermal anomalies during transition seasons (Park et al., 2020; Prowse et al., 2007). Together, these factors yield a near-surface temperature structure that is not primarily topography-controlled, and our hypsometry-based correction can over-adjust. We therefore recommend caution for leeward floodplain sites, particularly those proximal to major rivers. In this configuration, the better-performing air temperature is T_{sur}. This framing clarifies that the model performs as intended in incised, terrain-controlled valleys, while transferability is limited where floodplain and river energy budgets dominate boundary-layer thermo-dynamics.

5.5.4 Scale Effects on Hypsometry

We focused some effort into determining the best radius around each point location to compute the hypsometric position and concluded that even though there might exist intermediate radii for specific configurations, the most robust option was to consider a radius of 50 km, with no weighting. Recent studies have shown that the interplay between large-scale synoptic conditions and local radiative and cold-air drainage processes is scale-dependent, with larger valley systems having a more complex interaction between the two mechanisms (Crosman and Horel, 2017; Hughes et al., 2015; Sheridan, 2019). This suggests that the radius that performs best empirically (50 km) is of the order of the spatial footprint of the gridded reanalysis datasets, providing a physical rationale for the effective use scale for hypsometric position used in our model.

We showed the existence of a hierarchy of scales, with a local minimum in model performance reached for local valley scales (roughly 5 km radius for the study area), but a global and potentially location-independent best fit at larger scales (Section 5.7.1). However, the physical scales controlling cold-air pooling and inversion persistence in the western Canadian Arctic may differ from those in other regions, and thus the relationships should be interpreted cautiously. Moreover, considering larger areas in the hypsometry calculation is yet to be tested for various topographic conditions across the western Canadian Arctic.

5.6 Conclusion

The hypsometric temperature inversion model proposed in this study is a spatialized and dynamic surface-based inversion model. Previously, it was shown that there exists a simple relationship between inversion strength and elevation for a specific area. However, this relationship varies spatially, meaning it would need recalibration for every new location. Here, we find a variable transformation of elevation (hypsometry) that preserves the shape of the inversion strength (function α) across dissimilar valleys. This new approach reuses one of the REDCAPP (Cao et al., 2017) parameters while disregarding the valleyness index (MRVBF), which was shown not to decrease the amount of information lost by the model. The DReaMIT hypsometric model combines the spatialization of REDCAPP and the dynamic lapse rate calculations of Pozsgay and Gruber (2025), while retaining a simple expression and a minimal number of dependent variables.

We then started to test the model transferability by showing the high performance of cross-valley calibration, i.e., calibrating the model in a valley and testing it in another. This first step towards a proof of the spatialization power of the model was then followed by a larger test in the Dawson City area, and across numerous ECCC stations in the Yukon and Northwest Territories. It was found to be the most robust and reliable model of air temperature when compared to raw reanalysis data and the 'Dawson' model. This does not mean that the hypsometric model always performs best, but rather that it is, on average, the preferred option. However, we issue recommendations for the best use of this model: (a) use when the hypsometry is well-defined, i.e., when small variations in elevation do not lead to dramatic variations in h, (b) for applications outside of the western Canadian Arctic, recalibrate the reanalysis bias β locally with weather station data when available, or use the 'no-β' version of the model otherwise. With this caveat in mind, we thus present a reliable, spatialized, and dynamic model of temperature inversions for the mountainous western Canadian Arctic.

Code and data availability*:* The current version of DReaMIT is available as an integrated GlobSim module from the 'DReaMIT_demo' branch of the project https://github.com/geocryology/globsim under the license GNU General Public License v3.0. The exact version of the model used to produce the results used in this paper is archived on Zenodo under DOI: 10.5281/zenodo.17545268 (Pozsgay et al., 2025), as are input data and scripts to run the model and produce the plots for all the simulations presented in this paper. The observational data from the WS01 and WS02 valleys, and from the Dawson study area are also accessible there. The remaining observational data is from ECCC/NAVCAN. The reanalysis data is available from ECMWF and JMA for the ERA5 and JRA-3Q datasets.

Author contributions: Conceptualization: SG, VP, PB, NN. Data curation: VP, NN. Formal analysis: VP. Funding acquisition: PB, SG. Software: VP. Supervision: PB, SG. Visualization: VP, NN. Writing (original draft preparation): VP, NN. Writing (review and editing): PB, SG.

5.7 Appendix

5.7.1 Relative Importance of the Radius of the Hypsometric Position

The hypsometric position was defined in Equation 5-2. We here study the influence of adding a $2d$ Gaussian weight modulating the typical spatial scale of the inversions. Here, we weigh each cell c with a Gaussian weight with standard deviation r,

$$h_r(x_0) = \frac{\sum_c w(r,|c-x_0|\theta(d-|c-x_0|)\theta(z_c-z_0)}{\sum_c \theta(d-|c-x_0|)w(r,|c-x_0|)} \qquad \text{(Eq. 5-9)}$$

where the weights are defined by

$$w(r,|c-x_0|) = \exp\left\{\frac{|c-x_0|^2}{2r^2}\right\} \qquad \text{(Eq. 5-10)}$$

We can also compute the multiresolution valley bottom flatness (MRVBF) index (Gallant and Dowling, 2003), which is an index that parameterizes the valleyness of a given point.

The hypsometric position, as defined by Equation 5-2 (or in Equation 5-9 for its weighed version), is a variable transformation of the absolute elevation. It carries information not only on the elevation of the point of interest, but also on the neighbouring terrain, or neighbouring cells if the terrain is discretized, such as in a DEM. The choice of the radius within which elevation information is retained reflects the scale at which the processes happen. For small radii, the local topography bears more importance, whereas it is increasingly smoothed with increasing exponential weight radius.

For each Gaussian weight radius *r*, we perform the calibration and evaluate the goodness of fit by computing different statistical metrics: root mean square error (RMSE), mean absolute error (MAE), reduced chi-square (χ^2), coefficient of correlation R^2, and both Akaike and Bayesian information criteria (AIC and BIC respectively). They are compared to equivalent results for the case where no weight is applied, which is the optimal case (Figure 5-6). The results improve quickly with increasing radius r, up to r ~ 5 km, where the goodness of fit finds a local minimum. Further increasing the Gaussian weight radius leads to worse agreements with observations for the model calibration, until r ~ 10 km. After this maximum, all metrics improve again, and the limiting case where no weight is applied is found to lead to the best agreement between model and observations for the calibration dataset.

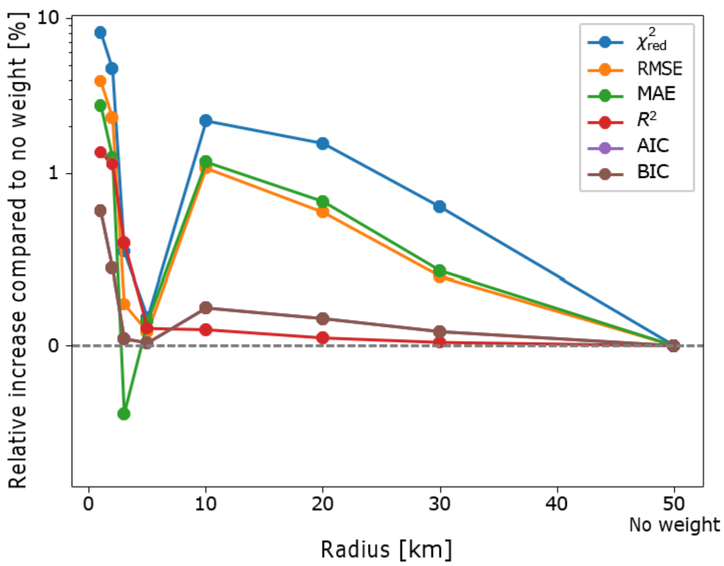

Figure 5-6. Comparison of the goodness of fit for the model calibration at different radii *r*, with respect to the limiting case without Gaussian weight.

We established the influence of the standard deviation of the 2*d* Gaussian weight *r*, not only in the value of *h* itself, but also in the performance of the inversion model. For each radius, reanalysis, and stations, the mean observed α_{exp} is computed and plotted in Figure 5-7. The exponential line of best fit is obtained from the calibrated parameters of the model (see Table 5-2 for the parameters used in the last column labelled 'No weight'). The line of best fit is thus not obtained directly at the level of the mean α_{exp}. However, the values of the correlation coefficient R^2 in Figure 5-7 correspond to the correlation between mean observed α_{exp} and modelled α_{exp}, i.e. for a dataset consisting of a single point per station. The value of R^2 starts as low as 0.30 and 0.29 for a radius of 1 km for ERA5 and JRA-3Q, respectively, and steadily increase until $r = 10$ km where they reach $R^2 = 0.91$ and 0.84, respectively. Further increasing the radius, or even dropping the $2d$ Gaussian weights altogether, has little to no impact on the correlation coefficient. However, the best agreement here too is found when no weighting scheme is applied (where 92 % of the variability in the mean observed α_{exp} is explained by the model for ERA5, and 86 % for JRA-3Q). This further motivates our choice to focus our analysis on this case.

5.7.2 Swapping Valleys

We perform single valley calibrations and apply the resulting fitted parameters to the other valley for all data points and not just the calibration dataset. This allows us to show the applicability of the model outside of its calibration area. In Figure 5-7, we plot the same quantities as in the Section 5.4.2, i.e., mean observed α against hypsometry, overlaid by a line representing the modelled α, whose parameters are either calibrated for both valleys at once (first column), or for each valley independently (next two columns). The values of the coefficient of correlation are given for all stations in black, and for stations of individual valleys WS01 and WS02 in blue and orange, respectively.

When the model is only calibrated using a year of data from WS01 (second column), the calculated values of α (for all data points and not solely the calibration set) explain 85 % and 78 % (for ERA5 and JRA-3Q) of the variation of the mean observed α in the valley WS01, however this drops to respectively 79 % and 60 % when applying it to WS02. Now, the calibration of WS02 for WS01 performs much better, with correlation coefficients as high as 0.84 for ERA5 and 0.80 for JRA-3Q. Note that the cross-valley modelling is better when calibrating on WS02 because its own calibration results are better than WS01. Indeed, the shape of the mean observed α as a function of the hypsometric position h is more closely aligned with the exponential choice of fitting function for WS02 than WS01, and hence the poorer performance of the WS01-calibrated WS02 model is directly inherited from the relatively poorer performance of the WS01-calibrated WS01 model. The WS02-calibrated WS01 model (third column) is largely successful, which demonstrates the wider scope of this model, beyond its own calibration area.

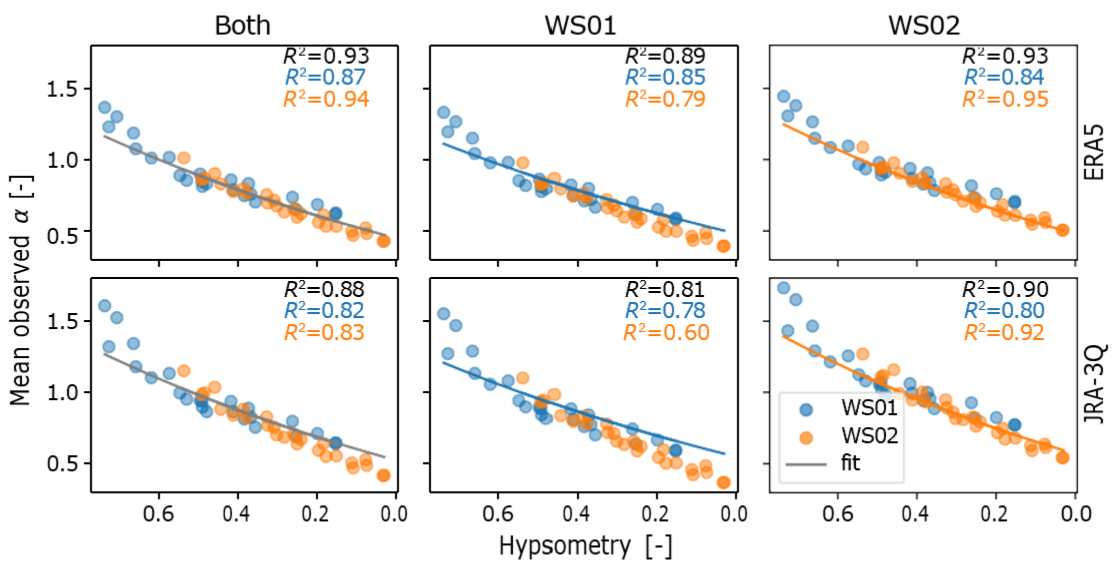

Figure 5-7: Mean observed and modelled values of the factor $\alpha(h)$ for a calibration over both valleys, or each valley individually, and for both reanalysis products.

5.7.3 Testing Model Performance Relative to Reanalysis Products

We demonstrated that the model from Equation 5-4, with and without the β term, globally outperformed the worst of the reanalysis products (corrected or not for the reanalysis bias) for the Dawson sites, and for most ECCC sites, except at intermediate to low hypsometric range. Here, we present the full picture and plot the values of MAE and R^2 with and without reanalysis bias correction in Figure 5-8, for the hypsometric model of Equation 5-4, the reanalysis products (both T_{pl} and T_{sur}), and the Dawson model of Pozsgay and Gruber (2025). For the Dawson area (left), the 'Dawson' model performs the best, but this comes as no surprise, as it was specifically calibrated for the area, but was not designed to include any spatial generalizability. Whether reanalysis bias is corrected or not, the hypsometric model performs better than pressure-level temperature and worse than surface temperature for high h, while the opposite is true for low h.

For the ECCC stations (right panel of Figure 5-8), stations with lower hypsometric range, i.e., milder topography, the temperature inversions are not as strong and the surface level reanalysis data is the one that performs the best, as expected. There, the hypsometric model exhibits similar values, that are not worse than the pressure-level reanalysis data. For intermediate values of the hypsometric range, especially for Tulita, Old Crow, and Norman Wells, the hypsometric model seems to have poorer performance. However, it is then outperforming any raw reanalysis data at even higher values, especially for Beaver Creek.

We note that general conclusions are valid whether we look at the full hypsometric model, or the simplified one calibrated without the β term.

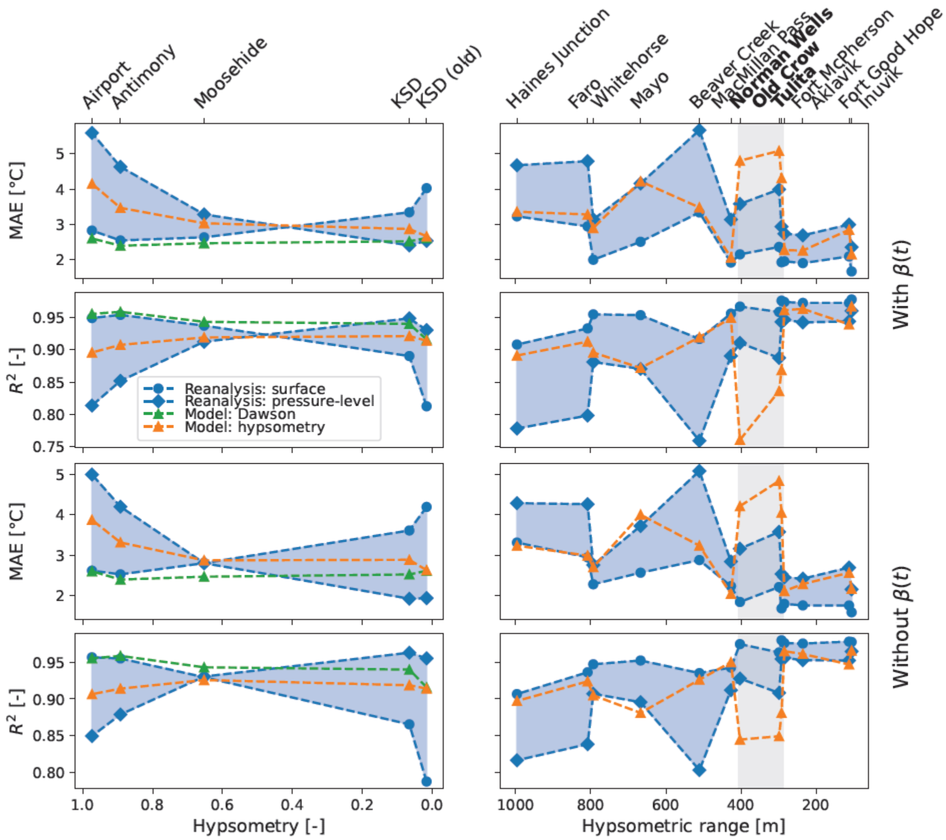

Figure 5-8. Statistical metrics for model versus observations. The hypsometric model calibrated with and without the reanalysis bias term $\beta(t)$ is compared to both T_{pl} and T_{sur} (respectively corrected or not with $\beta(t)$) for MAE and R^2. Stations where the hypsometric model performs worst overall appear in bold. (left) Comparison for the 5 locations around Dawson City, together with the model of Pozsgay and Gruber (2025) in orange. (right) Same metrics for the 13 ECCC/NAVCAN weather stations in the Yukon and Northwest Territories.

5.7.4 Study Area Temperature Inversions

We compare the modelled air temperature given by Eq. (5-4) to the bias-corrected T_{sur} and T_{pl} (i.e., to which we subtracted β), for two stations from the WS01 valley. Those were chosen to represent low and high hypsometric positions. For the top row of Figure 5-9, corresponding to high h, the best performing time series is the hypsometric model. The surface temperature is too low (MBE=−1.60 °C), while the pressure-level temperature is too high, especially towards the lowest temperatures, resulting in poor MAE and R^2. Next, when turning to low h (bottom row), the hypsometric model is still the preferred option, but the pressure-level temperature has similar performances, except for a cold bias (MBE=−0.95 °C). In this case, it is now the surface temperature that deviates at low temperatures but presents a significant cold bias there. This comparison confirms the non-intersecting domains of applicability of T_{sur} and T_{pl} found in Pozsgay and Gruber (2025), while demonstrating the advantage of the hypsometric model.

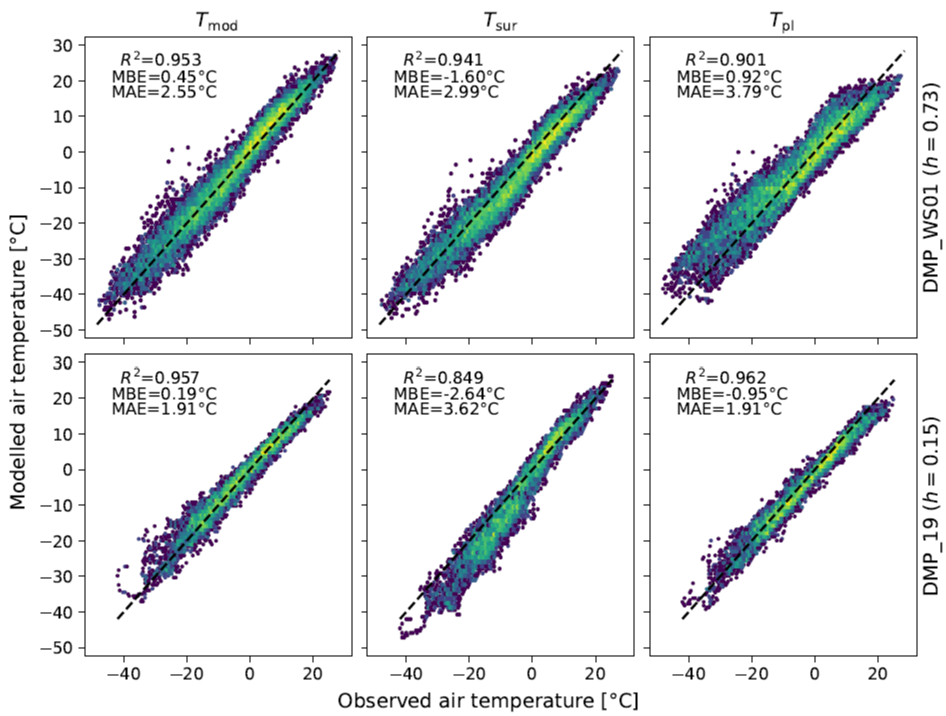

Figure 5-9: Parity plot of modelled versus observed temperatures for the two stations of diverse hypsometry from WS01 valley ($h = 0.73$ for the top row, and $h = 0.15$ for the bottom). We compare the results of the model to the bias-corrected T_{sur} and T_{pl}.

5.7.4 ECCC Stations

Table 5-3: Network of ECCC/NAVCAN weather stations used for air temperature data over 10 years, between 2015-08-01 and 2025-07-31.

Site	Station ID	Latitude [◦]	Longitude [◦]	Elevation [m]
Aklavik	52 962	68.2233	−135.0056	6
Inuvik	51 477	68.3039	−133.4831	68
Fort McPherson	52 963	67.4069	−134.8597	35
Forth Good	53 580	66.2406	−128.6475	81
Hope	27 549	66.2422	−128.6442	82
Beaver Creek	53 179	62.4103	−140.8689	650
Tulita	52 967	64.9097	−125.5694	100
Norman Wells	50 717	65.2814	−126.7986	72
	43 004	65.2875	−126.7534	94
Whitehorse	50 842	60.7094	−135.0672	706
	48 168	60.7331	−135.0978	707
Old Crow	53 023	67.57	−139.8400	250
	26 894	67.5706	−139.8392	251
Haines Junction	1556	60.7725	−137.5803	595
Mayo	51 426	63.6164	−135.8683	504
Faro	8964	62.2075	−133.3758	717
MacMillan Pass	27 339	63.2436	−130.0372	1379

6. Contrasting Controls of Snow and Surface-Based Temperature Inversions on Permafrost Thermal Regimes in Subarctic Mountain Valleys

Proposed submission to *Permafrost and Periglacial Processes*

Authorship: *Nick C. Noad[1], Philip P. Bonnaventure[1], & Yu Zhang[2]

[1]Department of Geography and Environment, University of Lethbridge, Lethbridge, AB, T1K 3M4, Canada

[2]Canada Centre for Mapping and Earth Observation, Natural Resources Canada, Ottawa, ON, K1A 0E8, Canada

*Corresponding Author email: nick.noad@uleth.ca

Keywords: Subarctic mountain environments, Permafrost modelling, Surface-based temperature inversions, Snow cover, Active layer thickness

6.0 Abstract

Permafrost distribution in mountain environments is often assumed to follow simple elevational gradients; however, local processes such as snow redistribution and surface-based temperature inversions (SBIs) can strongly modify ground thermal regimes. This study investigates the relative influence of local snow redistribution and atmospheric temperature variation on permafrost conditions using a process-based model (NEST) in two subarctic mountain valleys. The model was calibrated using multi-year ground temperature observations along two transects to quantify their impacts on active layer thickness (ALT) and mean annual ground temperature (MAGT). Results demonstrated that spatial variability in snow redistribution is the dominant control on ground thermal conditions and permafrost state. Removing this spatial variability resulted in widespread increases in snow depth, mean ground warming of approximately 2.8 °C, substantial increase in mean ALT of 3.45 m, and extensive talik formation or permafrost loss at sites previously predicted as stable. In contrast the removal of the local variation in atmospheric temperature leads to cooling of the ground (~1.0 °C) and thinning of the ALT (mean −0.82 m) across all sites, indicating the importance of SBI-related processes as an important secondary control that offsets parts of the effects of snow redistribution. These controls interact, as deeper snow reduces the sensitivity of the ground thermal regime to atmospheric forcing by increased insulation. This leads to strong spatial variability in permafrost stability and threshold responses at several sites.

6.1 Introduction

Permafrost is ground material that remains at or below 0 °C for two or more consecutive years (Lewkowicz et al., 2025), and plays a critical role in northern and mountain environments. In Canada, approximately 40% of the land is underlain by permafrost (Bush & Lemmen, 2019). Permafrost degradation can reduce landscape stability (Lewkowicz & Way, 2019; O'Neill et al., 2023), threaten the integrity of northern infrastructure (Hjort et al., 2018; O'Neill & Burn, 2017; Vincent et al., 2017) leading to high economic costs associated with maintenance, adaptation, or prevention (Canadian Climate Instittue, 2022; Hjort et al., 2018), mobilize soil organic carbon and release it as greenhouse gases into the atmosphere (Abbott et al., 2016; Schuur et al., 2015; Turetsky et al., 2019), alter hydrological pathways (Connon et al., 2014; Devoie et al., 2021; Walvoord & Striegl, 2007), and degrade water quality downstream (Favaro & Lamoureux, 2015; Schaefer et al., 2020; Schuster et al., 2011).

Active layer thickness (ALT) is a key indicator of permafrost response to environmental change as it governs the seasonal exchange of energy, water, and carbon between the atmosphere and land in permafrost regions (Bonnaventure & Lamoureux, 2013; Peng et al., 2023; Smith et al., 2009). Observational records from across the circumpolar north and other cold regions have documented widespread increase in active layer thickness in recent decades (Biskaborn et al., 2019; Garibaldi et al., 2022; Noetzli et al., 2024; Romanovsky et al., 2010; S. L. Smith et al., 2010, Smith et al., 2022). However, ALT does not only respond to air temperature alone but rather it reflects the combined influence of multiple interacting controls on heat transfer and storage with the ground (Bonnaventure & Lamoureux, 2013). For example, fire disturbance can drive rapid thickening of the active layer due to the removal of the buffering effect of vegetation at a site (Holloway et al., 2020; Smith et al., 2015; Zhang et al., 2015).

The ground thermal regime is influenced by multiple interacting factors including air temperature (Gruber, 2012), snow cover depth (Smith & Riseborough, 2002; Yinsuo Zhang et al., 2008a, 2008b) and density (Zhang, 2005), vegetation and organic layers (Shur & Jorgenson, 2007), soil thermal properties (Bonnaventure & Lamoureux, 2013), and topography and incoming solar radiation (Bonnaventure & Lewkowicz, 2008; Etzelmüller et al., 2006). Among these, snow cover is particularly important due to the insulating effect of winter ground temperatures (Garibaldi et al., 2026; Goodrich, 1982; Way & Lewkowicz, 2018; Zhang et al., 2018). Spatial redistribution of snow can produce large variations in ground thermal conditions over small horizontal distances (Gisnås et al., 2016; Romanovsky et al., 2010; Zhang et al., 2021).

In many mountain environments, permafrost distribution is usually described as following a simple elevational framework in which colder temperatures at higher elevations favour permafrost (Haeberli, 2013). Though this approach is useful in many settings, it is not universally applicable. In subarctic mountain valleys, SBIs and cold air pooling in the valley bottom and warmer conditions upslope (Mayfield & Fochesatto, 2013; Noad & Bonnaventure, 2022, 2026; Pozsgay & Gruber, 2025). These conditions can reverse typical SLR patterns, producing warmer temperatures at higher elevations (Bonnaventure & Lewkowicz, 2012, 2013; Lewkowicz & Bonnaventure, 2011), which influence the distribution of permafrost (Bonnaventure et al., 2012; Garibaldi et al., 2024b).

This recognition has already led to important advances in empirical and equilibrium type modelling of permafrost in northwest Canada. Bonnaventure et al. (2012) showed that in inversion prone terrain permafrost distribution is not linear with elevation due to SBI modified positive SLRs which alter the expected thermal gradient across the landscape. The work demonstrated that simple assumptions of steadily decreased temperature with elevations are insufficient in these environments. More recently, Garibaldi et al. (2024b) found that local lapse rates strongly affect air, ground surface, and near-surface permafrost temperatures across four dissimilar Yukon valleys. Together these studies make it clear that microclimate controlled by SBIs has a significant impact on mountain permafrost distribution and thermal state in these systems.

The influence of SBIs on ground temperatures is mediated by snow, vegetation, and soil properties, which can either amplify or dampen atmospheric forcing. For example, deep snow may buffer SBI effects on the ground thermal regime, whereas shallow snow and coarse substrates may enhance them (Garibaldi et al., 2024b). A transient, process-based framework is needed to determine not only whether SBI-related forcing bias matters, but also when, where, and under which surface conditions that bias becomes most important for permafrost predictions.

Transient permafrost models are often driven by coarse-resolution climate datasets, such as climate reanalysis datasets (Marchenko et al., 2008; Perreault et al., 2021; Yin et al., 2018), which often fail to capture local processes such as terrain driven microclimates (Fiddes et al., 2022; Fiddes & Gruber, 2012, 2014), cold air pooling (Cao et al., 2017; Noad & Bonnaventure, 2022; Pozsgay & Gruber, 2025), and snow redistribution (Gisnås et al., 2014; Gisnås et al., 2016; Zhou et al., 2021). As a result, forcing data may contain systematic biases when applied in complex terrain (Cao et al., 2019; Noad et al., *Submitted*; Pozsgay & Gruber, 2025; Pozsgay et al., 2026). The impact of these biases on modelled ground conditions remains poorly understood.

This study addresses that gap using the Northern Ecosystem Soil Temperature (NEST) model (Chen et al., 2003; Zhang et al., 2003), a process-based transient model that considers the effects of complex terrain and local variations in snow conditions. The model has been used widely to predict long-term ground thermal conditions and ALT (Zhang et al., 2008a, 2008b; Zhang et al., 2012; Zhang et al., 2018; Zhang et al., 2015). In this study the model is forced using ERA5-Land reanalysis data (Muñoz et al., 2019), with additional site-specific adjustment factors applied to account for local microclimatic conditions and SBIs.

This study explicitly links SBI-aware climate corrections to a transient permafrost model in complex terrain, allowing for assessment of how SBI-related forcing bias influences the ground thermal regime and active layer evolution. This is accomplished by: (1) quantifying spatial variability in ALT, MAGT, and snow conditions based on field observations, (2) calibrating and evaluating NEST using field observations, (3) assessing the sensitivity of modelled ground temperatures to SBI-related local air temperature adjustment and snow redistribution, and (4) examining long term trends in ALT and snow cover from 1950 to 2025.

6.2 Study Area

The study area consists of two valleys in the same range of the Ogilvie Mountains, referred to here as weather station one (WS01) valley and weather station two (WS02) valley (Figure 6-1). These two study valleys are located along the Dempster Highway approximately 100 km northeast of Dawson, Yukon and 8 km apart separated from each other by Distincta Peak (roughly 1800 m).

The study area lies near the boundary between continuous and discontinuous permafrost according to the national-scale permafrost map (Heginbottom et al., 1995). More recent high resolution permafrost modelling suggests permafrost is extensive discontinuous in the WS01 valley and continuous in the WS02 valley (Garibaldi et al., 2024b). Ground ice in the region is generally low (O'Neill et al., 2019). The landscape has been largely unglaciated since the Pre-

Reid Glaciation (2.6 Ma to > 200 ka) (Duk-Rodkin, 1999), resulting in well-developed periglacial features and weathered bedrock surfaces (French & Williams, 2013).

WS01 ranges in elevation from approximately 935 to 1720 m and is characterized by open boreal forest at the lower elevation (below approximately 1150 m) and blockfields with patches of moss at higher elevations. The valley is orientated east-west with the valley curving to the north in the up-valley direction. In contrast, WS02 ranges in elevation from approximately 1050 to 1790 m and is dominated by alpine tundra in the valley bottom and exposed blockfields with moss/grass patches on the slopes. The valley is orientated from north to south in the up-valley direction.

Valleys in this region are particularly prone to cold air pooling and formation of SBIs, which can persist through much of the winter season (Burn et al., 2015; Noad & Bonnaventure, 2022, 2026). These SBI processes exert strong controls on near surface air temperature patterns (Noad et al., 2023) and have been shown to influence the distribution of permafrost (Bonnaventure et al., 2012; Garibaldi et al., 2024b) and its sensitivity to climate warming (Bonnaventure & Lewkowicz, 2013; Garibaldi et al., 2024a). The contrasting topography, vegetation, and snow redistribution patterns between WS01 and WS02 valleys provides an ideal natural setting to investigate the relative influence of atmospheric and snow driven controls on permafrost thermal dynamics.

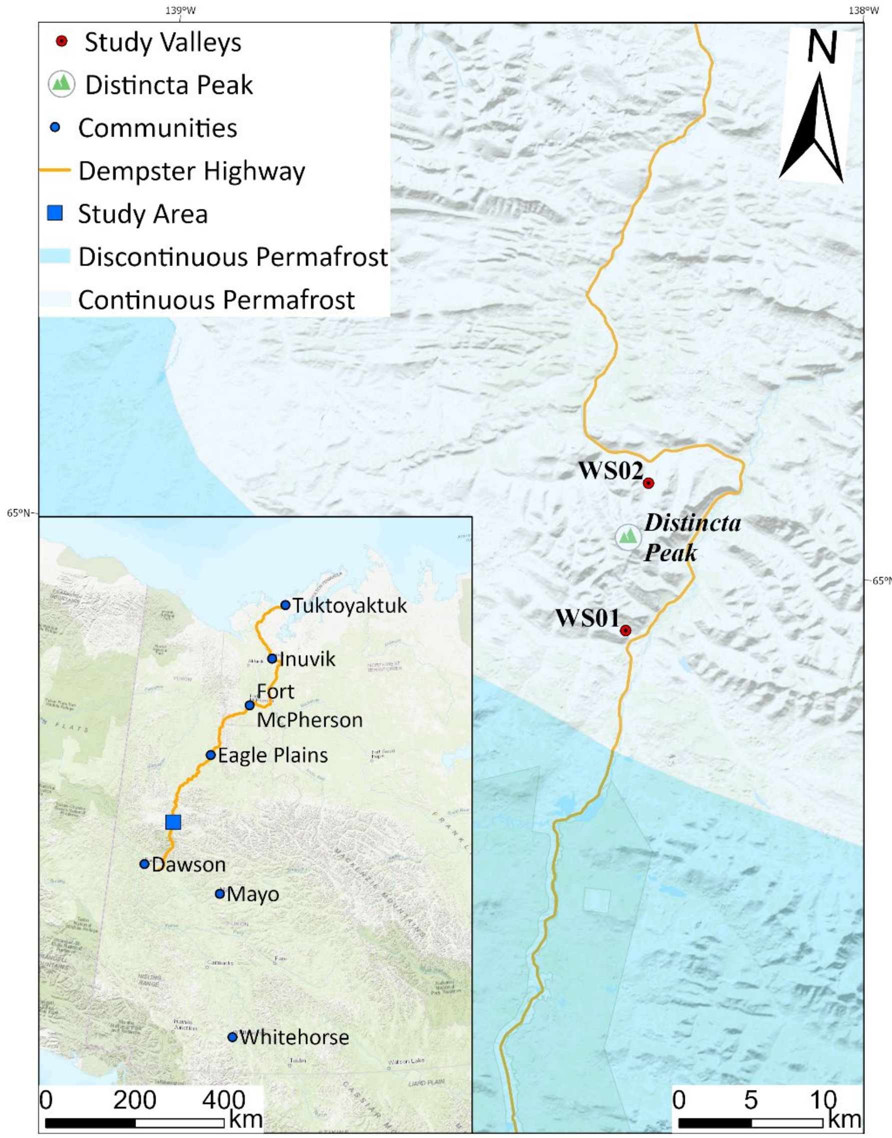

Figure 6-1: The study area located in northcentral Yukon along the Dempster Highway. The study area valleys consist of weather station one (WS01) and weather station two (WS02) valleys located roughly 8 km apart. The study areas are situated near the boundary between continuous and discontinuous permafrost (Heginbottom et al., 1995).

6.3 Methods

6.3.1 Network Transects and Data

An elevational transect was established for each study valley. The transects span valley bottom to ridge-top environments and include a range of elevations, slopes positions, and aspects (Table 6-1; Figure 6-2).

Table 6-1: Sites that make up each of the WS01 valley and WS02 valley transects.

Valley ID	Site Name	Latitude (dd)	Longitude (dd)	Elevation (m a.s.l.)	GT Depth (cm)	Slope (°C)	Aspect (°C)	Vegetation	Substrate	Year Deployed
WS01	DMP04	64.96209	-138.277	1142	70	28	217	Open Coniferous	Thin organic layer, stone rich	2017
	DMP05	64.95583	-138.285	1147	70	25	53	Patchy grass/moss	Stone rich	2017
	DMP10	64.96594	-138.275	1364	50	28	220	Patchy grass/moss	Stone rich	2021
	DMP11	64.95487	-138.287	1225	25	14	47	Patchy grass/moss	Stone rich	2021
	DMP12	64.9601	-138.279	1035	85	10	154	Open Coniferous	Thick organic layer, well-developed soil, less stones	2021
	DMP13	64.95692	-138.282	1059	30	21	41	Patchy grass/moss	Rocky	2021
	DMP18	64.96434	-138.278	1236	50	34	196	Alpine Tundra	Thin organic layer, stone rich	2022
	DMP31	64.95536	-138.266	957	30	9	60	Patchy grass/moss	Stone rich	2022
	DMP34	64.96881	-138.284	1425	N/A	16	213	Patchy grass/moss	Stone rich	2023
	DMP36	64.96002	-138.308	1316	N/A	14	74	Patchy grass/moss	Stone rich	2023
	WS01	64.95858	-138.28	997	55	14	212	Open Coniferous	Thick organic layer, well-developed soil, less stones	2017

	DMP06	65.04954	-138.259	1203	25	32	280	Patchy grass/moss	Stone rich	2017
	DMP09	65.05003	-138.274	1202	55	11	79	Alpine Tundra	Thin organic layer, stone rich	2018
	DMP14	65.05039	-138.271	1150	60	11	55	Alpine Tundra	Thin organic layer, stone rich	2021
	DMP15	65.04966	-138.261	1128	30	31	294	Alpine Tundra	Thin organic layer, stone rich	2021
	DMP16	65.05027	-138.285	1475	60	16	103	Exposed shale	Stone rich	2021
	DMP17	65.05249	-138.255	1308	30	20	271	Exposed blockfield	Stone rich	2021
WS02	DMP23	65.04903	-138.252	1406	N/A	12	329	Patchy grass/moss	Stone rich	2022
	DMP24	65.05013	-138.279	1321	15	26	115	Patchy grass/moss	Stone rich	2022
	DMP25	65.04995	-138.283	1417	15	29	105	Patchy grass/moss	Stone rich	2022
	DMP46	65.04491	-138.244	1595	N/A	17	327	Patchy grass/moss	Stone rich	2023
	DMP48	65.04567	-138.291	1593	N/A	4	53	Patchy grass/moss	Stone rich	2023
	WS02	65.04995	-138.263	1109	60	4	281	Apline Tundra	Thick organic layer, well-developed soil, less stones	2017

A total of 11 monitoring sites were used along the WS01 transect and 12 sites along the WS02 transect. At each site, surface air temperature was measured using U23-series or MX2301 Hobo loggers (accuracy ± 0.25 °C) (Onset, USA) mounted in a radiation shield approximately 2 meters above the ground surface. Ground surface temperature (GST) was recorded using either U23-series loggers or pendant temperature loggers installed at the soil-surface interface (roughly 5 cm depth).

Many sites additionally included a ground temperature at deeper depth (GT) collected via an external thermistor from a U23-series logger. Instruments were deployed between August 2017 and August 2023, resulting in temperature records ranging from approximately 2 to 8 years across the monitoring network.

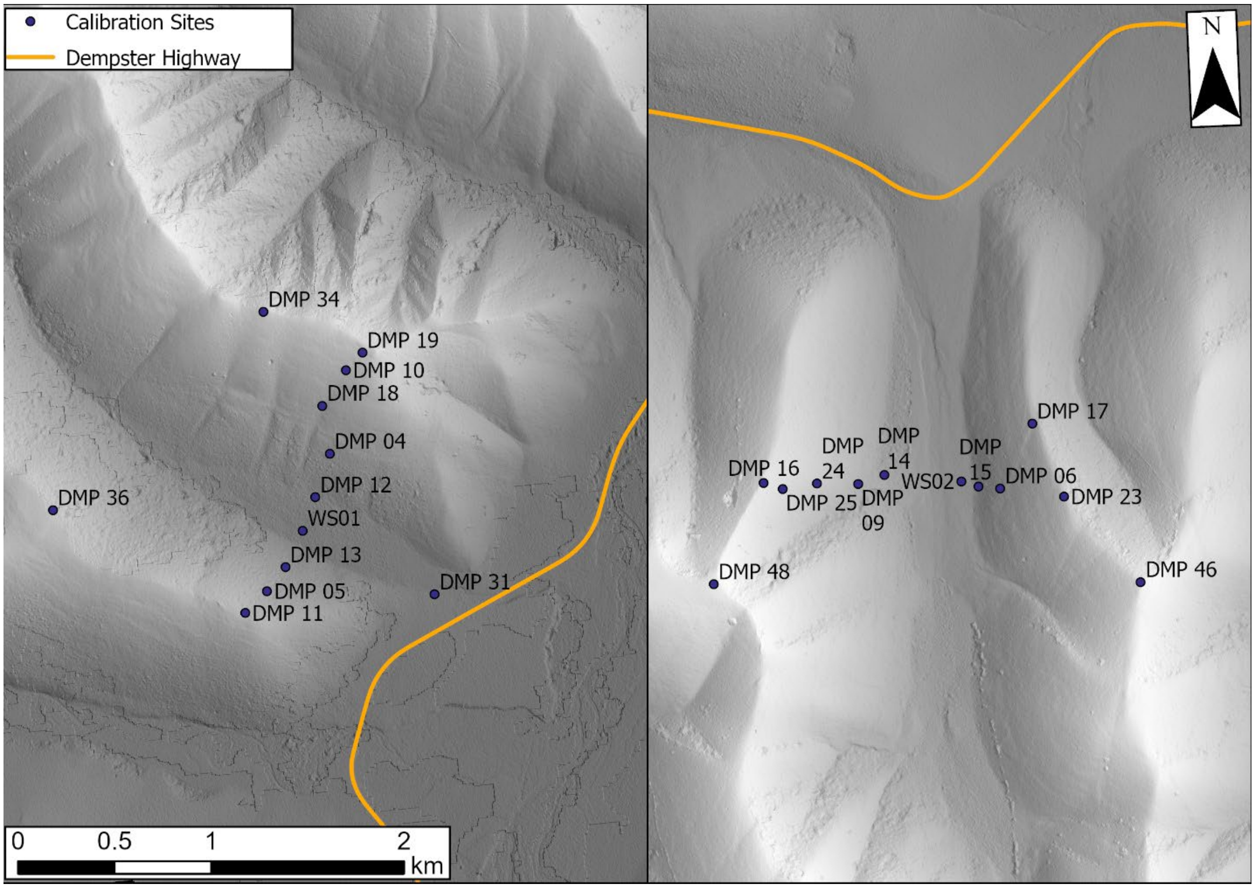

Figure 6-2: Spatial distribution of study sites along elevational transects in the WS01 (left) and WS02 (right) valleys. Topography is represented using a 2 m resolution ArcticDEM and corresponding hillshade (Porter et al., 2023).

6.3.2 Empirical Estimation of Parameters

Initial model calibration was guided by field observations and site-specific environmental characteristics to ensure physically realistic simulations prior to tuning (Figure 6-3). For each monitoring site, empirical data on soil thermal properties, snow conditions, vegetation structure, and near-surface climate processes were compiled, and parameter selection was constrained using observed ground thermal regime characteristics, including soil profile stratigraphy and texture, local thermal and seasonal boundary conditions, snow accumulation inferred from snow-ground interactions, soil moisture conditions, autumn zero-curtain duration, vegetation type, canopy height, Leaf Area Index (LAI), and snow-free surface albedo.

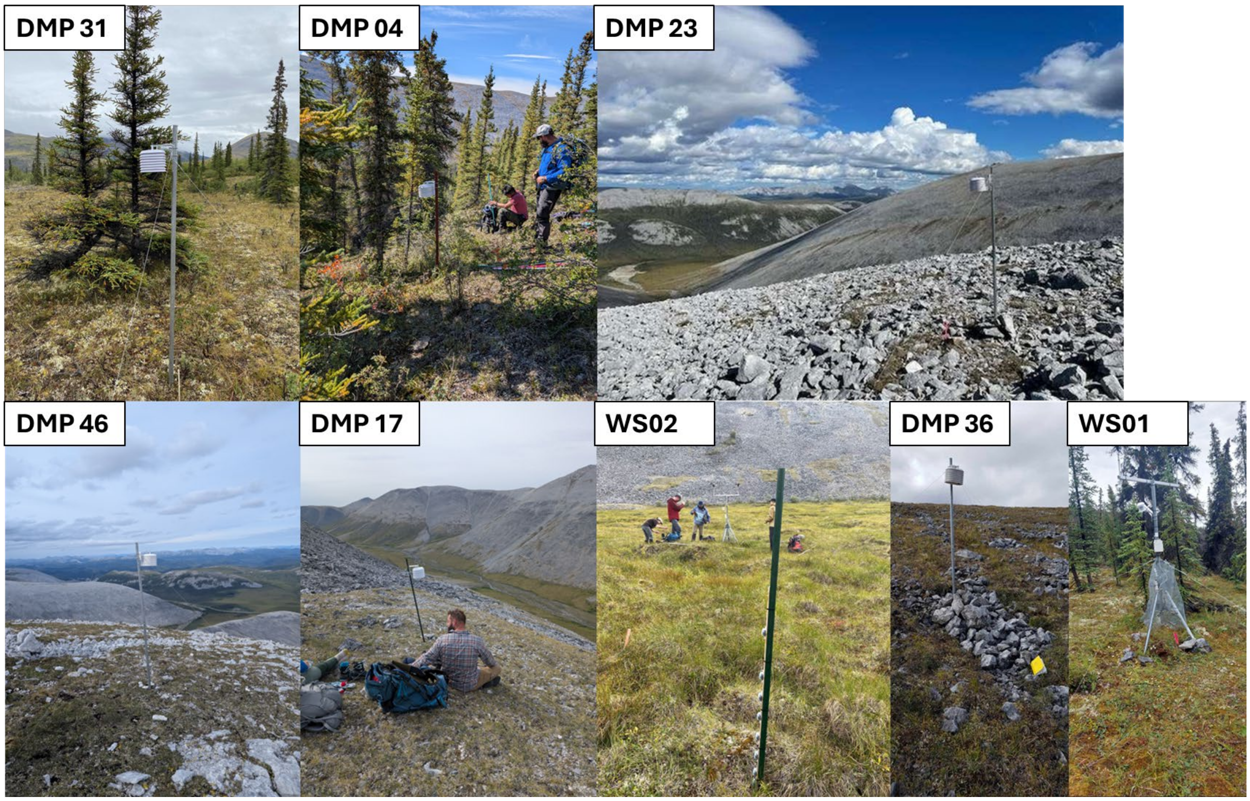

Figure 6-3: Representative site conditions across the study area illustrating variability in vegetation cover, substrate, and snow accumulation regimes. Sites range from wind-scoured, coarse blocky slopes with limited snow retention (e.g., DMP 23, DMP 46, DMP 17), to vegetation and moss-covered valley bottoms with strong thermal buffering (e.g., WS01, WS02), environments adjacent to the ridgetop where deep snow accumulates (e.g., DMP 36). The floodplain site DMP 31 illustrates conditions associated with deep thaw and talik development. DMP 04 represents a site near treeline on the south aspect slope that has warm ground temperatures and no permafrost. These contrasts underpin the spatial variability in ground thermal regimes and model sensitivity observed in this study.

6.3.2.1 Freezing n-Factors

Freezing n-factors were calculated to characterize the coupling between winter air and ground temperatures (Smith & Riseborough, 1996). Freezing n-factors were derived as:

$$n_f = \frac{\sum FDD_s}{\sum FDD_a} \qquad \text{(Eq. 6-1)}$$

where FDD_a is the freezing degree days for the air and the FDD_s is the freezing degree days for the ground surface. Freezing degree days at the ground surface were calculated using temperature measured approximately 0.05 m below the surface, and air freezing degree days were calculated from air temperature measurements at approximately 2 m height.

6.3.2.2 Snowmelt Timing

The date of spring snowmelt was estimated using ground surface temperature (GST) records. Snow disappearance was identified as the final occurrence of at least five consecutive days of daily mean temperature < 0.5 °C and standard deviation less than 3 °C reflecting the transition from snow-insulated to atmospherically coupled conditions. This methodology follows similar approaches to determine snow on and off dates in permafrost regions using ground surface temperatures (Lundquist & Lott, 2008; Schmid et al., 2012).

6.3.2.3 Autumn Zero Curtain

The duration of the autumn zero curtain was quantified as the cumulative number of days during autumn when mean daily ground temperature remained within ±0.5 °C of 0 °C and daily temperature standard deviation was <1 °C for at least five consecutive days (Outcalt et al., 1990; Romanovsky & Osterkamp, 2000). For each site, median zero-curtain duration across all years was used to characterize local freeze-back conditions.

6.3.2.4 Topographic Parameterization

Topographic controls on solar radiation, snow redistribution, and moisture availability were quantified using the 2 m resolution Arctic Digital Elevation Model (DEM; Porter et al., 2023) and spatial analysis tools in ArcGIS Pro. Derived terrain variables included slope, aspect, topographic shading, and the Topographic Wetness Index (TWI), the latter used to represent spatial variation in potential soil moisture conditions. TWI was calculated following Beven and Kirkby (1979) as:

$$TWI = \ln(a / \tan \beta) \tag{Eq. 6-2}$$

where a is the upslope contributing area and β is local slope. To generate this index, the DEM was first hydrologically conditioned by filling sinks, after which flow direction, flow accumulation, and slope rasters were derived and combined in the raster calculator to produce the final TWI surface.

Topographic shading was computed using the Skyline tools in ArcGIS Pro 3.5.3, which estimates the surrounding horizon angle for point locations based on the input DEM. The search radius was limited to 10 km around each site to reduce computational cost. A vertical offset of 2 m was applied to approximate the height of the surface air temperature logger at each monitoring location.

Empirically derived variables used to estimate the initial parameters of NEST are listed in Table 6-2.

Table 6-2: Empirically derived variables used to estimate the initial parameters for the NEST model. From here the NEST model was fine tuned.

Site	TWI	Median Zero Curtain Length (days)	Vegetation Type	Canopy Height (m)	nf
DMP 04	2	1	Coniferous Forest	6.00	0.17
DMP 05	5.1	7	Grasses/Sedges	0.02	0.37
DMP 06	5.3	2.5	Grasses/Sedges	0.02	0.78
DMP 09	2.3	5.5	Grasses/Sedges	0.05	0.57
DMP 10	5.5	7.5	Grasses/Sedges	0.02	0.55
DMP 11	6.3	18	Grasses/Sedges	0.02	0.38
DMP 12	4.9	12	Coniferous Forest	7.00	0.09
DMP 13	3.5	7	Grasses/Sedges	0.02	0.39
DMP 14	6.9	9	Grasses/Sedges	0.05	0.51
DMP 15	7.6	7	Grasses/Sedges	0.05	0.80
DMP 16	1.2	46	Grasses/Sedges	0.01	0.49
DMP 17	4.3	2	Grasses/Sedges	0.01	0.85
DMP 18	2.2	16.5	Shrubs	0.2	0.4
DMP 23	3.9	10	Grasses/Sedges	0.01	0.87
DMP 24	3.6	13	Grasses/Sedges	0.01	0.69
DMP 25	1.7	33	Grasses/Sedges	0.00	0.57
DMP 31	1.9	9	Mixed Forest	3.00	0.16
DMP 34	3	9	Grasses/Sedges	0.01	0.72
DMP 36	1.4	1	Grasses/Sedges	0.02	0.33
DMP 46	1.9	13.5	Grasses/Sedges	0.02	0.81
DMP 48	3.4	24	Grasses/Sedges	0.05	0.76
DMP WS01	2.6	10	Coniferous Forest	10.00	0.25
DMP WS02	2.4	14	Grasses/Sedges	0.10	0.48

6.3.3 Modelling Description

The model used in this study is the Northern Ecosystem Soil Temperature (NEST) model (Zhang et al., 2003). NEST is a process-based model developed to simulate ground temperature and permafrost with climate change. The temperature of ground is calculated based on heat conduction equation. The upper boundary condition is determined by energy balance on the ground surface or surface of snow when snow is present. The lower boundary condition at a depth of 119.7 m is defined based on geothermal heat flux, including the effects of climate warming on ground temperature gradients (Zhang et al., 2006).

The subsurface is divided into 63 layers, with layer thickness gradually increasing from 0.1 m in the top one-metre ground to 4.8 m at the bottom of the simulated depth (119.7 m). Topographic effects on surface energy balance are also incorporated (Zhang et al., 2013). The model also simulates soil water dynamics, including thawing and freezing processes and their influence on ground temperature.

Given the strong impacts of snow on ground temperature, the model simulates detailed processes of snow dynamics, including snowfall, snow sublimation, snow melt, compaction, and destructive metamorphism. The snowpack is divided into multiple layers with a thickness of about 10 cm (depending on the total snow depth), and the density and temperature of each layer are calculated (Zhang et al., 2003).

To account for wind driven snow redistribution, a snow input factor (F_{snow}) is used (Zhang et al., 2012). This factor modifies snowfall from gridded climate data as:

$$P_{snow} = P_{snow0} \cdot F_{snow}, \qquad \text{Eq. 6-3}$$

where P_{snow0} is the daily snowfall (mm in water) from a gridded climate data set, and P_{snow} is the estimated snow input (mm in water) at the site. F_{snow} is the snow input factor (≥ 0 unitless) represents the effects of snow redistribution and is equivalent to one minus the snow-drifting factor defined in the previous studies (Zhang et al., 2012). The F_{snow} is not considered (set as 1) when precipitation is rainfall.

The NEST model has been extensively evaluated across multiple sites and regions, demonstrating its ability to simulate ground temperature, permafrost conditions, and snow dynamics under a wide range of environmental settings (Chen et al., 2003; Zhang et al., 2003; Zhang et al., 2006; Zhang et al., 2008c; Zhang et al., 2012; Zhang et al., 2015).

6.3.3.1 Model input data

The required input data of the model include latitude of the site, climate, vegetation, soil and ground conditions, thermal conductivity of bedrock, geothermal heat flux, lateral water flow parameters, and the F_{snow}. Vegetation conditions include vegetation types (deciduous, coniferous or mix forest, shrub, sedges/grasses), height and leaf area index in the peak growing season. Soil and ground conditions include peat thickness on the top, texture of the mineral soil, volumetric fractions of organic matter, gravels and excess ice in the ground profile, and depth to bedrock.

The climate variables required to run the NEST model include daily air temperature (daily minimum (Tmin) and maximum temperature (Tmax)), precipitation, wind speed, vapour pressure, solar radiation, and downward longwave radiation (Zhang, 2025). The climate input data were derived from ERA5-Land reanalysis dataset. ERA5-Land provides globally consistent atmospheric reanalysis data at 0.1° latitude/longitude spatial resolution and hourly temporal resolution from 1950 to present (Muñoz et al., 2019). Since the two study valleys are located within the same ERA5-Land grid cell, identical climate forcing data were used for all sites prior to local calibration. ERA5-Land hourly data were downloaded for the period 1950 to 2025, and we calculated daily values based on the hourly data.

The slope, aspect, and topographic shading for each site were calculated using 2-m resolution ArcticDEM (Porter et al., 2023). Vegetation type and height index were determined based on situ observations. LAI was initially estimated visually and then fine-tuned in the tuning process. Top ground peat thickness and the texture of mineral soil were defined based on field observations. The volumetric fractions of stones in soil were broadly described in the field but were not quantitative measurements. The model was calibrated using measured ground temperature and the general conditions described in the field. The F_{snow} parameter was calibrated by comparing the measured and observed ground temperature, particularly in winter months.

The thermal conductivity of bedrock was set to 2.5 W m^{-1} K^{-1}, which falls within the typical range reported for fractured and partially saturated mineral substrates and bedrock in cold regions (e.g., Farouki, 1981; Williams & Smith, 1989). This value is consistent with previous permafrost modelling studies in similar northern environments (Bonnaventure & Lamoureux, 2013; Zhang et al., 2003). The geothermal heat flux was set to 0.054 W m^{-2}, which is consistent with reported values for northern Canada and the western Cordillera (e.g., Majorowicz & Grasby, 2010; Pollack et al., 1993). This value falls within the typical range of 0.04-0.06 W m^{-2} used in permafrost modelling studies (e.g., Zhang et al., 2006). Depth to bedrock was set based on field observations of soil thickness, substrate characteristics, and surface geomorphology at each site. Many locations are characterized by shallow soils overlying coarse blockfields and weathered bedrock, consistent with unglaciated terrain in the Ogilvie Mountains (e.g., Duk-Rodkin, 1999; French and Williams, 2013). Although these parameters are not directly measured at all sites, the selected values fall within well-established ranges and are consistent with both regional observations and previous permafrost modelling studies. Sensitivity to these parameters is expected to be secondary relative to the dominant controls of snow cover and atmospheric forcing examined in this study.

To consider the local variations in climate conditions compared to coarse gridded climate data, the current version of the model also includes local adjustment factors for monthly Tmin, Tmax and precipitation. They are monthly averages without variation from year to year. We defined the adjustment factors for Tmin and Tmax by comparing the observed and ERA5-Land air temperature. Monthly precipitation was not adjusted as there were no local observations for precipitation.

6.3.4 Model Calibration and Evaluation

6.3.4.1 Model Tuning

The NEST model was calibrated for each monitoring site using the observed ground surface temperature (GST) and ground temperature at depth (GT) (Table 6-1). The F_{snow}, LAI, Albedo, and volume of stone were calibrated so that the modelled ground temperature represents the observations at each site. The minimum thermal conductivity of snow (Min Snow TC) was calibrated using estimated snow depth and GST at WS01 and WS02 (2024–2025), yielding values of 0.15-0.18 W m^{-1} K^{-1}. This was then applied across all sites within a range of 0.13–0.20 W m^{-1} K^{-1} to represent snow insulation, improve predictions of ground temperatures, and snowmelt timing. The calibrated values for each site are included in Table 6-3.

Table 6-3: The fine-tuned parameters for input into the NEST model including Leaf Area Index (LAI), Snow free albedo, snow redistribution factor (F_{snow}), and the minimum snow thermal conductivity.

Site	LAI	Snow Free Albedo	F_{snow}	Min Snow TC
DMP 04	1.50	0.10	1.10	0.15
DMP 05	0.10	0.20	0.77	0.20
DMP 06	0.10	0.10	0.28	0.15
DMP 09	0.10	0.15	0.31	0.15
DMP 10	0.50	0.30	0.35	0.20
DMP 11	0.08	0.13	0.55	0.15
DMP 12	2.00	0.15	1.10	0.15
DMP 13	0.01	0.15	0.55	0.15
DMP 14	0.10	0.15	0.40	0.13
DMP 15	0.01	0.15	0.55	0.15
DMP 16	0.00	0.23	0.43	0.20
DMP 17	0.00	0.10	0.14	0.15
DMP 18	0.10	0.15	0.55	0.20
DMP 23	0.00	0.25	0.15	0.13
DMP 24	0.01	0.15	0.50	0.20
DMP 25	0.20	0.18	0.33	0.15
DMP 31	0.30	0.10	0.73	0.20
DMP 34	0.01	0.17	0.30	0.13
DMP 36	0.30	0.25	1.20	0.20
DMP 46	0.20	0.20	0.24	0.15
DMP 48	0.30	0.25	0.30	0.20
WS01	0.80	0.25	1.00	0.15
WS02	1.00	0.20	0.25	0.18

6.3.4.2 Model Calibration Evaluation

The performance of the model calibration was evaluated using several statistical metrics that compared simulated and observed temperatures. These include the coefficient of determination (R^2), root mean squared error (RMSE), Nash-Sutcliffe efficiency (NSE), Kling-Gupta efficiency (KGE). In addition, the difference in the timing of seasonal GST freezing and thawing between simulations and observations was assessed to evaluate the model's ability to reproduce seasonal transitions in the ground thermal regime.

The NSE evaluates model performance by comparing the variance of model residuals to the variance of the observed data (Nash & Sutcliffe, 1970) and is defined as:

$$NSE = 1 - \frac{\sum_{i=1}^{n}(O_i - S_i)^2}{\sum_{i=1}^{n}(O_i - \bar{O})^2} \qquad \text{(Eq. 6-4)}$$

Where O_i represents the observed temperature, S_i represents the modelled temperature, $\bar{O}$ represents the mean observed temperature, and n is the number of observations. NSE values range from $-\infty$ to 1, where a value of 1 indicates perfect agreement between simulations and observations, and values greater than 0 indicate that the model performs better than the mean of the observed data.

The KGE is a composite performance metric commonly used in hydrological modelling that evaluates model performance based on correlation, variability, and bias (Gupta et al., 2009; Vrugt & de Oliveira, 2022). KGE is defined as:

$$KGE = 1 - \sqrt{(r-1)^2 + (\alpha - 1)^2 + (\beta - 1)^2} \qquad \text{(Eq. 6-5)}$$

Where r represents the correlation between predicted and observed temperatures, α represents the variability ratio between simulated and observed standard deviations, and β represents the bias ratio between simulated and observed means. KGE values range from $-\infty$ to 1, with a value of 1 indicating perfect agreement between simulated and observed data.

6.3.5 Model Scenarios

After model calibration, four model scenarios were evaluated to isolate the effects of local air temperature adjustment factors and spatial variability in the snow input factor (F_{snow}): (1) considering both local air temperature adjustment factors and local snow redistribution as calibrated, (2) without considering local air temperature adjustment factors (setting the Tmin and

Tmax adjustment factors as 0) but retaining local snow variation (using the calibrated F_{snow}), (3) considering local air temperature adjustment factors effects but removing local snow variation (by setting F_{snow} as 1), and (4) without considering both local air temperature adjustments or local snow variations (setting the Tmin and Tmax adjustment factors as 0, and F_{snow} as 1). Model outputs were evaluated using active layer thickness (ALT), mean annual ground temperature (MAGT) at 0.05, 0.55, 1.07, 2.90, and 7.10 m depths.

6.3.6 Sensitivity Analysis

To evaluate the sensitivity of ground thermal conditions to model parametrization, changes in model outputs for each scenario were calculated relative to the control scenario. Sensitivity was assessed for ALT and MAGT at depth of 0.05, 0.55, 1.07, 2.90, and 7.10 m.

However, at sites where a talik developed or permafrost was no longer present, ALT is no longer representative of the depth to the permafrost table and instead represents seasonal freezing within a fully thawed profile. To ensure consistent comparison across all sites and scenarios, sensitivity analyses were therefore based primarily on MAGT.

For each site, the difference in MAGT between the control and scenario were calculated at all depths and averaged to produce a mean ground thermal response. These values were used to compare the relative influence of atmospheric forcing and snow redistribution on the ground thermal regime.

6.4 Results

6.4.1 Local Air Temperature Adjustment Factor

Linear regression analyses were used to evaluate the relationship between the monthly air temperature local adjustment factors and station elevation. Strong and statistically significant relationships were observed in most months for both valleys, with coefficients of determination frequently exceeding $R^2 > 0.8$, particularly in the winter and summer months (Figure 6-4; Table 6-9). During transitional months (March, April, October, and November), these relationships were often weaker or not statistically significant.

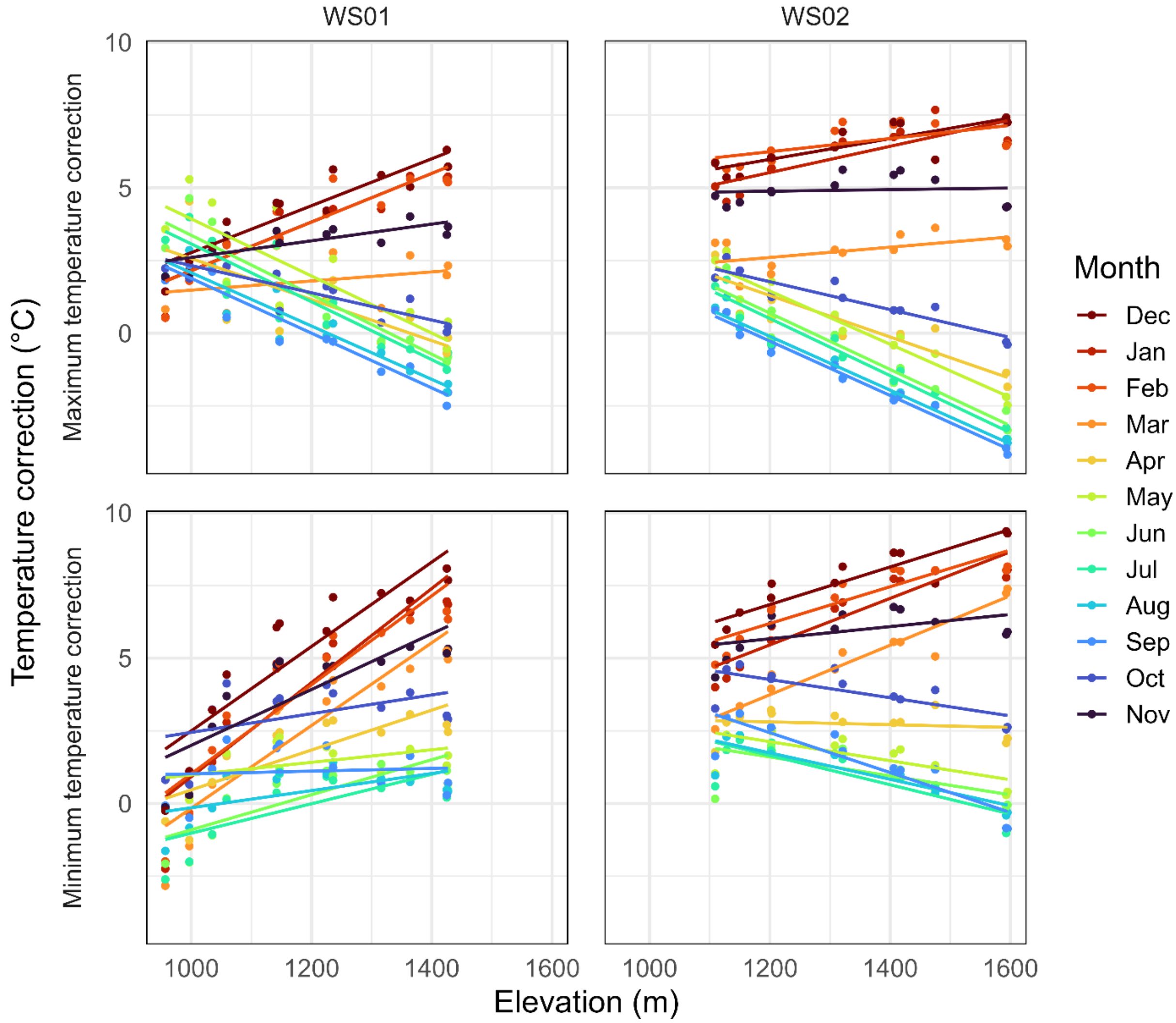

Figure 6-4: Elevational profiles of monthly maximum and minimum temperature adjustment factors applied to ERA5-Land daily minimum and maximum air temperatures for sites in the WS01 and WS02 valleys.

During the months November through April, Tmin local adjustment factors exhibited particularly strong positive relationships with elevation, with slopes ranging from 0.6 to 1.65 °C 100 m^{-1}. This pattern indicates that ERA5-Land minimum temperatures exhibit a systematic cold bias at higher elevations relative to the observations, consistent with the influence of persistent SBIs (Noad et al., *Submitted*). Tmax local adjustment factors displayed a similar but more moderate relationship during the winter season (December-February), with slopes ranging from 0.20 to 0.84 °C 100 m^{-1}. These patterns required positive adjustments up to +9.4 °C at the highest elevations in WS02 valley (Figure 6-5).

In contrast, during the summer months the relationship between Tmax adjustment factors and elevation became negative, with slopes ranging from -1.02 to -0.47 °C 100 m^{-1}. This indicates that ERA5-Land tends to overestimate daytime temperatures at higher elevations, likely due to the inability of the coarse-resolution reanalysis to fully resolve terrain driven lapse rates and surface energy balance differences. As a result, maximum temperature adjustments up to -4.2 °C were required at the highest elevation sites in the WS02 valley (Figure 6-5). Tmin adjustment factors exhibited weaker, at times not statistically significant, and more variable relationships with elevation during the summer months.

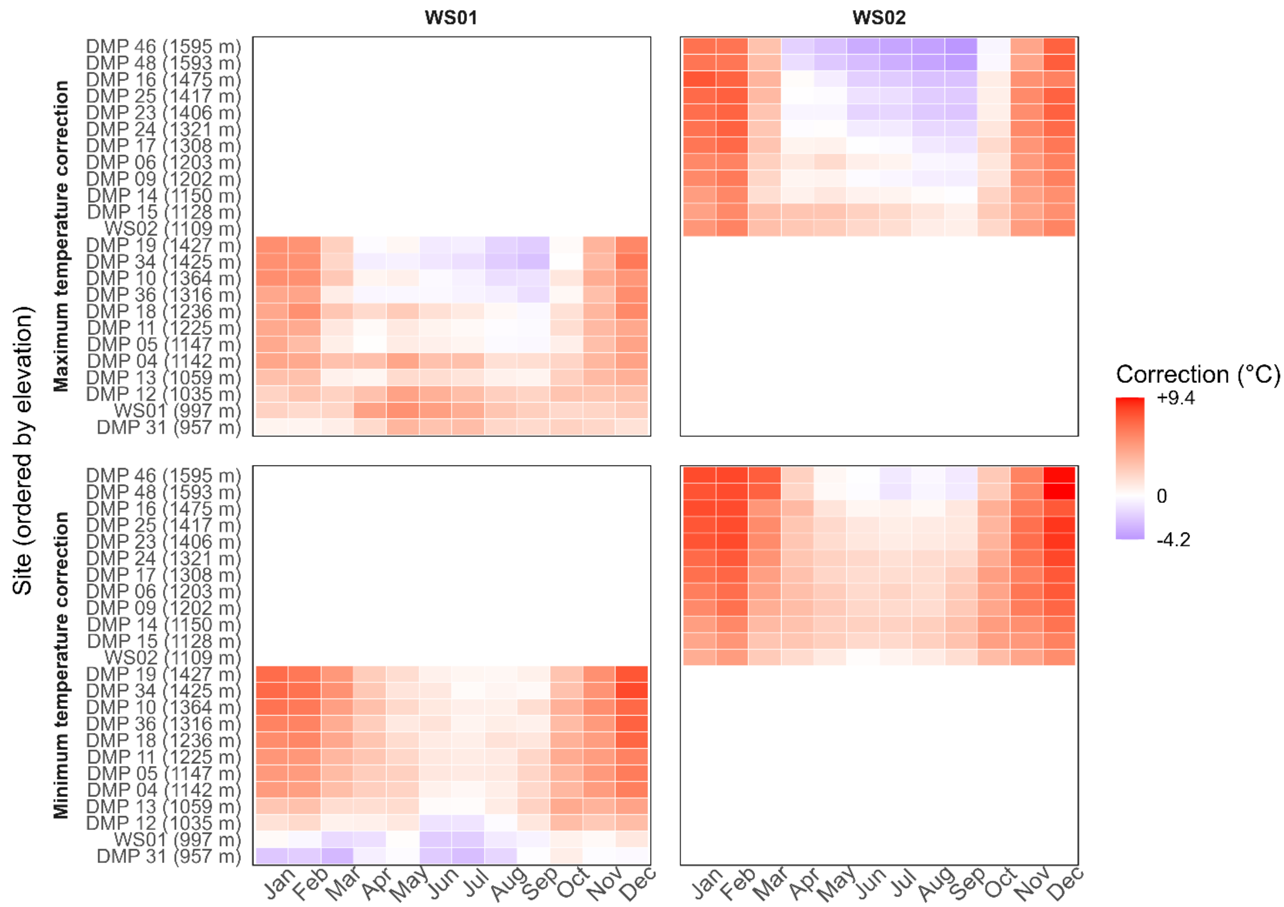

Figure 6-5: Monthly local adjustment factors applied to ERA5-Land daily minimum and maximum air temperatures for each monitoring site. Sites are grouped by valley and ordered by elevation to highlight the elevational structure of local temperature corrections associated with terrain effects and surface-based temperature inversions (SBIs).

Monthly air temperature biases between ERA5-Land and observations exhibit a consistent seasonal structure across all sites, with the largest positive biases occurring in winter months and minimal biases during summer. Although some interannual variability is present, the magnitude and shape of the bias remain stable from year to year (Figure 6-15).

When mean monthly air temperature adjustment factors were aggregated to annual mean, systematic relationships with elevation remained evident in three of four local air temperature adjustment factor combinations. Local Tmax adjustment factors exhibited significant decrease with elevation in both valleys (WS01: slope = −0.26 °C 100 m^{-1}, R^2 = 0.37, p-value = 0.035; WS02: slope = −0.40 °C 100 m^{-1}, R^2 = 0.87, p-value < 0.001). Local Tmin adjustments increased with elevation in the WS01 valley (slope = 0.80 °C 100 m^{-1}, R^2 = 0.67, p-value < 0.001), while no significant relationship was observed in the WS02 valley (R^2 = 0.05, p-value = 0.47).

Overall, the monthly local air temperature adjustment factors typically exhibited a clear elevational structure, with the largest positive adjustments made for the highest sites during the winter season when SBIs dominate the near surface temperature structure in the valleys (Noad & Bonnaventure, 2026). These adjustment factors directly influence the climate forcing used in the NEST model and therefore affect simulated ground thermal regimes.

6.4.2 Snow input factor F_{snow} and model calibration results

The snow input factor F_{snow} after calibration ranged from 1.20 at DMP 36 to 0.14 at DMP 17. Typically, the F_{snow} was greater at most sites in WS01, meaning the snow accumulation was greater in that valley (Figure 6-6). The snow effectively scoured at most sites leading to F_{snow} being less than 1 at all sites excluding DMP 36 which was situated in a ridgetop adjacent cornice and sites in the WS01 valley bottom and below treeline on the south aspect slope (WS01, DMP 12, and DMP 04).

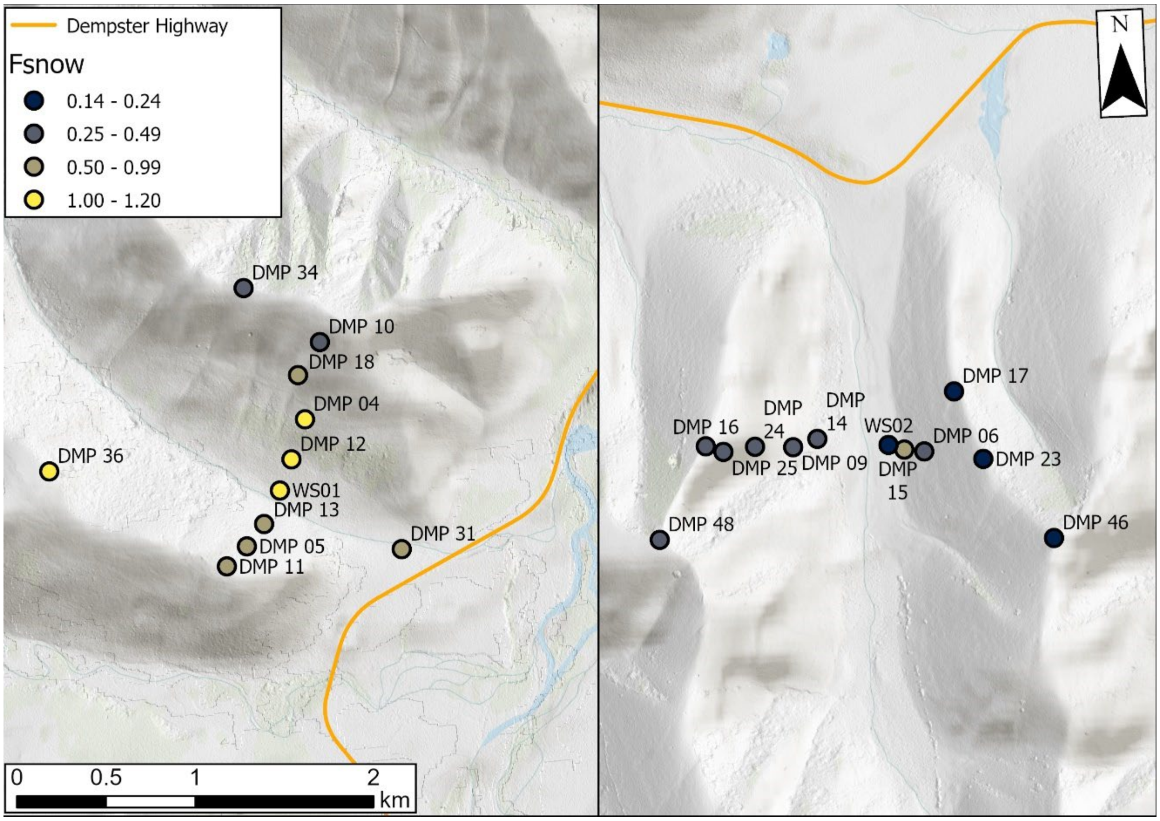

Figure 6-6: The spatial pattern of the snow input factor (F_{snow}) in the WS01 (left) and WS02 (right) valleys.

The NEST model simulated ground surface temperatures (GST) well across most sites (Table 6-4; for R^2 and KGE see Table 6-10). Mean GST biases were generally small, ranging between −0.49 and 0.49 °C, while RMSE values ranged from 1.62 to 3.82 °C. Model performance metrics were consistently high, with NSE values typically exceeding 0.85, and KGE typically > 0.75 at most sites.

Model performance was similarly strong for ground temperatures at depth (GT) where observations were available. GT biases ranged from -0.59 to 0.14 °C, RMSE values generally ranged between 0.77 and 3.19 °C, NSE values commonly exceeded 0.85, and KGE typically > 0.60.

The timing of seasonal transitions in GST was also reproduced reasonably well. The onset of thawed conditions at the surface was generally delayed by up to 21 days at some sites, though differences were typically ≤14 days at most sites. In contrast, the onset of freezing was reproduced more accurately, with deviations within ±5 days.

Table 6-4: Calibration metrics for both ground surface temperature (GST) and ground depth temperature (GT) for each of the study sites. * indicates that the calibration was only run based on part of the observational period. In the case of WS01 and WS02 only data from 2017-2019 were used due to issues with frost heaving of the GT sensor in later years.

		Ground Surface					Ground Depth		
Site	n	Bias (°C)	RMSE (°C)	NSE	Thaw Bias (days)	Freeze Bias (days)	Bias (°C)	RMSE (°C)	NSE
DMP04	2905	0.31	1.68	0.92	18	-1	0.15	0.93	0.93
DMP05	2317	-0.06	2.25	0.89	14	-1	-0.01	1.84	0.84
DMP06	2902	-0.16	3.82	0.88	16	0	-0.19	3.18	0.89
DMP09	2551	-0.03	3.14	0.89	21	0	-0.19	1.97	0.89
DMP10	1459	0.00	3.79	0.83	13	0	-0.57	2.92	0.84
DMP11	1459	-0.09	2.59	0.89	7	-3	-0.22	2.25	0.88
DMP12	1468	-0.12	1.62	0.89	21	-1	-0.26	0.77	0.64
DMP13	1468	-0.06	2.50	0.89	3	0	-0.22	2.31	0.89
DMP14	1457	0.44	3.45	0.84	14	-3	-0.34	2.22	0.78
DMP15	1456	-0.41	3.33	0.91	10	1	-0.26	2.67	0.93
DMP16	1457	-0.36	2.09	0.94	5	-4	0.14	1.90	0.92
DMP17	1457	-0.12	3.48	0.91	17	-2	-0.59	2.70	0.93
DMP18	719	0.10	2.04	0.92	-2	0	-0.05	1.53	0.91
DMP23	1090	-0.49	3.00	0.91	7	-4	NA	NA	NA
DMP24	1091	-0.31	3.44	0.89	21	0	-0.05	3.19	0.89
DMP25	1091	-0.23	2.55	0.91	2	3	0.04	2.03	0.90
DMP31	1098	-0.21	1.82	0.94	18	-5	0.11	1.22	0.96
DMP34	719	-0.34	2.70	0.92	6	0	NA	NA	NA
DMP36	719	0.49	2.02	0.91	6	-1	NA	NA	NA
DMP46	717	-0.46	2.48	0.91	2	-2	NA	NA	NA
DMP48	717	0.00	2.65	0.89	4	-3	NA	NA	NA
WS01*	857	-0.18	1.63	0.91	8	-4	-0.20	0.65	0.82
WS02*	1222	0.19	2.02	0.92	5	-2	-0.31	1.61	0.83

Model performance is evaluated using three representative sites that capture a range of agreement between observed and simulated temperatures (Figures 6-7 and 6-8). Sites were selected based on combined GST and GT performance metrics and include a high-performing site (DMP31), an intermediate site (DMP15), and a lower-performing site (DMP11). This comparison allows for assessment of how model skill varies under different site conditions and helps identify key sources of model uncertainty.

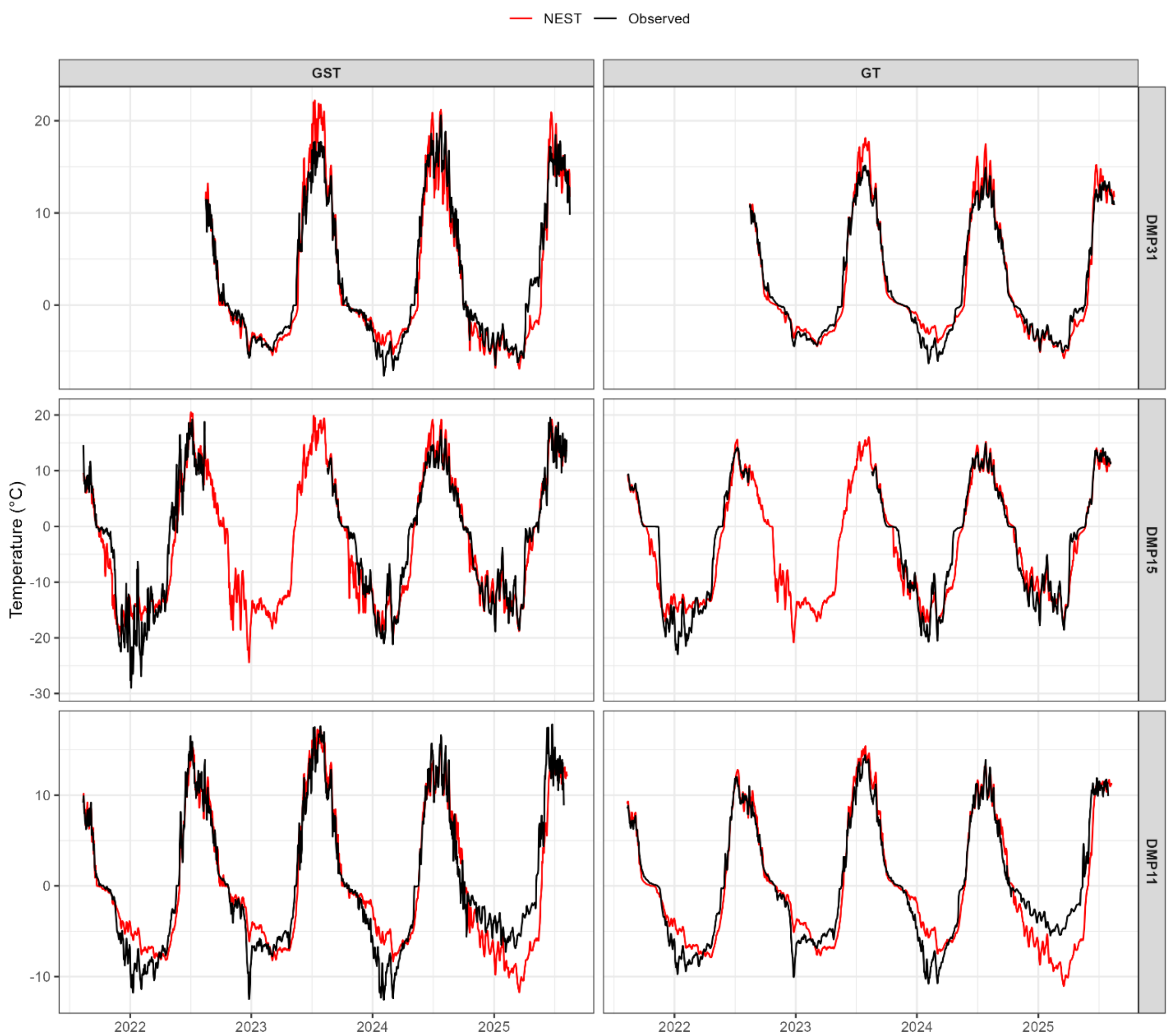

Figure 6-7: Observed and NEST-simulated daily ground surface temperature (GST) and ground temperature at depth (GT) for three representative calibration sites spanning high (DMP 31), intermediate (DMP 15), and low (DMP 11) model performance.

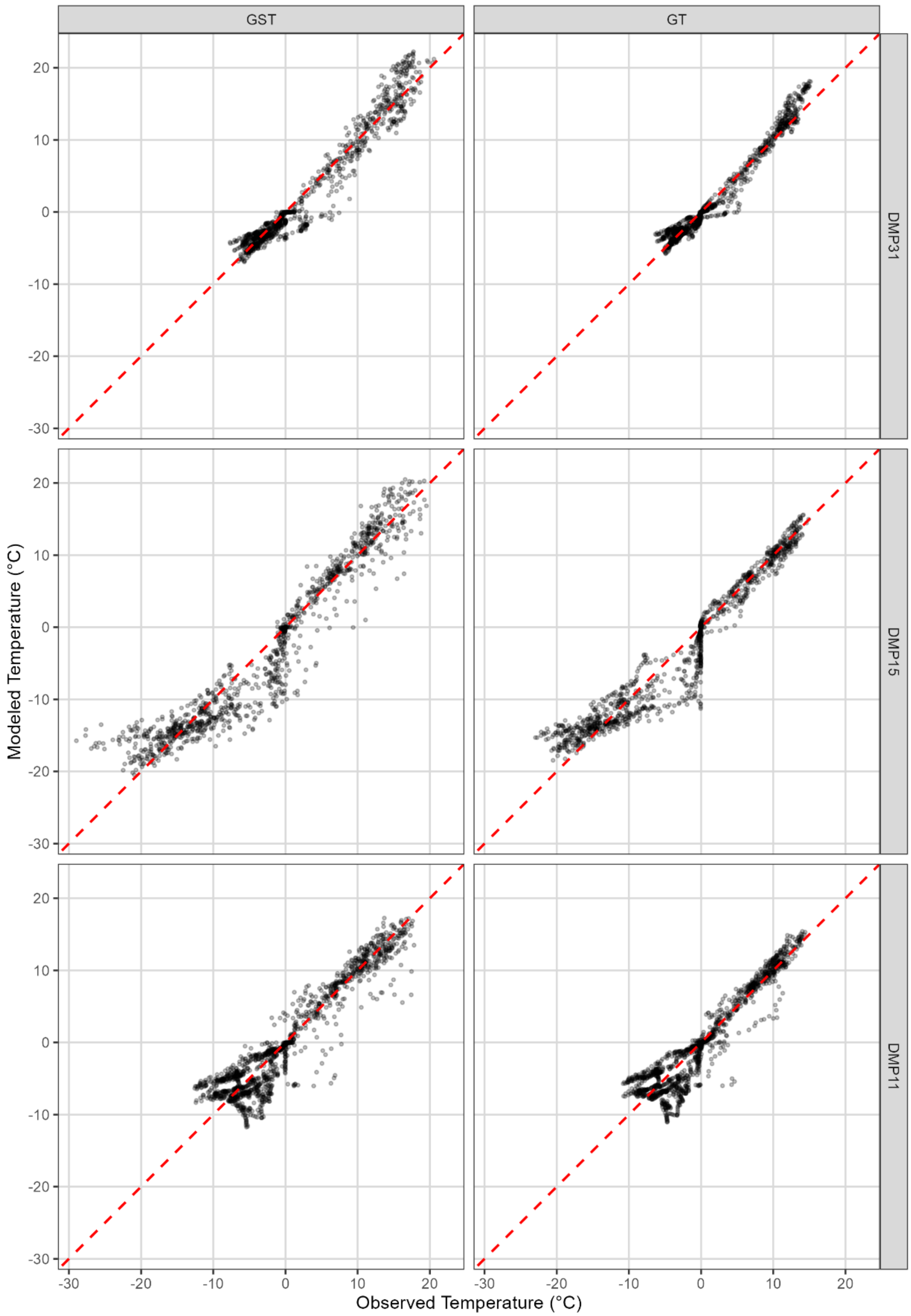

Figure 6-8: Scatterplots comparing observed and NEST-simulated daily ground surface temperature (GST) and ground temperature (GT) for three representative sites spanning high

(DMP31), intermediate (DMP15), and low (DMP11) model performance. The dashed red line indicates the 1:1 relationship.

Calibration proved more challenging at several sites with highly variable snow conditions or limited subsurface observations (e.g. absence of GT sensor). For example, site DMP14 exhibited slightly larger GST biases (0.44 °C) and lower KGE values (< 0.5), likely reflecting strong spatial variability in snow accumulation driven by wind redistribution along exposed slopes. Similar challenges were faced at other ridge and upper-slope locations where shallow soils and thin organic layers cover overly coarse gravel substrates, producing a rapid thermal response that is sensitive to small changes in snow depth and soil moisture. At sites such as DMP18, located on an upper south aspect slope, snow accumulation is minimal due to wind scouring and the ground surface consists of a moss–lichen cover over coarse substrate. These conditions resulted in larger seasonal temperature variability and slightly higher model error despite generally good overall agreement with observations.

Additional calibration challenges occurred at several blockfield and coarse talus sites, where large pore spaces between rocks may allow air circulation within the subsurface (e.g., DMP 24, DMP 25). Conversely, several forested sites with thick organic layers exhibited strongly buffered ground thermal regimes, which also required a careful calibration of soil and vegetation parameters. For example, DMP 12, located within coniferous forest with a relatively thick organic surface layer, displayed reduced seasonal temperature variability compared to most other sites. The insulating properties of the organic layer and forest canopy resulted in highly dampened seasonal ground temperature fluctuations that were difficult to reproduce within the model. Accurate calibration required careful adjustment of organic layer thickness, vegetation parameters, and snow accumulation to replicate the observed buffering of the ground thermal regime.

Sites located in areas of persistent snow accumulation also required careful calibration of snow parameters to reproduce the observed insulating effects of deep winter snowpacks. For example, DMP 36, located near the ridge of a north-facing slope where large snow cornices form, experiences delayed snowmelt until mid-June. At this site, model performance was notably weak with a KGE of -0.43 due to the thick snow depth and late spring thaw but persistently warmer wintertime ground temperatures than observed. The bias was kept to an acceptable value, 0.49 °C and other metrics such as R^2 (0.92) and NSE (0.91) supported reasonable model performance at this site.

Calibration challenges were also encountered at the WS01 and WS02 weather station sites, where the ground temperature sensors installed at depth exhibited increasing seasonal variability in later years of the record. This change likely reflects frost heave of the thermistor cables, which caused the sensors to shift upward within the substrate and therefore record temperatures at shallower depths. To reduce this source of uncertainty, model calibration at these locations was focused on the first two years of observations (2017–2019), during which the depth of the ground temperature sensors was well constrained.

Additional field observations were available at these sites to further inform the calibration process. Snow stake measurements and temperature/light sensor records were used to estimate maximum winter snow depth (Tutton & Way, 2021) during the 2024-2025 winter, while direct ALT measurements provided independent constraints on subsurface thermal conditions. The calibrated model successfully reproduced both the observed snow depths and active layer thickness at these locations, providing additional confidence in the parameter choices applied across the broader monitoring network.

6.4.3 NEST Predicted Active Layer Depth and Snow depth

Permafrost was predicted at each site except for DMP 04. Mean active layer thickness (ALT) between 2015 and 2025 ranged from approximately 0.7 m at WS02 weather station to over 7.2 m on the east aspect slope in the WS01 valley at site DMP 24 (Figure 6-9). At DMP 31 and DMP 36, modelled thaw depths increase substantially through time and the site transitioned to talik conditions late in the simulation period. As a result, values reported for these sites represent ALT prior to talik development (DMP 31 = 5.8 m, DMP 36 = 10.4 m), after which the metric is no longer directly comparable.

When plotted against elevation, ALT exhibited substantial variability with no clear elevational trend. Instead, spatial patterns of ALT were primarily associated with differences in rockiness of the substrate, vegetation type and buffering, and snow cover.

Active layer was generally the shallowest (< 2 m) at valley bottom locations characterized by thick moss and vegetation cover, which provided strong thermal insulation of the ground surface. In contrast, the thickest active layers (6-7 m) occurred at sites with coarse rocky substrates on middle to upper slopes where snow cover was limited and conductive heat transfer into the ground was enhanced. Ridgetop sites (e.g., DMP 34, DMP 46, and DMP 48) exhibited moderate active layer thickness reflecting their flatter slope leading to development of soils to buffer heat transfer in and out of the ground (approximately 2.5 – 3 m).

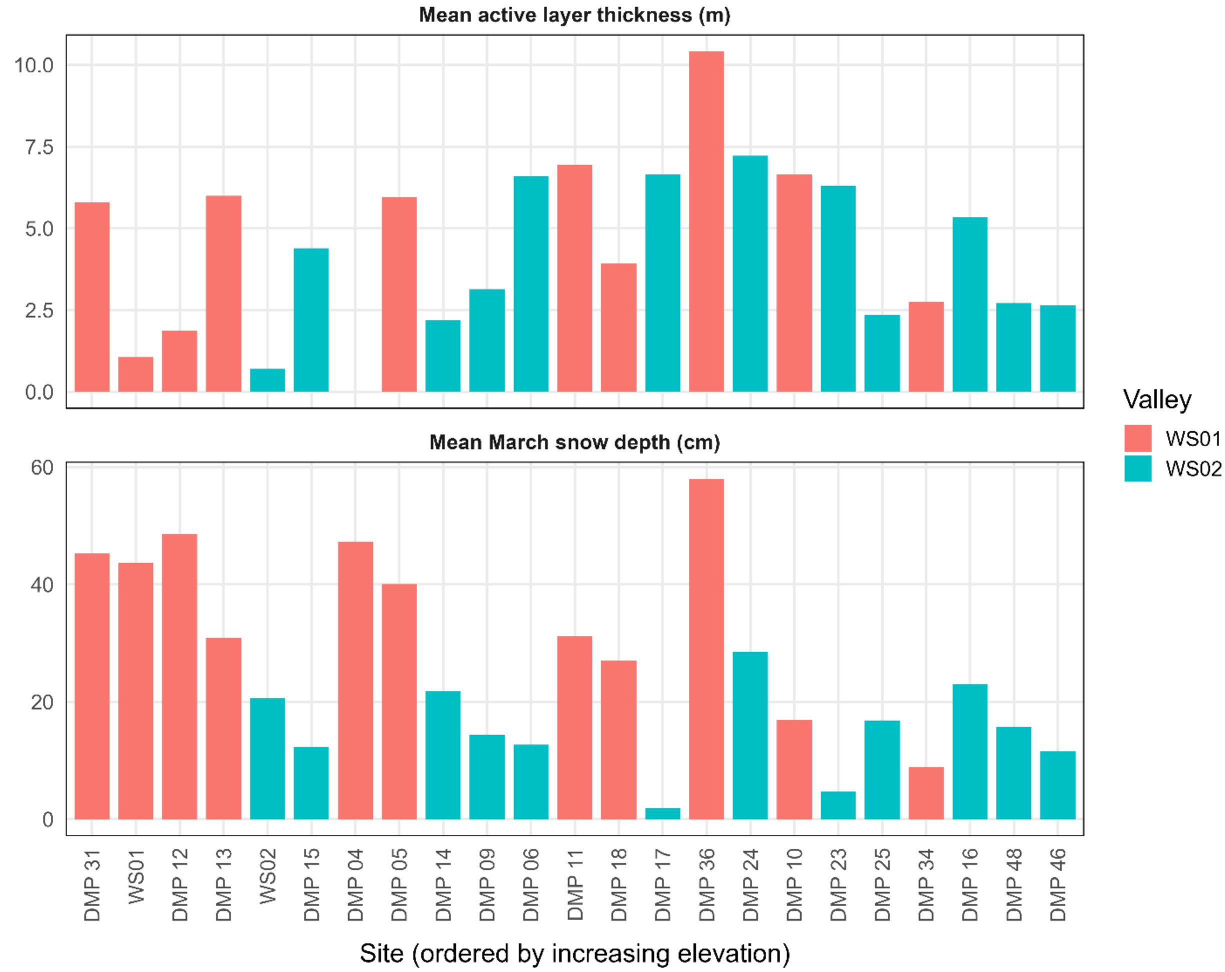

Figure 6-9: The NEST predicted mean active layer thickness (top) and mean March snow depth (bottom) at each site from 2015 to 2025. The years 2024 and 2025 were excluded for DMP 31 and DMP 36 ALT as a talik formed in those years.

ERA5-Land forcing data indicates a significant warming trend in mean annual air temperature between 1950 and 2025 (0.33 °C decade^{-1}, $R^2 = 0.37$, $p < 0.001$) and increase total annual precipitation (9.87 mm decade^{-1}, $R^2 = 0.12$, $p < 0.003$) (Figure 6-16). There was no significant trend in snowfall during the same time period. Linear trend analysis of the NEST model outputs (1950-2025) indicate that the MAGT at all sites and depths at a rate of roughly 0.21 to 0.53 °C decade^{-1} (R^2 0.29-0.50; p-value < 0.0001). Similarly, modelled ALT has increased significantly at all monitoring sites with permafrost present and no talik. ALT increased between 0.11 and 0.34 m per decade at most locations, with several sites exhibiting larger increases (Table 6-5). These trends were statistically significant at nearly all sites ($p < 0.01$), with coefficients of determination typically ranging between $R^2 = 0.25$-0.54, indicating a consistent long-term thickening of the active layer across the study region.

The largest increase in ALT (0.78 m decade^{-1}) occurred at DMP 36, located just below the crest of the north aspect slope in the WS01 valley. At this site, modelled ALT increased from approximately 9.3 m to nearly 13.4 m from 2015 to 2023, with the development of a talik since 2024. In contrast, the smallest changes were modelled at both weather stations (≤ 0.04 m decade^{-1}), where ground temperatures are strongly buffered by vegetation cover and a thick moss layer that limits seasonal heat transfer into the soil.

Table 6-5: The linear trends in active layer thickness modelled at each site (excluding DMP04 which has no permafrost) from 1950-2025.

Site	Slope (m 10 yr^{-1})	R^2	p-value
DMP_05	0.40	0.41	5.08E-10
DMP_06	0.23	0.44	6.28E-11
DMP_09	0.13	0.28	9.13E-07
DMP_10	0.34	0.50	1.35E-12
DMP_11	0.31	0.36	1.19E-08
DMP_12	0.12	0.29	5.68E-07
DMP_13	0.34	0.46	2.34E-11
DMP_14	0.07	0.38	3.30E-09
DMP_15	0.21	0.39	1.60E-09
DMP_16	0.24	0.43	9.44E-11
DMP_17	0.20	0.49	2.19E-12
DMP_18	0.19	0.13	0.001181
DMP_23	0.20	0.46	1.22E-11
DMP_24	0.31	0.54	5.31E-14
DMP_25	0.11	0.45	2.64E-11
DMP_31	0.44	0.12	0.01986
DMP_34	0.08	0.21	2.71E-05
DMP_36	0.78	0.53	1.45E-13
DMP_46	0.08	0.37	6.65E-09
DMP_48	0.08	0.34	2.84E-08
WS01	0.04	0.31	1.64E-07
WS02	0.02	0.27	1.31E-06

Representative modelled ALT trajectories illustrate contrasting permafrost responses across the study area, including rapid degradation, long-term stability, and intermediate behavior influenced by atmospheric forcing and snow insulation (Figure 6-10).

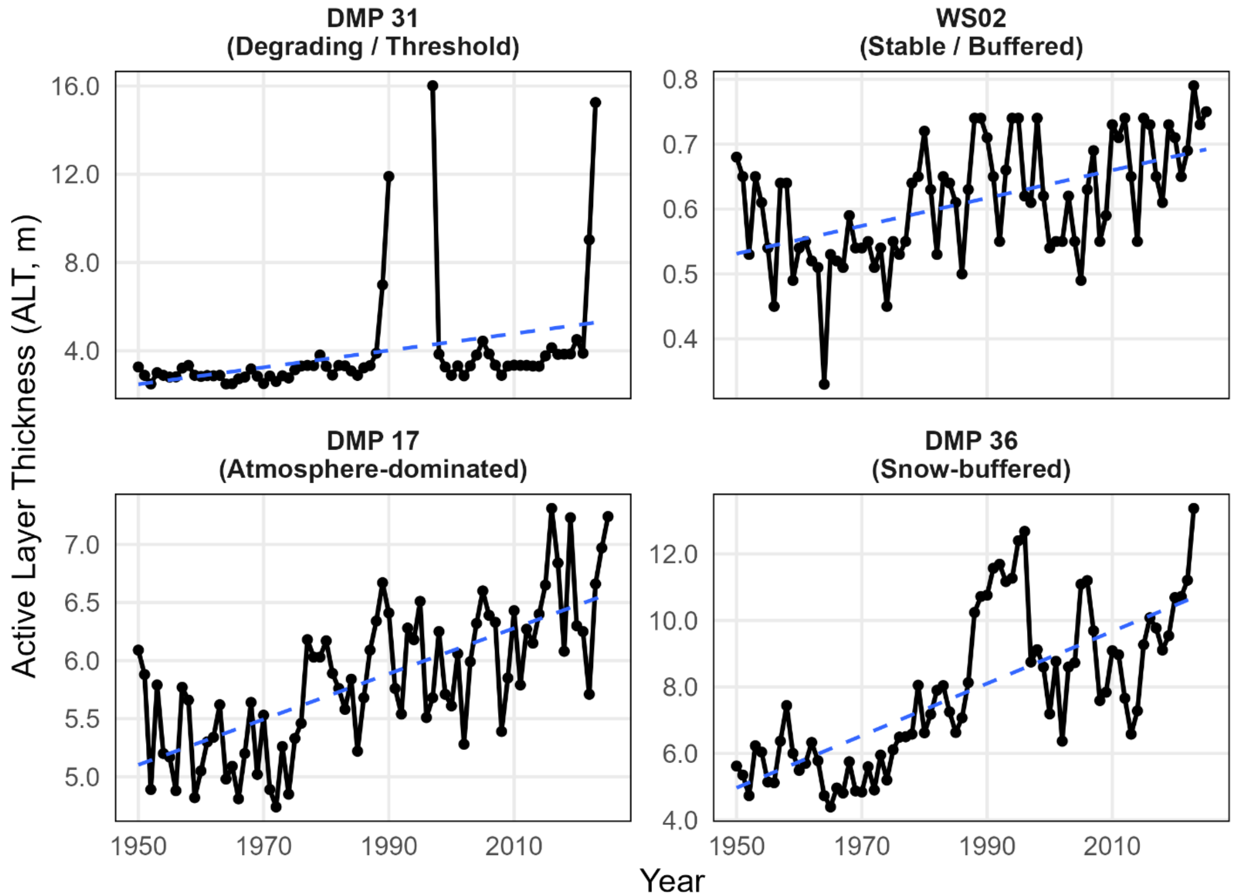

Figure 6-10: Modelled active layer thickness (ALT) from 1950-2025 for four representative sites illustrating contrasting permafrost response types. DMP 31 shows rapid, nonlinear increases in thaw depth indicative of permafrost degradation threshold behavior and formation of a talik (those years excluded), whereas WS02 remains relatively stable over time due to strong insulation from a thick moss layer. Intermediate responses are observed at DMP 17, where ALT is strongly influenced by atmospheric forcing due to shallow snow depth and rocky substrate, and DMP 36, where deep snow cover insulates the ground thermal regime form the winter atmosphere while the substrate is particularly rocky. These trajectories highlight the spatial variability in permafrost sensitivity across the study area.

Mean snow depth (2015 – 2025) in March ranged from 58.0 cm at DMP 36, where a persistent cornice formed just below the ridge crest, 1.9 cm at DMP 17, a strongly wind scoured slope site in WS02 valley (Figure 6-9). Typically snow depth was greater in the WS01 valley compared to the WS02 valley, particularly in the valley bottom where open coniferous forest promotes snow trapping. In contrast, the more open valley geometry and orientation promote wind exposure (Noad & Bonnaventure, 2023) leading to increased snow scouring at most sites in WS02.

Snow cover duration exhibited significant negative trends at most sites, with decreases ranging from approximately 1.4-2.3 days decade^{-1}. These results indicate a shortening of the seasonal snow cover period across the study area. Reduced snow cover duration likely contributes to the increases in ALT by extending the thaw season and increasing the cumulative energy available for ground warming.

6.4.4 Removal of the Local Adjustment Factor for Air Temperature

Removal of the local air temperature adjustment factor resulted in systematically cooler ground temperatures across all depths and a reduction in modeled ALT at all sites with permafrost present (Table 6-6). This scenario isolates the influence of SBI-related atmospheric forcing while retaining spatial variability in snow redistribution. On average, ALT decreased by 0.82 m, while MAGT decreased by approximately 0.9-1.0 °C from 0.05 to 7.1 m depths.

The largest reduction of ALT occurred at DMP 18, DMP 10, and DMP 36. DMP 10 and DMP 18 are wind scoured sites on the south facing slope in the WS01 valley. DMP 36 was located adjacent to the ridgetop of the north aspect slope where redistributed snow accumulated. The next largest ALT decrease, approximately 1.5 m, occurred at DMP 31, on the floodplain in the valley bottom of WS01 valley. The largest MAGT decrease occurred at DMP 17, a wind scoured site on the west facing slope in WS02 valley, where MAGT decreased by approximately 2.0 °C and ALT decreased by 1.44 m.

In addition to reducing ground temperature and thaw depths, removal of the local air temperature adjustment factor generally increased modelled snow depth and duration. Mean

March snow depth increased by 3.9 cm on average across the observational network, with the largest increase at DMP 04 (6.4 cm) and the smallest increase at DMP 31 (0.9 cm). Snow duration increased by an average of 13.8 days, ranging from 2.6 days at DMP 36 to 24.7 days at DMP 23.

Table 6-6: Mean, standard deviation (SD), minimum, and maximum changes in active layer thickness, mean snow depth, snow cover duration, and mean annual ground temperature (MAGT) at depths of 0.05, 0.55, 1.07, 2.9, and 7.1 m following removal of the local air temperature adjustment factor from the NEST model.

Metric	Mean Change	SD Change	Min Change	Max Change
Active layer thickness (m)	-0.82	0.56	-1.64	-0.09
Mean March snow depth (cm)	3.9	1.3	0.9	6.4
Snow cover duration (days)	13.8	6.0	2.6	24.7
MAGT 0.05 m (°C)	-0.9	0.4	-2.0	-0.3
MAGT 0.55 m (°C)	-0.9	0.4	-2.0	-0.3
MAGT 1.07 m (°C)	-0.9	0.4	-2.1	-0.3
MAGT 2.9 m (°C)	-1.0	0.5	-2.1	-0.3
MAGT 7.1 m (°C)	-1.0	0.5	-2.1	-0.3

Permafrost was present at all sites in this scenario, with talik formation at only two sites after 2015 (Figure 6-11). Notably, permafrost was present at DMP04 in 2015, with a talik forming in 2016 and complete loss of permafrost by 2019. In contrast, when the local air temperature adjustment factor was included as part of the calibration run, permafrost was absent at DMP 04 from 1987 onward. At DMP 31, talik formation occurred in 2024 in both the calibration and no local air temperature adjustment scenarios, indicating that the removal of the local adjustment factor had little influence on permafrost stability at this low elevation valley bottom site. DMP 36 had a talik form in the calibration scenario, but when the local air temperature adjustment was removed this location remained talik free from 2015 to 2025.

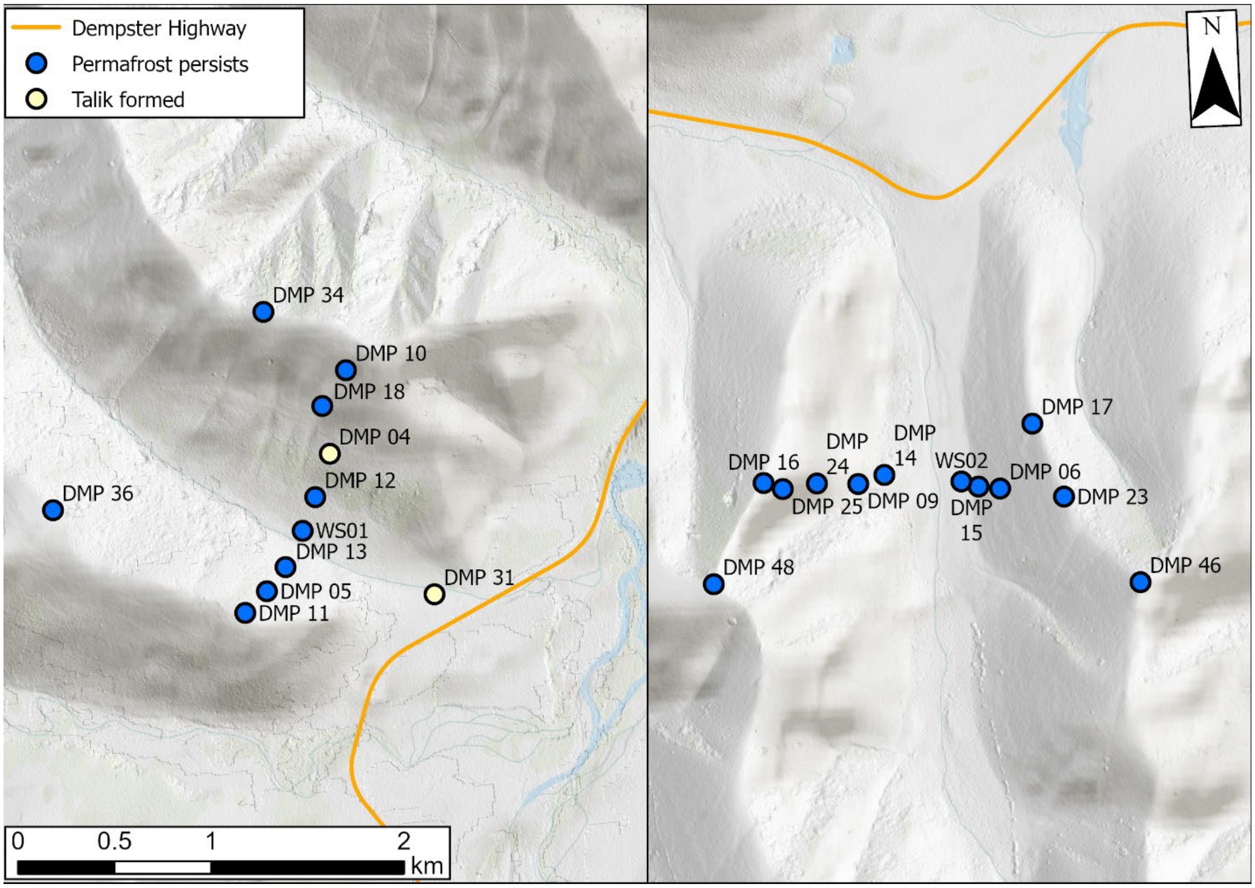

Figure 6-11: Spatial pattern of permafrost loss and talik formation in response to removing the local air temperature adjustment factor in WS01 valley (left) and WS02 valley (right). Permafrost absence was defined as no permafrost present between 2015 and 2025. Talik formation was defined as talik developing between 2015 and 2025. If talik had already formed prior to 2015, the site was classified as permafrost absent for the analysis period.

6.4.5 Removing Spatial Variability of Snow

Setting the F_{snow} equal to 1 at all sites increased modelled snow depth and duration at all sites where the original F_{snow} was less than 1. This scenario isolates the influence of snow redistribution by removing spatial variability in snow accumulation. The duration of snow cover increased on average by nearly 18 days, with snow duration increasing by nearly 60 days at DMP 17, where the F_{snow} was increased from 0.14 to 1. Similarly mean March snow depth increased on average by 23.5 cm, with the largest increase in mean snow depth by 47.8 cm at DMP 23. Snow duration and depth decreased only at sites (DMP 36 and DMP 12) with an original F_{snow} greater than 1. The largest decrease in mean snow depth was -7.9 cm and snow duration by 3.2 days at DMP 36 where F_{snow} decreased from 1.2 to 1.0.

A general increase in snow depth corresponded with warming of the ground temperature at all depths by 2.6 °C at 0.05 m depth with an increase in warming with depth to 2.9 °C at 7.1 m depth (Table 6-7). Where permafrost remained present and a talik absent, mean ALT generally increased, with an average change of 3.45 m. Under this adjusted F_{snow} scenario, permafrost was already absent prior to 2015 at 10 sites, a talik developed between 2015 and 2025 at 6 sites, and permafrost persisted without talik formation at 5 sites (Figure 6-12). The sites with calibrated F_{snow} equal to or greater than 1 (DMP 36, DMP 12, and WS01) all retained permafrost without talik formation, even though there was a talik formed at DMP 36 with the F_{snow} calibrated to 1.2. DMP 24 and WS02 were the only sites where permafrost persisted talik free and the F_{snow} increased to 1.0. In the case of DMP 24 the active layer still thickened by 3.68 m and the ground temperatures increased by approximately 1.7 °C. WS02 ALT was considerably much more stable. Although F_{snow} increased from 0.25 to 1, ALT increased only by 0.22 m, while ground temperatures increased by approximately 2.6 °C.

Table 6-7: Mean, standard deviation (SD), minimum, and maximum changes in active layer thickness (ALT), mean snow depth, snow cover duration, and mean annual ground temperature (MAGT) at depths of 0.05, 0.55, 1.07, 2.9, and 7.1 m following the assumption of spatially uniform snow input (F_{snow} = 1) relative to the calibrated simulations.

Metric	Mean Change	SD Change	Min Change	Max Change
Active layer thickness (m)	3.45	3.34	-1.46	9.02
Mean March snow depth (cm)	23.5	15.9	-7.9	47.8
Snow cover duration (days)	18.1	16.4	-3.2	60.5
MAGT 0.05 m (°C)	2.6	1.9	-0.6	5.4
MAGT 0.55 m (°C)	2.7	1.9	-0.6	5.5
MAGT 1.07 m (°C)	2.8	2.0	-0.6	5.6
MAGT 2.9 m (°C)	2.9	2.0	-0.6	5.7
MAGT 7.1 m (°C)	2.9	2.0	-0.6	5.6

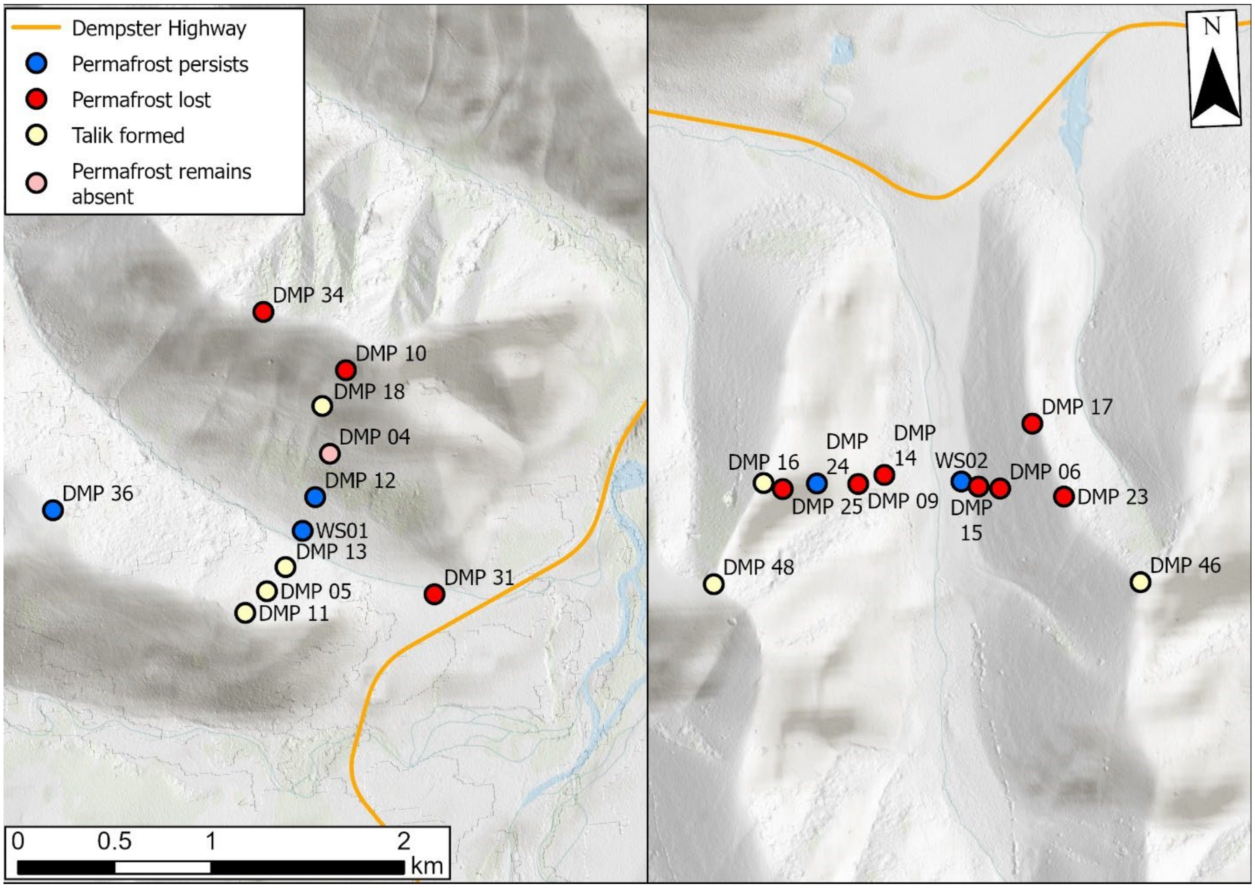

Figure 6-12: Spatial pattern of permafrost loss and talik formation response to setting $F_{snow} = 1$ in WS01 valley (left) and WS02 valley (right). Permafrost absence was defined as no permafrost present between 2015 and 2025. Talik formation was defined as talik developing between 2015 and 2025. If a talik had already formed prior to 2015, the site was classified as permafrost absent for the analysis period.

The largest ALT increase (9.02 m) occurred at the WS02 ridgetop site DMP 46, where talik developed in 2016 and ground temperatures increased by approximately 5.5 °C. In contrast, ALT and ground temperature did not change at WS01 because the calibrated F_{snow} already was equal to 1.0. DMP 36 had the largest calibrated F_{snow} value (1.2), and reducing it to 1.0 led to a decrease in ALT by 1.47 m and a decrease in ground temperature by approximately 0.6 °C.

6.4.6 Sensitivity to Local Air Temperature Adjustment Factor and F_{snow}

Only three sites exhibited a stronger ground thermal response to removal of the local air temperature adjustment factor than removal of the F_{snow} parameter (Figure 6-13). These sites were all located in the WS01 valley and include DMP 12 (near the base of the south aspect slope), WS01 (valley bottom), DMP 04 (treeline on the south aspect slope). All three sites had calibrated F_{snow} values close to 1.0 (1.0 – 1.2), resulting in limited sensitivity to the $F_{snow} = 1$ scenario. Among these, DMP 04 displayed the strongest response to removal of the local air temperature adjustment factor, likely reflecting reduced insulation from thinner vegetation and organic layers.

Sites with the greatest sensitivity to removal of the local air temperature adjustment factor were located in the WS02 valley or were above treeline on the south aspect slope in WS01 valley. These sites were characterized by rocky substrates, relatively thin snow cover (e.g., DMP 17, DMP 23, DMP 24), limited vegetation or organic layer (WS02 excluded), or being particularly exposed to solar energy on the south aspect slope (DMP 10 and DMP 18), which enhanced coupling between the atmospheric forcing and ground temperatures.

In contrast, sites most sensitive to removal of the F_{snow} parameter were typically at locations with low snow accumulation and the smallest calibrated F_{snow} values (e.g. DMP 17, DMP 23, and DMP 46). Most of these sites were located in the WS02 valley, where snow was generally thin. DMP 34 represents an exception within the WS01 valley, as its exposed ridgetop position results in strong snow scouring and correspondingly the lowest calibrated F_{snow} valley in this valley.

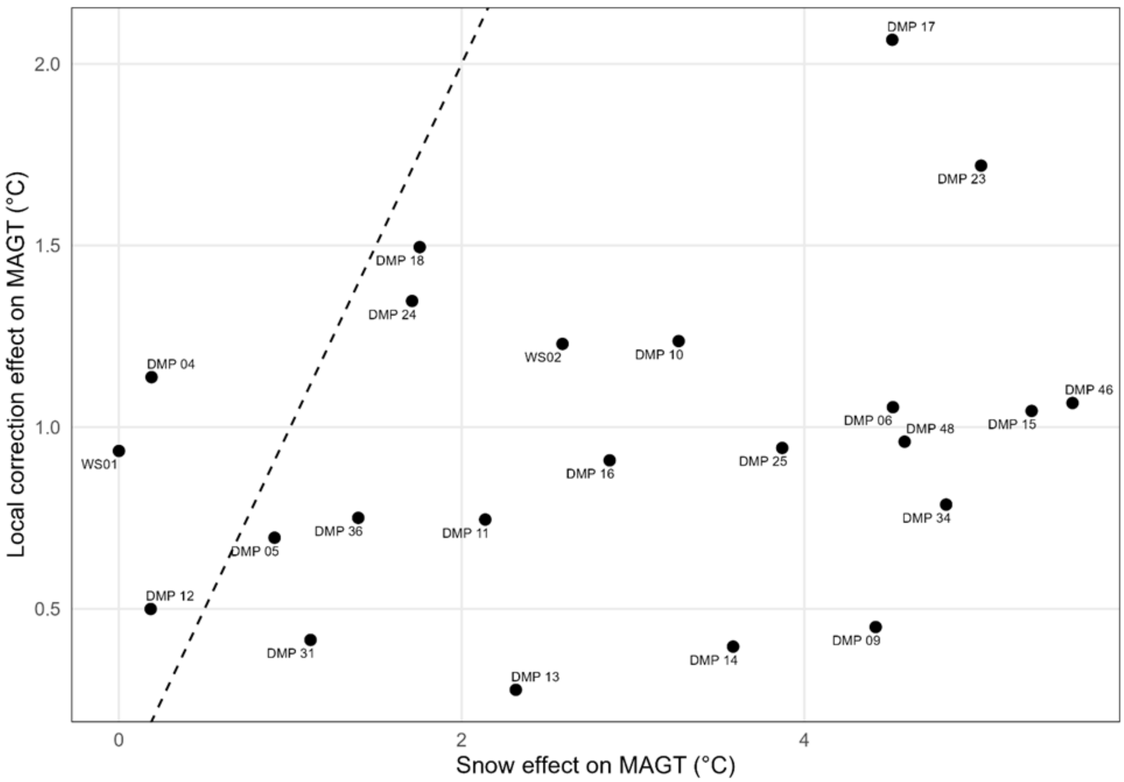

Figure 6-13: Distribution of mean annual ground temperature (MAGT) change, averaged across depths of 0.05, 0.55, 1.07, 2.90, and 7.10 m, in response to removal of the local atmospheric adjustment factor and the F_{snow} parameter. Points to the left of the 1:1 line indicate greater sensitivity to removal of the local air temperature adjustment factor, while points to the right indicate greater sensitivity to removal of F_{snow}.

While the individual sensitivity analysis experiments highlight the dominant role of snow redistribution and the secondary influence of local atmospheric adjustment, these processes do not operate independently in natural systems. To better understand their combined effects on ground thermal conditions and permafrost stability, the next section evaluates the NEST model behaviour when both F_{snow} and local atmospheric adjustments are removed.

6.4.7 Removal of both the Local Air Temperature Adjustment and F_{snow} Variability

When both the local air temperature adjustment factor and F_{snow} parameter were removed, the increases in ALT and ground temperatures modelled in the scenario where only F_{snow} was set to

1, was partially offset. The mean increase in ALT was 2.54 m, compared to 3.45 when only the F_{snow} was set to 1 (Table 6-8).

Despite the partial offset, substantial site-specific variations remained. At DMP 15, located at the base of the west aspect slope in WS02 valley, ALT increased by 9.90 m prior to talik development in 2016. In contrast, the largest decrease in ALT (-2.97) occurred at DMP 36, where F_{snow} was reduced from 1.2 to 1.0 and removal of the local air temperature adjustment factor resulted in cooler air temperatures.

Ground temperatures exhibited a similar but moderated response. MAGT increased by approximately 2.3 °C when both the local adjustment factor and F_{snow} variability were removed, compared to approximately 2.8 °C when only F_{snow} was set to 1. Ground temperature increased most at DMP 46 (approximately +5.3 °C), only slightly less than in the F_{snow} = 1 scenario. Ground temperature only decreased at two sites (DMP 12 and DMP 36), with the largest decrease, (-1.4 °C) occurring at DMP 36.

Mean March snow depth substantially increased (28.1 cm) in this combined scenario, exceeding increases observed in either individual sensitivity experiment (no local air temperature adjustment factor = 3.9 cm, no F_{snow} = 23.5 cm). The largest increase in mean March snow depth was 52.9 cm at DMP 23 where the F_{snow} was increased from 0.15 to 1.0 and the colder atmospheric forcing (due to the removal of the local air temperature adjustment factor) led to enhanced snow depth. Mean March snow depth decreased only at one site (DMP 36; -5.4 cm), where the reduction in F_{snow} dominated despite colder conditions.

Snow cover duration showed a similarly amplified response, with a mean increase of 26.9 days, compared to the 18.1 days for the removal of F_{snow} only and 13.8 days for the removal of only the local air temperature adjustment factor scenario. The largest increase in mean snow cover duration was 71.5 days at DMP 17, reflecting the combined effects of increased snow accumulation and colder air temperatures. Again, DMP 36 was the only location in this scenario that had a decrease in mean snow cover duration (-0.8 days).

Table 6-8: Mean, standard deviation (SD), minimum, and maximum changes in active layer thickness (ALT), mean March snow depth, snow cover duration, and mean annual ground temperature (MAGT) at depths of 0.05, 0.55, 1.07, 2.9, and 7.1 m following the assumption of spatially uniform snow input (F_{snow} = 1) and removal of the local air temperature adjustment factor for atmospheric forcing data relative to the calibrated simulations.

Metric	Mean Change	SD Change	Min Change	Max Change
Active layer thickness (m)	2.54	3.48	-2.97	9.90
Mean snow depth (cm)	28.1	16.2	-5.4	52.9
Snow cover duration (days)	26.9	14.8	-0.8	71.5
MAGT 0.05 m (°C)	2.1	2.0	-1.3	5.2
MAGT 0.55 m (°C)	2.2	2.1	-1.4	5.3
MAGT 1.07 m (°C)	2.3	2.1	-1.4	5.3
MAGT 2.9 m (°C)	2.3	2.1	-1.5	5.4
MAGT 7.1 m (°C)	2.3	2.1	-1.5	5.4

These combined effects led to substantial changes in permafrost state (Figure 6-14). Permafrost was absent or already developed a talik prior to 2015 at 7 sites, a talik formed between 2015 and 2025 at 10 sites, and permafrost persisted talik free at 6 sites. Notably, permafrost was present at DMP 04 in this scenario, with a talik forming in 2019. This indicates that removal of the local air temperature adjustment factor promotes permafrost presence at this site when it is absent in the control and the removal of F_{snow} scenario.

In comparison to the removal of F_{snow} scenario, four sites that previously exhibited permafrost absence or talik formation prior to 2015, instead developed a talik between 2015 and

2025. Additionally, two sites (DMP 05 and DMP 12) retained permafrost without talik formation in this combined scenario but developed a talik when only the F_{snow} was set to 1. Overall, these results indicate that removing the local atmospheric forcing adjustments partially offsets the strong warming effects associated with increased snow accumulation, leading to a modest stabilization of permafrost despite the deeper and more persistent snow cover. This highlights the competing roles of snow insulation and atmospheric forcing in controlling permafrost stability across the study area.

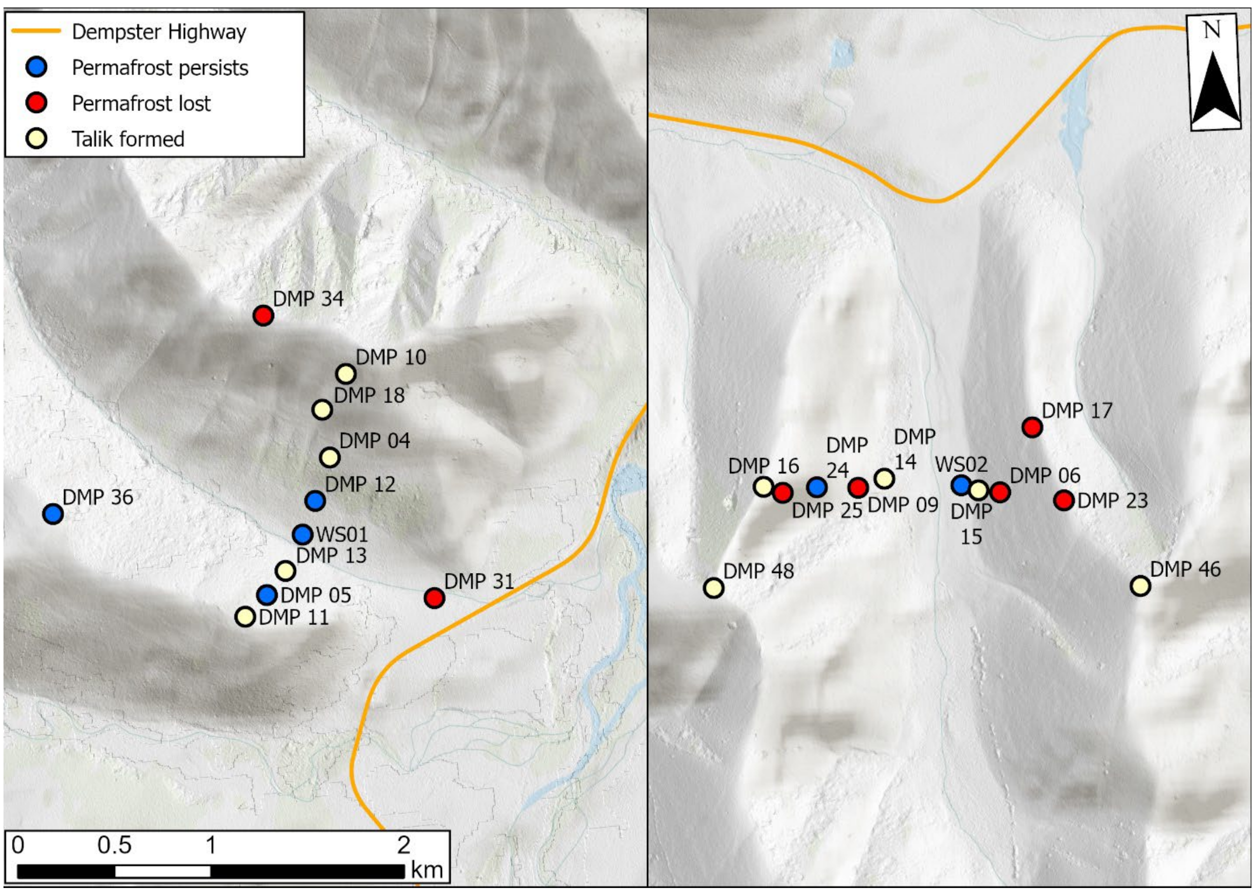

Figure 6-14: Spatial pattern of permafrost loss and talik formation in response to setting F_{snow} = 1 and removal of the local air temperature adjustment factor for the climate forcing data in WS01 valley (left) and WS02 valley (right). Permafrost absence was defined as no permafrost present between 2015 and 2025. Talik formation was defined as talik developing between 2015 and 2025. If talik had already formed prior to 2015, the site was classified as permafrost absent for the analysis period.

6.5 Discussion

6.5.1 Local Air Temperature Adjustment Factor

The local air temperature adjustment factor was applied to account for the local topographic influences on air temperature. Comparisons between ERA5-Land and in situ observations revealed a systematic cold bias, particularly for Tmin, which was strongest during the winter at higher elevations. This pattern reflects the influence of surface-based temperature inversions (SBIs), which dominate the winter temperature structure and nocturnal conditions throughout the year in these valleys (Noad & Bonnaventure, 2023; 2026). These findings are consistent with previous work showing that reanalysis surface temperature products often show strong elevation-dependent biases in complex terrain, particularly for Tmin due to cold air pooling (Cao et al., 2017; Roberts et al., 2019; Sadoti et al., 2018).

The magnitude and direction of the local air temperature adjustment factor varied seasonally. In winter, both Tmin and Tmax adjustment factors increased with elevation, reflecting colder than observed biases at higher elevation sites. In contrast, summer Tmax exhibited a warm bias at higher elevations, while Tmin at lower elevations in WS01 had cold bias due to regular nocturnal cold air pooling that frequently occurs in mountain valleys (Lundquist & Cayan, 2007; Rupp et al., 2020). Together, these results indicate that ERA5-Land does not capture lapse rate structure or SBI dynamics in these valleys, similar to the performance of the parent ERA5 surface air temperature metric when downscaled in nearby Dawson (Pozsgay & Gruber, 2025).

Notably, the largest biases occurred at high elevation sites, suggesting that reanalysis products are more representative of valley bottom conditions than ridgetop environments. This may reflect the influence of observational data used in reanalysis assimilation, which are typically concentrated at lower elevations. Thus, temperature gradients across complex terrain are not fully resolved. Previous work has shown that surface air temperature products better represent valley bottom conditions, whereas pressure level temperature more accurately reflects free-atmosphere conditions at high elevation locations (Cao et al., 2017). Inversion-aware correction approaches, such as DReaMIT, attempt to reconcile these differences by incorporating elevation or relative topographic position into reanalysis model bias correction (Pozsgay & Gruber, 2025; Pozsgay et al., 2026).

These findings highlight an important limitation of utilizing surface air temperature reanalysis forcing in complex terrain. Without accounting for systematic bias, temperature fields will misrepresent the spatial structure of SBIs, leading to systematic errors in permafrost predictions. Given that SBI strength varies with topographic position, failure to account for these effects may result in underestimation of ground temperatures at slope and ridgetop sites and overestimation of permafrost stability for these environments.

Consistency in the seasonal pattern of air temperature bias suggests that monthly air temperature adjustment factors derived from limited observational periods are transferable across years (Figure 6-15). This supports the assumption of temporally stable bias patterns, which is critical for applying bias corrections in transient permafrost modelling. Similar temporal stability has been observed in snow redistribution patterns in Arctic and mountainous environments (Parr et al., 2020; Pflug et al., 2021; Sturm & Wagner, 2010), suggesting that both atmospheric and snow processes exhibit persistent spatial and temporal structure. That said, long term changes in climate may alter elevational patterns of air temperature bias (Garibaldi et al., 2024a; Pepin et al., 2015; Pozsgay & Gruber, 2025) and snow redistribution with changes in snow density, wind patterns, and vegetation (Liston & Sturm, 1998; Sturm et al., 2001; Wang & Way, 2025).

Therefore, some uncertainty remains when assuming temporally stable patterns of air temperature bias and local snow redistribution.

6.5.2 The Dominant Control of Snow Redistribution

The calibrated F_{snow} values ranged from 0.14 to 1.20, indicating a significant spatial variability in snow accumulation across the landscape. When this variability was removed, large and systematic changes in ground thermal regime and permafrost state were observed at most sites. Since most sites in this exposed mountainous terrain are characterized by wind-scoured snowpacks, imposing uniform snow conditions resulted in substantial increases in snow depth at most locations. This led to mean increases in ground temperature of approximately 2.8 °C, mean thickening of the ALT by 3.45 m, and widespread permafrost degradation through talik formation or complete loss of permafrost at 14 sites previously simulated as stable permafrost.

These results demonstrate that, in snow-scoured mountain environments, failure to represent spatial variability of snow redistribution leads to systematic underprediction of permafrost presence and stability. In contrast, at only a few sites where calibrated F_{snow} was greater than 1 (e.g., DMP 36), reducing F_{snow} to 1 resulted in decreased snow depth, colder ground temperatures, and thinner active layers. This highlights that both under and overestimation of snow accumulation can lead to substantial biases in modeling ground thermal conditions.

Overall, these findings confirm that spatial variability of snow redistribution is a dominant control on ground thermal regimes in high-latitude mountainous environments, consistent with other studies (Etzelmüller & Frauenfelder, 2009; Gisnås et al., 2014; Gisnås et al., 2016; Hasler et al., 2015; MacDonald et al., 2009). These studies demonstrate that wind redistribution, vegetation, and topography generate highly heterogeneous snow cover, which in turn strongly controls ground temperatures and permafrost stability across short spatial distances. The results here extend this understanding by showing that neglected snow redistribution not only alters thermal conditions, but can fundamentally change modelled permafrost presence and state at locations across the landscape. Thus, accurate representation of snow redistribution patterns should be considered essential for modelling permafrost dynamics in complex mountainous terrain.

6.5.3 Hierarchy and Interactions of Controls

Snow redistribution, represented by F_{snow}, was the primary control on the ground thermal regime and permafrost state across the study area. That said, the local air temperature adjustment factor, which was strongly influenced by SBIs, acted as an important secondary control. These results demonstrate that snow and local atmospheric forcing adjustments do not operate independently but rather interact to regulate ground thermal conditions because snow conditions are also sensitive to air temperature.

The influence of local atmospheric adjustment factor was strongly mediated by snow conditions. At sites where F_{snow} was < 1, removing F_{snow} generally reduced the thermal response to removal of the local air temperature adjustment factor, consistent with deeper snow increasing decoupling of the atmosphere from the ground (Garibaldi et al., 2026; Smith & Riseborough, 2002). In contrast, at sites where calibrated F_{snow} was greater than 1, reducing snow input to 1 increased the thermal response to removal of the local air temperature adjustment factor, supporting stronger atmospheric coupling under thinner snow conditions. This shows that snow accumulation not only directly influences ground temperatures but also controls the extent to which atmospheric forcing propagates into the subsurface.

These findings are consistent with previous research showing that topography and vegetation driven snow accumulation exerts a dominant control on spatial patterns of permafrost stability (Garibaldi et al., 2021; Way & Lewkowicz, 2018; Zhang et al., 2018). In this study, this control operates both directly, through insulation of the ground, and indirectly by controlling sensitivity to atmospheric processes such as SBIs. This helps explain why SBI-driven air temperature patterns do not translate linearly to ground temperatures across this landscape (Garibaldi et al., 2024b).

Site-specific characteristics further influence these interactions. Locations with minimal snow cover, limited vegetation cover, and coarse substrates (e.g., DMP 17 and DMP 23) showed the greatest sensitivity to local atmospheric adjustments, reflecting strong coupling between the atmosphere and ground. This pattern was particularly evident in WS02 valley, where thin snow cover enhances coupling sensitivity to atmospheric variability despite having less impact on air temperature patterns in this valley (Noad & Bonnaventure, 2022, 2026). This makes permafrost conditions especially responsive to SBI-driven temperature variability.

Additionally, some sites (e.g., DMP 31) exhibited threshold behavior, where even relatively small changes to F_{snow} or atmospheric forcing resulted in large increases in ALT, talik formation, or complete permafrost loss. This indicates that permafrost at these location is near a critical threshold for stability, consistent with observations of rapid permafrost degradation in other studies (Devoie et al., 2019; Luo et al., 2025; Nitzbon et al., 2024). Spatial distribution of these sites suggest permafrost degradation may be progressing downslope into the valley bottom environments from treeline on the south aspect slope in the WS01 valley, consistent with conceptual models proposed by Bonnaventure and Lewkowicz (2013).

Finally, while snow redistribution exerts the dominant control on spatial variability, atmospheric forcing remains critical in settling the baseline thermal regime. Model results show that removal of the local air temperature adjustment factor led to widespread cooling of the ground and stabilization of permafrost, even though removing the local air temperature adjustment factor caused snow depth to increase. This indicates that the magnitude of atmospheric forcing can offset parts of the insulating effects of snow, particularly at exposed higher elevation sites. This highlights that snow and ground thermal interactions cannot be interpreted independently of the atmospheric conditions that control both snow accumulation, metamorphosis, and surface energy transfer (Smith & Riseborough, 2002; Zhang, 2005).

6.5.4 Comparison to Other Permafrost Modelling

Permafrost distribution in the study valleys has previously been modelled using the TTOP approach (Garibaldi et al., 2024b), which predicted permafrost presence at most sites in this study, except for DMP 04, DMP 12, and DMP 05. In this current study, calibrated runs of NEST predicted permafrost to be absent at DMP 04 and present at all other sites including DMP 12 and DMP 05. These results are broadly consistent with an earlier empirical-statistical model (Bonnaventure et al., 2012) and the TTOP model, both of which identified DMP 04 as having the lowest permafrost probability or warmest ground temperature.

However, model sensitivity experiments highlight important differences. When F_{snow} was set to 1, permafrost was lost or a talik formed at 14 sites, most of which were in the WS02 valley where permafrost was considered continuous in the TTOP model. In contrast, removal of the local air temperature adjustment factor resulted in permafrost being present at all sites, including DMP 04, indicating that neglecting SBI-related temperature variability leads to systematic overprediction of permafrost presence. Together, these results both demonstrate that representation of local snow redistribution and atmospheric forcing adjustment are required to accurately predict permafrost distribution in this landscape.

A key limitation of previous modelling is that they do not resolve ALT, the development of taliks, or the sensitivity of the ground thermal regime conditions to changes in climate forcing. This limitation is particularly important to the study areas, where direct measurements of ALT and permafrost presence are not feasible at many slope and ridgetop locations due to coarse substrates and deep ALT (Nicholson et al., *Submitted*).

NEST simulations extend these previous approaches by resolving both ALT and the transient response of permafrost to climatic forcing. While the TTOP model suggests colder and more continuous permafrost conditions in the WS02 than the WS01 valley (Garibaldi et al., 2024b), results from NEST suggest that this permafrost is often associated with thick active layers (> 2.5 m) and is sensitive to changes in atmospheric forcing or snow accumulation (Bonnaventure & Lamoureux, 2013). Overall, these findings demonstrate that process-based models capable of resolving snow redistribution and atmospheric forcing interactions provided essential insight into both the distribution and stability of permafrost in subarctic mountain environments.

6.5.5 Limitations of NEST Model Calibration in Coarse Mountain Environments

Calibration of the NEST model was generally successful for the study sites. There were, however, several limitations that should be considered when interpreting the results.

A primary challenge was representing heat transfer process in coarse, blocky substrates. Many slope sites are characterized by blockfields, where convective heat exchange through air-filled voids, otherwise known as the chimney effect (Juliussen & Humlum, 2007; Wicky &

Hauck, 2017; Wicky et al., 2024), enhancing coupling between the atmosphere and subsurface. This process is not explicitly represented in NEST, which assumes predominantly conductive heat transfer through the subsurface (Zhang et al., 2003). As a result, the model tended to slightly over-buffer ground temperatures at these sites. To compensate, the volumetric stone content was increased during calibration to approximate increased heat transfer, though this remains a simplified representation of a complex physical process.

A second limitation is the lack of direct ALT observations at most sites. The rocky substrate and deep thaw prevented direct probing of permafrost and ALT across much of the landscape (Nicholson et al., *Submitted*). Consequently, calibration relied primarily on ground temperature measurements at the surface and at shallow depths (in many cases ≤0.45 m). While this approach constrains the thermal regime, it introduces additional uncertainty in modelled ALT, particularly at sites with limited subsurface observations. Greater confidence was found at WS01 and WS02 weather station sites where ALT were available.

Uncertainty is also associated with snow depth representation, as snow depth was inferred at only the two weather station sites for the 2024-2025 winter using light and temperature pendants (Tutton & Way, 2021).

Finally, sensor stability issues related to frost heave affected some ground temperature measurements, as freezing-induced ground displacement which can cause vertical movement of soil and embedded instruments (Gruber, 2020). At both weather stations, rapidly increasing seasonal temperature amplitudes in later years suggest upwards movement of the depth ground temperature sensor. To minimize this bias, only early period data (2017-2019) were used for calibration, while later observations were excluded.

Despite these limitations, the calibration approach was designed to remain physically realistic and consistent across sites. The results therefore provide a realistic representation of relative differences in ground thermal dynamics and sensitivity across the landscape, even where absolute ALT and talik formation are more uncertain.

6.5.6 Implications of Findings and Future Work

Failure to represent snow redistribution is likely to result in the largest errors in both permafrost distribution and ALT. This is further supported by sensitivity analyses, which show that snow redistribution exerts a larger influence on ground thermal conditions than atmospheric forcing adjustments at most sites. Additionally, SBI-related local adjustments to air temperature represented an important secondary influence that interacts with snow accumulation and ground-atmosphere coupling. The process-based NEST model enabled these controls to be evaluated under transient climate conditions. Providing insight into active layer evolution and patterns of permafrost degradation, including talik formation.

The strong, nonlinear response observed at sites such as DMP 31 suggests that portions of the landscape may be near a tipping point, where modest climatic changes could trigger rapid permafrost degradation. This response is consistent with previous NEST modelling that showed ALT can increase rapidly as permafrost approaches talik formation, whereas changes remain comparatively much smaller under more stable permafrost conditions (Zhang, 2013). The most vulnerable areas include valley bottom and floodplain environments with coarse substrates and intermediate snow cover, as well as south aspect slopes below treeline where snow is thicker and increased solar radiation and warmer air promote thaw (Thaler et al., 2023). Together, these patterns suggest that topographic controls, particularly aspect and snow accumulation, play a critical role in determining where permafrost is most susceptible to near-term thaw.

These findings also highlight the importance of accurately representing atmospheric forcing in the permafrost models. In complex mountain terrain, SBIs strongly impact surface air temperature patterns (Noad & Bonnaventure, 2022, 2026), and failure to account for these effects can introduce bias (Noad et al., *Submitted*). Options for correcting for SBI-related bias have recently been developed (Pozsgay & Gruber, 2025; Pozsgay et al., 2026) and provide an important next step for improving model forcing and enabling more realistic local or regional scale permafrost predictions.

A key uncertainty for future projections is the potential for evolution of SBI dynamics due to climate change. Recent studies suggest that the frequency, depth, and strength of SBIs may shift in a warming climate (Pozsgay & Gruber, 2025; Ruman et al., 2022). If SBIs become weaker and less frequent the local air temperature adjustment factors derived under present day conditions may no longer be valid, potentially altering SLRs and amplifying warming at valley bottom locations (Garibaldi et al., 2024a). Therefore, incorporating time varying SBI dynamics represents an important direction for improving permafrost projections in high-latitude mountain environments.

This study also highlights the need to extend modelling beyond the predominantly coarse substrate, sparsely vegetated slope environments considered here. Many sites are characterized by limited soil development, thin organic layers, and shallow snow cover, conditions that promote strong coupling between air and ground temperatures. In contrast, lower elevation environments are likely to exhibit greater vegetation cover, thicker organic layers, and deeper snowpacks, resulting in more thermally buffered ground conditions and potentially different responses to climatic forcing. These contrasts are further amplified by topographic controls, as low lying areas across the landscape are most prone to the impacts of cold air pooling and SBI occurrence, leading to the coldest wintertime and nocturnal air temperatures (Cao et al., 2017; Noad et al., 2023; Pozsgay et al., 2026).

Future work should therefore include a broader range of ecological and geomorphic settings to better capture landscape-scale variability in permafrost sensitivity (e.g., Tutton et al., 2021), particularly in relation to SBI-dominated temperature regimes. Expanding observations across diverse vegetation and substrate types within and adjacent to the study valleys would support the development of spatially run NEST simulations of active layer thickness and ground thermal conditions (Zhang et al., 2013). Such an approach would provide critical insight into which areas of the landscape are most vulnerable to near-term climate change and disturbance, and where permafrost is likely to persist longest.

Finally, the results have important implications for permafrost related hazards and ecological change. Field observations in this region have noted the occurrences of active layer detachment and retrogressive thaw slumps on the slopes. Given the strong coupling between atmospheric forcing and permafrost degradation, continued rapid warming in this region (Bush & Lemmen, 2019) is likely to accelerate these processes, with potentially significant consequences for landscape stability, hydrology, and ecosystem dynamics.

6.6 Conclusion

Permafrost in subarctic mountain environments is primarily controlled by spatial variability in snow redistribution, which governs both the ground thermal regime and presence or absence of permafrost across the landscape. Model results demonstrate that failure to represent this variability leads to large and systematic errors in ALT, ground thermal regime, and the state of permafrost, including widespread talik formation and permafrost loss.

Atmospheric forcing, particularly as modified by SBI processes, represents an important secondary control that sets the baseline thermal regime. While its direct influence on ground temperature is smaller than that of snow redistribution, it remains essential for accurately capturing spatial patterns of permafrost. Critically, these controls do not operate independently as snow accumulation drives the degree of decoupling between the atmosphere and ground.

The results also highlight that permafrost presence does not necessarily imply stability. Several sites exhibited strong nonlinear responses to relatively small changes in snow conditions or atmospheric forcing, indicating that portions of the landscape are near critical thresholds of permafrost degradation. These threshold dynamics suggest that modest climatic changes may trigger transitions to talik formation and permafrost loss in vulnerable areas of the landscape (e.g., south aspect slope, floodplains, and areas of deep snow accumulation in WS01 valley).

Overall, this study highlights the importance of process-based modelling approaches, such as NEST, that explicitly represent local snow redistribution, local atmospheric forcing adjustments, and their interactions. Accurate representation of these coupled processes is essential for predicting both the distribution and stability of permafrost in high-latitude complex mountain terrain that is prone to SBIs.

Ultimately, this work demonstrates that spatial variability of snow redistribution is the dominant control on permafrost in these environments, and that neglecting it can fundamentally misrepresent both the current state and future trajectory of permafrost across the landscape.

Data Availability Statement

Data used in this study can be requested upon request by contacting the corresponding author at nick.noad@uleth.ca.

Funding Statement

This research was funded by the NSERC Discovery Grant, NSERC Discovery Development Grant Program, the Northern Scientific Training Program, and Natural Resources Canada.

Conflict of Interests Statement

The authors of this manuscript have no conflicts of interest to declare in association with research presented in this article.

Acknowledgements

We acknowledge and thank the Tr'ondëk Hwëch'in and the Na-Cho Nyäk Dun First Nations for allowing us to conduct research on their traditional territory. We thank the Government of Yukon for providing us with Yukon Scientists and Explorers research licenses to complete this research. We acknowledge the time and effort provided by various field teams of researchers and students since 2017. This fieldwork has been essential to allow for this research to succeed. We acknowledge members of Nick Noad's PhD committee including Hester Jiskoot, Robert Way, Yu Zhang, and Sebastian Westermann who provided support and feedback to help improve this work. We acknowledge the resources that the University of Lethbridge and Natural Resources Canada provided that were necessary to complete this research. The funding provided by NSERC, the Northern Scientific Training program, and the Government of Canada has been essential for the success of this research.

6.7 Appendix

Table 6-9: Linear relationship between elevation and the monthly daily maximum and minimum air temperature adjustment factors. Bolded values are statistically significant. Red values indicate a negative linear slope between these variables.

Variable	Valley	Month	Slope (°C 100 m^{-1})	R^2	p-value
Maximum temperature adjustment	WS01	**Dec**	**0.81**	**0.84**	**2.80E-05**
		Jan	**0.83**	**0.84**	**2.90E-05**
		Feb	**0.84**	**0.81**	**6.20E-05**
		Mar	0.16	0.09	0.35
		Apr	**-0.71**	**0.50**	**0.01**
		May	**-0.98**	**0.66**	**0.0013**
		Jun	**-1.02**	**0.81**	**7.30E-05**
		Jul	**-1.00**	**0.82**	**5.10E-05**
		Aug	**-0.92**	**0.87**	**8.40E-06**
		Sep	**-0.94**	**0.88**	**5.90E-06**
		Oct	**-0.47**	**0.72**	**0.00053**
		Nov	**0.29**	**0.57**	**0.0043**
	WS02	**Dec**	**0.36**	**0.66**	**0.0013**
		Jan	**0.45**	**0.66**	**0.0014**
		Feb	**0.23**	**0.38**	**0.033**
		Mar	0.18	0.28	0.078
		Apr	**-0.71**	**0.79**	**0.00011**
		May	**-0.92**	**0.92**	**9.00E-07**
		Jun	**-0.97**	**0.93**	**5.90E-07**
		Jul	**-1.01**	**0.97**	**5.00E-09**
		Aug	**-0.97**	**0.97**	**7.10E-09**
		Sep	**-0.94**	**0.98**	**1.30E-09**
		Oct	**-0.48**	**0.84**	**2.80E-05**
		Nov	0.03	0.01	0.77
Minimum temperature adjustment	WS01	**Dec**	**1.45**	**0.80**	**8.60E-05**
		Jan	**1.62**	**0.84**	**2.80E-05**
		Feb	**1.53**	**0.80**	**7.80E-05**
		Mar	**1.42**	**0.82**	**5.50E-05**
		Apr	**0.69**	**0.63**	**0.0022**
		May	0.22	0.22	0.12
		Jun	**0.6**	**0.62**	**0.0025**
		Jul	**0.51**	**0.49**	**0.012**
		Aug	0.3	0.30	0.065
		Sep	0.05	0.01	0.79
		Oct	0.32	0.21	0.13
		Nov	**0.96**	**0.67**	**0.0011**
	WS02	**Dec**	**0.65**	**0.82**	**5.30E-05**
		Jan	**0.8**	**0.86**	**1.60E-05**
		Feb	**0.63**	**0.80**	**9.40E-05**

	Mar	**0.85**	**0.92**	**8.40E-07**
	Apr	-0.05	0.03	0.6
	May	**-0.33**	**0.51**	**0.0086**
	Jun	**-0.33**	**0.43**	**0.021**
	Jul	-0.36	0.21	0.14
	Aug	-0.31	0.18	0.17
	Sep	**-0.69**	**0.80**	**8.70E-05**
	Oct	**-0.31**	**0.52**	**0.0086**
	Nov	0.21	0.25	0.1

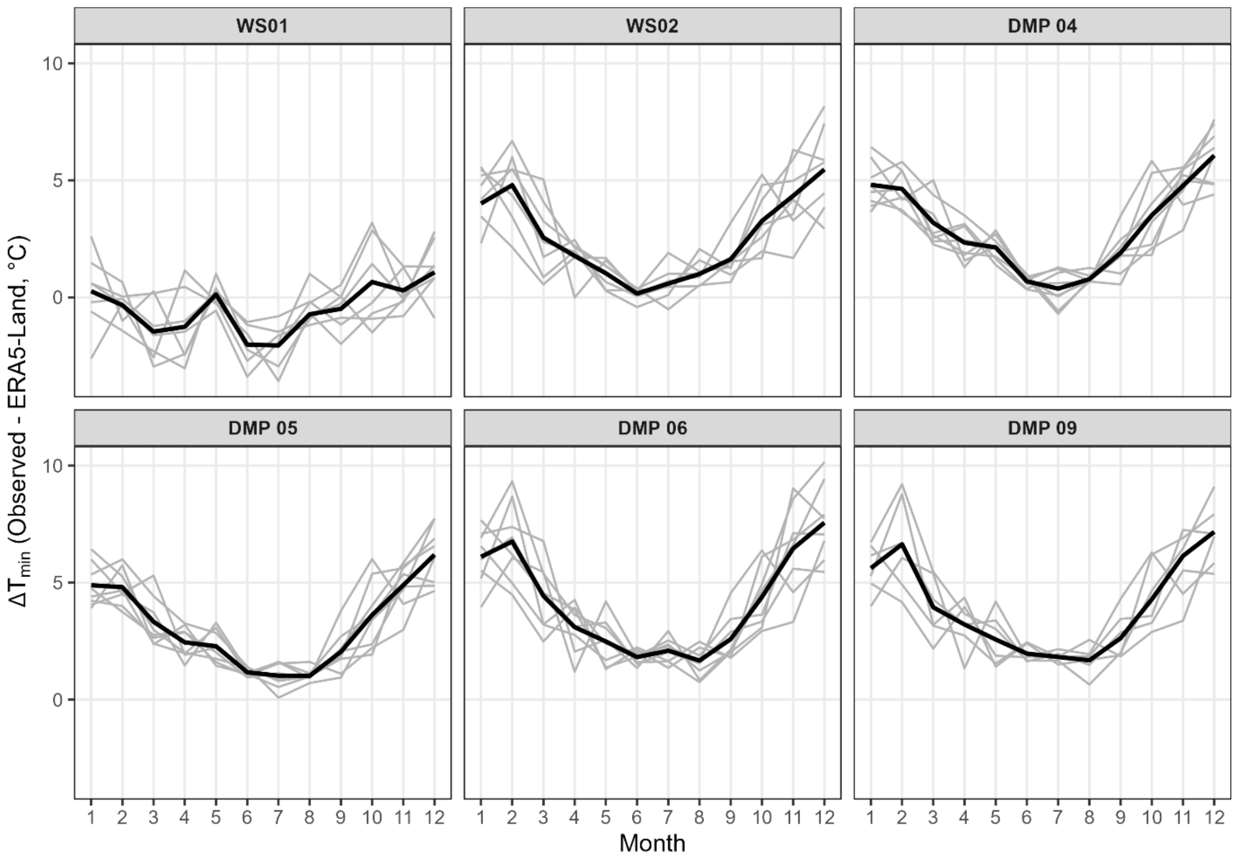

Figure 6-15: Mean Monthly air temperature adjustment factors for daily minimum temperatures (dTmin) for six sites with the longest air temperature records (WS01, WS02, DMP 04, DMP 05, DMP 06, and DMP 09). The black line is the study period mean (2017-2025) and the grey lines interannual variability.

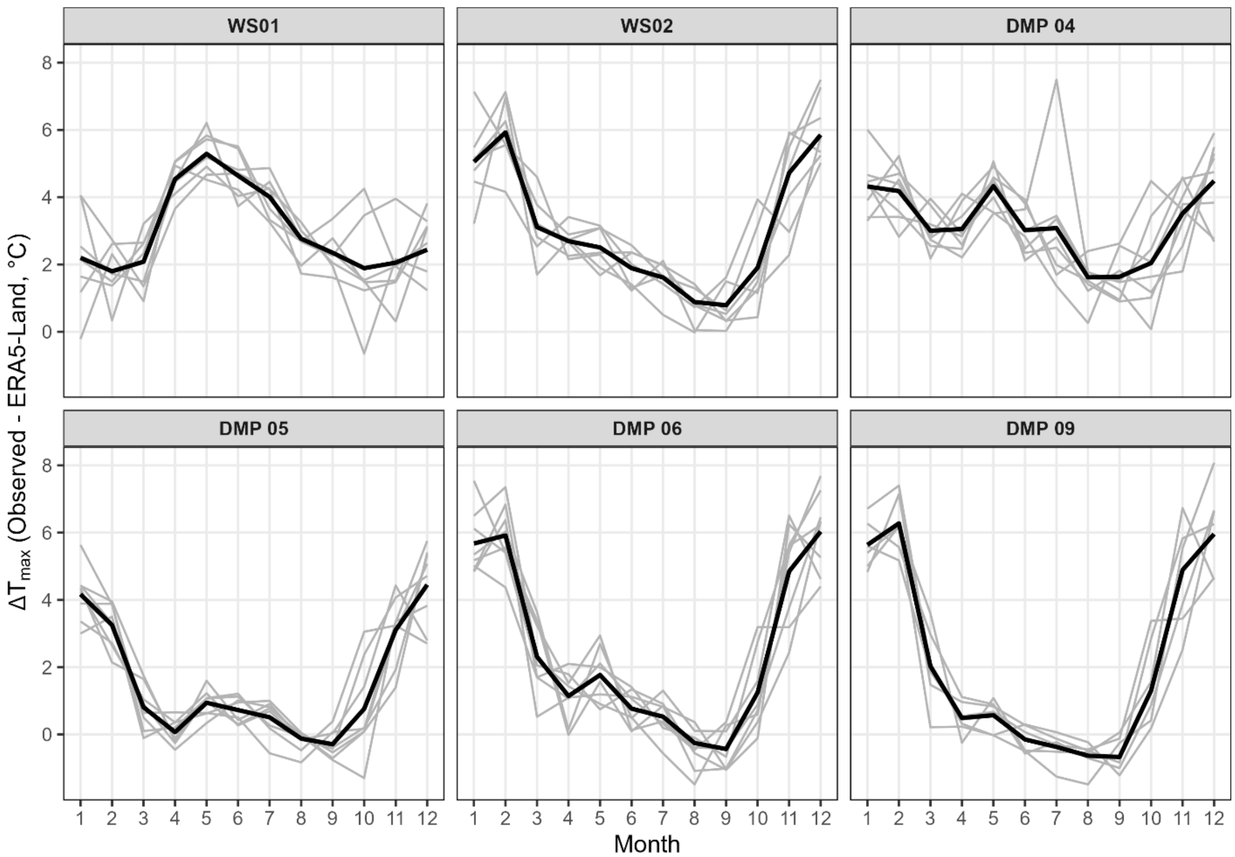

Figure 6-16: Mean Monthly air temperature adjustment factors for daily maximum temperatures (dTmax) for six sites with the longest air temperature records (WS01, WS02, DMP 04, DMP 05, DMP 06, and DMP 09). The black line is the study period mean (2017-2025) and the grey lines interannual variability. Occasional anomalous summer biases (e.g., at DMP 04) are likely related to short term sensor exposure or site-specific conditions and do not meaningfully affect the overall seasonal bias structure.

Table 6-10: Calibration metrics including R^2 and KGE for both ground surface temperature (GST) and ground depth temperature (GT) for each of the study sites. * indicates that the calibration was only run based on part of the observational period. In the case of WS01 and WS02 only data from 2017-2019 were used due to issues with frost heaving of the GT sensor in later years.

Site	n	GST R^2	GST KGE	GT R^2	GT KGE
DMP04	2905	0.93	0.85	0.93	0.92
DMP05	2317	0.90	0.85	0.85	0.91
DMP06	2902	0.89	0.89	0.91	0.86
DMP09	2551	0.90	0.93	0.91	0.69
DMP10	1459	0.84	0.92	0.86	0.18
DMP11	1459	0.89	0.56	0.89	-0.3
DMP12	1468	0.90	0.91	0.68	0.57
DMP13	1468	0.91	0.62	0.89	0.15
DMP14	1457	0.84	0.35	0.79	0.47
DMP15	1456	0.92	0.84	0.93	0.89
DMP16	1457	0.94	0.68	0.92	0.92
DMP17	1457	0.93	0.88	0.96	0.69
DMP18	719	0.92	0.07	0.92	0.65
DMP23	1090	0.95	0.76	NA	NA
DMP24	1091	0.90	0.30	0.91	0.85
DMP25	1091	0.92	0.08	0.90	0.94
DMP31	1098	0.95	0.90	0.97	0.92
DMP34	719	0.92	0.83	NA	NA
DMP36	719	0.92	-0.43	NA	NA
DMP46	717	0.95	0.79	NA	NA
DMP48	717	0.91	0.91	NA	NA
WS01	1588	0.87	0.79	0.68	0.76
WS02	1222	0.92	0.87	0.84	0.75

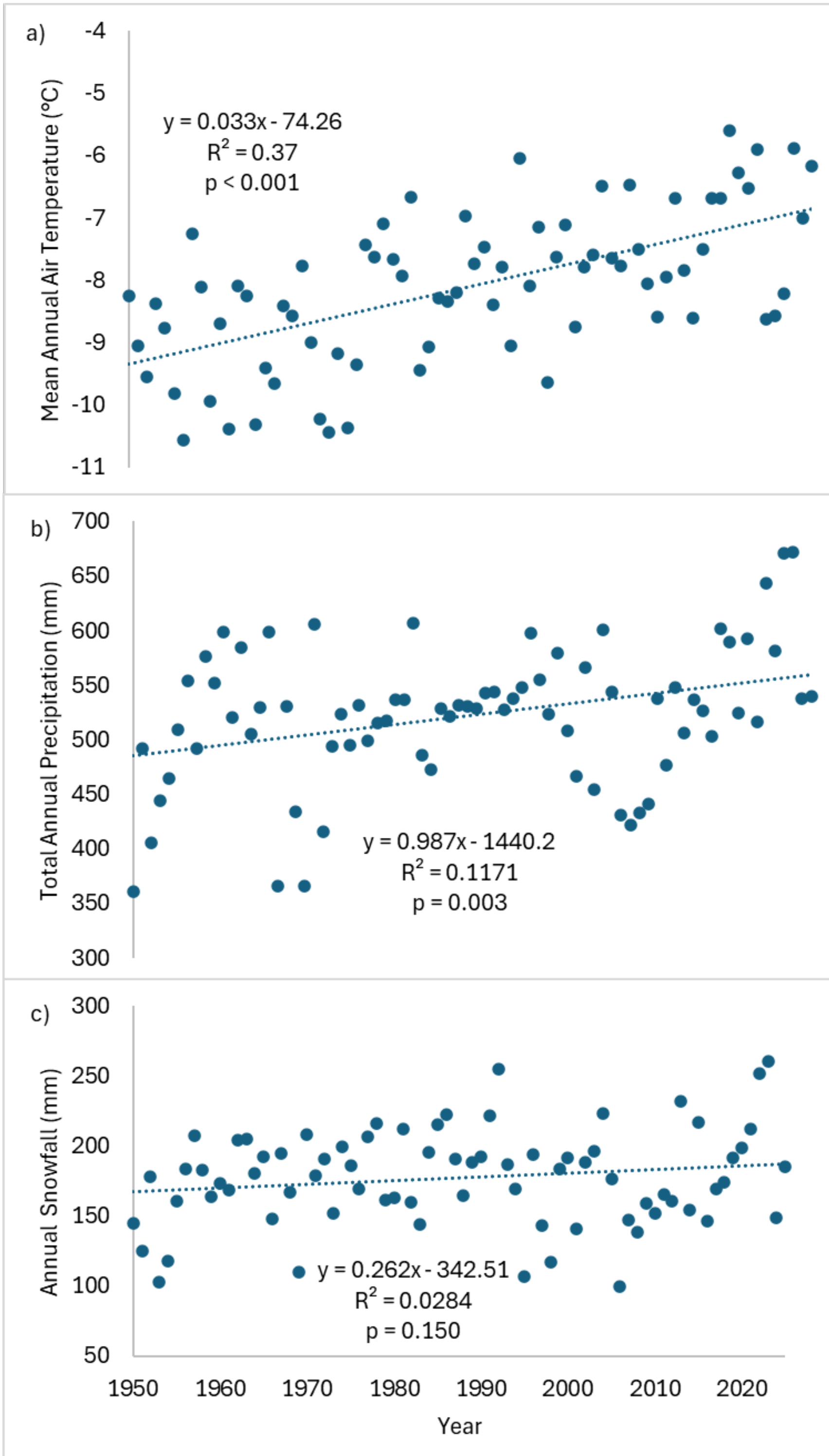

Figure 6-17: Trends in a) Mean annual Air temperature, b) Total Annual Precipitation, and c) Annual Snowfall from 1950-2025 in the ERA5-Land dataset.

Table 6-11: Site-specific changes to active layer thickness (ALT), snow depth, snow cover duration, and ground temperatures at the depths of 0.05, 0.55, 1.07, 2.90, and 7.10 m in response to removal of the local atmosphere forcing adjustment parameter.

Site	Valley	Elevation	dALT (m)	dSnow Depth (cm)	dSnow Cover (days)	dT 0.05 m (°C)	dT_0.55 (°C)	dT_1.07 m (°C)	dT 2.9 m (°C)	dT 7.1 m (°C)
DMP 31	WS01	957	-1.51	0.9	7.6	-0.4	-0.4	-0.4	-0.4	-0.4
WS01	WS01	997	-0.24	3.1	16.2	-1.1	-0.9	-0.9	-0.9	-0.9
DMP 12	WS01	1035	-0.62	5.9	18.2	-0.7	-0.5	-0.5	-0.3	-0.4
DMP 13	WS01	1059	-0.54	3.4	8.5	-0.3	-0.3	-0.3	-0.3	-0.3
WS02	WS02	1109	-0.12	3.1	14.5	-1.4	-1.2	-1.2	-1.2	-1.2
DMP 15	WS02	1128	-1.16	4.7	21.6	-1.0	-1.0	-1.0	-1.0	-1.3
DMP 04	WS01	1142	NA	6.4	20.1	-1.1	-1.1	-1.1	-1.2	-1.2
DMP 05	WS01	1147	-1.16	3.1	7.9	-0.7	-0.7	-0.7	-0.7	-0.7
DMP 14	WS02	1150	-0.13	3.5	12.7	-0.4	-0.4	-0.4	-0.4	-0.5
DMP 09	WS02	1202	-0.44	4.6	15.0	-0.4	-0.4	-0.4	-0.4	-0.7
DMP 06	WS02	1203	-1.09	5.1	19.7	-1.0	-1.0	-1.0	-1.1	-1.2
DMP 11	WS01	1225	-1.01	2.7	7.9	-0.7	-0.7	-0.7	-0.8	-0.8
DMP 18	WS01	1236	-1.55	4.0	17.2	-1.5	-1.5	-1.5	-1.5	-1.5
DMP 17	WS02	1308	-1.44	4.6	20.1	-2.0	-2.0	-2.1	-2.1	-2.1
DMP 36	WS01	1316	-1.64	3.7	2.6	-0.6	-0.6	-0.6	-0.6	-0.6
DMP 24	WS02	1321	-1.39	3.8	10.2	-1.3	-1.3	-1.3	-1.4	-1.4
DMP 10	WS01	1364	-1.52	3.6	15.2	-1.1	-1.2	-1.2	-1.3	-1.4
DMP 23	WS02	1406	-1.20	5.3	24.7	-1.6	-1.6	-1.7	-1.8	-1.9
DMP 25	WS02	1417	-0.32	4.1	17.7	-0.9	-0.9	-0.9	-0.9	-1.1
DMP 34	WS01	1425	-0.26	6.0	16.7	-0.7	-0.7	-0.7	-0.8	-1.0
DMP 16	WS02	1475	-0.47	3.8	7.7	-0.8	-0.9	-0.9	-0.9	-1.0
DMP 48	WS02	1593	-0.09	2.0	3.4	-0.9	-0.9	-1.0	-1.0	-1.0
DMP 46	WS02	1595	-0.14	2.3	11.3	-1.0	-1.0	-1.1	-1.1	-1.2

7. Thesis Conclusions

Each chapter of this thesis addressed the challenge of bias induced by SBIs in climate forcing datasets. This was achieved by (1) quantifying how SBIs shape air temperature patterns in subarctic valleys, (2) evaluating methods to incorporate inversion effects into downscaled climate reanalysis data, and (3) assessing how reducing SBI-related bias influences predictions of permafrost thermal conditions.

This section synthesizes the main findings of Chapters 3-6 and highlights their broader implications for modelling permafrost in high-latitude mountainous environments,

7.1 The main Findings and Implications of this Research

1. **High resolution characterization of SBIs**

SBIs were quantified using a high-resolution network of elevational transects which provided detailed insight into their spatial structure, temporal variability, and controlling mechanisms of developments and breakup in subarctic valley environments. SLRs were non-linear during inversion events, with strongly positive lapse rates in the lowest approximately 60 vertical meters of the valley bottom that transitioned towards near isothermal conditions above 150 vertical meters.

This represents a substantial advancement in understanding the physical structure of SBIs in subarctic valleys, where previous observations were limited in both spatial and temporal resolution. These results demonstrate that SBI structure cannot be adequately represented using linear lapse rate assumptions, which has important implications for climate downscaling and environmental modelling.

2. **Evaluation of a downscaling method for reanalysis data designed to reduce systematic bias associated with SBIs in subarctic valleys**

Evaluation of an existing inversion-aware bias reduction model demonstrated that, while the approach improved temperature predictions when calibrated locally, it lacked transferability across sites. The model successfully captured the combined effects of downscaled reanalysis predicted surface air temperatures at lower elevations and pressure level temperatures at higher elevations. Its reliance on linear lapse rates however, resulted in systematic bias.

Specifically, the model underestimated temperature at higher elevations by maintaining positive (inverted) lapse rates where observations showed near isothermal or negative lapse rates. At the lowest elevation sites, failure to represent observed non-linear lapse rates contributed to bias there. These findings highlighted some key limitations to the existing approach that needed to be addressed in an updated version of the model.

3. **Development of a transferable and with a more robust inversion-aware correction framework (DReaMIT) for downscaled climate reanalysis data**

Building on this evaluation, a revised modelling framework (DReaMIT) was developed that incorporates hypsometric position and non-linear lapse rates. This updated model improved the spatial transferability and physical realism of reducing inversion-related systematic bias.

The DReaMIT model was successfully applied to multiple other mountainous locations across northwestern Canada without site-specific recalibration. This represents a major advance in reducing SBI-related bias in downscaled climate reanalysis datasets that can be used as climate forcing inputs in downstream modelling such as permafrost models in subarctic valley environments.

4. **Quantification of SBI influence on permafrost thermal regimes relative to snow redistribution**

Results demonstrate that while snow redistribution remains the dominant control on spatial variability in ground thermal conditions and permafrost characteristics, site-specific SBI-driven air temperature adjustments represent an important secondary control.

These finding show that SBI forcing interact with snow processes to influence the distribution and stability of permafrost in subarctic mountain environments. Therefore, failure to account for SBI-related bias in climate forcing datasets introduces uncertainty into permafrost modelling, particularly in regions where strong and persistent SBIs are common.

7.2 Transferability of the Research Framework

Although this research was undertaken in the Ogilvie Mountains of Yukon, persistent winter surface-based temperature inversions are characteristic of many cold-region mountainous environments. Consequently, the observational approaches, inversion-aware climate correction methods, and modelling framework developed in this thesis have potential applicability beyond the present study area. Examples include the Brooks and Alaska ranges of Alaska, the Mackenzie and Richardson mountains of northwestern Canada, Axel Heidburg Island and Elsmere Island in Canada's far north, the Scandinavian Mountains, Svalbard, the mountain permafrost regions of Mongolia, several mountainous regions of northern Russia, including the Ural Mountains and the Verkhoyansk range, and southern high-latitude mountain environments such as Patagonia (Figure 7-1). These regions share climatic and topographic characteristics that likely promote persistent winter SBIs, including long periods of winter stability, complex valley terrain, and sparse meteorological observations.

The degree of transferability will depend on local climatic conditions, valley geometry, snow and ice cover, and the frequency and persistence of winter SBIs. Consequently, additional field observations remain essential for evaluating and refining these approaches in new environments.

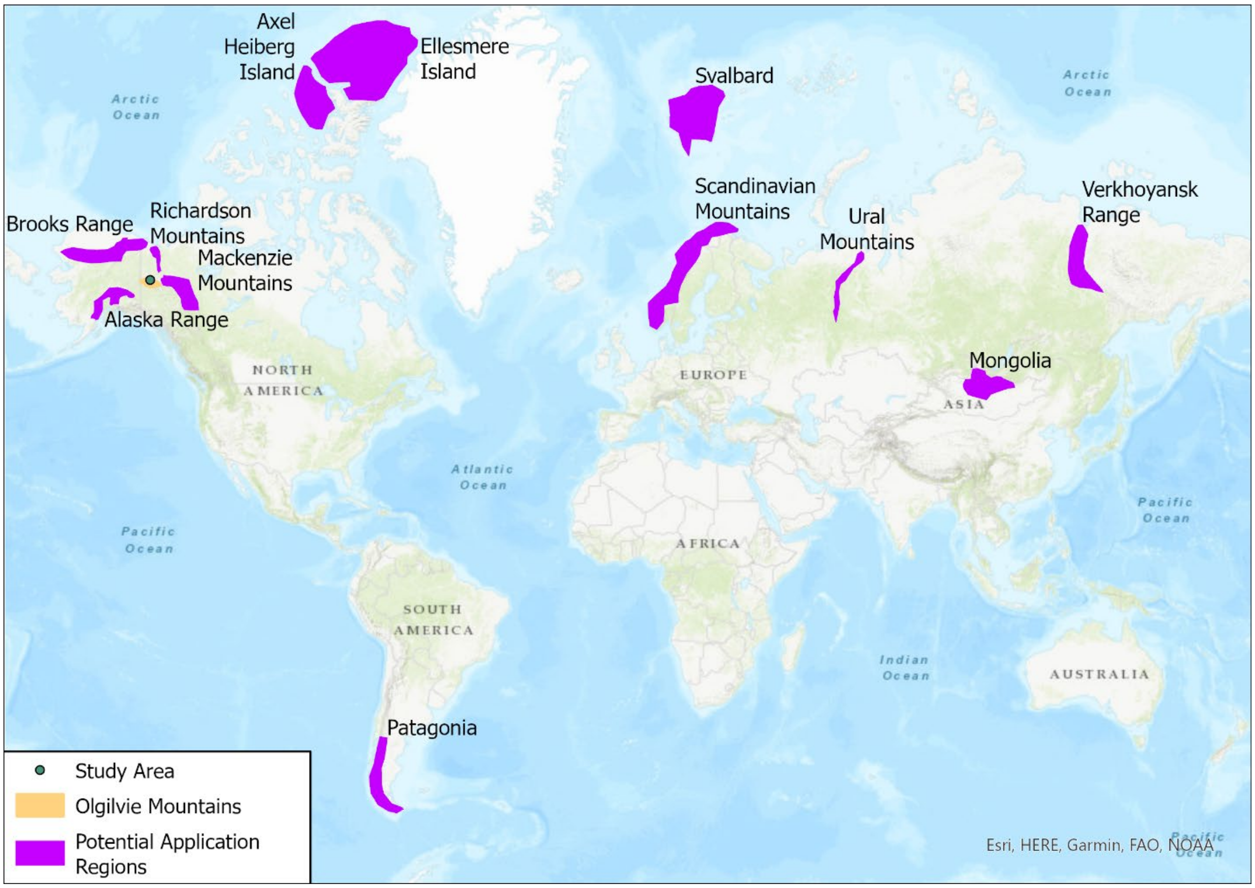

Figure 7-1: Figure 7-1. Examples of cold-region mountainous regions where the observational framework, inversion correction methodology, and permafrost modelling approaches developed in this thesis may have broader applicability. The Dempster Valleys within the Ogilvie Mountains are shown as the study area. The highlighted regions are illustrative examples rather than an exhaustive inventory.

7.3 Next Steps and Future Research

This thesis directly leads into several key research direction that are aligned with ongoing efforts to improve permafrost modelling in high-latitude mountain environments.

1. **Model evaluation and validation**

Building on the development of the DReaMIT framework in Chapter 5, further evaluation using independent datasets is a critical next step. Recently compiled observational datasets from central and southern Yukon (e.g., Wolf Creek, Faro, Johnson's Crossing, Keno, Sa Dena Hes, MacMillan and Dawson) provide the opportunity to evaluate model performance across a wider range of elevations, hypsometric positions, terrain types, and climatic conditions (Figure 7-1).

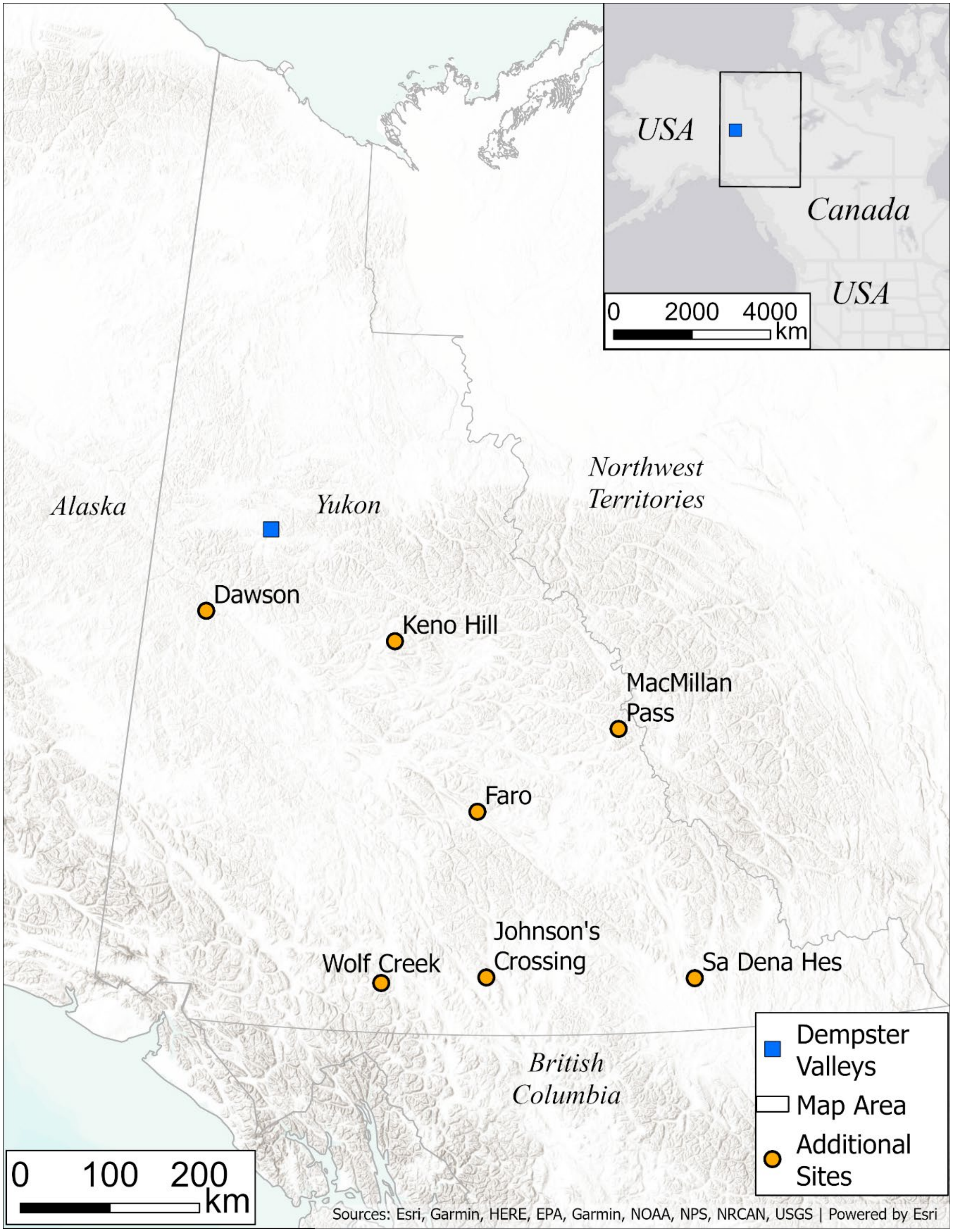

Figure 7-2: The location of additional sites that could be used to evaluate the performance of the DReaMIT model as calibrated in the Dempster Highway valleys.

This expanded evaluation of DReaMIT will allow for rigorous testing of its transferability, a key limitation identified in Chapter 4. This will support further refinement of the model structure to better represent processes across heterogeneous mountain environments. Such work directly contributes to improving the reliability of climate forcing inputs used in permafrost modelling.

2. **Integration with process-based permafrost models**

Building on the development of the DReaMIT approach to reducing SBI biases in climate forcing data in Chapter 5 and the NEST modelling in Chapter 6, an important next step is integrating DReaMIT-adjusted climate forcing into process-based transient permafrost models such as NEST. This would enable a direct assessment of how improved representation of surface air temperatures influences predicted ground thermal regimes and permafrost characteristics.

Comparisons between DReaMIT adjusted climate forcing, uncorrected reanalysis data, and locally calibrated air temperatures would provide critical insight into sensitivity the model has to atmospheric forcing and the propagation of SBI-related bias through transient permafrost simulations.

This work would help quantify the importance of accurately representing sub-grid atmospheric processes in complex terrain and reduce uncertainty in predictions of permafrost stability and response to changing climate.

3. **Temporal evolution of SBIs under climate change**

Building on the characterization of SBI processes in Chapter 3, their role in biasing climate forcing identified in Chapters 4 and 5, and transient permafrost modelling using locally adjusted climate forcing in Chapter 6, a key next step is to examine how SBI frequency, strength, and structure evolve in response to climate change. This can be achieved through combined analysis of long-term reanalysis datasets and observational records (e.g., radiosonde soundings).

Recent studies indicate that SBI characteristics are already changing. For example, global analyses using radiosonde data have identified rapid changes in SBI characteristics (Zeng et al., 2021). More locally, Pozsgay and Gruber (2025) used climate reanalysis data to demonstrate that inversions have decreased in strength, depth, and frequency since 1948 in Dawson Yukon. Extending this analysis to additional field sites would provide a more comprehensive understanding of how SBI characteristics vary through time across heterogenous mountain environments.

The temporal trends in SBI characteristics have important implications for permafrost modelling. Incorporating evolving SBI behaviour into climate forcing datasets would allow dynamic changes of local air temperature adjustments in process-based models such as NEST. This approach would improve representation of atmospheric forcing and reduce uncertainties associated with applying static bias corrections when predicting future permafrost conditions.

Ultimately, this work would help constrain how changes in winter climate processes influence thresholds of permafrost stability in high-latitude alpine environments.

4. Empirical modelling of SBI characteristics

Building on the high-resolution observations of SBI structure and variability presented in Chapter 3, an important next step will be the development of statistical models that link SBI characteristics to large-scale atmospheric processes within long-term observational datasets (e.g., Dawson, Yukon) and coarse-resolution reanalysis products.

This could be done by leveraging the continually growing high-resolution datasets used in this thesis. Machine learning and empirical-statistical approaches could be used to relate synoptic scale meteorological conditions to local SBI frequency, strength, and depth. This would allow for prediction of SBI occurrence and characteristics in areas and during periods of time where direct observations are limited.

Incorporating these relationships into climate forcing datasets would improve representation of sub-grid atmospheric processes in complex terrain and reduce uncertainty in applications such as downscaling and permafrost modelling.

5. Expanding ecological and terrain representation in transient permafrost modelling

Building on the application of the NEST model in Chapter 6, a key next step is to expand modelling efforts to environments or locations that span a wider range of vegetation types and soil conditions. Extending NEST modelling efforts beyond predominately sparsely vegetated, rocky substrate, snow scoured, high elevation sites considered in this thesis would improve understanding of how SBI-driven air temperature patterns interact with ecosystem controls on ground thermal regimes.

Incorporating these more densely vegetated environments would allow for assessment of how vegetation, soil properties, and disturbances such as fire modify the response of permafrost to atmospheric forcing. Previous studies have shown that disturbances can accelerate permafrost degradation well beyond the effects of climate forcing alone (Gibson et al., 2018; Holloway et al., 2020; Zhang et al., 2015). In addition, succession of vegetation due to climate warming can have a strong control on changes to snow accumulation and insulation, further influencing permafrost stability (Wang & Way, 2025).

By integrating these processes into transient modelling frameworks, thresholds of permafrost stability across different landcover types and disturbance regimes could be identified. This is particularly important in SBI-dominated mountain environments, where strong spatial variability in air temperature interacts with ecosystem controls to govern permafrost persistence and evolution under climate warming.

6. Improved representation of snow processes across the mountain valley landscape

Building on the findings of Chapter 6, which demonstrated that snow redistribution is the dominant control on spatial variability in ground temperature regimes, a key priority for future research must be to improve the representation of snow processes across the heterogenous mountain landscapes.

High-resolution observations of snow depth, distribution, density, and duration including through the use of trail cameras, snow stakes (Tutton & Way, 2021), remote sensing approaches (Bonney & Zhang, 2026), ground temperature node networks (Garibaldi et al., 2021; Lundquist & Lott, 2008), and winter field campaigns to collect in-situ snow depth and density measures should be integrated to better quantify the spatial variability of snow insulation and its influence on ground temperatures.

These datasets could be used to develop empirical or machine learning models that predict snow distribution across complex terrain, supporting the parametrization of snow spatial variability in permafrost models.

Importantly, by improving the representation of snow processes, there can be more accurate assessments of how snow redistribution interacts with SBI-driven air temperature patterns and how they control permafrost stability. This is critical for reducing uncertainty in modelling permafrost responses to climate change in high-latitude mountain environments.

7. Review of potential impacts of permafrost loss in this high-latitude alpine region

Building on the Chapter 6 finding that permafrost in parts of this region may be nearing a threshold for loss, understanding the impacts of permafrost degradation in this environment is a key next step. While ground ice is generally low to negligible in this subarctic mountain region (O'Neill et al., 2019), the impacts of permafrost degradation in these systems may be nevertheless significant and complex. Field observations from this study area note landscape disturbance, including active layer detachments and retrogressive thaw slumps. This demonstrates that permafrost loss can still lead to geomorphological instability in these environments.

Beyond geomorphic change, permafrost degradation could have serious implications for hydrology and water quality. For example, in the Red Creek and Engineer Creek basin reduced water quality, characterized by elevated dissolved metals and low pH, highlights a potential sensitivity of headwater systems to permafrost related changes in subsurface flow patterns. As permafrost thaws, alterations to groundwater flow and storage may further influence the mobilization of solutes, with downstream, impacts on the Peel and Mackenzie rivers.

These changes have broader implications for northern communities, as permafrost plays a critical role in supporting infrastructure, regulating hydrological systems, and sustaining ecosystem function. Disruptions to those systems can affect water resources, landscape stability, and traditional land use, with cascading impacts on cultural practices and livelihoods (Wang et al., 2026).

The findings of this thesis highlight that accurately representing climate forcing particularly in environments dominated by SBIs is essential to predicting where and when these impacts may occur. By improving the representation of sub-grid atmospheric processes and their interactions with snow, this work contributes to a more robust understanding of thresholds of permafrost stability and potential consequences of passing these thresholds in high-latitude mountain environments.

7.4 Closing Statement

This thesis advances understanding of how SBIs introduce systematic bias into climate forcing datasets in high-latitude mountain environments. Demonstrating that this bias propagates into permafrost modelling. By combining high-resolution field observations, model evaluation, and developments of a transferable bias reduction approach, this research improves the representation of sub-grid atmospheric processes in complex terrain.

These findings highlight that accurate prediction of permafrost responses to climate change requires not only improved process-based models, but also improved representation of atmospheric forcing that drives them. In addressing this gap, this work contributes to advancing predictive capability of permafrost models and provides a direction for future research that examines thresholds of permafrost stability and their implication for landscape change, hydrology, and northern communities.

8. References

Abbott, B. W., & Jones, J. B. (2015). Permafrost collapse alters soil carbon stocks, respiration, CH4, and N2O in upland tundra. *Global Change Biology*, *21*(12), 4570-4587. https://doi.org/10.1111/gcb.13069

Abbott, B. W., Jones, J. B., Schuur, E. A. G., Chapin Iii, F. S., Bowden, W. B., Bret-Harte, M. S., Epstein, H. E., Flannigan, M. D., Harms, T. K., Hollingsworth, T. N., Mack, M. C., McGuire, A. D., Natali, S. M., Rocha, A. V., Tank, S. E., Turetsky, M. R., Vonk, J. E., Wickland, K. P., Aiken, G. R., . . . Sveriges, l. (2016). Biomass offsets little or none of permafrost carbon release from soils, streams, and wildfire: an expert assessment. *Environmental Research Letters*, *11*(3), 34014-34026. https://doi.org/10.1088/1748-9326/11/3/034014

Akperov, M. G., Mokhov, I. I., Dembitskaya, M. A., Parfenova, M. R., & Rinke, A. (2019). Lapse Rate Peculiarities in the Arctic from Reanalysis Data and Model Simulations. *Russian Meteorology and Hydrology*, *44*(2), 97-102. https://doi.org/10.3103/S106837391902002X

Anisimov, O., & Reneva, S. (2006). Permafrost and Changing Climate: The Russian Perspective. *Ambio*, *35*(4), 169-175. https://doi.org/10.1579/0044-7447(2006)35[169:PACCTR]2.0.CO;2

Barnes, C., Hopkinson, C., Porter, T., & Xi, Z. (2020). In-Situ LED-Based Observation of Snow Surface and Depth Transects. *Sensors (Basel, Switzerland)*, *20*(8), 2292. https://doi.org/10.3390/s20082292

Beck, H. E., Zimmermann, N. E., McVicar, T. R., Vergopolan, N., Berg, A., & Wood, E. F. (2018). Present and future Köppen-Geiger climate classification maps at 1-km resolution. *Scientific data*, *5*(1), 180214. https://doi.org/10.1038/sdata.2018.214

Benestad, R. E. A., Hanssen-Bauer, I., & Chen, D. (2008). *Empirical-Statistical Downscaling*. World Scientific. https://doi.org/10.1142/6908

Beven, K. J., & Kirkby, M. J. (1979). A physically based, variable contributing area model of basin hydrology / Un modèle à base physique de zone d'appel variable de l'hydrologie du bassin versant. *Hydrological Sciences Bulletin*, *24*(1), 43-69. https://doi.org/10.1080/02626667909491834

Bevington, A., & Lewkowicz, A. (2015). Assessment of a land cover driven TTOP model for mountain and lowland permafrost using field data, southern Yukon and northern British Columbia, Canada. In Proceedings of the 7th Canadian Permafrost Conference (Quebec City, QC).

Bieniek, P. A., Bhatt, U. S., Walsh, J. E., Rupp, T. S., Zhang, J., Krieger, J. R., & Lader, R. (2016). Dynamical Downscaling of ERA-Interim Temperature and Precipitation for Alaska. *Journal of Applied Meteorology and Climatology*, *55*(3), 635-654. https://doi.org/10.1175/JAMC-D-15-0153.1

Biskaborn, B. K., Smith, S. L., Noetzli, J., Matthes, H., Vieira, G., Streletskiy, D. A., Schoeneich, P., Romanovsky, V. E., Lewkowicz, A. G., Abramov, A., Allard, M., Boike, J., Cable, W. L., Christiansen, H. H., Delaloye, R., Diekmann, B., Drozdov, D., Etzelmüller, B., Grosse, G., . . . Lantuit, H. (2019). Permafrost is warming at a global scale. *Nature Communications*, *10*(1), 264-264. https://doi.org/10.1038/s41467-018-08240-4

Blandford, T. R., Humes, K. S., Harshburger, B. J., Moore, B. C., Walden, V. P., & Ye, H. (2008). Seasonal and Synoptic Variations in Near-Surface Air Temperature Lapse Rates in a Mountainous Basin. *Journal of Applied Meteorology and Climatology*, *47*(1), 249-261. https://doi.org/10.1175/2007JAMC1565.1

Boeckli, L., Brenning, A., Gruber, S., & Noetzli, J. (2012). Permafrost distribution in the European Alps: calculation and evaluation of an index map and summary statistics. *The Cryosphere*, *6*(4), 807-820. https://doi.org/10.5194/tc-6-807-2012

Bonnaventure, P. P., & Lamoureux, S. F. (2013). The active layer: A conceptual review of monitoring, modelling techniques and changes in a warming climate. *Progress in Physical Geography*, *37*(3), 352-376. https://doi.org/10.1177/0309133313478314

Bonnaventure, P. P., Lamoureux, S. F., & Favaro, E. A. (2017). Over-Winter Channel Bed Temperature Regimes Generated by Contrasting Snow Accumulation in a High Arctic River: Over-Winter Channel Bed Temperature Regimes. *Permafrost and Periglacial Processes*, *28*(1), 339-346. https://doi.org/10.1002/ppp.1902

Bonnaventure, P. P., & Lewkowicz, A. G. (2008). Mountain permafrost probability mapping using the BTS method in two climatically dissimilar locations, northwest Canada. *Canadian Journal of Earth Sciences*, *45*(4), 443-455. https://doi.org/10.1139/E08-013

Bonnaventure, P. P., & Lewkowicz, A. G. (2011). Modelling climate change effects on the spatial distribution of mountain permafrost at three sites in northwest Canada. *Climatic Change*, *105*(1), 293-312. https://doi.org/10.1007/s10584-010-9818-5

Bonnaventure, P. P., & Lewkowicz, A. G. (2012). Permafrost probability modeling above and below treeline, Yukon, Canada. *Cold Regions Science and Technology*, *79-80*, 92-106. https://doi.org/10.1016/j.coldregions.2012.03.004

Bonnaventure, P. P., & Lewkowicz, A. G. (2013). Impacts of mean annual air temperature change on a regional permafrost probability model for the southern Yukon and northern British Columbia, Canada. *The Cryosphere*, *7*(3), 935-946. https://doi.org/10.5194/tc-7-935-2013

Bonnaventure, P. P., Lewkowicz, A. G., Kremer, M., & Sawada, M. C. (2012). A Permafrost Probability Model for the Southern Yukon and Northern British Columbia, Canada. *Permafrost and Periglacial Processes*, *23*(1), 52-68. https://doi.org/10.1002/ppp.1733

Bonney, M. T., & Zhang, Y. (2026). Monitoring snow cover dynamics at 30-m resolution in higher latitude regions using Harmonized Landsat Sentinel-2. *ISPRS Journal of Photogrammetry and Remote Sensing*, *233*, 360-382. https://doi.org/10.1016/j.isprsjprs.2026.01.032

Bourne, S. M., Bhatt, U. S., Zhang, J., & Thoman, R. (2010). Surface-based temperature inversions in Alaska from a climate perspective. *Atmospheric Research*, *95*(2), 353-366. https://doi.org/10.1016/j.atmosres.2009.09.013

Bradley, R. S., Keimig, F. T., & Diaz, H. F. (1992). Climatology of surface-based inversions in the North American Arctic. *Journal of Geophysical Research: Atmospheres*, *97*(D14), 15699-15712. https://doi.org/10.1029/92JD01451

Bradley, R. S., Keimig, F. T., & Diaz, H. F. (1993). Recent changes in the North American Arctic boundary layer in winter. *Journal of Geophysical Research: Atmospheres*, *98*(D5), 8851-8858. https://doi.org/10.1029/93JD00311

Burn, C., Moore, J., O'Neil, B., Haley, D., Calmels, F., Orban, S., & Idrees, M. (2015). *Permafrost Characterizations of the Dempster Highway, Yukon and Northwest Territories*

Burn, C. R., & Smith, C. A. S. (1988). Observations of the "Thermal Offset" in Near-Surface Mean Annual Ground Temperatures at Several Sites near Mayo, Yukon Territory, Canada. *Arctic*, *41*(2), 99-104. https://doi.org/10.14430/arctic1700

Burn, C. R., & Zhang, Y. (2010). *Permafrost and climate change at Herschel Island (Qikiqtaruk), Yukon Territory, Canada*. In Proceedings of the 6th Canadian Permafrost Conference. University of Calgary.

Bush, E., & Lemmen, D. S. (2019). *Canada's Changing Climate Report*. Government of Canada.

Byrne, M. P., Boos, W. R., & Hu, S. (2024). Elevation-dependent warming: observations, models, and energetic mechanisms. *Weather Climate Dynamics*, *5*(2), 763-777. https://doi.org/10.5194/wcd-5-763-2024

Canadian Climate Institute. (2022). *Due North: Facing the costs of climate change for Northern infrastructure*. https://climateinstitute.ca/wp-content/uploads/2022/06/Due-North.pdf

Cannon, A. J., Neilsen, D., & Taylor, B. (2012). Lapse Rate Adjustments of Gridded Surface Temperature Normals in an Area of Complex Terrain: Atmospheric Reanalysis versus Statistical Up-Sampling. *Atmosphere-Ocean*, *50*(1), 9-16. https://doi.org/10.1080/07055900.2011.649035

Cao, B., Gruber, S., & Zhang, T. (2017). REDCAPP (v1.0): parameterizing valley inversions in air temperature data downscaled from reanalyses. *GEOSCIENTIFIC MODEL DEVELOPMENT*, *10*(8), 2905-2923. https://doi.org/10.5194/gmd-10-2905-2017

Cao, B., Quan, X., Brown, N., Stewart-Jones, E., & Gruber, S. (2019). GlobSim (v1.0): deriving meteorological time series for point locations from multiple global reanalyses. *Geoscientific Model Development*, *12*(11), 4661-4679. https://doi.org/10.5194/gmd-12-4661-2019

Carpino, O., Haynes, K., Connon, R., Craig, J., Devoie, Ã., & Quinton, W. (2021). Long-term climate-influenced land cover change in discontinuous permafrost peatland complexes. *Hydrology and Earth System Sciences*, *25*(6), 3301-3317. https://doi.org/10.5194/hess-25-3301-2021

Cartwright, K., Hopkinson, C., Kienzle, S., & Rood, S. B. (2020). Evaluation of temporal consistency of snow depth drivers of a Rocky Mountain watershed in southern Alberta. *Hydrological Processes*, *34*(25), 4996-5012. https://doi.org/10.1002/hyp.13920

Chen, Y., Sharma, S., Zhou, X., Yang, K., Li, X., Niu, X., Hu, X., & Khadka, N. (2021). Spatial performance of multiple reanalysis precipitation datasets on the southern slope of central Himalaya. *Atmospheric Research*, *250*, 105365. https://doi.org/10.1016/j.atmosres.2020.105365

Chen, W., Zhang, Y., Cihlar, J., Smith, S. L., & Riseborough, D. W. (2003). Changes in soil temperature and active layer thickness during the twentieth century in a region in western Canada. *Journal of Geophysical Research: Atmospheres*, *108*(D22), 4696-n/a. https://doi.org/10.1029/2002JD003355

Clark, M. P., Hendrikx, J., Slater, A. G., Kavetski, D., Anderson, B., Cullen, N. J., Kerr, T., Örn Hreinsson, E., & Woods, R. A. (2011). Representing spatial variability of snow water equivalent in hydrologic and land-surface models: A review. *Water Resources Research*, *47*(7). https://doi.org/10.1029/2011WR010745

Clements, C. B., Whiteman, C. D., & Horel, J. D. (2003). Cold-Air-Pool Structure and Evolution in a Mountain Basin: Peter Sinks, Utah. *Journal of Applied Meteorology (1988-2005)*, *42*(6), 752-768. https://doi.org/10.1175/1520-0450(2003)042<0752:CSAEIA>2.0.CO;2

Compo, G. P., Whitaker, J. S., Sardeshmukh, P. D., Matsui, N., Allan, R. J., Yin, X., Gleason, B. E., Vose, R. S., Rutledge, G., Bessemoulin, P., Brönnimann, S., Brunet, M., Crouthamel, R. I., Grant, A. N., Groisman, P. Y., Jones, P. D., Kruk, M. C., Kruger, A. C., Marshall, G. J., . . . Univ. of California, O. C. A. (2011). The Twentieth Century Reanalysis Project. *Quarterly Journal of the Royal Meteorological Society*, *137*(654), 1-28. https://doi.org/10.1002/qj.776

Connon, R. F., Quinton, W. L., Craig, J. R., Hanisch, J., & Sonnentag, O. (2015). The hydrology of interconnected bog complexes in discontinuous permafrost terrains: Hydrology of Interconnected Bogs in Discontinuous Permafrost. *Hydrological Processes*, *29*(18), 3831-3847. https://doi.org/10.1002/hyp.10604

Connon, R. F., Quinton, W. L., Craig, J. R., & Hayashi, M. (2014). Changing hydrologic connectivity due to permafrost thaw in the lower Liard River valley, NWT, Canada. *Hydrological Processes*, *28*(14), 4163-4178. https://doi.org/10.1002/hyp.10206

Cowtan, K., & Way, R. G. (2013). Coverage bias in the HadCRUT4 temperature series and its impact on recent temperature trends. *Quarterly Journal of the Royal Meteorological Society*, *140*(683), 1935-1944. https://doi.org/10.1002/qj.2297

Cullen, R. M., & Marshall, S. J. (2011). Mesoscale Temperature Patterns in the Rocky Mountains and Foothills Region of Southern Alberta. *Atmosphere-Ocean*, *49*(3), 189-205. https://doi.org/10.1080/07055900.2011.592130

Daly, C., Conklin, D. R., & Unsworth, M. H. (2010). Local atmospheric decoupling in complex topography alters climate change impacts. *International Journal of Climatology*, *30*(12), 1857-1864. https://doi.org/10.1002/joc.2007

Daly, C., Halbleib, M., Smith, J. I., Gibson, W. P., Doggett, M. K., Taylor, G. H., Curtis, J., & Pasteris, P. P. (2008). Physiographically sensitive mapping of climatological temperature and precipitation across the conterminous United States. *International Journal of Climatology*, *28*(15), 2031-2064. https://doi.org/10.1002/joc.1688

Daly, S. V., Bonnaventure, P. P., & Kochtitzky, W. (2022). Influence of ecosystem and disturbance on near-surface permafrost distribution, Whatì, Northwest Territories, Canada. *Permafrost and Periglacial Processes*, *33*(4), 339-352. https://doi.org/10.1002/ppp.2160

Dawn Reeves, H., & Stensrud, D. J. (2009). Synoptic-Scale Flow and Valley Cold Pool Evolution in the Western United States. *Weather and Forecasting*, *24*(6), 1625-1643. https://doi.org/10.1175/2009WAF2222234.1

De Wekker, S., Kossmann, M., Knievel, J., Giovannini, L., Gutmann, E., & Zardi, D. (2018). Meteorological Applications Benefiting from an Improved Understanding of Atmospheric Exchange Processes over Mountains. *Atmosphere*, *9*(10), 371. https://doi.org/10.3390/atmos9100371

Deems, J. S., Painter, T. H., & Finnegan, D. C. (2013). Lidar measurement of snow depth: a review. *Journal of Glaciology*, *59*(215), 467-479. https://doi.org/10.3189/2013JoG12J154

Devoie, É. G., Craig, J. R., Connon, R. F., & Quinton, W. L. (2019). Taliks: A tipping point in discontinuous permafrost degradation in peatlands. Water Resources Research, 55(11), 9838–9857. https://doi.org/10.1029/2018WR024488

Devoie, É. G., & Craig, J. R. (2020). A semianalytical interface model of soil freeze/thaw and permafrost evolution. Water Resources Research, 56(8). https://doi.org/10.1029/2020WR027638

Devoie, É. G., Craig, J. R., Dominico, M., Carpino, O., Connon, R. F., Rudy, A. C. A., & Quinton, W. L. (2021). Mechanisms of discontinuous permafrost thaw in peatlands. Journal of Geophysical Research: Earth Surface, 126(11). https://doi.org/10.1029/2021JF006204

Dice, M. J., Cassano, J. J., and Jozef, G. C. 2024. Forcing for varying boundary layer stability across Antarctica, *Weather and Climate Dynamics*, 5, 369–394, https://doi.org/10.5194/wcd-5-369-2024.

Draeger, C., Radic´, V., White, R. H., and Tessema, M. A. 2024. Evaluation of reanalysis data and dynamical downscaling for surface energy balance modeling at mountain glaciers in western Canada, *The Cryosphere*, 18, 17–42, https://doi.org/10.5194/tc-18-17-2024.

Duchesne, C., Smith, S. L., Ednie, M., & Bonnaventure, P. P. (2015). Active layer variability and change in the Mackenzie Valley, Northwest Territories.

Duk-Rodkin, A. (1999). *Glacial limits map of Yukon* (Geoscience Map 1999-2). Indian and Northern Affairs Canada, Exploration and Geological Services Division.

Egli, L., Griessinger, N., & Jonas, T. (2011). Seasonal development of spatial snow-depth variability across different scales in the Swiss Alps. *Annals of Glaciology*, *52*(58), 216-222. https://doi.org/10.3189/172756411797252211

Ehret, U., Zehe, E., Wulfmeyer, V., Warrach-Sagi, K., & Liebert, J. (2012). HESS Opinions "Should we apply bias correction to global and regional climate model data?". *Hydrology and Earth Systems Science*, *16*(9), 3391-3404. https://doi.org/10.5194/hess-16-3391-2012

Ensom, T., Makarieva, O., Morse, P., Kane, D., Alekseev, V., & Marsh, P. (2020). The distribution and dynamics of aufeis in permafrost regions. *Permafrost and Periglacial Processes*, *31*(3), 383-395. https://doi.org /10.1002/ppp.2051

Environment and Climate Change Canada. (2025). Historical climate data. Retrieved April 9, 2025, from https://climate.weather.gc.ca/historical_data/search_historic_data_e.html

Erell, E., Leal, V., & Maldonado, E. (2005). Measurement of air temperature in the presence of a large radiant flux: an assessment of passively ventilated thermometer screens. *Boundary-Layer Meteorology*, *114*(1), 205-231. https://doi.org/10.1007/s10546-004-8946-8

Etzelmüller, B. (2013). Recent Advances in Mountain Permafrost Research. *Permafrost and Periglacial Processes*, *24*(2), 99-107. https://doi.org/10.1002/ppp.1772

Etzelmüller, B., & Frauenfelder, R. (2009). Factors Controlling The Distribution of Mountain Permafrost in The Northern Hemisphere and Their Influence on Sediment Transfer. *Arctic, Antarctic, and Alpine Research*, *41*(1), 48-58. https://doi.org/10.1657/1523-0430-41.1.48

Etzelmüller, B., Heggem, E. S. F., Sharkhuu, N., Frauenfelder, R., Kääb, A., & Goulden, C. (2006). Mountain permafrost distribution modelling using a multi-criteria approach in the Hövsgöl area, northern Mongolia. *Permafrost and Periglacial Processes*, *17*(2), 91-104. https://doi.org/10.1002/ppp.554

Farouki, O. T. (1981). The thermal properties of soils in cold regions. *Cold Regions Science and Technology*, *5*(1), 67-75. https://doi.org /10.1016/0165-232X(81)90041-0

Favaro, E. A., & Lamoureux, S. F. (2015). Downstream patterns of suspended sediment transport in a High Arctic river influenced by permafrost disturbance and recent climate change. *Geomorphology (Amsterdam, Netherlands)*, *246*, 359-369. https://doi.org/10.1016/j.geomorph.2015.06.038

Fazel-Rastgar, F., & Sivakumar, V. (2022). Weather pattern associated with climate change during Canadian Arctic wildfires: A case study in July 2019. *Remote Sensing*

Applications: Society and Environment, *25*, 100698. https://doi.org/10.1016/j.rsase.2022.100698
Feng, X., Wang, S., & Guo, J. (2022). Temperature inversions in the lower troposphere over the Sichuan Basin, China: Seasonal feature and relation with regional atmospheric circulations. *Atmospheric Research*, *271*, 106097. https://doi.org/10.1016/j.atmosres.2022.106097
Fiddes, J., Aalstad, K., & Lehning, M. (2022). TopoCLIM: rapid topography-based downscaling of regional climate model output in complex terrain v1.1. *Geoscientific Model Development*, *15*(4), 1753-1768. https://doi.org/10.5194/gmd-15-1753-2022
Fiddes, J., Endrizzi, S., and Gruber, S. (2015). Large-area land surface simulations in heterogeneous terrain driven by global data sets: application to mountain permafrost, *The Cryosphere*, 9, 411–426, https://doi.org/10.5194/tc-9-411-2015.
Fiddes, J., & Gruber, S. (2012). TopoSUB: a tool for efficient large area numerical modelling in complex topography at sub-grid scales. *Geoscientific Model Development*, *5*(5), 1245-1257. https://doi.org/10.5194/gmd-5-1245-2012
Fiddes, J., & Gruber, S. (2014). TopoSCALE v.1.0: downscaling gridded climate data in complex terrain. *GEOSCIENTIFIC MODEL DEVELOPMENT*, *7*(1), 387-405. https://doi.org/10.5194/gmd-7-387-2014
Fochesatto, G. J., Mayfield, J. A., Starkenburg, D. P., Gruber, M. A., & Conner, J. (2015). Occurrence of shallow cold flows in the winter atmospheric boundary layer of interior of Alaska. *Meteorology and Atmospheric Physics*, *127*(4), 369-382. https://doi.org/10.1007/s00703-013-0274-4
French, H. M., & Williams, P. (2013). *The Periglacial Environment*. Wiley.
Frost, G. V., Epstein, H. E., Walker, D. A., Matyshak, G., & Ermokhina, K. (2018). Seasonal and Long-Term Changes to Active-Layer Temperatures after Tall Shrubland Expansion and Succession in Arctic Tundra. *Ecosystems (New York)*, *21*(3), 507-520. https://doi.org/10.1007/s10021-017-0165-5
Gallant, J. C., & Dowling, T. I. (2003). A multiresolution index of valley bottom flatness for mapping depositional areas. *Water Resources Research*, *39*(12), 1347. https://doi.org/10.1029/2002WR001426
Gao, L., Bernhardt, M., & Schulz, K. (2012). Elevation correction of ERA-Interim temperature data in complex terrain. *Hydrology and Earth System Sciences*, *16*(12), 4661-4673. https://doi.org/10.5194/hess-16-4661-2012
Garibaldi, M. C. (2023). *Understanding the spatial and temporal heterogeneity of permafrost at a range of scales across the Western Canadian Arctic and Subarctic* (Dissertation/Thesis), University of Lethbridge. https://go.exlibris.link/9qFG2phm
Garibaldi, M. C., Bonnaventure, P. P., & Lamoureux, S. F. (2021). Utilizing the TTOP model to understand spatial permafrost temperature variability in a High Arctic landscape, Cape Bounty, Nunavut, Canada. *Permafrost and Periglacial Processes*, *32*(1), 19-34. https://doi.org/10.1002/ppp.2086
Garibaldi, M. C., Bonnaventure, P. P., Noad, N. C., & Kochtitzky, W. (2024a). Exploring the impact of surface lapse rate change scenarios on mountain permafrost distribution in four dissimilar valleys in Yukon, Canada. *Arctic Science*, *10*(4), 749-763. https://doi.org/10.1139/as-2023-0066

Garibaldi, M. C., Bonnaventure, P. P., Noad, N. C., & Kochtitzky, W. (2024b). Modelling air, ground surface and permafrost temperature variability across four dissimilar valleys, Yukon, Canada. *Arctic Science*, *10*(4), 611-629. https://doi.org/10.1139/as-2023-0067

Garibaldi, M. C., Bonnaventure, P. P., Smith, S. L., & Duchesne, C. (2022). Active layer variability and change in the Mackenzie Valley, Northwest Territories between 1991-2014: An ecoregional assessment. *Arctic, Antarctic, and Alpine Research*, *54*(1), 274-293. https://doi.org/10.1080/15230430.2022.2097156

Garibaldi, M. C., Bonnaventure, P. P., Way, R. G., Bevington, A., Smith, S. L., Lamoureux, S. F., Holloway, J. E., Lewkowicz, A. G., and Ackerman, H. (2026). Determining TTOP model parameter importance and overall performance across northern Canada, *The Cryosphere*, 20, 2375–2392, https://doi.org/10.5194/tc-20-2375-2026.

Gelaro, R., McCarty, W., Suárez, M. J., Todling, R., Molod, A., Takacs, L., Randles, C. A., Darmenov, A., Bosilovich, M. G., Reichle, R., Wargan, K., Coy, L., Cullather, R., Draper, C., Akella, S., Buchard, V., Conaty, A., Da Silva, A. M., Gu, W., . . . Zhao, B. (2017). The Modern-Era Retrospective Analysis for Research and Applications, Version 2 (MERRA-2). *Journal of Climate*, *30*(14), 5419-5454. https://doi.org/10.1175/JCLI-D-16-0758.1

Gibson, C. M., Chasmer, L. E., Thompson, D. K., Quinton, W. L., Flannigan, M. D., & Olefeldt, D. (2018). Wildfire as a major driver of recent permafrost thaw in boreal peatlands. *Nature Communications*, *9*(1), 3041-3049. https://doi.org/10.1038/s41467-018-05457-1

Gilson, G. F., Jiskoot, H., Cassano, J. J., & Nielsen, T. R. (2018). Radiosonde-Derived Temperature Inversions and Their Association With Fog Over 37 Melt Seasons in East Greenland. *Journal of Geophysical Research: Atmospheres*, *123*(17), 9571-9588. https://doi.org/10.1029/2018JD028886

Gisnås, K., Etzelmüller, B., Lussana, C., Hjort, J., Sannel, A. B. K., Isaksen, K., Westermann, S., Kuhry, P., Christiansen, H. H., Frampton, A., & Åkerman, J. (2017). Permafrost Map for Norway, Sweden and Finland. *Permafrost and Periglacial Processes*, *28*(2), 359-378. https://doi.org/10.1002/ppp.1922

Gisnås, K., Westermann, S., Schuler, T. V., Litherland, T., Isaksen, K., Boike, J., & Etzelmüller, B. (2014). A statistical approach to represent small-scale variability of permafrost temperatures due to snow cover. *The Cryosphere*, *8*(6), 2063-2074. https://doi.org/10.5194/tc-8-2063-2014

Gisnås, K., Westermann, S., Schuler, T. V., Melvold, K., & Etzelmüller, B. (2016). Small-scale variation of snow in a regional permafrost model. *The Cryosphere*, *10*(3), 1201-1215. https://doi.org/10.5194/tc-10-1201-2016

Goodrich, L. E. (1982). The influence of snow cover on the ground thermal regime. *Canadian Geotechnical Journal*, *19*(4), 421-432. https://doi.org/10.1139/t82-047

Graham, R. M., Hudson, S. R., & Maturilli, M. (2019). Improved Performance of ERA5 in Arctic Gateway Relative to Four Global Atmospheric Reanalyses. *Geophysical Research Letters*, *46*(11), 6138-6147. https://doi.org/10.1029/2019GL082781

Green, M. C., Chow, J. C., Watson, J. G., Dick, K., & Inouye, D. (2015). Effects of Snow Cover and Atmospheric Stability on Winter PM2.5 Concentrations in Western U.S. Valleys. *Journal of Applied Meteorology and Climatology*, *54*(6), 1191-1201. https://doi.org/10.1175/JAMC-D-14-0191.1

Gruber, S. (2012). Derivation and analysis of a high-resolution estimate of global permafrost zonation. The *Cryosphere*. https://doi.org/10.5167/uzh-68821;10.5194/tc-6-221-2012;

Gruber, S. (2020). Ground subsidence and heave over permafrost: hourly time series reveal interannual, seasonal and shorter-term movement caused by freezing, thawing and water movement. *The cryosphere*, *14*(4), 1437-1447. https://doi.org/10.5194/tc-14-1437-2020

Gubler, S., Endrizzi, S., Gruber, S., & Purves, R. S. (2013). Sensitivities and uncertainties of modeled ground temperatures in mountain environments. *Geoscientific Model Development*, *6*(4), 1319-1336. https://doi.org/10.5194/gmd-6-1319-2013

Gubler, S., Fiddes, J., Keller, M., & Gruber, S. (2011). Scale-dependent measurement and analysis of ground surface temperature variability in alpine terrain. *The Cryosphere*, *5*(2), 431-443. https://doi.org/10.5194/tc-5-431-2011

Gupta, H. V., Kling, H., Yilmaz, K. K., & Martinez, G. F. (2009). Decomposition of the mean squared error and NSE performance criteria: Implications for improving hydrological modelling. *Journal of Hydrology*, *377*(1), 80-91. https://doi.org /10.1016/j.jhydrol.2009.08.003

Gultepe, I. (2015). Mountain weather: Observation and modeling. In R. Dmowska (Ed.), *Advances in geophysics* (Vol. 56, pp. 229–312). Elsevier. https://doi.org/10.1016/bs.agph.2015.01.001

Haeberli, W. (2013). Mountain permafrost — research frontiers and a special long-term challenge. *Cold Regions Science and Technology*, *96*, 71-76. https://doi.org/10.1016/j.coldregions.2013.02.004

Harris, S. A. (1982). Cold air drainage west of Fort Nelson, British Columbia. *Arctic*, 35(4), 537–541. https://doi.org/10.14430/arctic2362

Harris, S. A., French, H. M., Heginbottom, J. A., Johnston, G. H., Ladanyi, B., Sego, D. C., & Everdingen, R. O. (1988). Glossary of permafrost and related ground-ice terms. In. National Research Council of Canada. Associate Committee on Geotechnical Research. Permafrost Subcommittee. https://doi.org/10.4224/20386561

Hasler, A., Geertsema, M., Foord, V., Gruber, S., & Noetzli, J. (2015). The influence of surface characteristics, topography and continentality on mountain permafrost in British Columbia. *The Cryosphere*, *9*(3), 1025-1038. https://doi.org/10.5194/tc-9-1025-2015

Hassink, N., Bonnaventure, P. P., & Johnson, D. L. (2025). Air and surface temperature modelling across a temperate mountain landscape: An investigation of microclimatic influences on surface offsets viewed within the context of epigaeic arthropod thermal habitat. *Canadian Geographies / Géographies canadiennes*, *69*(1), e70003. https://doi.org /10.1111/cag.70003

Heginbottom, J., Dubreuil, M., & Harker, P. (1995). *Canada permafrost* (National Atlas of Canada, Sheet 4177). Natural Resources Canada.

Henry, K., & Smith, M. (2001). A model-based map of ground temperatures for the permafrost regions of Canada. *Permafrost and Periglacial Processes*, *12*(4), 389-398. https://doi.org/10.1002/ppp.399

Hersbach, H., Bell, B., Berrisford, P., Hirahara, S., Horányi, A., Muñoz-Sabater, J., Nicolas, J., Peubey, C., Radu, R., Schepers, D., Simmons, A., Soci, C., Abdalla, S., Abellan, X., Balsamo, G., Bechtold, P., Biavati, G., Bidlot, J., Bonavita, M., … Thépaut, J.-N. (2020). The ERA5 global reanalysis. *Quarterly Journal of the Royal Meteorological Society*, 146(730), 1999–2049. https://doi.org/10.1002/qj.3803

Hersbach, H., Bell, B., Berrisford, P., Biavati, G., Horányi, A., Muñoz-Sabater, J., Nicolas, J., Peubey, C., Radu, R., Rozum, I., Schepers, D., Simmons, A., Soci, C., Dee, D., & Thépaut, J.-N. (2023a). *ERA5 hourly data on pressure levels from 1940 to present* [Data set]. Copernicus Climate Change Service (C3S) Climate Data Store (CDS). https://doi.org/10.24381/cds.bd0915c6

Hersbach, H., Bell, B., Berrisford, P., Biavati, G., Horányi, A., Muñoz-Sabater, J., Nicolas, J., Peubey, C., Radu, R., Rozum, I., Schepers, D., Simmons, A., Soci, C., Dee, D., & Thépaut, J.-N. (2023b). *ERA5 hourly data on single levels from 1940 to present* [Data set]. Copernicus Climate Change Service (C3S) Climate Data Store (CDS). https://doi.org/10.24381/cds.adbb2d47

Höge, M., Wöhling, T., & Nowak, W. (2018). A Primer for Model Selection: The Decisive Role of Model Complexity. *Water Resources Research*, *54*(3), 1688-1715. https://doi.org/10.1002/2017WR021902

Holloway, J. E., Lewkowicz, A. G., Douglas, T. A., Li, X., Turetsky, M. R., Baltzer, J. L., & Jin, H. (2020). Impact of wildfire on permafrost landscapes: A review of recent advances and future prospects. *Permafrost and Periglacial Processes*, *31*(3), 371-382. https://doi.org/10.1002/ppp.2048

Hjort, J., Karjalainen, O., Aalto, J., Westermann, S., Romanovsky, V. E., Nelson, F. E., Etzelmüller, B., & Luoto, M. (2018). Degrading permafrost puts Arctic infrastructure at risk by mid-century. *Nature Communications*, *9*(1), 5147-5147. https://doi.org/10.1038/s41467-018-07557-4

Hrebtov, M., & Hanjalić, K. (2017). Numerical study of winter diurnal convection over the city of Krasnoyarsk: Effects of non-freezing river, undulating fog and steam devils. *Boundary-Layer Meteorology*, 163, 469–495. https://doi.org/10.1007/s10546-016-0231-0

Hubbard, K. G., Lin, X., & Walter-Shea, E. A. (2001). The Effectiveness of the ASOS, MMTS, Gill, and CRS Air Temperature Radiation Shields. *Journal of Atmospheric and Oceanic Technology*, *18*(6), 851-864. https://doi.org/https://doi.org/10.1175/1520-0426(2001)018<0851:TEOTAM>2.0.CO;2

Hughes, J. K., Ross, A. N., Vosper, S. B., Lock, A. P., & Jemmett-Smith, B. C. (2015). Assessment of valley cold pools and clouds in a very high-resolution numerical weather prediction model. *Geoscientific Model Development*, 8, 3105–3117. https://doi.org/10.5194/gmd-8-3105-2015

Jafarov, E. E., Marchenko, S. S., & Romanovsky, V. E. (2012). Numerical modeling of permafrost dynamics in Alaska using a high spatial resolution dataset. *The Cryosphere*, *6*(3), 613-624. https://doi.org/10.5194/tc-6-613-2012

Jemmett-Smith, B., Ross, A. N., & Sheridan, P. (2018). A short climatological study of cold air pools and drainage flows in small valleys. *Weather*, *73*(8), 256-262. https://doi.org/10.1002/wea.3281

Johannessen, O. M., Kuzmina, S. I., Bobylev, L. P., & Miles, M. W. (2016). Surface air temperature variability and trends in the Arctic: new amplification assessment and regionalisation. *Tellus A: Dynamic Meteorology and Oceanography*, *68*(1), 28234. https://doi.org/10.3402/tellusa.v68.28234

Jorgenson, M. T., Romanovsky, V., Harden, J., Shur, Y., O'Donnell, J., Schuur, E. A. G., Kanevskiy, M., & Marchenko, S. (2010). Resilience and vulnerability of permafrost to climate change. *Canadian Journal of Forest Research*, *40*(7), 1219-1236. https://doi.org/10.1139/X10-060

Jost, G., Weiler, M., Gluns, D. R., & Alila, Y. (2007). The influence of forest and topography on snow accumulation and melt at the watershed-scale. *Journal of Hydrology*, *347*(1), 101-115. https://doi.org /10.1016/j.jhydrol.2007.09.006

Juliussen, H., & Humlum, O. (2007). Towards a TTOP ground temperature model for mountainous terrain in central-eastern Norway. *Permafrost and Periglacial Processes*, *18*(2), 161-184. https://doi.org/10.1002/ppp.586

Kahl, J. D., Serreze, M. C., & Schnell, R. C. (1992). Tropospheric low-level temperature inversions in the Canadian Arctic. *Atmosphere-Ocean*, 30(4), 511–529. https://doi.org/10.1080/07055900.1992.9649453

Karlsson, I. M. (2000). Nocturnal Air Temperature Variations between Forest and Open Areas. *Journal of Applied Meteorology*, *39*(6), 851-862. https://doi.org/10.1175/1520-0450(2000)039<0851:NATVBF>2.0.CO;2

Karunaratne, K. C., & Burn, C. R. (2004). Relations between air and surface temperature in discontinuous permafrost terrain near Mayo, Yukon Territory. *Canadian Journal of Earth Sciences*, *41*(12), 1437-1451. https://doi.org/10.1139/e04-082

Kiefer, M. T., & Zhong, S. (2015). The role of forest cover and valley geometry in cold-air pool evolution. *Journal of Geophysical Research: Atmospheres*, *120*(17), 8693-8711. https://doi.org/10.1002/2014JD022998

Kokelj, S. V., & Jorgenson, M. T. (2013). Advances in Thermokarst Research. *Permafrost and Periglacial Processes*, *24*(2), 108-119. https://doi.org/10.1002/ppp.1779

Kosaka, Y., Kobayashi, S., Harada, Y., Kobayashi, C., Naoe, H., Yoshimoto, K., Harada, M., Goto, N., Chiba, J., Miyaoka, K., Sekiguchi, R., Deushi, M., Kamahori, H., Nakaegawa, T., Tanaka, T. Y., Tokuhiro, T., Sato, Y., Matsushita, Y., & Onogi, K. (2024). The JRA-3Q Reanalysis. *Journal of the Meteorological Society of Japan. Ser. II*, *102*(1), 49-109. https://doi.org/10.2151/jmsj.2024-004

Kossmann, M., & Sturman, A. P. (2003). Pressure-Driven Channeling Effects in Bent Valleys. *Journal of Applied Meteorology (1988)*, *42*(1), 151-158. https://doi.org/10.1175/1520-0450(2003)042<0151:PDCEIB>2.0.CO;2

Kurylyk, B. L., & Hayashi, M. (2016). Improved Stefan Equation Correction Factors to Accommodate Sensible Heat Storage during Soil Freezing or Thawing. *Permafrost and Periglacial Processes*, *27*(2), 189-203. https://doi.org/10.1002/ppp.1865

Kurylyk, B. L., McKenzie, J. M., MacQuarrie, K. T. B., & Voss, C. I. (2014). Analytical solutions for benchmarking cold regions subsurface water flow and energy transport models: One-dimensional soil thaw with conduction and advection. *Advances in Water Resources*, *70*, 172-184. https://doi.org/10.1016/j.advwatres.2014.05.005

Largeron, Y., & Staquet, C. (2016). Persistent inversion dynamics and wintertime PM10 air pollution in Alpine valleys. *Atmospheric Environment*, *135*, 92-108. https://doi.org/10.1016/j.atmosenv.2016.03.045

Lareau, N. P., & Horel, J. D. (2015a). Dynamically Induced Displacements of a Persistent Cold-Air Pool. *Boundary-Layer Meteorology*, *154*(2), 291-316. https://doi.org/10.1007/s10546-014-9968-5

Lareau, N. P., & Horel, J. D. (2015b). Turbulent Erosion of Persistent Cold-Air Pools: Numerical Simulations. *Journal of the Atmospheric Sciences*, *72*(4), 1409-1427. https://doi.org/10.1175/JAS-D-14-0173.1

Lavers, D. A., Simmons, A., Vamborg, F., & Rodwell, M. J. (2022). An evaluation of ERA5 precipitation for climate monitoring. *Quarterly Journal of the Royal Meteorological Society*, *148*(748), 3152-3165. https://doi.org/ 10.1002/qj.4351

LaZerte, S. E. and Albers, S. (2018). weathercan: Download and format weather data from Environment and Climate Change Canada, *The Journal of Open Source Software*, 3, 571, https://doi.org/10.21105/joss.00571.

Lehner, M., Whiteman, C. D., & Dorninger, M. (2017). Inversion Build-Up and Cold-Air Outflow in a Small Alpine Sinkhole. *Boundary-Layer Meteorology*, *163*(3), 497-522. https://doi.org/10.1007/s10546-017-0232-7

Lewkowicz, A. G., & Bonnaventure, P. P. (2011). Equivalent Elevation: A New Method to Incorporate Variable Surface Lapse Rates into Mountain Permafrost Modelling. *Permafrost and Periglacial Processes*, *22*(2), 153-162. https://doi.org/10.1002/ppp.720

Lewkowicz, A. G., Bonnaventure, P. P., Smith, S. L., & Kuntz, Z. (2012). Spatial and thermal characteristics of mountain permafrost, northwest canada. *Geografiska Annaler: Series A, Physical Geography*, *94*(2), 195-213. https://doi.org/10.1111/j.1468-0459.2012.00462.x

Lewkowicz, A. G., & Ednie, M. (2004). Probability mapping of mountain permafrost using the BTS method, Wolf Creek, Yukon Territory, Canada. *Permafrost and Periglacial Processes*, *15*(1), 67-80. https://doi.org/10.1002/ppp.480

Lewkowicz, A. G., O'Neill, H. B., Wolfe, S. A., Roy-Léveillée, P., Roujanski V, H. E., Gruber, S., Brook, E. J., Rudy, A. C. A., Brown, N., & Bonnaventure, P. P. (2025). *Glossary of Permafrost Science and Engineering*. Canadian Permafrost Association. https://doi.org/http://doi.org/10.3138/cpa-gpse

Lewkowicz, A. G., & Way, R. G. (2019). Extremes of summer climate trigger thousands of thermokarst landslides in a High Arctic environment. *Nature Communications*, *10*(1), 1329. https://doi.org/10.1038/s41467-019-09314-7

Li, Y., Zhao, M., Motesharrei, S., Mu, Q., Kalnay, E., & Li, S. (2015). Local cooling and warming effects of forests based on satellite observations. *Nature Communications*, *6*, 6603. https://doi.org/10.1038/ncomms7603

Li, X., Jin, H., He, R., Huang, Y., Wang, H., Luo, D., Jin, X., Lü, L., Wang, L., Li, W. h., Wei, C., Chang, X., Yang, S., & Yu, S. (2019). Effects of forest fires on the permafrost environment in the northern Da Xing'anling (Hinggan) mountains, Northeast China. *Permafrost and Periglacial Processes*, *30*(3), 163-177. https://doi.org/10.1002/ppp.2001

Lin, Z., Burn, C. R., Niu, F., Luo, J., Liu, M., & Yin, G. (2015). The Thermal Regime, including a Reversed Thermal Offset, of Arid Permafrost Sites with Variations in Vegetation Cover Density, Wudaoliang Basin, Qinghai-Tibet Plateau. *Permafrost and Periglacial Processes*, *26*(2), 142-159. https://doi.org/https://doi.org/10.1002/ppp.1840

Liston, G. E., & Sturm, M. (1998). A snow-transport model for complex terrain. *Journal of Glaciology*, *44*(148), 498-516. https://doi.org/10.3189/S0022143000002021

Liu, Z., Guo, D., Hua, W., and Chen, Y. (2025). Near-surface permafrost extent and active layer thickness characterized by reanalysis/assimilation data, *Atmospheric Science Letters*, 26, https://doi.org/10.1002/asl.1289.

Lunardini, V.J. 1978. 'Theory of n-factors and Correlation of Data', in 3rd International Conference on Permafrost. Edmonton, Alberta, Canada: July 10–13, 1978, vol. 1, pp. 40–46.

Lundquist, J. D., & Cayan, D. R. (2007). Surface temperature patterns in complex terrain: Daily variations and long-term change in the central Sierra Nevada, California. *Journal of Geophysical Research: Atmospheres*, *112*(D11), D11124. https://doi.org/10.1029/2006JD007561

Lundquist, J. D., & Lott, F. (2008). Using inexpensive temperature sensors to monitor the duration and heterogeneity of snow-covered areas. *Water Resources Research*, *44*(4). https://doi.org /10.1029/2008WR007035

Luo, D., Jin, H., Wu, Q., Bense, V. F., He, R., Ma, Q., Gao, S., Jin, X., & Lü, L. (2018). Thermal regime of warm-dry permafrost in relation to ground surface temperature in the Source Areas of the Yangtze and Yellow rivers on the Qinghai-Tibet Plateau, SW China. *Science of the Total Environment*, *618*, 1033-1045. https://doi.org/10.1016/j.scitotenv.2017.09.083

Luo, D., Liu, J., Chen, F., & Li, S. (2025). Observed talik development triggers a tipping point in marginal permafrost of the Qinghai-Xizang Plateau. *Geoscience Frontiers*, *16*(5), 102122. https://doi.org/ 10.1016/j.gsf.2025.102122

Luo, J., Yin, G., Niu, F., Lin, Z., & Liu, M. (2019). High Spatial Resolution Modeling of Climate Change Impacts on Permafrost Thermal Conditions for the Beiluhe Basin, Qinghai-Tibet Plateau. *Remote sensing (Basel, Switzerland)*, *11*(11), 1294. https://doi.org/10.3390/rs11111294

MacDonald, A. A. C., Stralberg, D., & Nielsen, S. E. (2025). Alpine Summer Surface Temperature Amplification Is Spatially Heterogeneous and Intensified by Wind and Sun. *Ecology and Evolution*, *15*(11), e72542. https://doi.org/ 10.1002/ece3.72542

MacDonald, H., McKenney, D. W., Papadopol, P., Lawrence, K., Pedlar, J., & Hutchinson, M. F. (2020). North American historical monthly spatial climate dataset, 1901-2016. *Scientific Data*, *7*(1), 411-411. https://doi.org/10.1038/s41597-020-00737-2

MacDonald, M. K., Pomeroy, J. W., & Pietroniro, A. (2009). Parameterizing redistribution and sublimation of blowing snow for hydrological models: tests in a mountainous subarctic catchment. *Hydrological Processes*, *23*(18), 2570-2583. https://doi.org/10.1002/hyp.7356

Maillard, J., Ravetta, F., Raut, J.-C., Fochesatto, G. J., & Law, K. S. (2022). Modulation of Boundary-Layer Stability and the Surface Energy Budget by a Local Flow in Central Alaska. *Boundary-Layer Meteorology*, *185*(3), 395-414. https://doi.org/10.1007/s10546-022-00737-2

Majorowicz, J., & Grasby, S. E. (2010). Heat flow, depth–temperature variations and stored thermal energy for enhanced geothermal systems in Canada. *Geophysics*, *7*(3), 232-241. https://doi.org/10.1088/1742-2132/7/3/002

Marchenko, S., Romanovsky, V., & Tipenko, G. (2008). *Numerical modeling of spatial permafrost dynamics in Alaska*. In Proceedings of the Ninth International Conference on Permafrost (Fairbanks, AK).

Marsh, P., Bartlett, P., MacKay, M., Pohl, S., & Lantz, T. (2010). Snowmelt energetics at a shrub tundra site in the western Canadian Arctic. *Hydrological Processes*, *24*(25), 3603-3620. https://doi.org/10.1002/hyp.7786

Mayfield, J. A., & Fochesatto, G. J. (2013). The Layered Structure of the Winter Atmospheric Boundary Layer in the Interior of Alaska. *Journal of Applied Meteorology and Climatology*, *52*(4), 953-973. https://doi.org/10.1175/JAMC-D-12-01.1

Mayfield, J. A., & Fochesatto, G. J. (2018). The turbulence regime of the atmospheric surface layer in the presence of shallow cold drainage flows: Application of laser scintillometry. In B. Régis (Ed.), *Turbulence and related phenomena* (pp. 59–82). IntechOpen. https://doi.org/10.5772/intechopen.80290

McCray, C. D., Atallah, E. H., & Gyakum, J. R. (2019). Long-Duration Freezing Rain Events over North America: Regional Climatology and Thermodynamic Evolution. *Weather and Forecasting*, *34*(3), 665-681. https://doi.org/10.1175/WAF-D-18-0154.1

Ménard, C. B., Essery, R., & Pomeroy, J. (2014). Modelled sensitivity of the snow regime to topography, shrub fraction and shrub height. *Hydrology and Earth System Sciences*, *18*(6), 2375-2392. https://doi.org/10.5194/hess-18-2375-2014

Minder, J. R., Mote, P. W., & Lundquist, J. D. (2010). Surface temperature lapse rates over complex terrain: Lessons from the Cascade Mountains. *Journal of Geophysical Research*, *115*(D14). https://doi.org/10.1029/2009jd013493

Morse, P. D., & Wolfe, S. A. (2015). Geological and meteorological controls on icing (aufeis) dynamics (1985 to 2014) in subarctic Canada. *Journal of Geophysical Research: Atmsopheres or Earth*, *120*(9), 1670-1686. https://doi.org/10.1002/2015JF003534

Morse, P. D., Wolfe, S. A., Kokelj, S. V., & Gaanderse, A. J. R. (2016). The Occurrence and Thermal Disequilibrium State of Permafrost in Forest Ecotopes of the Great Slave Region, Northwest Territories, Canada. *Permafrost and Periglacial Processes*, *27*(2), 145-162. https://doi.org/10.1002/ppp.1858

Müller, H., & Whiteman, C. D. (1988). Breakup of a Nocturnal Temperature Inversion in the Dischma Valley during DISKUS. *Journal of Applied Meteorology (1988)*, *27*(2), 188-194. https://doi.org/10.1175/1520-0450(1988)027<0188:BOANTI>2.0.CO;2

Muñoz-Sabater, J. (2019). ERA5-Land hourly data from 1950 to present [Data set]. Copernicus Climate Change Service (C3S) Climate Data Store (CDS). https://doi.org/10.24381/cds.e2161bac

Myers-Smith, I. H., Forbes, B. C., Wilmking, M., Hallinger, M., Lantz, T., Blok, D., Tape, K. D., Macias-Fauria, M., Sass-Klaassen, U., Lévesque, E., Boudreau, S., Ropars, P., Hermanutz, L., Trant, A., Collier, L. S., Weijers, S., Rozema, J., Rayback, S. A., Schmidt, N. M., . . . Hik, D. S. (2011). Shrub expansion in tundra ecosystems: dynamics, impacts and research priorities. *Environmental Research Letters*, *6*(4), 045509. https://doi.org/10.1088/1748-9326/6/4/045509

Nakamura, R., & Mahrt, L. (2005). Air Temperature Measurement Errors in Naturally Ventilated Radiation Shields. *Journal of Atmospheric and Oceanic Technology*, *22*(7), 1046-1058. https://doi.org/https://doi.org/10.1175/JTECH1762.1

Nash, J. E., & Sutcliffe, J. V. (1970). River flow forecasting through conceptual models part I — A discussion of principles. *Journal of Hydrology*, *10*(3), 282-290. https://doi.org/10.1016/0022-1694(70)90255-6

Neff, W. D., & King, C. W. (1989). The Accumulation and Pooling of Drainage Flows in a Large Basin. *Journal of Applied Meteorology (1988)*, *28*(6), 518-529. https://doi.org/10.1175/1520-0450(1989)028<0518:TAAPOD>2.0.CO;2

Nicholson, R., Bonnaventure, P. P., Noad, N. C., Garibaldi, M. C., Thiessen, R., & Kochtitzky, W. (*Submitted*). Evaluating Testability of Permafrost Models Through Physical and Thermal Testing in Complex Mountain Terrain, Yukon, Canada. *Permafrost and Periglacial Processes*.

Nitzbon, J., Schneider von Deimling, T., Aliyeva, M., Chadburn, S. E., Grosse, G., Laboor, S., Lee, H., Lohmann, G., Steinert, N. J., Stuenzi, S. M., Werner, M., Westermann, S., & Langer, M. (2024). No respite from permafrost-thaw impacts in the absence of a global tipping point. *Nature Climate Change*, *14*(6), 573-585. https://doi.org/10.1038/s41558-024-02011-4

Nkiaka, E., Nawaz, N. R., and Lovett, J. C. (2017). Evaluating Global Reanalysis Datasets as Input for Hydrological Modelling in the Sudano-Sahel Region, *Hydrology*, 4, https://doi.org/10.3390/hydrology4010013.

Noad, N. C., & Bonnaventure, P. P. (2026). Spatiotemporal variability of surface-based temperature inversions in high-latitude northcentral Yukon valleys utilizing a dense network of elevation transects. *Arctic, Antarctic, and Alpine Research*, 58(1), 2614790. https://doi.org/10.1080/15230430.2026.2614790

Noad, N. C., & Bonnaventure, P. P. (2023). Examining the influence of microclimate conditions on the breakup of surface-based temperature inversions in two proximal but dissimilar Yukon valleys. *Canadian Geographies / Géographies canadiennes*, 1-17. https://doi.org/10.1111/cag.12886

Noad, N. C., & Bonnaventure, P. P. (2022). Surface temperature inversion characteristics in dissimilar valleys, Yukon Canada. *Arctic Science*, *8*(4), 1320-1339. https://doi.org/10.1139/as-2021-0048

Noad, N. C., Bonnaventure, P. P., Gilson, G. F., Jiskoot, H., & Garibaldi, M. C. (2023). Surface-based temperature inversion characteristics and impact on surface air temperatures in northwestern Canada from radiosonde data between 1990 and 2016. *Arctic Science*, *9*(3), 545-563. https://doi.org/10.1139/AS-2022-0031

Noad, N. C., Pozsgay, V., Bonnaventure, P. P., & Gruber, S. (Submitted). Validation of Point-Scale Climate Reanalysis Models Calibrated for Surface-Based Temperature Inversions Utilizing In-Situ Measures in Northcentral Yukon Valleys. *Arctic Science*.

Noetzli, J., Isaksen, K., Barnett, J., Christiansen, H. H., Delaloye, R., Etzelmüller, B., Farinotti, D., Gallemann, T., Guglielmin, M., Hauck, C., Hilbich, C., Hoelzle, M., Lambiel, C., Magnin, F., Oliva, M., Paro, L., Pogliotti, P., Riedl, C., Schoeneich, P., . . . Phillips, M. (2024). Enhanced warming of European mountain permafrost in the early 21st century. *Nature Communications*, *15*(1), 10508. https://doi.org/10.1038/s41467-024-54831-9

Ntagkounakis, G. E., Nastos, P. T., and Kapsomenakis, Y. (2023). Statistical Downscaling of ERA5 Reanalysis Precipitation over the Complex Terrain of Greece, *Environmental Sciences Proceedings*, 26, https://doi.org/10.3390/environsciproc2023026081.

O'Kuinghttons, R., Koziol, B., Oehmke, R., DeLuca, C., Theurich, G., Li, P., & Jacob, J. (2016). ESMPy and OpenClimateGIS: Python interfaces for high performance grid remapping and geospatial dataset manipulation. In *EGU General Assembly* 2016 (Vienna, Austria). https://ui.adsabs.harvard.edu/abs/2016EGUGA..1810050O

O'Neill, H. B., Wolfe, S. A., & Duchesne, C. (2019). New ground ice maps for Canada using a paleogeographic modelling approach. *The Cryosphere*, *13*(3), 753-773. https://doi.org/10.5194/tc-13-753-2019

O'Neill, H. B., & Burn, C. R. (2017). Impacts of variations in snow cover on permafrost stability, including simulated snow management, Dempster Highway, Peel Plateau, Northwest Territories. *Arctic Science*, *3*(2), 150-178. https://doi.org/10.1139/as-2016-0036

O'Neill, H. B., Smith, S. L., Burn, C. R., Duchesne, C., & Zhang, Y. (2023). Widespread Permafrost Degradation and Thaw Subsidence in Northwest Canada. *Journal of Geophysical Research. Earth surface*, *128*(8), n/a-n/a. https://doi.org/10.1029/2023JF007262

Obu, J., Westermann, S., Bartsch, A., Berdnikov, N., Christiansen, H. H., Dashtseren, A., Delaloye, R., Elberling, B., Etzelmüller, B., Kholodov, A., Khomutov, A., Kääb, A., Leibman, M. O., Lewkowicz, A. G., Panda, S. K., Romanovsky, V., Way, R. G., Westergaard-Nielsen, A., Wu, T., . . . Zou, D. (2019). Northern Hemisphere permafrost map based on TTOP modelling for 2000–2016 at 1 km2 scale. *Earth-Science Reviews*, *193*, 299-316. https://doi.org/10.1016/j.earscirev.2019.04.023

Obu, J. (2021). How Much of the Earth's Surface is Underlain by Permafrost? *Journal of Geophysical Research: Earth Surface*, *126*(5), e2021JF006123. https://doi.org/https://doi.org/10.1029/2021JF006123

Oelke, C., Zhang, T., Serreze, M. C., & Armstrong, R. L. (2003). Regional-scale modeling of soil freeze/thaw over the Arctic drainage basin. *Journal of Geophysical Research: Atmospheres*, *108*(D10), 4314-n/a. https://doi.org/10.1029/2002JD002722

Oke, T. R. (2002). *Boundary Layer Climates*. Taylor & Francis. https://doi.org/10.4324/9780203407219

Olefeldt, D., Goswami, S., Grosse, G., Hayes, D., Hugelius, G., Kuhry, P., McGuire, A. D., Romanovsky, V. E., Sannel, A. B. K., Schuur, E. A. G., & Turetsky, M. R. (2016). Circumpolar distribution and carbon storage of thermokarst landscapes. *Nature Communications*, 7(1), 13043. https://doi.org/10.1038/ncomms13043

Olson, C., Jiskra, M., Biester, H., Chow, J., & Obrist, D. (2018). Mercury in Active-Layer Tundra Soils of Alaska: Concentrations, Pools, Origins, and Spatial Distribution. *Global Biogeochemical Cycles*, *32*(7), 1058-1073. https://doi.org/10.1029/2017GB005840

Outcalt, S. I., Nelson, F. E., & Hinkel, K. M. (1990). The zero-curtain effect: Heat and mass transfer across an isothermal region in freezing soil. *Water Resources Research*, *26*(7), 1509-1516. https://doi.org/10.1029/WR026i007p01509

Oyler, J. W., Dobrowski, S. Z., Ballantyne, A. P., Klene, A. E., & Running, S. W. (2015). Artificial amplification of warming trends across the mountains of the western United States. *Geophysical Research Letters*, 42, 153–161. https://doi.org/10.1002/2014GL062803

Palazzi, E., Mortarini, L., Terzago, S., & von Hardenberg, J. (2019). Elevation-dependent warming in global climate model simulations at high spatial resolution. *Climate Dynamics*, 52(5), 2685–2702. https://doi.org/10.1007/s00382-018-4287-z

Park, H., Watanabe, E., Kim, Y., Polyakov, I., Oshima, K., Zhang, X., Kimball, J. S., & Yang, D. (2020). Increasing riverine heat influx triggers Arctic sea ice decline and oceanic and atmospheric warming. *Science Advances*, 6. https://doi.org/10.1126/sciadv.abc4699

Parr, C., Sturm, M., & Larsen, C. (2020). Snowdrift Landscape Patterns: An Arctic Investigation. *Water Resources Research*, *56*(12), e2020WR027823. https://doi.org/10.1029/2020WR027823

Peng, X., Zhang, T., Frauenfeld, O. W., Mu, C., Wang, K., Wu, X., Guo, D., Luo, J., Hjort, J., Aalto, J., Karjalainen, O., & Luoto, M. (2023). Active Layer Thickness and Permafrost Area Projections for the 21st Century. *Earth's Future*, *11*(8), e2023EF003573. https://doi.org/10.1029/2023EF003573

Pepin, N., Bradley, R. S., Diaz, H. F., Baraer, M., Caceres, E. B., Forsythe, N., Fowler, H., Greenwood, G., Hashmi, M. Z., Liu, X. D., Miller, J. R., Ning, L., Ohmura, A., Palazzi, E., Rangwala, I., Schoner, W., Severskiy, I., Shahgedanova, M., Wang, M. B., . . . Yang, D. Q. (2015). Elevation-dependent warming in mountain regions of the world. *Nature Climate Change*, *5*(5), 424-430. https://doi.org/10.1038/NCLIMATE2563

Pepin, N. C., Arnone, E., Gobiet, A., Haslinger, K., Kotlarski, S., Notarnicola, C., Palazzi, E., Seibert, P., Serafin, S., Schöner, W., Terzago, S., Thornton, J. M., Vuille, M., & Adler, C.

(2022). Climate Changes and Their Elevational Patterns in the Mountains of the World. *Reviews of Geophysics*, *60*(1), e2020RG000730. https://doi.org/10.1029/2020RG000730
Pepin, N. C., Daly, C., & Lundquist, J. (2011). The influence of surface versus free-air decoupling on temperature trend patterns in the western United States. *Journal of Geophysical Research: Atmospheres*, *116*(D10). https://doi.org/10.1029/2010JD014769
Perreault, J., Fortier, R., & Molson, J. W. (2021). Numerical modelling of permafrost dynamics under climate change and evolving ground surface conditions: application to an instrumented permafrost mound at Umiujaq, Nunavik (Québec), Canada. *Écoscience*, *28*(3-4), 377-397. https://doi.org/10.1080/11956860.2021.1949819
Peterson, T. C., & Vose, R. S. (1997). An Overview of the Global Historical Climatology Network Temperature Database. *Bulletin of the American Meteorological Society*, *78*(12), 2837-2849. https://doi.org/10.1175/1520-0477(1997)078<2837:AOOTGH>2.0.CO;2
Pflug, J. M., Hughes, M., & Lundquist, J. D. (2021). Downscaling Snow Deposition Using Historic Snow Depth Patterns: Diagnosing Limitations From Snowfall Biases, Winter Snow Losses, and Interannual Snow Pattern Repeatability. *Water Resources Research*, *57*(8), e2021WR029999. https://doi.org/10.1029/2021WR029999
Pigeon, K. E., & Jiskoot, H. (2008). Meteorological Controls on Snowpack Formation and Dynamics in the Southern Canadian Rocky Mountains. *Arctic, Antarctic, and Alpine Research*, *40*(4), 716-730. https://doi.org/10.1657/1523-0430(07-054)[PIGEON]2.0.CO;2
Pike, G., Pepin, N. C., & Schaefer, M. (2013). High latitude local scale temperature complexity: the example of Kevo Valley, Finnish Lapland. *International Journal of Climatology*, *33*(8), 2050-2067. https://doi.org/10.1002/joc.3573
Ping, C. L., Jastrow, J. D., Jorgenson, M. T., Michaelson, G. J., & Shur, Y. L. (2015). Permafrost soils and carbon cycling. *Soil*, *1*(1), 147-171. https://doi.org/10.5194/soil-1-147-2015
Pollack, H. N., Hurter, S. J., & Johnson, J. R. (1993). Heat flow from the Earth's interior: Analysis of the global data set. *Reviews of Geophysics*, *31*(3), 267-280. https://doi.org/10.1029/93RG01249
Porter, C., Howat, I., Noh, M.-J., Husby, E., Khuvis, S., Danish, E., Tomko, K., Gardiner, J., Negrete, A., Yadav, B., Klassen, J., Kelleher, C., Cloutier, M., Bakker, J., Enos, J., Arnold, G., Bauer, G., & Morin, P. (2023). ArcticDEM—Mosaics, version 4.1 [Data set]. https://doi.org/10.7910/DVN/3VDC4W
Pozsgay, V., & Gruber, S. (2025). Modelling the temporal dynamics of subarctic surface temperature inversions from atmospheric reanalysis for producing point-scale multi-decade meteorological time series in mountains. *Arctic Science*. https://doi.org/10.1139/as-2025-0027
Pozsgay, V., Noad, N. C., Bonnaventure, P. P., & Gruber, S. (2026). DReaMIT: A Dynamical Reanalysis Framework for Modelling Surface-Based Temperature Inversions in Cold Environments. *EGUsphere*, 2026, 1-26. https://doi.org/10.5194/egusphere-2025-5512
Prowse, T. D., Bonsal, B. R., Duguay, C. R., & Lacroix, M. P. (2007). River-ice break-up/freeze-up: A review of climatic drivers, historical trends and future predictions. *Annals of Glaciology*, 46, 443–451. https://doi.org/10.3189/172756407782871431
Przybylak, R. (2016). *The climate of the Arctic* (2nd ed., Vol. 52). Springer.
Quéno, L., Mott, R., Morin, P., Cluzet, B., Mazzotti, G., & Jonas, T. (2024). Snow redistribution in an intermediate-complexity snow hydrology modelling framework. *The Cryosphere*, *18*(8), 3533-3557. https://doi.org/10.5194/tc-18-3533-2024

Rangecroft, S., Suggitt, A. J., Anderson, K., & Harrison, S. (2016). Future climate warming and changes to mountain permafrost in the Bolivian Andes. *Climatic Change*, *137*(1-2), 231-243. https://doi.org/10.1007/s10584-016-1655-8

Rasmus, S., Lundell, R., & Saarinen, T. (2011). Interactions between snow, canopy, and vegetation in a boreal coniferous forest. *Plant Ecology & Diversity*, *4*(1), 55-65. https://doi.org/10.1080/17550874.2011.558126

Rawlins, M. A., & Karmalkar, A. V. (2024). Regime shifts in Arctic terrestrial hydrology manifested from impacts of climate warming. *The Cryosphere*, *18*(3), 1033-1052. https://doi.org/10.5194/tc-18-1033-2024

Rendón, A. M., Salazar, J. F., & Wirth, V. (2020). Daytime air pollution transport mechanisms in stable atmospheres of narrow versus wide urban valleys. *Environmental fluid mechanics (Dordrecht, Netherlands : 2001)*, *20*(4), 1101-1118. https://doi.org/10.1007/s10652-020-09743-9

Riseborough, D. (2007). The effect of transient conditions on an equilibrium permafrost-climate model. *Permafrost and Periglacial Processes*, *18*, 21-32. https://doi.org/10.1002/ppp.579

Riseborough, D., Shiklomanov, N., Etzelmüller, B., Gruber, S., & Marchenko, S. (2008). Recent advances in permafrost modelling. *Permafrost and Periglacial Processes*, *19*(2), 137-156. https://doi.org/10.1002/ppp.615

Riseborough, D. W. (2003). *Thawing and freezing indices in the active layer*. Swets & Zeitlinger.

Roberts, D. R., Wood, W. H., & Marshall, S. J. (2019). Assessments of downscaled climate data with a high-resolution weather station network reveal consistent but predictable bias. *International Journal of Climatology*, *39*(6), 3091-3103. https://doi.org/10.1002/joc.6005

Romanovsky, V. E., & Osterkamp, T. E. (1995). Interannual variations of the thermal regime of the active layer and near-surface permafrost in northern Alaska. *Permafrost and Periglacial Processes*, *6*(4), 313-335. https://doi.org/10.1002/ppp.3430060404

Romanovsky, V. E., & Osterkamp, T. E. (2000). Effects of unfrozen water on heat and mass transport processes in the active layer and permafrost. *Permafrost and Periglacial Processes*, *11*(3), 219-239. https://doi.org/10.1002/1099-1530(200007/09)11:3<219::AID-PPP352>3.0.CO;2-7

Romanovsky, V. E., Smith, S. L., & Christiansen, H. H. (2010). Permafrost thermal state in the polar Northern Hemisphere during the international polar year 2007-2009: a synthesis. *Permafrost and Periglacial Processes*, *21*(2), 106-116. https://doi.org/10.1002/ppp.689

Ross, S. L. (2024). *Weather and climate: An introduction* (3rd ed.). Oxford University Press.

Roy-Léveillée, P., Burn, C. R., & McDonald, I. D. (2014). Vegetation-Permafrost Relations within the Forest-Tundra Ecotone near Old Crow, Northern Yukon, Canada. *Permafrost and Periglacial Processes*, *25*(2), 127-135. https://doi.org/10.1002/ppp.1805

Ruman, C. J., Monahan, A. H., & Sushama, L. (2022). Climatology of Arctic temperature inversions in current and future climates. *Theoretical and Applied Climatology*, *150*(1-2), 121-134. https://doi.org/10.1007/s00704-022-04147-9

Rupp, D. E., Shafer, S. L., Daly, C., Jones, J. A., & Frey, S. J. K. (2020). Temperature Gradients and Inversions in a Forested Cascade Range Basin: Synoptic- to Local-Scale Controls. *Journal of Geophysical Research: Atmospheres*, *125*(23). https://doi.org/10.1029/2020JD032686

Sadoti, G., McAfee, S. A., Roland, C. A., Fleur Nicklen, E., & Sousanes, P. J. (2018). Modelling high-latitude summer temperature patterns using physiographic variables. *International Journal of Climatology*, *38*(10), 4033-4042. https://doi.org/10.1002/joc.5538

Sakiyama, S. K. (1990). Drainage Flow Characteristics and Inversion Breakup in Two Alberta Mountain Valleys. *Journal of Applied Meteorology*, *29*(10), 1015-1030. https://doi.org/10.1175/1520-0450(1990)029<1015:DFCAIB>2.0.CO;2

Sazonova, T. S., & Romanovsky, V. E. (2003). A model for regional-scale estimation of temporal and spatial variability of active layer thickness and mean annual ground temperatures. *Permafrost and Periglacial Processes*, *14*(2), 125-139. https://doi.org/10.1002/ppp.449

Schaefer, K., Elshorbany, Y., Jafarov, E., Schuster, P. F., Striegl, R. G., Wickland, K. P., & Sunderland, E. M. (2020). Potential impacts of mercury released from thawing permafrost. *Nature Communications*, *11*(1), 4650-4650. https://doi.org/10.1038/s41467-020-18398-5

Schmid, M. O., Gubler, S., Fiddes, J., & Gruber, S. (2012). Inferring snowpack ripening and melt-out from distributed measurements of near-surface ground temperatures. *The Cryosphere*, *6*(5), 1127-1139. https://doi.org/10.5194/tc-6-1127-2012

Schroeder, M. J., & Buck, C. C. (1970). *Fire weather: A guide for application of meteorological information to forest fire control operations* (Agriculture Handbook No. 360). U.S. Department of Agriculture, Forest Service.

Schuster, P. F., Striegl, R. G., Aiken, G. R., Krabbenhoft, D. P., Dewild, J. F., Butler, K., Kamark, B., & Dornblaser, M. (2011). Mercury Export from the Yukon River Basin and Potential Response to a Changing Climate. *Environmental Science & Technology*, *45*(21), 9262-9267. https://doi.org/10.1021/es202068b

Schuur, E. A. G., McGuire, A. D., Schädel, C., Grosse, G., Harden, J. W., Hayes, D. J., Hugelius, G., Koven, C. D., Kuhry, P., Lawrence, D. M., Natali, S. M., Olefeldt, D., Romanovsky, V. E., Schaefer, K., Turetsky, M. R., Treat, C. C., & Vonk, J. E. (2015). Climate change and the permafrost carbon feedback. *Nature*, 520(7546), 171–179. https://doi.org/10.1038/nature14338

Scudder, G. G. E. (1997). Environment of the Yukon. In *Insects of the Yukon*. https://www.researchgate.net/publication/252860187_Environment_of_the_Yukon

Seidel, D. J., Ao, C. O., & Li, K. (2010). Estimating climatological planetary boundary layer heights from radiosonde observations: Comparison of methods and uncertainty analysis. *Journal of Geophysical Research: Atmospheres*, *115*(D16). https://doi.org/10.1029/2009JD013680

Sen Gupta, A., & Tarboton, D. G. (2016). A tool for downscaling weather data from large-grid reanalysis products to finer spatial scales for distributed hydrological applications. *Environmental Modelling & Software : with Environment Data News*, *84*, 50-69. https://doi.org/10.1016/j.envsoft.2016.06.014

Serreze, M. C., & Barry, R. G. (2011). Processes and impacts of Arctic amplification: A research synthesis. *Global and Planetary Change*, *77*(1), 85-96. https://doi.org/10.1016/j.gloplacha.2011.03.004

Serreze, M. C., & Barry, R. G. (2014). *The Arctic Climate System*. Cambridge University Press. https://doi.org/10.1017/CBO9781139583817

Shahi, S., Abermann, J., Heinrich, G., Prinz, R., & Schöner, W. (2020). Regional variability and trends of temperature inversions in Greenland. *Journal of Climate*, 1-48. https://doi.org/10.1175/JCLI-D-19-0962.1
Shen, Y.-J., Shen, Y., Goetz, J., & Brenning, A. (2016). Spatial-temporal variation of near-surface temperature lapse rates over the Tianshan Mountains, central Asia. *Journal of Geophysical Research: Atmospheres*, *121*(23), 14,006-014,017. https://doi.org/10.1002/2016JD025711
Sheridan, P. F. (2019). Synoptic-flow interaction with valley cold-air pools and effects on cold-air pool persistence: Influence of valley size and atmospheric stability. *Quarterly Journal of the Royal Meteorological Society*, *145*(721), 1636-1659. https://doi.org/10.1002/qj.3517
Shur, Y. L., & Jorgenson, M. T. (2007). Patterns of permafrost formation and degradation in relation to climate and ecosystems. *Permafrost and Periglacial Processes*, *18*(1), 7-19. https://doi.org/10.1002/ppp.582
Smith, M. W., & Riseborough, D. W. (2002). Climate and the limits of permafrost: a zonal analysis. *Permafrost and Periglacial Processes*, *13*(1), 1-15. https://doi.org/10.1002/ppp.410
Smith, S. A., Brown, A. R., Vosper, S. B., Murkin, P. A., & Veal, A. T. (2010). Observations and Simulations of Cold Air Pooling in Valleys. *Boundary-Layer Meteorology*, *134*(1), 85-108. https://doi.org/10.1007/s10546-009-9436-9
Smith, S. L., Roman M. W., & Riseborough, D. W. (1996). Permafrost monitoring and detection of climate change. *Permafrost and Periglacial Processes*, *7*(4), 301-309. https://doi.org/10.1002/(SICI)1099-1530(199610)7:4<301::AID-PPP231>3.0.CO;2-R
Smith, S. L., Romanovsky, V. E., Lewkowicz, A., Burn, C., Allard, M., Clow, G., Yoshikawa, K., & Throop, J. (2010). Thermal state of permafrost in North America: A contribution to the International Polar Year. Permafrost and Periglacial Processes, 21(2), 117–135. https://doi.org/10.1002/ppp.690
Smith, S. L., & Bonnaventure, P. P. (2017). Quantifying Surface Temperature Inversions and Their Impact on the Ground Thermal Regime at a High Arctic Site. *Arctic, Antarctic, and Alpine Research*, *49*(1), 173-185. https://doi.org/10.1657/AAAR0016-039
Smith, S. L., O'Neill, H. B., Isaksen, K., Noetzli, J., & Romanovsky, V. E. (2022). The changing thermal state of permafrost. *Nature Reviews Earth & Environment*, *3*(1), 10-23. https://doi.org/10.1038/s43017-021-00240-1
Smith, S. L., Riseborough, D. W., & Bonnaventure, P. P. (2015). Eighteen Year Record of Forest Fire Effects on Ground Thermal Regimes and Permafrost in the Central Mackenzie Valley, NWT, Canada. *Permafrost and Periglacial Processes*, *26*(4), 289-303. https://doi.org/10.1002/ppp.1849
Smith, S. L., Wolfe, S. A., Riseborough, D. W., & Nixon, F. M. (2009). Active-layer characteristics and summer climatic indices, Mackenzie Valley, Northwest Territories, Canada. *Permafrost and Periglacial Processes*, *20*(2), 201-220. https://doi.org/10.1002/ppp.651
Steiner, J. L., Briske, D. D., Brown, D. P., & Rottler, C. M. (2018). Vulnerability of Southern Plains agriculture to climate change. *Climatic Change*, *146*(1), 201-218. https://doi.org/10.1007/s10584-017-1965-5
Sturm, M., Holmgren, J., McFadden, J. P., Liston, G. E., Chapin, F. S., & Racine, C. H. (2001). Snow–Shrub Interactions in Arctic Tundra: A Hypothesis with Climatic Implications.

Journal of Climate, *14*(3), 336-344. https://doi.org/10.1175/1520-0442(2001)014<0336:SSIIAT>2.0.CO;2
Sturm, M., & Wagner, A. M. (2010). Using repeated patterns in snow distribution modeling: An Arctic example. *Water Resources Research*, *46*(12). https://doi.org/10.1029/2010WR009434
Sun, X., & Holmes, H. A. (2019). Surface Turbulent Fluxes during Persistent Cold-Air Pool Events in the Salt Lake Valley, Utah. Part I: Observations. *Journal of Applied Meteorology and Climatology*, *58*(12), 2553-2568. https://doi.org/10.1175/JAMC-D-19-0053.1
Tao, J., Koster, R. D., Reichle, R. H., Forman, B. A., Xue, Y., Chen, R. H., & Moghaddam, M. (2019). Permafrost variability over the Northern Hemisphere based on the MERRA-2 reanalysis. *The Cryosphere*, 13, 2087–2110. https://doi.org/10.5194/tc-13-2087-2019
Tarek, M., Brissette, F. P., & Arsenault, R. (2020). Evaluation of the ERA5 reanalysis as a potential reference dataset for hydrological modelling over North America. *Hydrology and Earth System Sciences,* 24, 2527–2544. https://doi.org/10.5194/hess-24-2527-2020
Thaler, E. A., Uhleman, S., Rowland, J. C., Schwenk, J., Wang, C., Dafflon, B., & Bennett, K. E. (2023). High-Resolution Maps of Near-Surface Permafrost for Three Watersheds on the Seward Peninsula, Alaska Derived From Machine Learning. *Earth & Space Science*, *10*(12), e2023EA003015. https://doi.org/10.1029/2023EA003015
Tikhomirov, A. B., Lesins, G., & Drummond, J. R. (2021). Drone measurements of surface-based winter temperature inversions in the High Arctic at Eureka. *Atmospheric Measurement Techniques*, *14*(11), 7123-7145. https://doi.org/10.5194/amt-14-7123-2021
Tjernström, M., Shupe, M. D., Brooks, I. M., Achtert, P., Prytherch, J., Sedlar, J., & Univ. of Colorado, B. C. O. (2019). Arctic Summer Airmass Transformation, Surface Inversions, and the Surface Energy Budget. *Journal of Climate*, *32*(3), 769-789. https://doi.org/10.1175/JCLI-D-18-0216.1
Turcotte, B., Dubnick, A., & McKillop, R. (2024). Icing and aufeis in cold regions II: consequences and mitigation. *Canadian Journal of Civil Engineering*, *51*(2), 125-139. https://doi.org/10.1139/cjce-2023-0119
Turetsky, M. R., Abbott, B. W., Jones, M. C., Walter Anthony, K., Olefeldt, D., Schuur, E. A. G., Koven, C., McGuire, A. D., Grosse, G., Kuhry, P., Hugelius, G., Lawrence, D. M., Gibson, C., & Sannel, A. B. K. (2019). Permafrost collapse is accelerating carbon release. *Nature*, *569*(7754), 32-34. https://doi.org/10.1038/d41586-019-01313-4
Tutton, R., Way, R. G., Beddoe, R., Zhang, Y., & Trant, A. (2021). Modelled soil temperature sensitivity to variable snow and vegetation conditions in low-relief coastal mountains, Nunatsiavut and NunatuKavut, Labrador. In J. Zufelt (Ed.), *Permafrost 2021: Merging permafrost science and cold regions engineering* (pp. 71–81). American Society of Civil Engineers. https://doi.org/10.1061/9780784483589.007
Tutton, R. J., & Way, R. G. (2021). A low-cost method for monitoring snow characteristics at remote field sites. *The Cryosphere*, *15*(1), 1-15. https://doi.org/10.5194/tc-15-1-2021
Urban, M., Eberle, J., Hüttich, C., Schmullius, C., & Herold, M. (2013). Comparison of satellite-derived land surface temperature and air temperature from meteorological stations on the Pan-Arctic scale. *Remote Sensing*, *5*(5), 2348-2367. https://doi.org/10.3390/rs5052348
Urraca, R. and Gobron, N. (2023). Temporal stability of long-term satellite and reanalysis products to monitor snow cover trends, *The Cryosphere*, 17, 1023–1052, https://doi.org/10.5194/tc-17-1023-2023.

Vegter, S., Bonnaventure, P. P., Daly, S., & Kochtitzky, W. (2024). Modelling permafrost distribution using the temperature at top of permafrost model in the boreal forest environment of Whatì, NT. *Arctic Science*, *10*(3), 455-475. https://doi.org/10.1139/as-2023-0010
Vincent, L. A., Milewska, E. J., Wang, X. L., & Hartwell, M. M. (2018). Uncertainty in homogenized daily temperatures and derived indices of extremes illustrated using parallel observations in Canada. *International Journal of Climatology*, *38*(2), 692-707. https://doi.org/10.1002/joc.5203
Vincent, L. A., Wang, X. L., Milewska, E. J., Wan, H., Yang, F., & Swail, V. (2012). A second generation of homogenized Canadian monthly surface air temperature for climate trend analysis. *Journal of Geophysical Research: Atmospheres*, *117*(D18), 148-163. https://doi.org/10.1029/2012JD017859
Vincent, L. A., Zhang, X., Bonsal, B. R., & Hogg, W. D. (2002). Homogenization of Daily Temperatures over Canada. *Journal of Climate*, *15*(11), 1322-1334. https://doi.org/10.1175/1520-0442(2002)015<1322:HODTOC>2.0.CO;2
Vincent, W. F., Lemay, M., & Allard, M. (2017). Arctic permafrost landscapes in transition: towards an integrated Earth system approach. *Arctic Science*, *3*(2), 39-64. https://doi.org/10.1139/as-2016-0027
Vitasse, Y., Klein, G., Kirchner, J. W., & Rebetez, M. (2017). Intensity, frequency and spatial configuration of winter temperature inversions in the closed La Brevine valley, Switzerland. *Theoretical and Applied Climatology*, *130*(3), 1073-1083. https://doi.org/10.1007/s00704-016-1944-1
Vosper, S. B., & Brown, A. R. (2008). Numerical Simulations of Sheltering in Valleys: The Formation of Nighttime Cold-Air Pools. *Boundary-Layer Meteorology*, *127*(3), 429-448. https://doi.org/10.1007/s10546-008-9272-3
Vosper, S. B., Hughes, J. K., Lock, A. P., Sheridan, P. F., Ross, A. N., Jemmett-Smith, B., & Brown, A. R. (2014). Cold-pool formation in a narrow valley. *Quarterly Journal of the Royal Meteorological Society*, *140*(679), 699-714. https://doi.org/10.1002/qj.2160
Vrugt, J. A., & de Oliveira, D. Y. (2022). Confidence intervals of the Kling-Gupta efficiency. *Journal of Hydrology*, *612*, 127968. https://doi.org/10.1016/j.jhydrol.2022.127968
Wahl, H. E., Fraser, D. B., Harvey, R. C., & Maxwell, J. B. (1987). *Climate of Yukon.* Environment Canada. Retrieved May 5, 2025, from https://publications.gc.ca/collections/collection_2020/eccc/En57-7-40-eng.pdf
Walden, V. P., Mahesh, A., & Warren, S. G. (1996). Comment on "Recent changes in the North American Arctic boundary layer in winter" by R. S. Bradley et al. *Journal of Geophysical Research: Atmospheres*, *101*(D3), 7127-7134. https://doi.org/10.1029/95JD03233
Walvoord, M. A., & Striegl, R. G. (2007). Increased groundwater to stream discharge from permafrost thawing in the Yukon River basin: Potential impacts on lateral export of carbon and nitrogen. *Geophysical Research Letters*, *34*(12), L12402. https://doi.org/10.1029/2007GL030216
Wang, T., Hamann, A., Spittlehouse, D. L., & Aitken, S. N. (2006). Development of scale-free climate data for Western Canada for use in resource management. *International Journal of Climatology*, *26*(3), 383-397. https://doi.org/10.1002/joc.1247
Wang, T., Hamann, A., Spittlehouse, D., & Carroll, C. (2016). Locally Downscaled and Spatially Customizable Climate Data for Historical and Future Periods for North America. *PLOS ONE*, *11*(6), e0156720-e0156720. https://doi.org/10.1371/journal.pone.0156720

Wang, X., Tolksdorf, V., Otto, M., & Scherer, D. (2021). WRF-based dynamical downscaling of ERA5 reanalysis data for High Mountain Asia: Towards a new version of the High Asia Refined analysis. *International Journal of Climatology*, *41*(1), 743-762. https://doi.org/10.1002/joc.6686

Wang, X. L., Chen, H., Wu, Y., & Pu, Q. (2010). New Techniques for Detection and Adjustment of Shifts in Daily Precipitation Data Series. *Journal of Applied Meteorology and Climatology*, *49*(12), 2416-2436. https://doi.org/10.1175/2010JAMC2376.1

Wang, X. L., Wen, Q. H., & Wu, Y. (2007). Penalized maximal t test for detecting undocumented mean change in climate data series. *Journal of Applied Meteorology and Climatology*, *46*(6), 916-931. https://doi.org/10.1175/JAM2504.1

Wang, Y., & Way, R. G. (2025). Future Trajectories of Peatland Permafrost Under Climate and Ecosystem Change in Northeastern Canada. *Journal of Geophysical Research: Earth Surface*, *130*(2), e2024JF007930. https://doi.org/10.1029/2024JF007930

Wang, Y., Street, E., & Way, R. G. (2026). Impacts of permafrost thaw on Indigenous cultures, practices, and livelihoods. In *Reference module in Earth systems and environmental sciences*. Elsevier. https://doi.org/10.1016/B978-0-323-85242-5.00061-0

Way, R. G., & Bonnaventure, P. P. (2015). Testing a reanalysis-based infilling method for areas with sparse discontinuous air temperature data in northeastern Canada. *Atmospheric Science Letters*, *16*(3), 398-407. https://doi.org/10.1002/asl2.574

Way, R. G., & Lewkowicz, A. G. (2016). Modelling the spatial distribution of permafrost in Labrador-Ungava using the temperature at the top of permafrost. *Canadian Journal of Earth Sciences*, *53*(10), 1010-1028. https://doi.org/10.1139/cjes-2016-0034

Way, R. G., & Lewkowicz, A. G. (2018). Environmental controls on ground temperature and permafrost in Labrador, northeast Canada. *Permafrost and Periglacial Processes*, *29*(2), 73-85. https://doi.org/10.1002/ppp.1972

Werner, A. T., Schnorbus, M. A., Shrestha, R. R., Cannon, A. J., Zwiers, F. W., Dayon, G., & Anslow, F. (2019). A long-term, temporally consistent, gridded daily meteorological dataset for northwestern North America. *Scientific Data*, *6*(1), 180299-180299. https://doi.org/10.1038/sdata.2018.299

Whiteman, C. D. (1982). Breakup of Temperature Inversions in Deep Mountain Valleys: Part I. Observations. *Journal of Applied Meteorology (1962-1982)*, *21*(3), 270-289. https://doi.org/10.1175/1520-0450(1982)021<0270:BOTIID>2.0.CO;2

Whiteman, C. D. (2000). *Mountain Meteorology: Fundamentals and Applications*. Oxford University Press, New York, NY (US).

Whiteman, C. D., Bian, X., & Zhong, S. (1999). Wintertime Evolution of the Temperature Inversion in the Colorado Plateau Basin. *Journal of Applied Meteorology*, *38*(8), 1103-1117. https://doi.org/10.1175/1520-0450(1999)038<1103:WEOTTI>2.0.CO;2

Whiteman, C. D., Haiden, T., Pospichal, B., Eisenbach, S., & Steinacker, R. (2004a). Minimum Temperatures, Diurnal Temperature Ranges, and Temperature Inversions in Limestone Sinkholes of Different Sizes and Shapes. *Journal of Applied Meteorology*, *43*(8), 1224-1236. https://doi.org/10.1175/1520-0450(2004)043<1224:MTDTRA>2.0.CO;2

Whiteman, C. D., & McKee, T. B. (1982). Breakup of Temperature Inversions in Deep Mountain Valleys: Part II. Thermodynamic Model. *Journal of Applied Meteorology*, *21*(3), 290-302. https://doi.org/10.1175/1520-0450(1982)021<0290:BOTIID>2.0.CO;2

Whiteman, C. D., Muschinski, A., Zhong, S., Fritts, D., Hoch, S. W., Hahnenberger, M., Yao, W., Hohreiter, V., Behn, M., Cheon, Y., Clements, C. B., Horst, T. W., Brown, W. O. J.,

& Oncley, S. P. (2008). METCRAX 2006: Meteorological Experiments in Arizona's Meteor Crater. *Bulletin of the American Meteorological Society*, *89*(11), 1665-1680. https://doi.org/10.1175/2008BAMS2574.1
Whiteman, C. D., Pospichal, B., Eisenbach, S., Weihs, P., Clements, C. B., Steinacker, R., Mursch-Radlgruber, E., & Dorninger, M. (2004b). Inversion Breakup in Small Rocky Mountain and Alpine Basins. *Journal of Applied Meteorology*, *43*(8), 1069-1082. https://doi.org/10.1175/1520-0450(2004)043<1069:IBISRM>2.0.CO;2
Whiteman, C. D., Zhong, S., Shaw, W. J., Hubbe, J. M., Bian, X., & Mittelstadt, J. (2001). Cold Pools in the Columbia Basin. *Weather and Forecasting*, *16*(4), 432-447. https://doi.org/10.1175/1520-0434(2001)016<0432:CPITCB>2.0.CO;2
Wicky, J., & Hauck, C. (2017). Numerical modelling of convective heat transport by air flow in permafrost talus slopes. *The Cryosphere*, *11*(3), 1311-1325. https://doi.org/10.5194/tc-11-1311-2017
Wicky, J., Hilbich, C., Delaloye, R., & Hauck, C. (2024). Modeling the Link Between Air Convection and the Occurrence of Short-Term Permafrost in a Low-Altitude Cold Talus Slope. *Permafrost and Periglacial Processes*, *35*(2), 202-217. https://doi.org/10.1002/ppp.2224
Williams, P. J., & Smith, M. W. (1989). *The frozen earth: fundamentals of geocryology*. Cambridge University Press. https://doi.org/10.1017/CBO9780511564437
Williams, R., & Thorp, T. (2015). Characteristics of springtime nocturnal temperature inversions in a high latitude environment. *Weather*, *70*(S1), S37-S43. https://doi.org/10.1002/wea.2554
Williamson, S. N., Zdanowicz, C., Anslow, F. S., Clarke, G. K. C., Copland, L., Danby, R. K., Flowers, G. E., Holdsworth, G., Jarosch, A. H., & Hik, D. S. (2020). Evidence for Elevation-Dependent Warming in the St. Elias Mountains, Yukon, Canada. *Journal of Climate*, 33(8), 3253-3269. https://doi.org/10.1175/JCLI-D-19-040
Winstral, A., Elder, K., & Davis, R. E. (2002). Spatial Snow Modeling of Wind-Redistributed Snow Using Terrain-Based Parameters. *Journal of Hydrometeorology*, *3*(5), 524-538. https://doi.org/10.1175/1525-7541(2002)003<0524:SSMOWR>2.0.CO;2
Winstral, A., & Marks, D. (2014). Long-term snow distribution observations in a mountain catchment: Assessing variability, time stability, and the representativeness of an index site. *Water Resources Research*, *50*(1), 293-305. https://doi.org/10.1002/2012WR013038
World Meterological Organization. (2012). *Guide to the Global Observing System, 2010 edition Updated in 2012*. http://www.wmo.int/pages/index_en.html
Wright, J. F., Duchesne, C., & Côté, M. M. (2003). Regional-scale permafrost mapping using the TTOP ground temperature model. In *Proceedings of the 8th International Conference on Permafrost* (pp. 1241–1246). Swets & Zeitlinger.
Ye, L., & Wang, Y. (2020). Long-Term Air Quality Study in Fairbanks, Alaska: Air Pollutant Temporal Variations, Correlations, and PM2.5 Source Apportionment. *Atmosphere*, *11*(11), 1203. https://doi.org/10.3390/atmos11111203
Yin, G., Zheng, H., Niu, F., Luo, J., Lin, Z., & Liu, M. (2018). Numerical Mapping and Modeling Permafrost Thermal Dynamics across the Qinghai-Tibet Engineering Corridor, China Integrated with Remote Sensing. *Remote Sensing (Basel, Switzerland)*, *10*(12), 2069. https://doi.org/10.3390/rs10122069

Young, K. L., Woo, M. K., & Edlund, S. A. (1997). Influence of local topography, soils, and vegetation on microclimate and hydrology at a high arctic site, Ellesmere Island, Canada. *Arctic, Antarctic, and Alpine Research*, *29*(3), 270-284. https://doi.org/10.2307/1552141
Yukon Ecoregions Working Group (2004). Yukon Coastal Plain. In: Ecoregions of the Yukon Territory: Biophysical properties of Yukon landscapes, C.A.S. Smith, J.C. Meikle and C.F. Roots (eds.), Agriculture and Agri-Food Canada, PARC Technical Bulletin No. 04-01, Summerland, British Columbia, p. 63-72. Retreived March 1, 2024 from https://yukon.ca/sites/yukon.ca/files/env/env-ecoregions-yukon-territory.pdf
Zeng, H., Tian, P., Zhang, M., Cao, X., Liang, J., & Zhang, L. (2021). Rapid change in surface-based temperature inversions across the world during the last three decades. *Journal of Applied Meteorology and Climatology*, *61*(2), 175-184. https://doi.org/10.1175/JAMC-D-21-0093.1
Zhang, L., Li, J., Ding, M., Guo, J., Bian, L., Sun, Q., Yang, Q., Dou, T., Zhang, W., Tian, B., Lu, C., & Zhang, D. (2021). Characteristics of low-level temperature inversions over the Arctic Ocean during the CHINARE 2018 campaign in summer. *Atmospheric Environment*, *253*, 118333. https://doi.org/10.1016/j.atmosenv.2021.118333
Zhang, T. (2005). Influence of the seasonal snow cover on the ground thermal regime: An overview. *Reviews of Geophysics (1985)*, *43*(4), RG4002. https://doi.org/10.1029/2004RG000157
Zhang, X., Flato, G., Kirchmeier-Young, M., Vincent, L., Wan, H., Wang, X., Rong, R., Fyfe, J., Li, G., & Kharin, V. V. (2019). Changes in temperature and precipitation across Canada. In E. Bush & D. S. Lemmen (Eds.), *Canada's changing climate report* (pp. 112–193). Government of Canada.
Zhang, Y. (2025). *User's manual for the Northern Ecosystem Soil Temperature (NEST) model* (Version 2025). Natural Resources Canada.
Zhang, Y. (2013). Spatio-temporal features of permafrost thaw projected from long-term high-resolution modeling for a region in the Hudson Bay Lowlands in Canada. *Journal of Geophysical Research: Earth Surface*, *118*(2), 542-552. https://doi.org/10.1002/jgrf.20045
Zhang, Y., Chen, W., & Cihlar, J. (2003). A process-based model for quantifying the impact of climate change on permafrost thermal regimes. *Journal of Geophysical Research: Atmospheres*, *108*(D22), 4695-1511. https://doi.org/10.1029/2002JD003354
Zhang, Y., Chen, W., & Riseborough, D. W. (2006). Temporal and spatial changes of permafrost in Canada since the end of the Little Ice Age. *Journal of Geophysical Research*, *111*(D22), D22103-n/a. https://doi.org/10.1029/2006JD007284
Zhang, Y., Chen, W., & Riseborough, D. W. (2008a). Disequilibrium response of permafrost thaw to climate warming in Canada over 1850–2100. *Geophysical Research Letters*, *35*(2), L02502. https://doi.org/10.1029/2007GL032117
Zhang, Y., Chen, W., & Riseborough, D. W. (2008b). Transient projections of permafrost distribution in Canada during the 21st century under scenarios of climate change. *Global and Planetary Change*, *60*(3), 443-456. https://doi.org/10.1016/j.gloplacha.2007.05.003
Zhang, Y., Li, J., Wang, X., Chen, W., Sladen, W., Dyke, L., Dredge, L., Poitevin, J., McLennan, D., Stewart, H., Kowalchuk, S., Wu, W., Kershaw, G. P., & Brook, R. K. (2012). Modelling and mapping permafrost at high spatial resolution in Wapusk National Park, Hudson Bay Lowlands. *Canadian Journal of Earth Sciences*, *49*(8), 925-937. https://doi.org/10.1139/e2012-031

Zhang, Y., Qian, B., & Hong, G. (2020). A long-term, 1-km resolution daily meteorological dataset for modeling and mapping permafrost in Canada. *Atmosphere*, *11*(9), 1-27. https://doi.org/10.3390/atmos11121363

Zhang, Y., & Seidel, D. J. (2011). Challenges in estimating trends in Arctic surface-based inversions from radiosonde data. *Geophysical Research Letters*, *38*(17). https://doi.org/10.1029/2011GL048728

Zhang, Y., Seidel, D. J., Golaz, J.-C., Deser, C., & Tomas, R. A. (2011). Climatological Characteristics of Arctic and Antarctic Surface-Based Inversions. *Journal of Climate*, *24*(19), 5167-5186. https://doi.org/10.1175/2011JCLI4004.1

Zhang, Y., Sherstiukov, A. B., Qian, B., Kokelj, S. V., & Lantz, T. C. (2018). Impacts of snow on soil temperature observed across the circumpolar north. *Environmental Research Letters*, *13*(4), 044012. https://doi.org/10.1088/1748-9326/aab1e7

Zhang, Y., Touzi, R., Feng, W., Hong, G., Lantz, T. C., & Kokelj, S. V. (2021). Landscape-scale variations in near-surface soil temperature and active-layer thickness: Implications for high-resolution permafrost mapping. *Permafrost and Periglacial Processes*, *32*(4), 627-640. https://doi.org/10.1002/ppp.2104

Zhang, Y., Wang, S., Barr, A. G., & Black, T. A. (2008c). Impact of snow cover on soil temperature and its simulation in a boreal aspen forest. *Cold Regions Science and Technology*, *52*(3), 355-370. https://doi.org/10.1016/j.coldregions.2007.07.001

Zhang, Y., Wang, X., Fraser, R., Olthof, I., Chen, W., McLennan, D., Ponomarenko, S., & Wu, W. (2013). Modelling and mapping climate change impacts on permafrost at high spatial resolution for an Arctic region with complex terrain. *The Cryosphere*, *7*(4), 1121-1137. https://doi.org/10.5194/tc-7-1121-2013

Zhang, Y., Wolfe, S. A., Morse, P. D., Olthof, I., & Fraser, R. H. (2015). Spatiotemporal impacts of wildfire and climate warming on permafrost across a subarctic region, Canada. *Journal of Geophysical Research: Earth Surface*, *120*, 2338-2356. https://doi.org/10.1002/2015JF003679

Zhong, S., Whiteman, C. D., Bian, X., Shaw, W. J., & Hubbe, J. M. (2001). Meteorological processes affecting the evolution of a wintertime cold air pool in the Columbia basin. *Monthly Weather Review*, *129*(10), 2600-2613. https://doi.org/10.1175/1520-0493(2001)129<2600:MPATEO>2.0.CO;2

Zhou, L., Stroeve, J., Xu, S., Petty, A., Tilling, R., Winstrup, M., Rostosky, P., Lawrence, I. R., Liston, G. E., Ridout, A., Tsamados, M., & Nandan, V. (2021). Inter-comparison of snow depth over Arctic sea ice from reanalysis reconstructions and satellite retrieval. *The Cryosphere*, *15*(1), 345-367. https://doi.org/10.5194/tc-15-345-2021

Zou, D., Zhao, L., Sheng, Y., Chen, J., Hu, G., Wu, T., Wu, J., Xie, C., Wu, X., Pang, Q., Wang, W., Du, E., Li, W., Liu, G., Li, J., Qin, Y., Qiao, Y., Wang, Z., Shi, J., & Cheng, G. (2017). A new map of permafrost distribution on the Tibetan Plateau. *The Cryosphere*, *11*(6), 2527-2542. https://doi.org/10.5194/tc-11-2527-2017